An Investigation of Microstructure and Texture Evolution in the Near-α Titanium Alloy Timetal® 834

Peter Stephen Davies

Department of Engineering Materials

The University of Sheffield

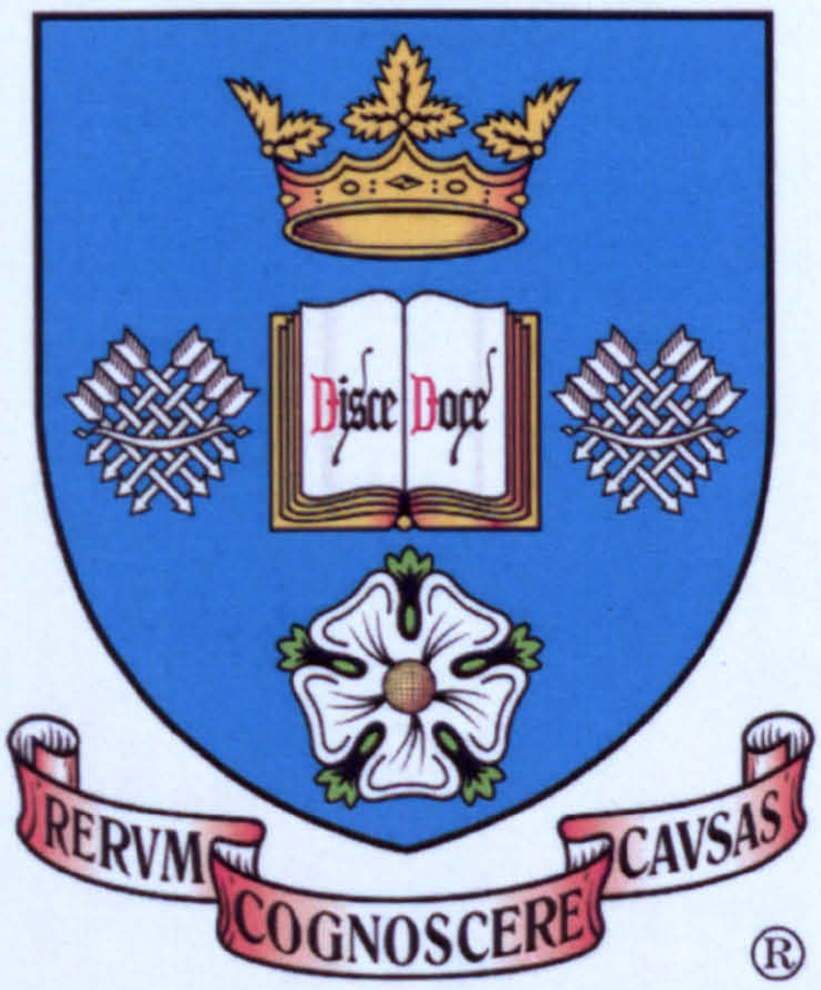

Thesis submitted for the degree of Doctor of Philosophy

March 2009

Volume 1

SUMMARY

Aspects of microstructure and texture evolution in the near-α, titanium alloy, Timetal 834 were investigated. The electron back scatter diffraction (EBSD) technique was used extensively to acquire microtexture data. To aid analysis of this data, a computer program was written in Visual Basic .NET. The two main functions of the program were: (1) to separate the two forms of α phase, primary-α (α_p) and secondary-α (α_s) that are present in bimodal microstructures at room temperature, and (2) to reconstruct the parent β phase, which transforms to α_s on cooling. The β reconstruction was validated using a metastable titanium alloy, which retains enough β phase at room temperature to allow orientations to be measured directly using EBSD. Parent β orientation maps were successfully reconstructed for several alloys, cooled from above and below the β transus, at a range of cooling rates. The limitations of the method are discussed.

Timetal 834 and other titanium alloy forgings can contain regions of closely aligned α_p grains called macrozones that can have a deleterious effect on fatigue performance. Understanding the origin of macrozones and how they change during processing is an important step in optimising process routes for these alloys. A detailed characterisation was carried out on a slice from a Timetal 834 billet using optical metallography, EBSD and neutron texture analysis. Results showed there was a variation in texture and macrozones through the billet, related to the ingot to billet forging process.

The effect of cooling rate on the $\beta \rightarrow \alpha_s$ transformation in a bimodal microstructure was investigated using a Jominy end quench test. At the highest cooling rates, a martensitic microstructure was observed. At lower cooling rates, a diffusional transformation to Widmanstätten α_s, allotriomorphic α at β/β grain boundaries and growth of the existing α_p grains was observed. Variant selection in Widmanstätten α_s was observed at β/β boundaries with specific misorientations and at α_p/β boundaries with a specific orientation relation.

Forging to produce a bimodal microstructure was simulated using laboratory plane strain compression tests at 1010°C. The majority of the strain was accommodated in the β phase. The β phase undergoes dynamic recovery resulting in a subgrain structure. At strain rates above $0.18s^{-1}$, selective recrystallisation in the β phase occurred in the vicinity of β/β grain boundaries and α_p grains. The α_p grains deform by slip and additionally by deformation twinning at strain rates above $1.8s^{-1}$. Some localised dynamic recrystallisation was observed but the majority of the α_p phase remained unrecrystallised. Macrozones remained at a strain of 0.63 but were less apparent at a strain of 1.23.

CONTENTS

ACKNOWLEDGEMENTS

My greatest thanks go to my supervisor Professor W. Mark Rainforth for his guidance, encouragement and patience throughout my time at Sheffield. I would also like to thank my second supervisor Dr Brad Wynne for the valuable input and enthusiasm he has shown towards my work.

I would like to thank Dr Andrew Wilson of Timet UK, for offering advice, information and supplying material for this investigation. I am also grateful to Dr Winfried Kockelmann of The Rutherford Appleton Laboratory for his help with the neutron texture measurements.

Numerous members of staff at the University have helped me to carry out experimental work. I would particularly like to thank Dr Heath Bagshaw, Dr Mike Frolish, Dr Peter Korgul, Mr Dave Manvell, Mr Philip Staton and Mr Ian Watts. I would also like to thank fellow researchers Dr Matthew Thomas, Dr John Hinton and Dr Mike Blackmore for their help with my work.

I would like to thank all of the friends I have made during my time in D1 and IMMPETUS, whose friendship, good humour and encouragement have made it such an enjoyable place to work. I wish everyone success in their studies and future careers.

I am grateful to all of the friends I have made during my time in Sheffield, regardless of whether or not they ever believed I would finish this thesis! I am especially grateful to Catriona for her loving support and encouragement. Thanks also to Andy, Ian, Vince, Tim, Ross, Bob, Jenny, Sophie, Duncan and Will.

Finally, I would like to thank my parents Roger and Pat and my sister Anna and dedicate this thesis to them.

LIST OF FIGURES

LIST OF TABLES

NOMENCLATURE

a	Lattice parameter
A_1	Aspect ratio of undeformed grains
A_2	Aspect ratio of deformed grains
$[Al]_{eq.}$	Aluminium equivalent of α-stabilising elements
$b_{1\rightarrow3}$	Breadth measurements on a PSC specimen
b	Burger's vector
b_h	Instantaneous hot breadth of a deforming PSC specimen
b_{0h}	Initial hot breadth of an undeformed PSC specimen
b_{fc}	Final cold breadth of a deformed PSC specimen
b_{fh}	Final hot breadth of a deformed PSC specimen
bcc	body-centred cubic
c	Lattice parameter
C_b	Spread coefficient for PSC tests
C_c	Crystal coordinate system
C_s	Specimen coordinate system
d	Interplanar spacing
D	Rotation matrix for the Burgers relation
$\vec{d}$	Rotation axis for an orientation expressed as an angle/axis pair
DRE	Dynamic recovery
DRX	Dynamic recrystallisation
EBSD	Electron back scatter diffraction
EBSP	Electron back scatter pattern
f	Correction factor for breadth spreading
g	Rotation describing a crystallographic orientation
Δg	Rotation describing a misorientation between two orientations
g^{α}	An orientation in an inherited α phase
g^{β}	An orientation in a parent β phase
$G^{\beta}_{i=1\rightarrow6}$	The 6 potential parents for an α variant calculated from the average orientation of the variant
GEM	General Materials Diffractomer (a neutron beamline instrument at ISIS)
H	Specimen height for the ring test to determine the friction coeffiecient
$h_{1\rightarrow3}$	Height measurements on a PSC specimen
h_h	Instantaneous hot height of a deforming PSC specimen
h_{0h}	Initial hot height of an undeformed PSC specimen
h_{fc}	Final cold height of a deformed PSC specimen
h_{fh}	Final hot height of a deformed PSC specimen

H_V	Vicker's hardness
hcp	hexagonal close-packed
hk*i*l	Miller-Bravais crystallographic indices
(hk*i*l)	Crystallographic plane
{hk*i*l}	Family of equivalent crystallographic planes
[hk*i*l]	Crystallographic direction
<hk*i*l>	Family of equivalent crystallographic directions
hkl	Miller crystallographic indices
ID	Specimen inner diameter for the ring test to determine the friction coeffiecient
IPF	Inverse pole figure
k	Shear flow stress
L	Transformation matrix for normalising a crystal coordinate system
L	Load
m	Strain rate sensitivity
MAD	Mean angular deviation
MAUD	Materials analysis using diffraction (software for Rietveld refinement)
MDRX	Metadynamic recrystallisation
M_f	Martensite finish temperature
M_s	Martensite start temperature
$[Mo]_{eq.}$	Molybdenum equivalent of β-stabilising elements
m.r.d.	Multiples of random distribution
MUD	Multiples of uniform density (an alternative term for m.r.d. also in use)
ND	Macroscopic normal direction
OD	Specimen outer diameter for the ring test to determine the friction coeffiecient
ODF	Orientation distribution function
$\bar{p}$	Average pressure
PSC	Plane strain compression
$\mathbf{q}$	Unit quaternion
$\tilde{\mathbf{q}}$	Average quaternion
$\mathbf{q}^*$	Inverse of a quaternion (complex conjugate)
q_1, q_2, q_3, q_4	Euler symmetric parameters in a unit quaternion
QE	Quenched end of the Jominy specimen
R1	Arbitrary axis in the plane perpendicular to the billet axis
R2	Axis in the plane perpendicular to the billet axis and perpendicular to R1
RD	Macroscopic rolling direction
S	Stretch parameter for relative Euler contrast
S_i	A set of symmetry operators for a given crystal symmetry
S_i^{α}	The set of 12 symmetry operators for the hexagonal α phase

S_i^β	The set of 24 symmetry operators for the cubic β phase
SIBM	Strain induced boundary migration
T	Temperature
T^0	Initial temperature
T_{nom}	Nominal test temperature
TD	Macroscopic transverse direction
TMC	Thermomechanical Compression
w	width of PSC tool
WQ	Water quench
x	Tool displacement
x_{corr}	Corrected tool displacement
x_{max}	Maximum recorded tool displacement
z_0	The position of the boundary between sliding and sticking friction conditions
α	Low temperature hexagonal close packed phase
α'	Martensitic α
α_{GB}	Allotriomorphic grain boundary α
α_m	Massive α
α_p	Primary-α grain morphology formed in primary processing
α_s	Secondary-α morphology formed in secondary processing by transformation of β
α_t	Thermal expansion coefficient
β	High temperature body centred cubic phase
ε	True strain
$\bar{\varepsilon}$	Equivalent true tensile strain
ε_{nom}	Nominal strain
$\dot{\varepsilon}$	Strain rate
$\dot{\varepsilon}_{nom}$	Nominal strain rate
ε_1	Strain component
ε_2	Strain component
ε_3	Strain component
ϕ_1	First Euler angle (Bunge notation)
Φ	Second Euler angle (Bunge notation)
ϕ_2	Third Euler angle (Bunge notation)
λ	Wavelength
μ	Friction coefficient
θ	Angle
σ	Stress
ρ	Coordinate in Hough space
τ	Shear stress

1 INTRODUCTION

1.1 The Role of Titanium Alloys in the Aero Engine

Titanium alloys are an important class of aero engine materials where high strength to weight ratios at elevated temperatures are key to improved engine performance and enhanced fuel efficiency. Titanium alloys are utilised in the low to moderate temperature regions of the engine for components such as fan blades, compressor blades, stator vanes, and compressor discs (Fig. 1.1). Near-α alloys such as Timetal 834, which have the best high temperature performance of the titanium alloys, are capable of operating at service temperatures up to 600°C. The development of these alloys led to the replacement of heavier nickel based super alloys for parts of the medium and high pressure compressor sections.

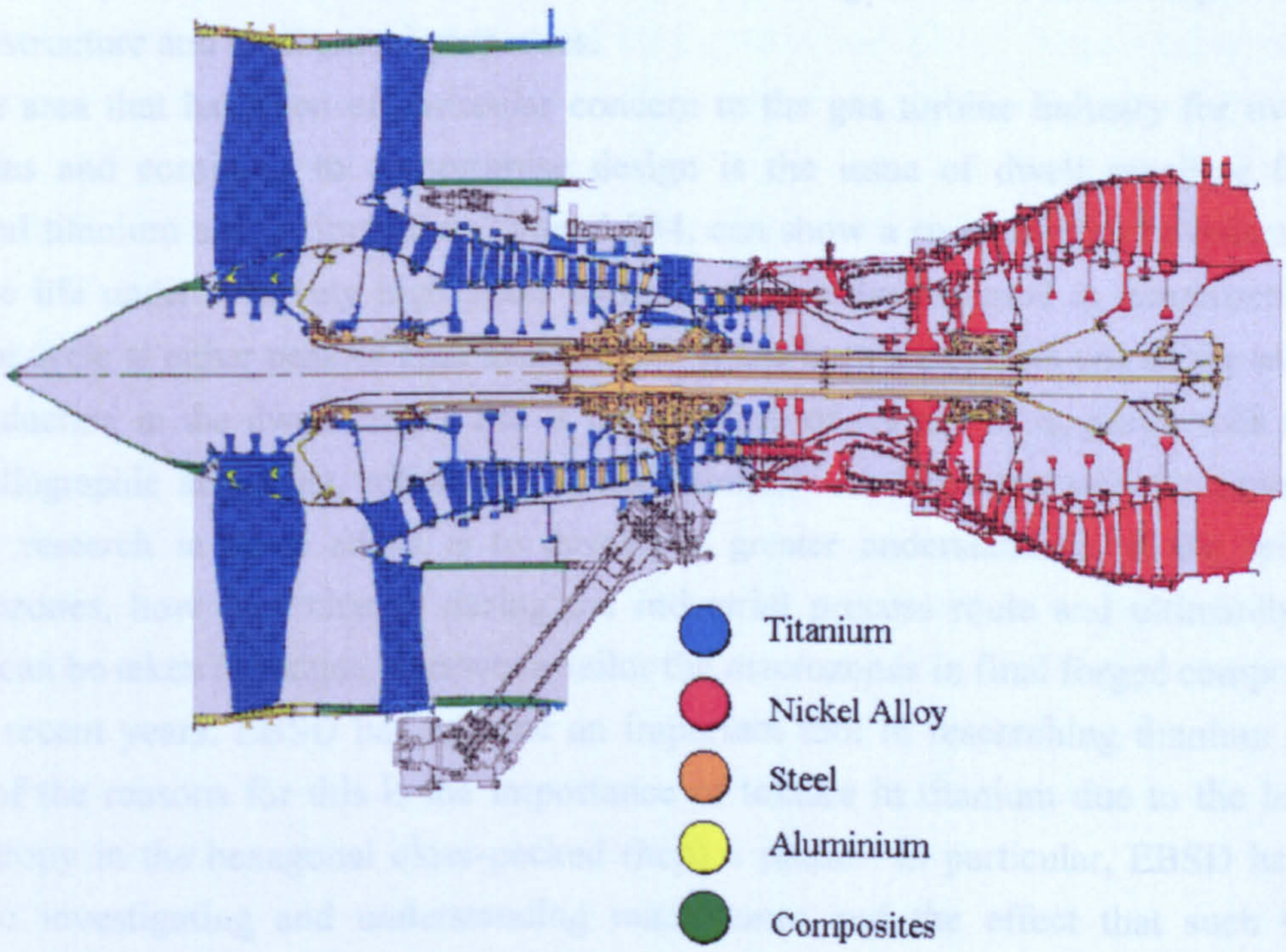

Fig. 1.1 Materials used in a gas turbine engine (Cervenka, 2000).

1.2 The Motivation for Researching Thermomechanical Processing in Titanium Alloys

A good balance of creep and fatigue strength in near-α alloys can be achieved with a bimodal microstructure consisting of equiaxed primary-α grains (α_p) in a matrix of secondary-α (α_s). Converting large cast ingots into final forged components with this microstructure requires a sequence of carefully controlled thermal and thermomechanical processing steps. These include deformation and heat treatments in both the β phase field and the α+β phase field, and several β→α phase transformations on cooling between specific stages of the process. Due to this multitude of steps and the number of variables within each one such as forging temperatures, type of forging, strains, strain rates, cooling rates etc., there is considerable scope to further optimise the manufacturing process. To achieve this, greater understanding is needed of the microstructural evolution through the current process and how this is affected by the process parameters within each of the various steps. Also needed is further understanding of the relationships between microstructure and mechanical properties.

An area that has been of particular concern to the gas turbine industry for over two decades and continues to compromise design is the issue of dwell sensitive fatigue. Several titanium alloys, including Timetal 834, can show a susceptibility to reductions in fatigue life under relatively high stress regimes when a dwell period is introduced to the fatigue cycle at either peak or high mean stress. It has been shown that one of the causes of the reduction in the dwell fatigue life is the presence of regions of α_p grains with a close crystallographic alignment, referred to as macrozones. An important area for current and future research in these alloys is to develop a greater understanding of the origin of macrozones, how they change during the industrial process route and ultimately what steps can be taken to reduce, remove or tailor the macrozones in final forged components.

In recent years, EBSD has become an important tool in researching titanium alloys. One of the reasons for this is the importance of texture in titanium due to the inherent anisotropy in the hexagonal close-packed (hcp) α phase. In particular, EBSD has been key to investigating and understanding macrozones and the effect that such texture heterogeneities have on dwell fatigue. Another important use of the technique is in the study of variant selection phenomena occurring in the β→α phase transformation. Going beyond a standard EBSD analysis of the phases present at room temperature, through post-processing of the data from an inherited α_s phase, it is possible to reconstruct orientation image maps and textures for the parent β phase. In cases where the phase transformation is complete or there are only small amounts of the retained parent phase, an ability to reconstruct the parent β phase from EBSD data for the low temperature phase is a powerful investigative tool with potential applications in numerous areas of titanium research.

1.3 Project Aim

The aim of this work is to develop EBSD post-processing techniques that will aid current and future research efforts into titanium and other hcp alloys, and where appropriate, to apply these techniques to the investigation of microstructure and texture evolution in Timetal 834 under conditions relevant to the industrial process route.

1.4 Project Objectives

The first objectives are concerned with EBSD post-processing:

- To find a technique to accurately separate the α_p and α_s phase in EBSD datasets for bimodal microstructures.

- To develop a means of automatically reconstructing EBSD maps of the parent β phase from a standard EBSD analysis of the inherited α_s phase.

The material for this work was in the form of offcuts from a Timetal 834 billet. As this would form the starting material for subsequent investigation and could give valuable insight into the ingot to billet forging process, a key aim was to:

- Characterise the starting material in terms of microstructure and texture.

Two areas for experimental investigation with relevance to the industrial process route were identified, forming two further objectives:

- Investigate the effect of cooling rate on the $\beta \rightarrow \alpha$ phase transformation in a bimodal microstructure.

- Investigate the effect of process parameters on microstructural evolution in the α_p and β phases for the secondary forging of a bimodal microstructure.

1.5 Thesis Outline

Chapter 2 is a literature review. It includes a general background to titanium and its alloys and then focuses on previous work relevant to the work detailed in this thesis: the $\beta \rightarrow \alpha$ phase transformation, microstructural evolution during thermomechanical processing and EBSD post-processing techniques.

Chapter 3 describes the experimental procedures used in this work. It describes the methodology that was used to characterise the Timetal 834 billet, which was the starting material used in this study. Three experimental techniques are then described: heat treatments to determine a β approach curve, a modified Jominy end quench test to investigate the $\beta \rightarrow \alpha$ phase transformation and simulated industrial forging using laboratory plane strain compression tests. Finally, metallography and analysis techniques used to investigate the various specimens are described.

Chapter 4 describes the development of the EBSD post-processing techniques that were developed to aid the analysis of microtexture data. These were incorporated into a computer program written in Visual Basic .NET. The most important features of the program are a technique to separate α_p and α_s in EBSD datasets of bimodal microstructures and a technique to automatically reconstruct the orientations of the parent β phase from a dataset of inherited α_s. The validation and testing of the β reconstruction technique is described.

Chapter 5 concerns the work that was carried out to fully characterise the starting material used in this study, which was in the form of a round billet supplied by Timet UK. This work focused on the macrozones and global textures in the billet and how these are related to the ingot to billet forging process.

Chapter 6 describes the determination of the β approach curve for the as-received material, which was an important first step before undertaking further experiments.

Chapter 7 reports and discusses the results of the investigation into the effect of cooling rate on the $\beta \rightarrow \alpha$ phase transformation in a bimodal microstructure using a modified Jominy test. EBSD analysis together with the β reconstruction technique was used to study variant selection in this transformation.

Chapter 8 reports and discusses the results of simulated secondary working (forging in the $\alpha+\beta$ phase field at 1010°C) using laboratory plane strain compression tests. This work focuses on the deformation and dynamic restoration processes occurring in the

equiaxed α_p grains and the continuous β matrix. The β reconstruction technique was an important tool for understanding microstructural evolution in the high temperature β phase.

Chapter 9 summarises the principal observations and draws conclusions from this work.

Chapter 10 suggests areas requiring further investigation if future work is undertaken.

2 LITERATURE REVIEW

2.1 Titanium, Alloy Classifications and the Near-α Alloy Timetal 834

2.1.1 Titanium

Titanium oxide was first discovered in 1791 but it was not until 1910 that the metal was first isolated by the reduction of titanium tetrachloride ($TiCl_4$) with sodium. At the start of the Second World War, Wilhelm Justin Kroll demonstrated that titanium could be extracted commercially from $TiCl_4$ using magnesium as the reducing agent. Today, this is still the most widely used method of extracting titanium commercially and is known as the "Kroll Process". After the Second World War, titanium alloys quickly became important materials for aircraft engines and air frames (Leyens and Peters, 2003). Today the aerospace industry is still the primary user of titanium alloys, with aerospace accounting for 55% of titanium use in the USA in 2002 (Gambogi, 2004). The most important non-aerospace applications are chemical processing and marine equipment. Other uses include those in the oil and gas, pulp and paper, consumer goods and medical industries. In 2001, world production of titanium was estimated at 60,000 tons per year (Ginatta, 2001).

The properties that make titanium and its alloys attractive engineering materials are high specific strength and excellent corrosion resistance. The high specific strength when compared with other light alloys, steels and nickel based alloys is shown in Fig. 2.1 (Polmear, 1989). It is this high specific strength maintained at elevated temperatures, which explains the important role of titanium alloys in aero engines. The main disadvantage of titanium and its alloys is the higher cost relative to competing materials, primarily steels and aluminium alloys. This is due to higher raw material costs arising from the extraction process and higher secondary costs of semi-finished and final products.

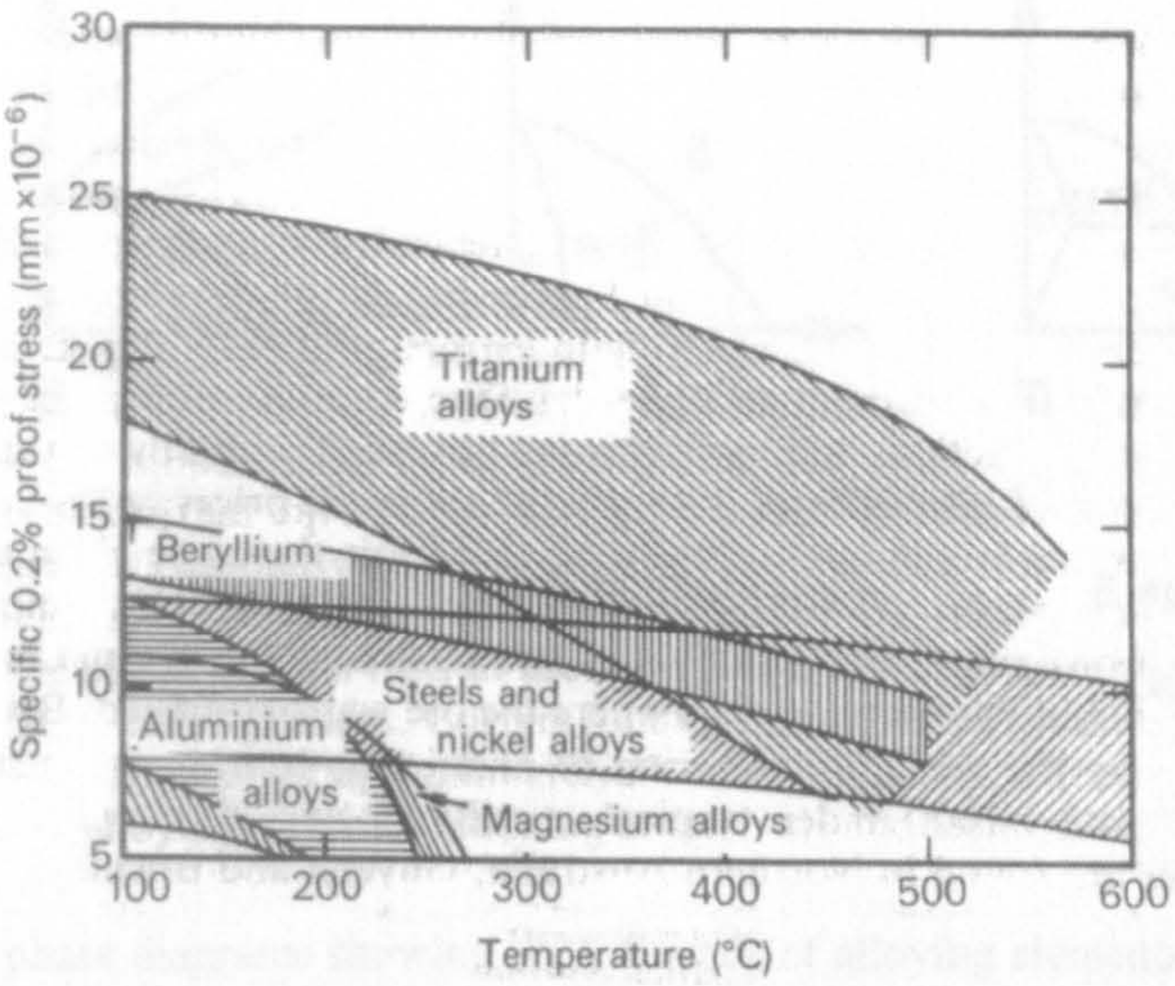

Fig. 2.1 Relationship of specific 0.2% proof stress with temperature for light alloys, steels and nickel alloys (Polmear, 1989).

2.1.2 Alloying Elements

Titanium is an allotropic element, which means it can have more than one crystal structure. At low temperatures, titanium has a modified ideally hexagonal close packed (hcp) structure, which is referred to as the α phase. At high temperatures up to the melting point, the body centred cubic (bcc) structure is stable and is referred to as the β phase. The transition between these two phases occurs at the β transus temperature, which is defined as the lowest equilibrium temperature at which the material is 100% β (Boyer, 1985). The β transus temperature for pure titanium is 882 ±2 °C (Leyens and Peters, 2003). The allotropic transformation means that it is possible to have alloys with α, β or mixed α/β microstructures, which enables a range of properties to be achieved.

Alloying additions influence the β transus and open up a two phase α+β field on the phase diagram. Alloying elements are classified as α-stabilisers, β-stabilisers or neutral, depending on their influence on the β transus temperature, as shown in Fig. 2.2 (Leyens and Peters, 2003). α-stabilising elements dissolve preferentially in the α phase, expanding this phase field, thus raising the β transus temperature. β-stabilising elements expand the β phase field to lower temperatures, lowering the β transus temperature. Elements which do not significantly alter the β transus temperature are classified as neutral.

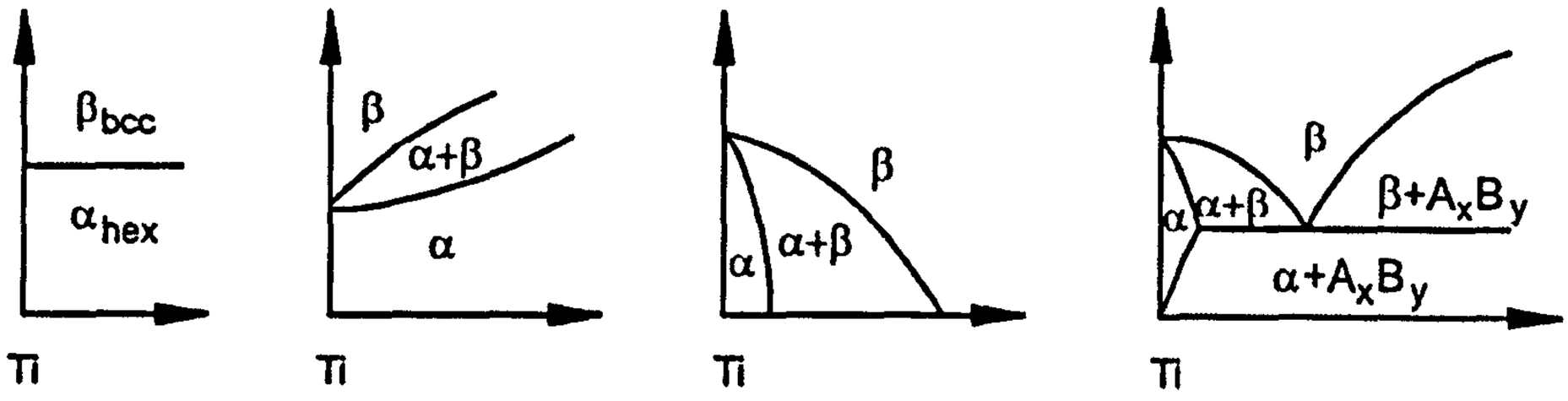

Fig. 2.2 Schematic phase diagrams showing the influence of alloying elements on titanium alloys (Leyens and Peters, 2003).

Aluminium is the most important α stabiliser. It causes solid solution hardening of the α phase at ambient and elevated temperatures and is a major constituent of most commercial alloys (Duncan *et al.*, 1981). One estimate suggests that there is an increase in strength of approximately 55 MPa for each one weight percent added (Baxter, 1994). The addition of aluminium also increases creep strength and moduli; lower alloy density is an important additional advantage.

The interstitial elements oxygen, nitrogen and carbon are strong α-stabilisers. These elements are usually present as impurities in commercial alloys and cause interstitial hardening of the α phase. In commercially pure (CP) titanium, the oxygen content is controlled to provide several grades offering different combinations of strength and ductility.

The α phase is also strengthened by additions of tin and zirconium. These elements exhibit extensive solubility in the α and β phases, and are regarded as neutral because they do not significantly alter the β transus temperature. These elements increase strength by between 35 and 70 MPa for each one weight percent added (Polmear, 1989).

There is a practical limit to the amount of α-stabilising elements that can be added to titanium alloys because if the 'aluminium equivalent' exceeds approximately 9%, an alloy embrittling, ordering reaction occurs (Boyer, 1995). The aluminium equivalent, or ordering parameter, can be calculated from the following empirical formula (Leyens and Peters, 2003).

$$[Al]_{eq.} = [Al] + 0.33\,[Sn] + 0.17\,[Zr] + 10\,[O] \qquad (2.1)$$

β-stabilising elements are divided into two groups, β-isomorphous and β-eutectoid. Commonly used β-isomorphous elements include Molybdenum, Vanadium and Niobium. As well as stabilising the β phase, these elements solid solution harden the β phase. Niobium also increases oxidation resistance at high temperatures. β-eutectoid elements, e.g. iron, manganese, chromium, cobalt, nickel, copper, silicon and hydrogen, have restricted solubilities in the β phase and form intermetallic compounds by eutectoid decomposition. However, the kinetics of the eutectoid reactions are very slow for a number of alloys such that they can be considered to behave as if they conformed to the β-isomorphous phase diagram (Polmear, 1989). Examples of elements for which the reactions are very sluggish are iron, chromium and manganese. For copper and silicon, the decomposition occurs more rapidly and the precipitation of intermetallics can enhance mechanical properties (Duncan *et al.*, 1981). Copper is used in certain alloys to give strengthening by a classical age hardening reaction, while silicon has a major effect on strength and creep resistance, by solid solution hardening and precipitation of silicide particles if the solubility limit is exceeded (Meetham and Van de Voorde, 2000). The solid solution strengthening and β-stabilising capacity of β stabilising alloying elements is given in Table 2.1 (Polmear, 1989).

Table 2.1 Solid solution strengthening and β-stabilising capacity of β-stabilising elements (Polmear, 1989).

	Element							
	V	Cr	Mn	Fe	Co	Ni	Cu	Mo
Solid solution strengthening (MPa $wt\%^{-1}$)	19	21	34	46	48	35	14	27
Minimum alloy content to retain β on quenching (%)	14.9	6.3	6.4	3.5	7	9	13	10

The combined effect of β-stabilising alloying additions is given by the molybdenum equivalent, which can be calculated from the following empirical formula (Polmear, 1989).

$$[Mo]_{eq.} = [Mo] + 0.2\,[Ta] + 0.28\,[Nb] + 0.4\,[W] + 0.67\,[V] + 1.25\,[Cr] + 1.25\,[Ni] + 1.7\,[Mn] + 1.7\,[Co] + 2.5\,[Fe] \quad (2.2)$$

2.1.3 Classification of Titanium Alloys

Titanium alloys are classified into five groups depending on which major phases are present at room temperature. These five groups are: α alloys, near-α alloys, α+β alloys, near β alloys and β alloys. A schematic section through a ternary titanium system

containing both α and β stabilising elements is shown in Fig. 2.3 (Flower, 1990). The composition ranges corresponding to the five groups of alloys are indicated in the upper part of the diagram. The dashed line marked M_s/M_f indicates the martensitic start and finish lines, which are typically very close together for titanium alloys.

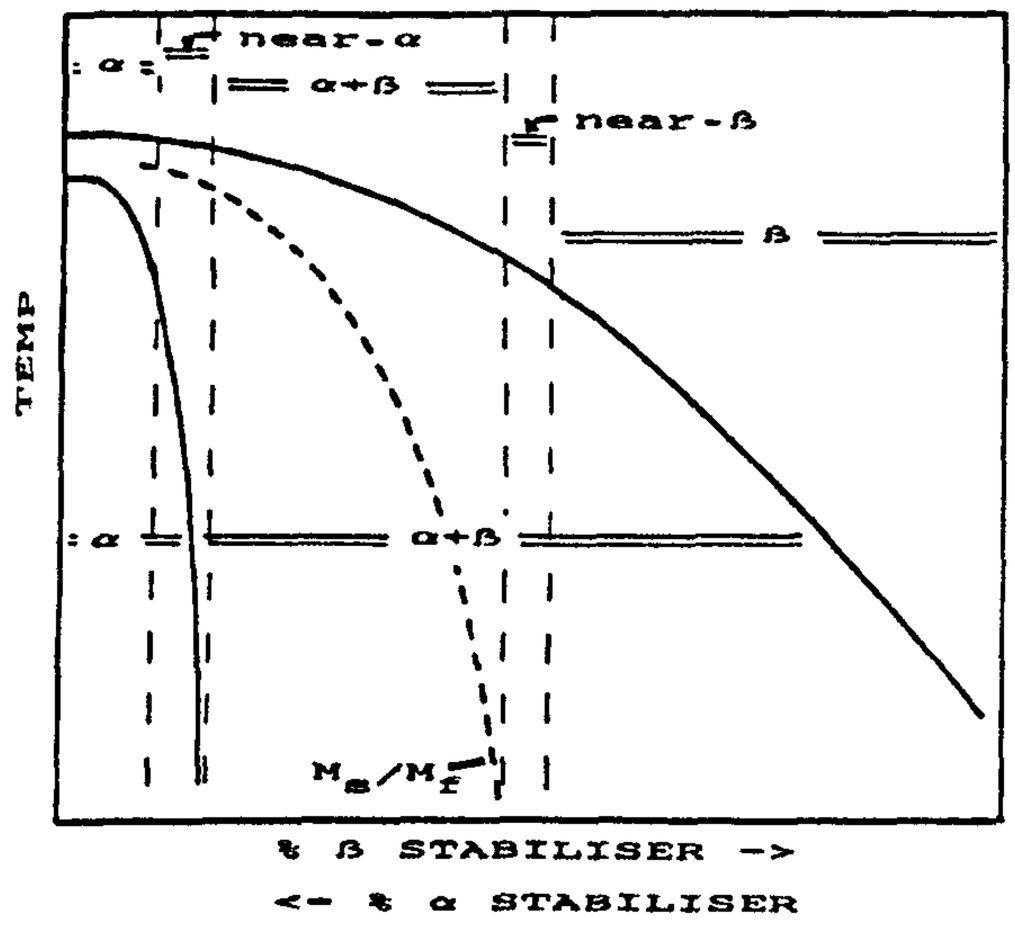

Fig. 2.3 Schematic vertical section for ternary titanium alloys containing both α and β stabilising solute elements (Flower, 1990).

The α range covers compositions in which β, even in metastable form, cannot be retained at room temperature because the composition of the β is such that it lies to the left of the M_s/M_f line at room temperature and thus transforms to martensite when quenched. Consequently, α alloys have microstructures consisting of either α, martensitic α' or a combination of the two depending on the cooling rate. The near-α range covers compositions in which α+β heat treatment can produce β with a composition to the right of the M_s/M_f line at room temperature and as a result retain this β in metastable form at room temperature. The α+β alloys contain a mixture of α and β phases at room temperature. The α+β range extends to the composition of the M_s/M_f line at room temperature, beyond which it is possible to have microstructures consisting of 100% retained β. The near β composition range lies just to the right of the M_s/M_f line at room temperature; the retained β is highly metastable and it can transform to martensite (α') upon deformation. With further additions of β stabilisers, the retained β can only be transformed by precipitation reactions within the α+β field, these are the β alloys.

2.1.4 Near-α Alloys

Near-α alloys have the best mechanical properties retention and creep resistance at high temperatures and as a result are the preferred alloys for high temperature applications (Boyer, 1985). They were developed for use in the compressor sections of aircraft gas turbine engines and today are used for components such as blades, vanes, discs and rings at service temperatures as high as 600°C. This upper bound is due mainly to long-term surface and bulk metallurgical stability problems (Eylon *et al.*, 1984). In long term elevated temperature applications, oxygen enrichment at the surface results in the formation of a brittle 'α case', which dramatically reduces ductility and fatigue strength (Leyens and Peters, 2003).

Near-α alloys have microstructures consisting predominantly of highly alloyed α phases, which exploit the superior creep resistance of the α phase. The morphologies of the α phases present in the microstructure, which are controlled by the process route, influence important properties such as fracture toughness, and fatigue resistance. This gives considerable scope for alloy and process design.

Near-α alloys contain solutes which stabilise the α phase but also contain small amounts of β stabilising elements such as molybdenum and vanadium (Weiss and Semiatin, 1999), which opens up the α+β temperature range sufficiently for both α+β and β processing to be possible. Ti-6242S is an example of an alloy normally processed entirely within the β phase field at temperatures around 1100°C, while Timetal 834 is an alloy designed to be processed at lower temperatures within the α+β phase field. In β processed alloys, the microstructure consists of α produced by transformation of the large β grained structure. At slower cooling rates, a small volume fraction of metastable β is retained at the α platelet boundaries (Flower, 1990). In α+β processed alloys, the prior β grain size is much smaller due to the pinning effect of the α_p phase. An optimum of about 15 vol% α_p is retained in the structure after processing, the balance being transformed β i.e. α_s and small amounts of retained β.

2.1.5 Timetal 834

Timetal 834 is an example of the state of the art in the development of high temperature titanium alloys, having a maximum application temperature of 600°C (Leyens and Peters, 2003). The philosophy behind the design of Timetal 834 is illustrated in Fig. 2.4 (Goosey, 1989). The bimodal microstructure that results from α+β processing combines the advantages of β heat treated near-α alloys with those of α+β alloys that have been α+β heat treated. In addition to creep resistance, the main advantages of a transformed β

structure are high fracture toughness and crack propagation resistance. The fine equiaxed structure of $\alpha+\beta$ alloys gives good fatigue resistance, ductility and defect tolerance. In Timetal 834, correct processing and heat treatment results in a microstructure which combines these properties. Fig. 2.5 shows how the best balance of properties are achieved with an α_p volume fraction of about 15%. The optimum microstructure of Timetal 834 is shown in Fig. 2.6 (Lütjering, 1998).

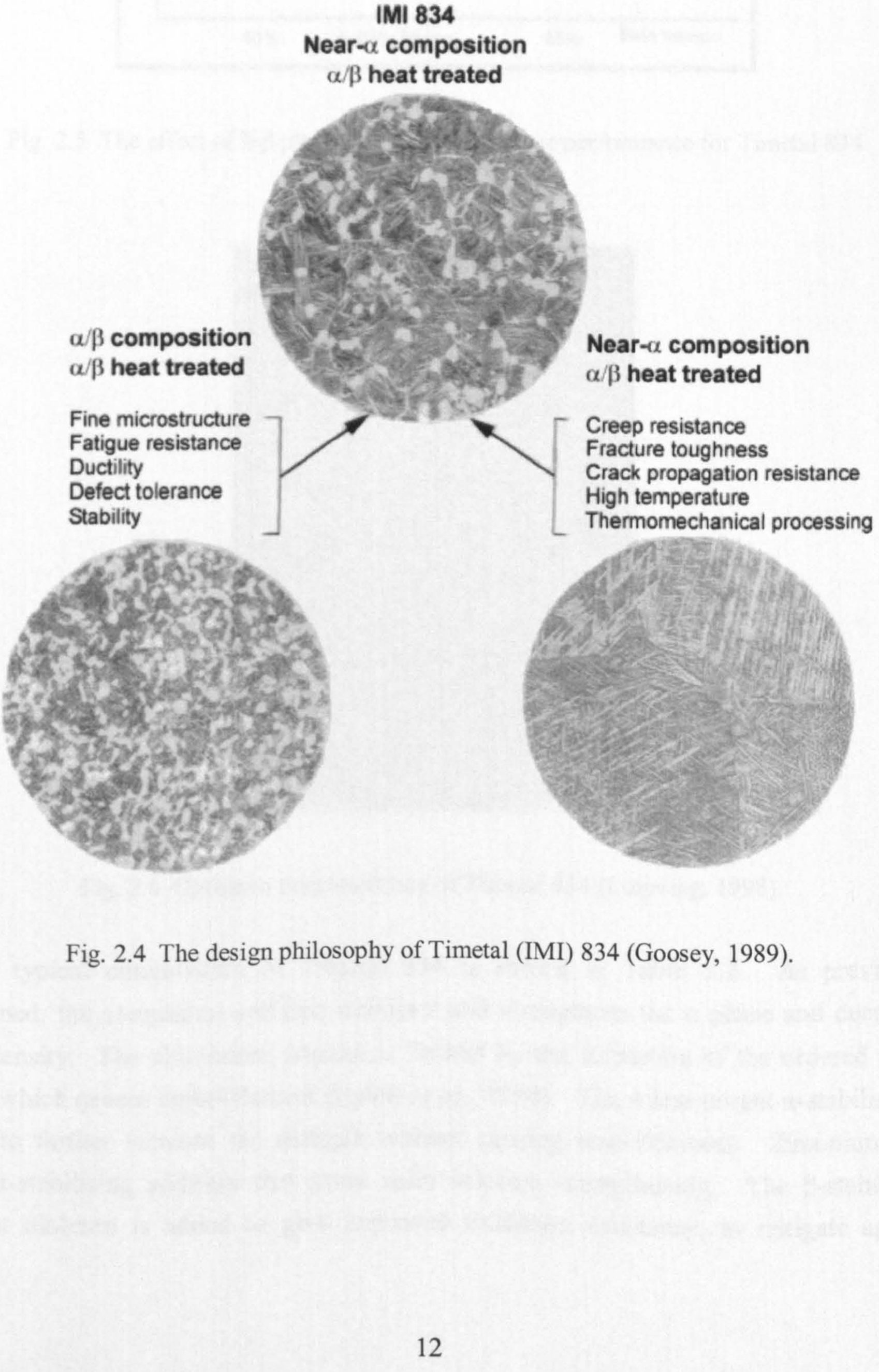

Fig. 2.4 The design philosophy of Timetal (IMI) 834 (Goosey, 1989).

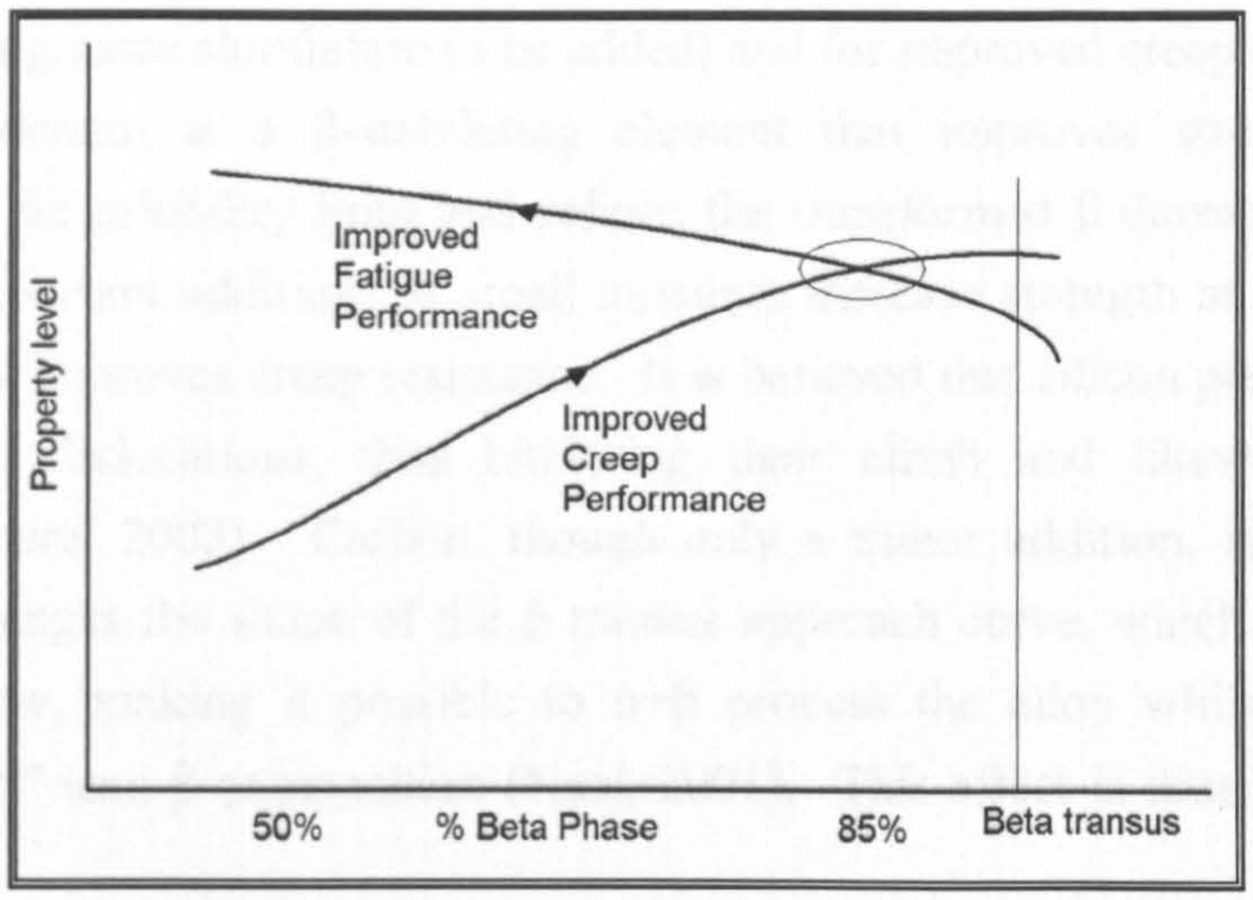

Fig. 2.5 The effect of %β phase on creep and fatigue performance for Timetal 834 (Daeubler *et al.*, 1990).

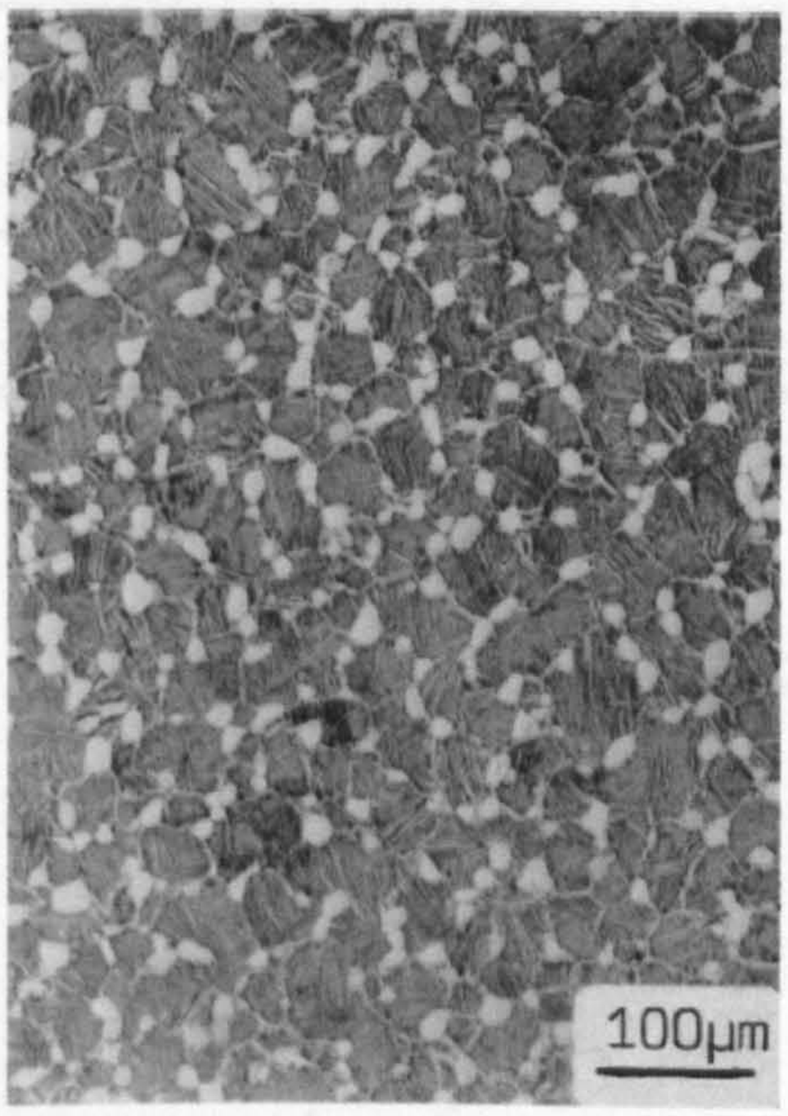

Fig. 2.6 Optimum microstructure of Timetal 834 (Lütjering, 1998).

The typical composition of Timetal 834 is shown in Table 2.2. As previously mentioned, the aluminium addition stabilises and strengthens the α phase and decreases alloy density. The aluminium content is limited by the formation of the ordered phase Ti_3Al, which causes embrittlement (Eylon *et al.*, 1984). Tin, a less potent α-stabiliser, is added to further increase the strength without causing embrittlement. Zirconium is a weak α-stabilising addition that gives solid solution strengthening. The β-stabilising element niobium is added to give improved oxidation resistance, to mitigate against

ordering (allowing more aluminium to be added) and for improved creep resistance (Neal, 2001). Molybdenum is a β-stabilising element that improves strength and creep resistance up to its solubility limit and refines the transformed β during heat treatment. Silicon is an important addition, as small amounts increase strength at all temperatures and substantially improves creep resistance. It is believed that silicon precipitates at high temperatures on dislocations, thus hindering their climb and likewise deformation (Leyens and Peters, 2003). Carbon, though only a minor addition, is a key alloying element as it changes the shape of the β transus approach curve, which widens the heat treatment window, making it possible to α+β process the alloy whilst maintaining a "creep optimised" lean β composition (Neal, 2001). This effect is illustrated in Fig. 2.7 (Neal, 1988).

Table 2.2 Nominal composition of Timetal 834.

	Element							
	Al	Sn	Zr	Nb	Mo	Si	C	Ti
Wt%	5.8	4	3.5	0.7	0.5	0.35	0.06	Balance

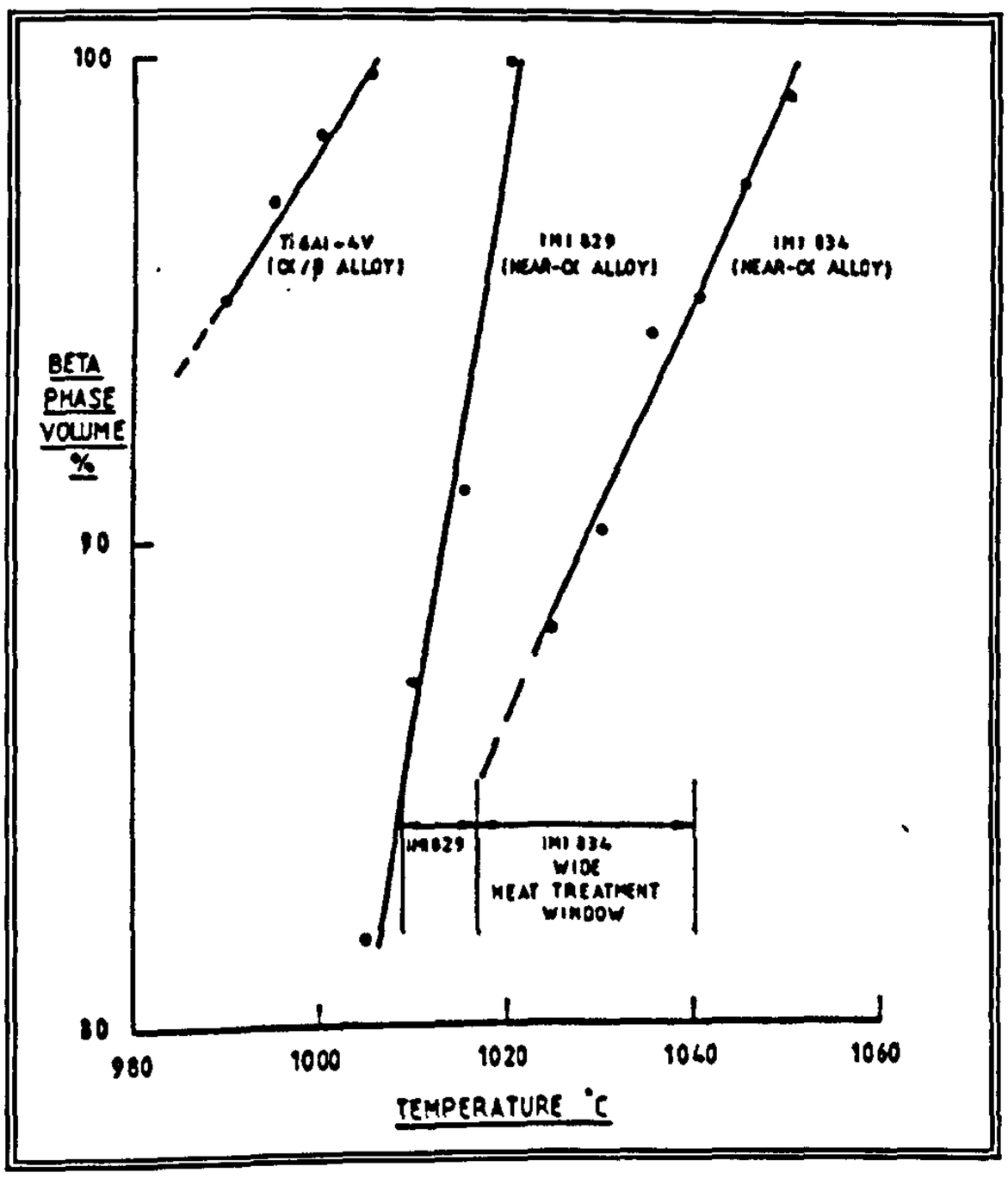

Fig. 2.7 β transus approach curves of the alloys Timetal (formerly IMI) 834, Timetal (formerly IMI) 829 and Ti6Al-4V (Neal, 1988).

2.2 Crystallography and Deformation Modes of α Titanium

Pure titanium and near-α alloys consist predominantly of the hexagonal α phase at low temperatures. A general background on dislocations in hexagonal close-packed (hcp) metals is given by Hull and Bacon (2001). A comprehensive review of the crystallography, deformation modes and dislocations in hcp metals was given by Partridge (1967).

2.2.1 Crystal Structure

The primitive unit cell for hcp metals is shown in Fig. 2.8(a), together with the unit cell parameters a and c. The hexagonal symmetry of the hcp lattice is more commonly illustrated by means of the hexagonal prism shown in Fig. 2.8(b), which consists of three primitive unit cells in different orientations; it is not a true cell because repetition in three dimensions will not build up a three dimensional lattice. The ABAB stacking sequence of the close packed basal planes perpendicular to the c-axis is shown in Fig. 2.8(c). The ideal c/a ratio for the close packing of hard spheres is 1.633 ($\sqrt{8/3}$). No pure hcp metal has this ideal c/a ratio, the c/a ratios for some of the important hcp metals are shown in Table 2.3 (Hull and Bacon, 2001).

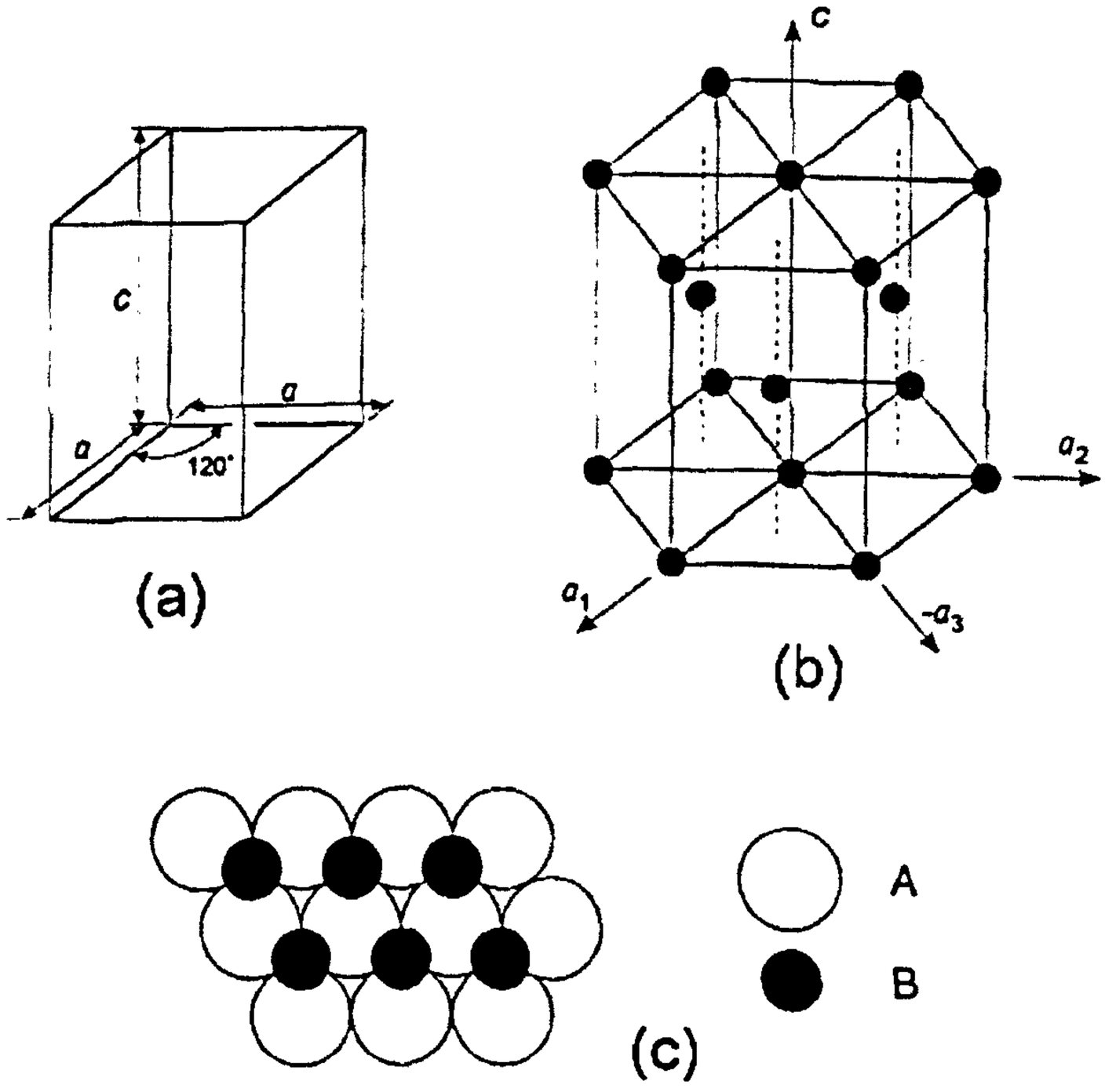

Fig. 2.8 Close-packed hexagonal structure: (a) the unit cell of the lattice, (b) the hexagonal cell showing the arrangement of atoms, (c) ABAB... stacking sequence of the close-packed basal planes perpendicular to the c-axis (Hull and Bacon, 2001).

Table 2.3 c/a ratios and preferred crystallographic slip plane for some hcp metals at 300 K (Hull and Bacon, 2001).

	Metal						
	Be	Ti	Zr	Mg	Co	Zn	Cd
c/a ratio	1.568	1.587	1.593	1.623	1.628	1.856	1.886
preferred slip plane for **b=a**	basal	prism	prism	basal	basal	basal	basal

2.2.2 Crystallographic Indices

If Miller indices are used to define crystallographic planes and directions in the hexagonal structure, crystallographically equivalent sets of planes and directions can have combinations of different numbers. For this reason, indexing in hexagonal crystals is usually based on the Miller-Bravais four index notation. The position of the four axes a_1, a_2, a_3 and c used for this notation are shown in Fig. 2.8(b). Planes are denoted by the Miller-Bravais indices (hkil) with h+k+i=0. Equivalent planes are obtained by interchanging the positions and signs of the first three indices. Similarly, directions in Miller-Bravais indices are described by [uvtw], with u+v+t=0. Since the third index in Miller-Bravais notation can be derived from the first two, it is sometimes omitted or replaced by a dot. When this is the case, it should not be confused with Miller indices.

2.2.3 Deformation Modes

The Peierls-Nabarro stress for slip in a crystal is expected to be smaller for the most widely spaced planes and the shortest lattice translations, meaning slip should occur most easily along close-packed directions on close-packed planes (Hull and Bacon, 2001). The close-packed directions for easy crystallographic slip in hcp crystals are the three $<1\bar{2}10>$ or <a> directions. The three most widely spaced sets of planes which contain this direction are the (0002) basal planes, the three $\{10\bar{1}0\}$ prismatic planes and the six $\{10\bar{1}1\}$ pyramidal planes, see Fig. 2.9.

The slip modes of hcp titanium were first established by Churchman (1954) and others (Williams and Eppelschiemer, 1953. Rosi *et al.*, 1953. Anderson *et al.*, 1953) by observing the slip lines on deformed single crystals of commercially pure titanium. It is now well established that prismatic $<1\bar{2}10>\{10\bar{1}0\}$ slip is always the easiest slip mode at low temperatures, followed by basal slip $<1\bar{2}10>\{0002\}$ slip. Both of these slip

systems are commonly observed. In addition, activation of pyramidal <a> slip systems in polycrystalline aggregates occurs primarily due to the large stresses generated in grain boundary regions because of the misorientation between neighbouring grains (Balasubramanian and Anand, 2002).

A polycrystal requires five independent shear systems to satisfy Von Mises' criterion that every grain should be able to undergo homogeneous strain to meet the shape changes imposed by its neighbours (von Mises and Angew, 1928. Taylor, 1938. Groves and Kelly, 1963). A shear system is independent of others if its operation produces a change in shape that cannot be produced by a combination of strains on those other systems. The basal, prismatic and pyramidal slip systems mentioned thus far, all slip in the $<1\bar{2}10>$ or <a> close-packed directions. These directions are all perpendicular to the c-axis and therefore slip on these systems cannot produce a strain in the c direction. This is reflected in the fact that these three systems only contribute four independent slip systems. Consequently, to accommodate straining in the c-direction, deformation twinning and <c+a> slip must be operative (Balasubramanian and Anand, 2002). Six possible titanium twinning systems are listed in Table 2.4 (Mironov *et al.*, 2006). Deformation twinning is the dominant mechanism for strain in the c-direction at low homologous temperatures. At high homologous temperatures, slip is the dominant mechanism and <c+a> slip in the $<\bar{2}113>$ directions on first order $\{10\bar{1}1\}$ and second order $\{2\bar{1}\,\bar{1}2\}$ planes becomes possible, see Fig. 2.9 (Paton and Backofen, 1970. Balasubramanian and Anand, 2002).

Table 2.4 Twin systems in α titanium (Mironov *et al.*, 2006)

Twin Plane	Shear Direction	Misorientation θ <*uvtw*>
$\{11\bar{2}2\}$	$\langle\bar{1}\,\bar{1}23\rangle$	64.62° $\langle10\bar{1}0\rangle$
$\{11\bar{2}1\}$	$\langle\bar{1}\,\bar{1}26\rangle$	35.1° $\langle10\bar{1}0\rangle$
$\{10\bar{1}2\}$	$\langle\bar{1}011\rangle$	84.78° $\langle2\bar{1}\,\bar{1}0\rangle$
$\{10\bar{1}1\}$	$\langle\bar{1}012\rangle$	57.42° $\langle2\bar{1}\,\bar{1}0\rangle$
$\{1\,\bar{1}24\}$	$\langle\bar{2}\bar{2}43\rangle$	76.66° $\langle10\bar{1}0\rangle$
$\{11\bar{2}3\}$	$\langle\bar{1}\,\bar{1}22\rangle$	86.98° $\langle10\bar{1}0\rangle$

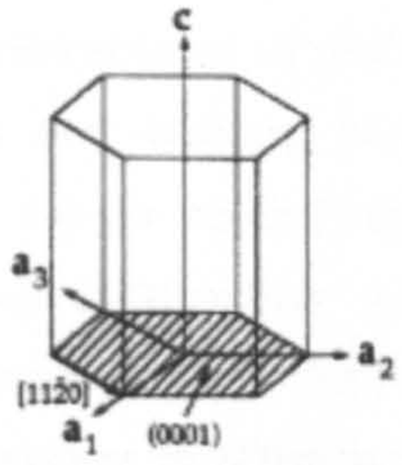

Basal-< a >
(0001) < 11$\bar{2}$0 >, 3

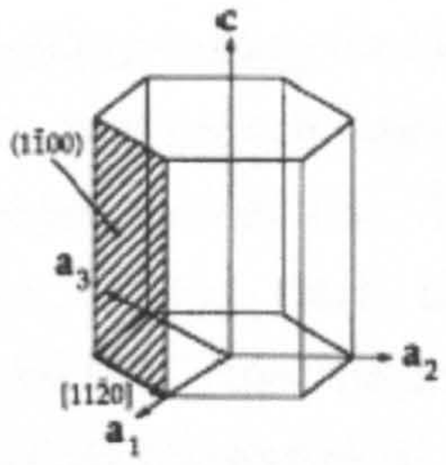

Prismatic-< a >
{10$\bar{1}$0} < 11$\bar{2}$0 >, 3

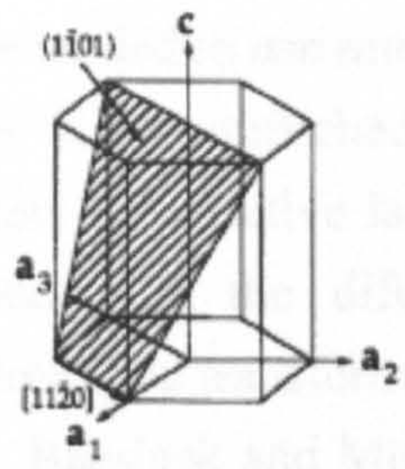

Pyramidal-< a >
{10$\bar{1}$1} < 11$\bar{2}$0 >, 6

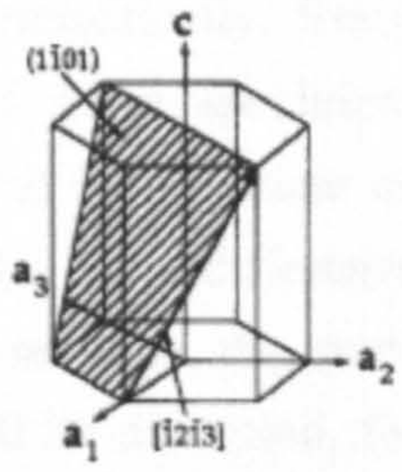

1st order Pyramidal-< c + a >
{10$\bar{1}$1} < 11$\bar{2}$3 >, 12

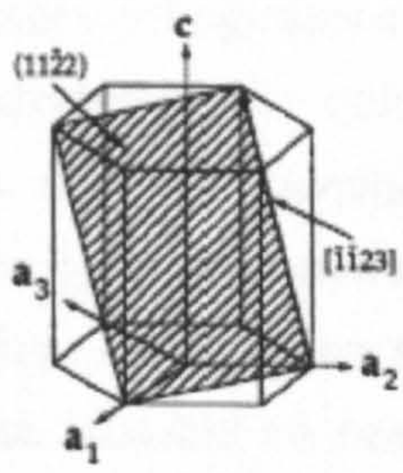

2nd order Pyramidal-< c + a >
{11$\bar{2}$2} < 11$\bar{2}$3 >, 6

Fig. 2.9 Basal <a>, prismatic <a>, pyramidal <a> slip systems, and first and second-order pyramidal <c+a> slip systems in hcp materials (Balasubramanian and Anand, 2002).

2.3 The β→α Phase Transformation

When near-α and α+β titanium alloys are cooled from elevated temperatures, various phase transformations can take place depending on the chemical composition of the β phase and the cooling rate. Depending on these factors, the transformation may involve martensitic, possibly massive mechanisms and diffusion controlled nucleation and growth. In many cases the bcc β phase transforms to the hcp α phase in transformations which obey the Burgers (1934) orientation relation

$$(0001)_\alpha \,//\, \{110\}_\beta$$
$$<1\,\bar{2}\,10>_\alpha \,//\, <111>_\beta \qquad (2.3)$$

In Burgers type transformations, a single β orientation gives rise to a maximum of 12 distinct α orientations or variants. This range of inherited α orientations is a feature of the transformed microstructures. When one or more of the α orientations is selected preferentially, it is termed variant selection. Variant selection has been reported in both martensitic and diffusion controlled transformations.

Most prior studies of phase transformations during cooling have tended to use multiple specimens and cooling rates that are descriptively defined as water quenched, oil quenched, fan-air cooled, air cooled, furnace cooled etc. Thus there is a relative lack of quantitative information regarding the cooling rates associated with the different transformation modes. Another reason for this is that the change from one transformation mode to another is often not clearly defined (Flower *et al*, 1974. Baeslack and Mullins, 1982).

There is a clear consensus that the transformation in small water quenched specimens occurs martensitically. Similarly, at slower cooling rates corresponding to air and furnace cooling of small specimens, the transformation is completely diffusional in nature. However, at intermediate cooling rates, (e.g. oil quenching of small specimens), there seems to be some differences of opinion as to the nature of the transformation. In the following sections, the martensitic, diffusional and then the intermediate transformation modes will be discussed, focusing where possible on near-α alloys although inevitably, much of the work conducted has been on the widely used α+β alloy, Ti-6Al-4V.

2.3.1 Martensitic Transformation

At sufficiently high cooling rates, the β phase transforms completely into α phase by a displacive transformation to form a martensitic structure. In alloys with low solute contents such as the near-α alloys (e.g. Timetal 834), the martensitic phase has a hexagonal structure and is designated α'. This transformation strictly obeys the Burgers relation. At higher solute contents, the α phase loses its hexagonal symmetry and becomes orthorhombic. Orthorhombic martensite is designated α'' (Lutjering, 2007). Hexagonal martensite can be divided into two morphologies, massive (also referred to as "lath" or "packet") and acicular. The massive martensite, which only occurs in pure titanium, very dilute alloys and alloys with a high martensite start temperature (M_s), consists of packets of fine parallel laths belonging to the same α variant. It is called massive martensite because the laths cannot be observed clearly by optical microscopy, so that the packets appear as large irregular regions, with no discernable features. The acicular martensite has a basket-weave structure, consisting of an intimate mixture of individual α' plates, each belonging to a different variant of the Burgers relation (Leyens and Peters, 2003, Lutjering, 2007).

There have been various TEM investigations of the martensite in near-α alloys. Ramachandra *et al.* (1993) examined small specimens water quenched from above the β transus and from the α+β phase field for Timetal 834. In both cases, the transformed microstructure consisted of acicular plates of α' containing faults and a high dislocation density. Thin films of retained β were identified at the interplatelet boundaries. Sridhar

et al. (1987) examined transformed structures from above the β transus and from the α+β phase field at several cooling rates for the near-α alloy, Timetal 829. Again, in water quenched specimens, the transformed microstructure consisted of faulted and dislocated acicular α' martensite.

A more quantitative technique for studying the effect of cooling rate was described by Ahmed and Rack (1998). This used a modified Jominy procedure (ASTM, 1995) to investigate the effects of cooling rate on the phase transformations in Ti-6Al-4V cooled from above the β transus. Microstructures were interpreted using optical and electron microscopy, from which a schematic continuous cooling diagram was developed (Fig. 2.10). Cooling rates above 410°C s^{-1} were required to produce a fully martensitic structure (Fig. 2.11).

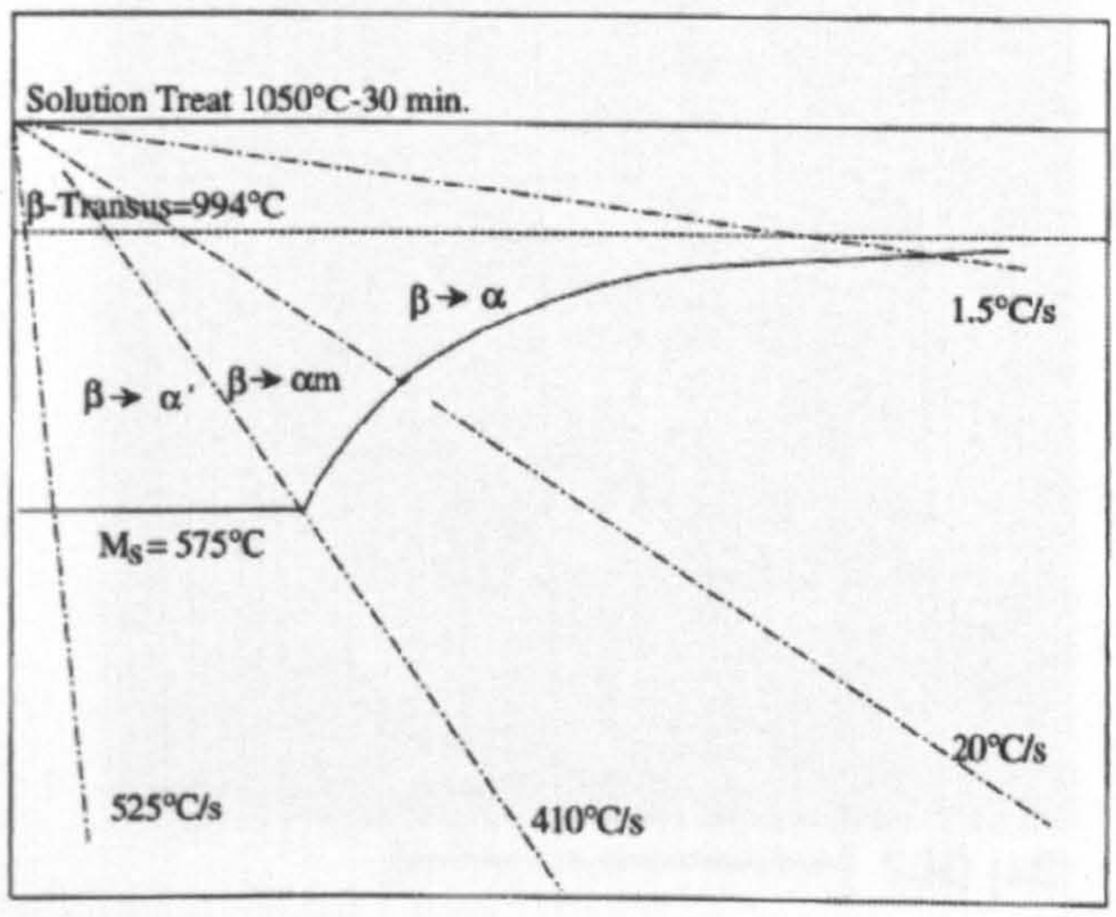

Fig. 2.10 Schematic continuous cooling diagram for Ti-6Al-4V solution treated in the β phase field at 1050°C for 30 min (Ahmed and Rack, 1998).

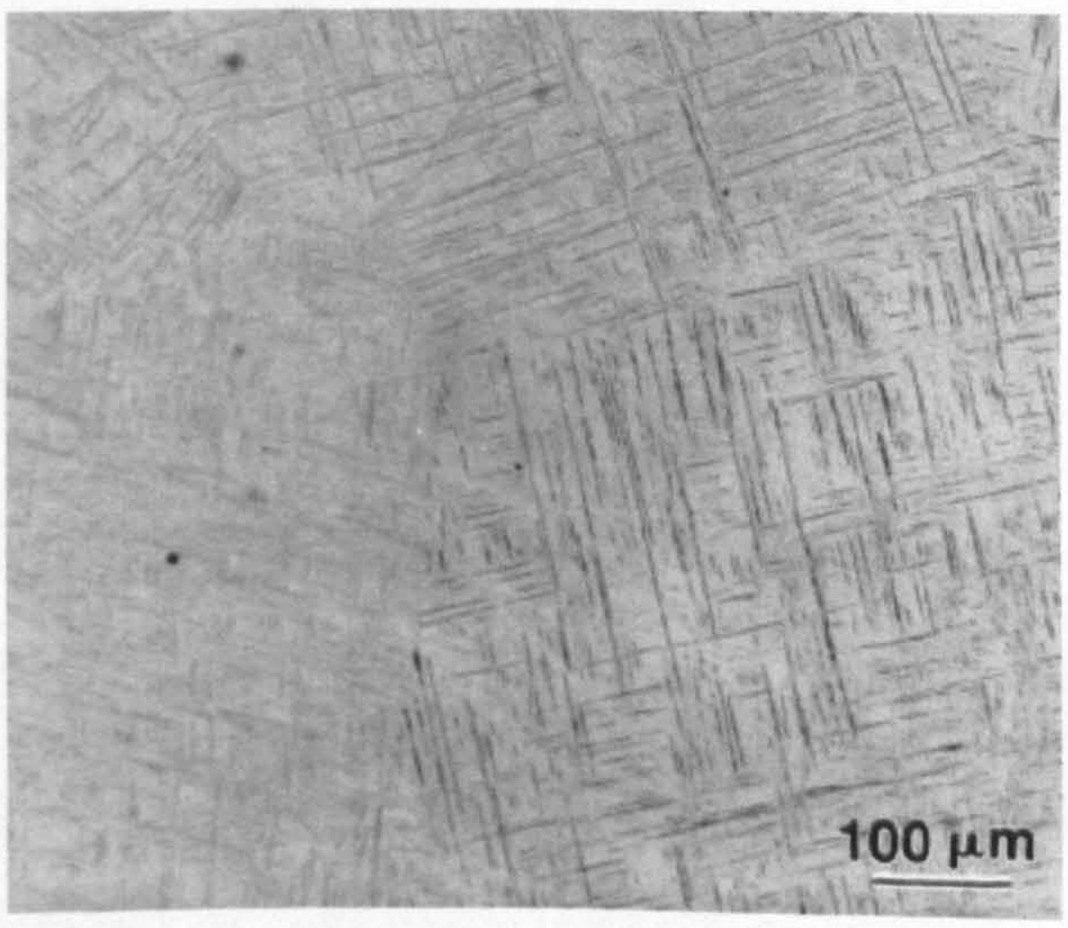

Fig. 2.11 Optical micrograph of fully α' martensite formation in Ti-6Al-4V cooled at 525°C s^{-1} (Ahmed and Rack, 1998).

2.3.1.1 Variant Selection in the Martensitic Transformation

A fully martensitic structure was produced in work described by Stanford and Bate (2005) for a specimen of water quenched Ti-6Al-4V (cooling rate ~500°C s^{-1}). EBSD mapping of the martensite revealed a basket-weave, acicular α' structure, consisting of long primary laths and shorter secondary laths. A star shaped growth effect was evident at the end of some laths (Fig. 2.12). Analysis of the variants showed that all 12 variants were consistently produced within each parent β grain but that significant variant selection was occurring (Fig. 2.13). The variant selection was modelled on the basis of elastic interaction between martensitic events.

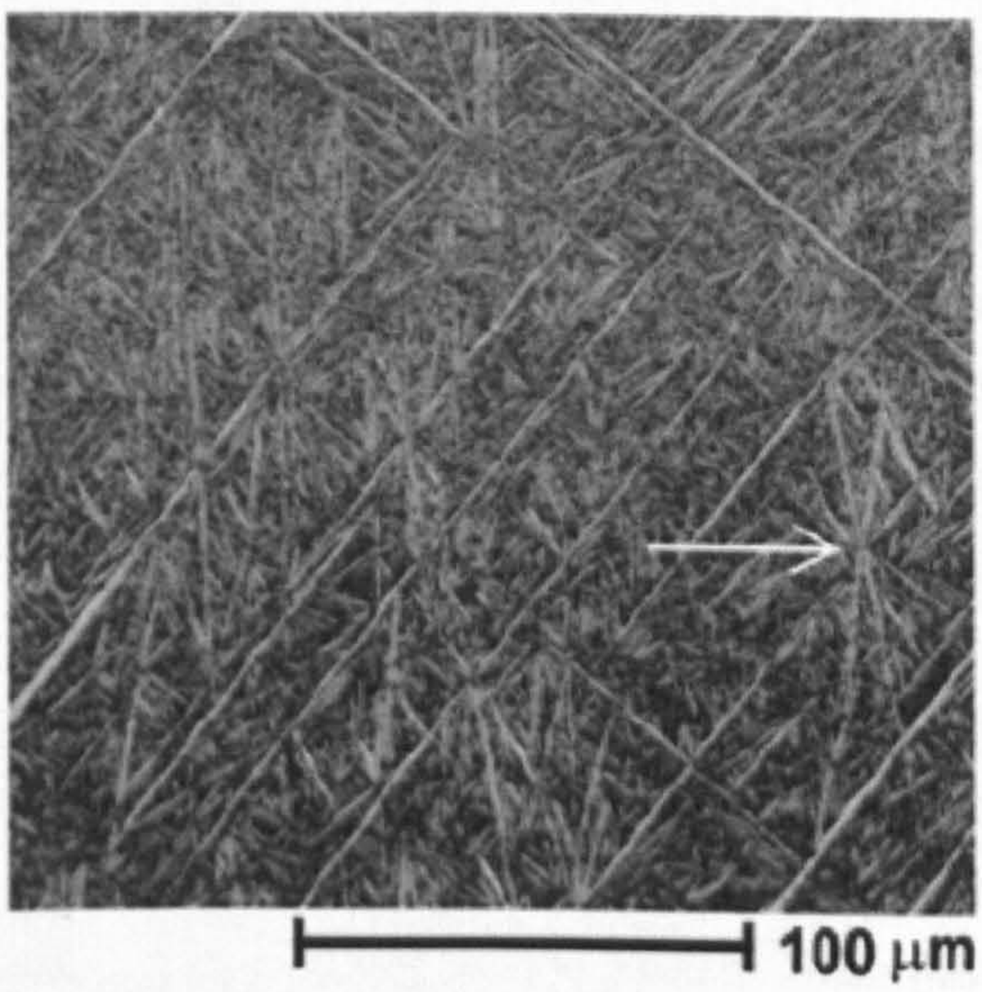

Fig. 2.12 EBSD mapping shown with band contrast for martensite formed in Ti-6Al-4V at a cooling rate of ~ 500°C s^{-1}. The arrow indicates a star shaped growth effect (Stanford and Bate, 2005).

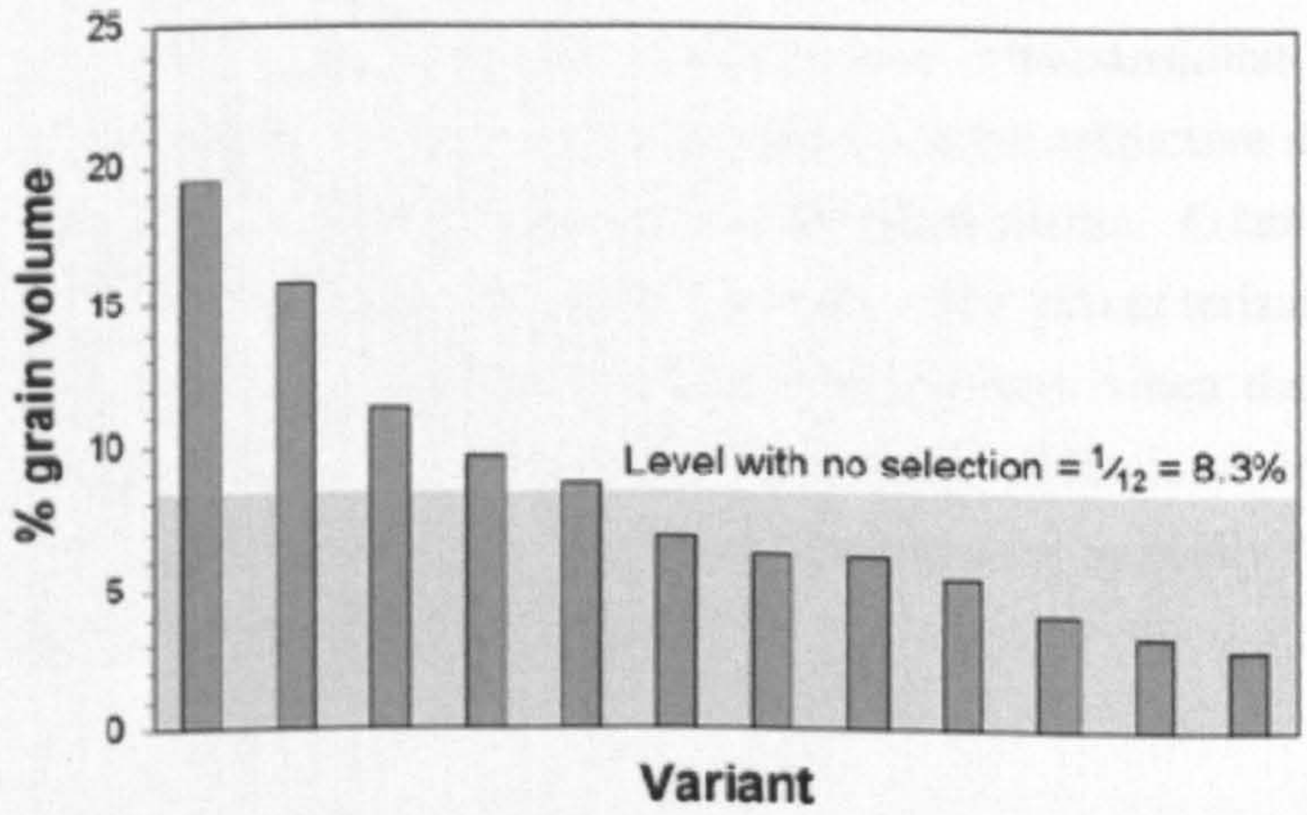

Fig. 2.13 The area fractions of all 12 inherited variants within a single prior β grain. The significantly different areas indicate variant selection has occurred (Stanford and Bate, 2005).

2.3.2 Diffusional Transformation

2.3.2.1 Cooling From the β Phase Field

When titanium alloys are cooled at moderate to low cooling rates from elevated temperatures in the β phase field, α phase nucleates first at β grain boundaries forming a more or less continuous layer of grain boundary α (α_{GB}). Stanford and Bate (2004) found that α_{GB} often exhibits a Burgers orientation relationship with one of the β grains at the β grain boundary but in other cases may not "belong" to either, with its orientation some form of compromise. During continued cooling, α plates nucleate either on the interfaces of the α_{GB} or on the β grain boundaries themselves and then proceed to grow into the β grains, separated from each other by small amounts of the retained β matrix (Ahmed and Rack, 1998. Lutjering, 2007). The α plates tend to have a low angle grain boundary when they nucleate from an α_{GB} interface and satisfy the Burgers orientation relationship with the β phase. This α+β morphology, where the product phase is related to the parent phase by a crystallographic relationship and the product grains attain a plate shape, is known as a Widmanstätten morphology (Kelly, 2004). Depending on the cooling rate, the Widmanstätten α can take two forms, colony and basket-weave.

The colony form of Widmanstätten α forms at slower cooling rates. A number of plates belonging to the same variant grow parallel to one another to form the α colonies. The crystallographic relationship between the α plates and the retained β matrix is shown schematically in Fig. 2.14. The colonies of plates grow into the centre of the β grains until they are met by other colonies, which have nucleated from other parts of the β grain boundary and may belong to different variants of the Burgers relation (Lutjering, 2007). As the cooling rate is increased, the width of the α plates decreases as does the number of plates in a colony. Due to the increased undercooling, α plates begin to nucleate not only at the boundaries of the β grains and α_{GB} interfaces but from points on existing α plates in the grain interior. This results in the basket-weave Widmanstätten morphology. Describing a microstructure as colony or basket-weave can be subjective as it is unusual for a microstructure to be composed entirely of individual plates. Often there will be colonies containing small numbers of plates as well. For characterisation purposes, Searles *et al.* (2005) classify a microstructure as basket-weave when the number of α plates in individual colonies is 3 or less. The sequence of diffusional transformations during continuous cooling from the β phase field is illustrated by Kelly (2004) using a schematic continuous cooling diagram in Fig. 2.14.

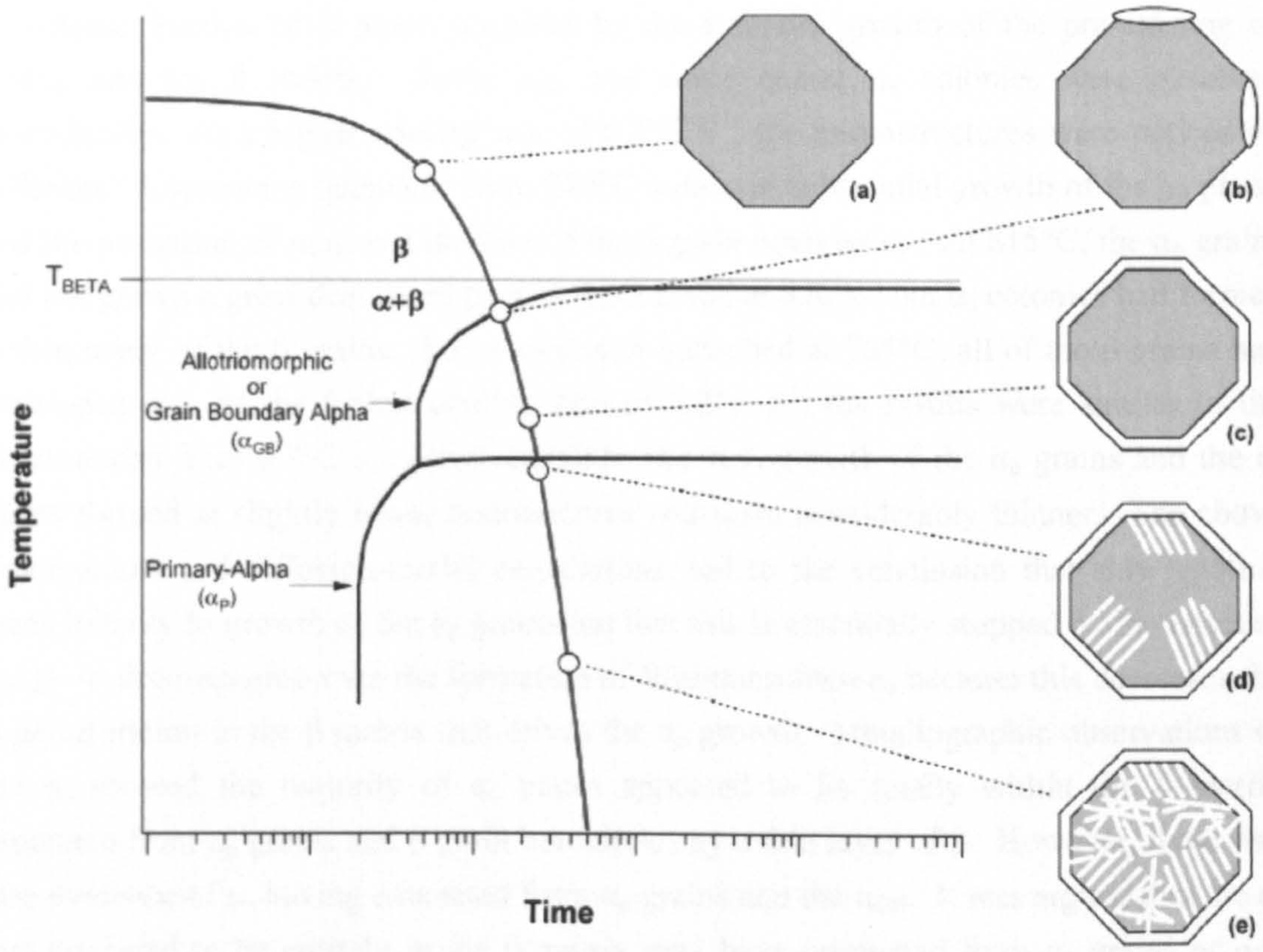

Fig. 2.14 The sequence of diffusion controlled phase transformation events occurring during continuous cooling of Ti-6Al-4V (applicable to other near-α and α+β alloys) through the β transus. Black lines show start curves for α_{GB} and Widmanstätten α_p. (a) A single β grain is shown in gray. (b) The first α to form is allotriomorphic Widmanstätten alpha (α_{GB}) at the β grain boundaries. (c) α continues to grow along the β grain boundaries. (d) α plates begin to nucleate and grow first at the α_{GB} as colonies and finally with increased undercooling (e), α nucleates within the remaining β in a basket-weave morphology (Kelly, 2004).

2.3.2.2 Cooling From the α+β Phase Field

The diffusional transformations which occur on cooling from an α+β heat treatment show some differences compared to cooling from above the β transus due to the pre-existing α phase which is usually present in the form of equiaxed α grains. To distinguish the pre-existing α and new α, which forms by transformation of the β phase during cooling, the former is termed primary-α (α_p) and the later secondary-α (α_s).

Detailed quantitative investigations were carried out for Ti-6Al-4V by Semiatin *et al.* (2003). In this work, specimens were soaked in the α+β phase field at 955°C, giving 27 vol.% of α_p grains in a β matrix. The specimens were then cooled at 3 constant cooling rates and water quenched at various temperatures to transform any remaining β at that temperature to martensite. At the slowest cooling rate of 0.18°C s^{-1}, most of the reduction

in volume fraction of β phase occurred by the epitaxial growth of the pre-existing α_p grains into the β matrix. Some α_{GB} and some coarse α_s colonies were observed sporadically. At a higher cooling rate of 0.7°C s^{-1}, the microstructures were noticeably different. A specimen quenched from 870°C indicated substantial growth of the α_p phase and the formation of α_{GB} on a number of the β grain boundaries. At 815°C, the α_p grains had not grown a great deal more from that observed at 870°C, but α_s colonies had formed within many of the β grains. For a specimen quenched at 705°C, all of the β grains had developed α_s. At the fastest cooling rate of 3.2°C s^{-1}, the results were similar to the observations from 0.7°C s^{-1}; however, there was less growth of the α_p grains and the α_s plates formed at slightly lower temperatures and were considerably thinner. The above observations and diffusion-model calculations, led to the conclusion that slow cooling leads initially to growth of the α_p grains but that this is essentially stopped by the onset of the β→α decomposition via the formation of Widmanstätten α_s because this decreases the supersaturation in the β matrix that drives the α_p growth. Metallographic observations of the α_s showed the majority of α_s plates appeared to lie totally within the β matrix separated from α_p grains and β grain boundaries by a thin layer of β. However, there was also evidence of α_s having emanated from α_p grains and the α_{GB}. It was argued that the α_s that appeared to be entirely in the β matrix may have originated from α_p grains or α_{GB} away from the plane of view.

2.3.3.3 Variant Selection in Diffusional Transformations

It has been shown that variant selection can occur for diffusional transformations on cooling from the β phase field (Bhattacharyya *et al.*, 2003, 2007. Stanford and Bate, 2004) and the α+β phase field (Germain *et al.*, 2005. Humbert *et al.*, 2006). In the case of cooling from the β phase field, work has shown that when adjacent β grains have a nearly common (110) pole, precipitation of α phase at the boundary will occur with the (0002) pole parallel to that particular (110) pole in preference to the other five possible (110) poles (Stanford and Bate, 2004). Results reported by Bhattacharyya *et al.* (2007) were similar, except in this work certain specific misorientations with a common (110) pole between adjacent β grains were identified that could lead to the same α orientation being nucleated in colonies on either side of the β boundary but having different growth directions.

In investigations by Humbert *et al.* (2006) on material cooled from the α+β phase field, the presence of the pre-existing α_p grains was believed to result in another important variant selection mechanism. It was found that statistically 10% of the α_p/β boundaries had misorientations close to the Burgers orientation relation and in these cases, 80% of the α_s was crystallographically closest to the neighbouring α_p grains. This mechanism means that texture heterogeneities (macrozones) caused by closely aligned α_p grains are

further strengthened by the preferentially selected α_s variants (Germain *et al.*, 2005). When the β/β grain boundaries were examined, it was also observed that in cases where adjacent β grains had a common (110) (with 10° tolerance), in 50% of cases the α_s precipitated at the β/β boundaries had their (0002) pole parallel to the common (110) pole. This indicated that a local selection of variants by this mechanism also occurred.

2.3.3 The Transition From a Martensitic to a Diffusional Transformation

Several investigators have shown that changes from one transformation mode to another during cooling are often not clearly defined and that it can be difficult to distinguish the contribution of each mode to the growth of the transformed α phase. Using optical microscopy, Baeslack and Mullins (1982) reported an essentially continuous transition from an initially nucleation and growth transformation to a martensitic transformation during continuous cooling for Timetal 829. In other work, the existence of a massive transformation (α_m) that is competitive with diffusional and martensitic transformations at low and high cooling rates within the overall cooling rate region where it forms has been reported. This was originally in relation to Ti-X (X: Ag, Au, or Si) alloys (Plichta *et al.*, 1977, 1978, 1980) and more recently in Ti-6Al-4V (Ahmed and Rack, 1998). Massive transformations are a short-range, compositionally invariant, diffusional transformation, in which the transformation front advances by random diffusive atom movements across the front by distances in the range of the nearest atomic neighbour (Banerjee, 2007). The α_m formation reported by Ahmed and Rack in Ti-6Al-4V was observed for cooling rates between 410 and 20°C s^{-1} (Fig. 2.10). At the highest cooling rates it was confined to the β grain boundaries but with decreasing cooling rate progressively occurred at martensite plates adjacent to the β grain boundaries and ultimately at individual martensite plates within the grains. TEM studies indicated that it had a blocky morphology, a heavily dislocated substructure and an hcp structure identical to the α' martensite observed at higher cooling rates. The authors report that the α_m was absent at cooling rates <20°C s^{-1}, where heterogeneous nucleation of a grain boundary α layer (α_{GB}) was observed with the intragranular microstructure consisting of Widmanstätten α plates i.e. a completely diffusionally transformed microstructure.

2.4 Thermomechanical Processing of Near-α and α+β Titanium Alloys

2.4.1 Introduction

Thermomechanical processing is the term used to describe the sequence of hot working processes that are used to convert a cast ingot into desired shapes while at the same time optimising the mechanical properties through microstructure control. Processing can be divided into primary working, which produces intermediate product forms such as billet or bar, and secondary working (e.g. hot rolling or forging), which produces the desired shape before final machining and fabrication operations take place. Typical industrial practise for these two stages is described. Microstructural evolution occurring in the α and β phases during primary and secondary working is reviewed. During the later stages of primary working, sub-transus working is used to break up colonies of α lamellae into individual α_p grains by a process known as globularisation. This is a particularly important process that has a large bearing on the final microstructure, microtexture and properties of a forging. Texture development during sub-transus working, the dwell fatigue phenomenon and microtexture are also discussed.

2.4.2 Primary Working

Cast cylindrical ingots are usually processed to billets or bars by open die forging and/or radial forging. The microstructural aims are to break up the cast structure and to produce a fine-grained α+β microstructure (Leyens and Peters, 2003). Usually a number of forging steps and reheats are required to achieve the desired microstructure and shape change. Initially forging takes place well above the β transus, where large shape changes can be achieved using relatively low forces. Alternate forging above and below the β transus may then be used to reduce the β grain size (Leyens and Peters, 2003). The final forging step takes place below the β transus i.e. within the α+β phase field. In this important step, an initially coarse lamellar α+β microstructure, which was formed after the last forging step on cooling from above the β transus, is broken up by a process known as globularisation, resulting in a microstructure containing individual α_p grains. If the cooling rate from the final α+β forging step is sufficiently low, only the α_p grains will grow and no α_s lamellae are formed within the β grains resulting in a globular structure, with the equilibrium volume fraction of β phase located at the triple points of the α_p grains (Lütjering, 1998). At higher cooling rates, α_s lamellae may also form. A typical primary working process route is shown schematically in Fig. 2.15.

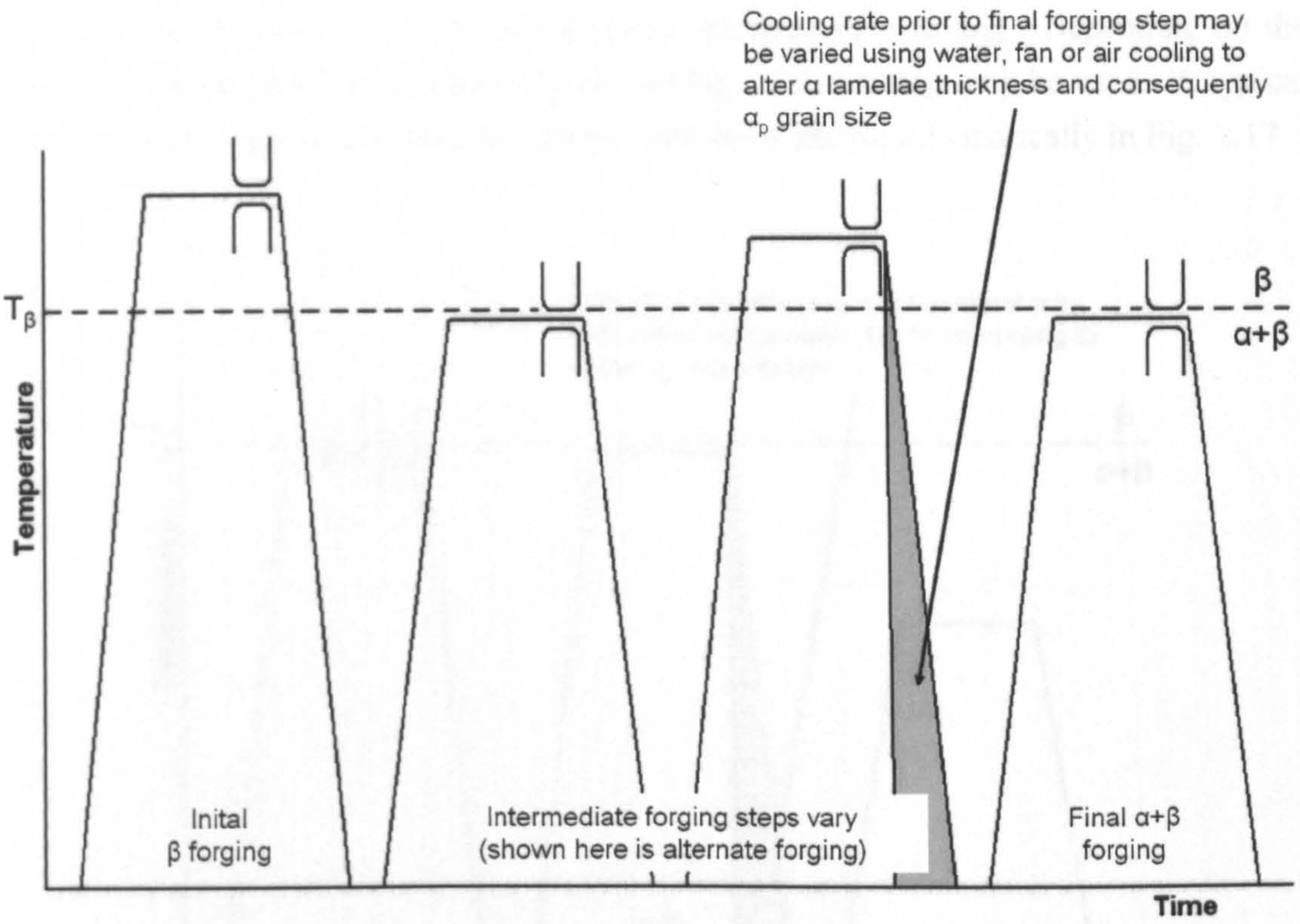

Fig. 2.15 A typical primary working process route used to convert cast ingot into billet.

2.4.3 Secondary Working

Secondary working e.g. by closed die forging or rolling, can take place either below or above the β transus depending on the final product requirements. α+β processing produces a bimodal microstructure on cooling, whereas β processing produces a fully lamellar microstructure. During α+β processing the material is heated to a temperature 30°C to 100°C below the β transus (Leyens and Peters, 2003). The temperature must be sufficiently high that crack-free deformation is possible at high strains but low enough that deformation heating will not lead to temperatures exceeding the β transus. After α+β processing, cooling is usually carried out in air. A further α+β solution annealing heat treatment, followed by air cooling is usually used to produce exactly the desired volume fraction of α_p throughout the final part (Flower, 1990). After the solution heat treatment, a lower temperature anneal is usually performed for stress relief and in certain alloys to give precipitation strengthening. A typical secondary working process route for the α+β condition is shown schematically in Fig. 2.16.

During β processing, the material is first heated above the β transus. The deformation must then be completed before the β to α transformation starts unless specifically seeking to through transus process the material. Too much hold time at temperatures above the β transus must be avoided to minimise β grain coarsening. After forging, the cooling rate

must be controlled to avoid detrimental microstructures such as α_{GB}. Depending on the alloy, water quenching, oil quenching, fan cooling or air cooling may be used. A typical secondary working process route for the β condition is shown schematically in Fig. 2.17.

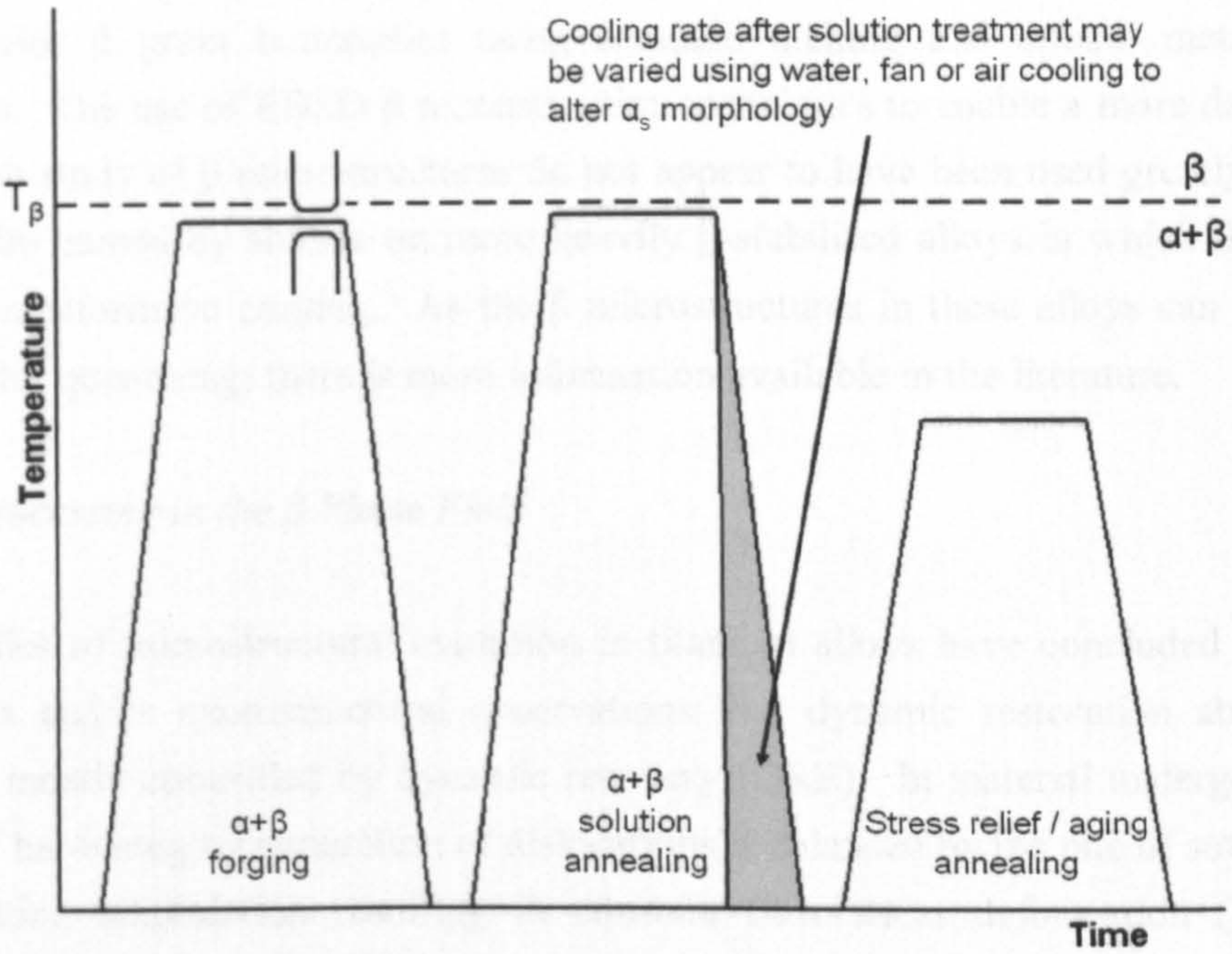

Fig. 2.16 Typical α+β secondary working and heat treatment to produce a bimodal microstructure.

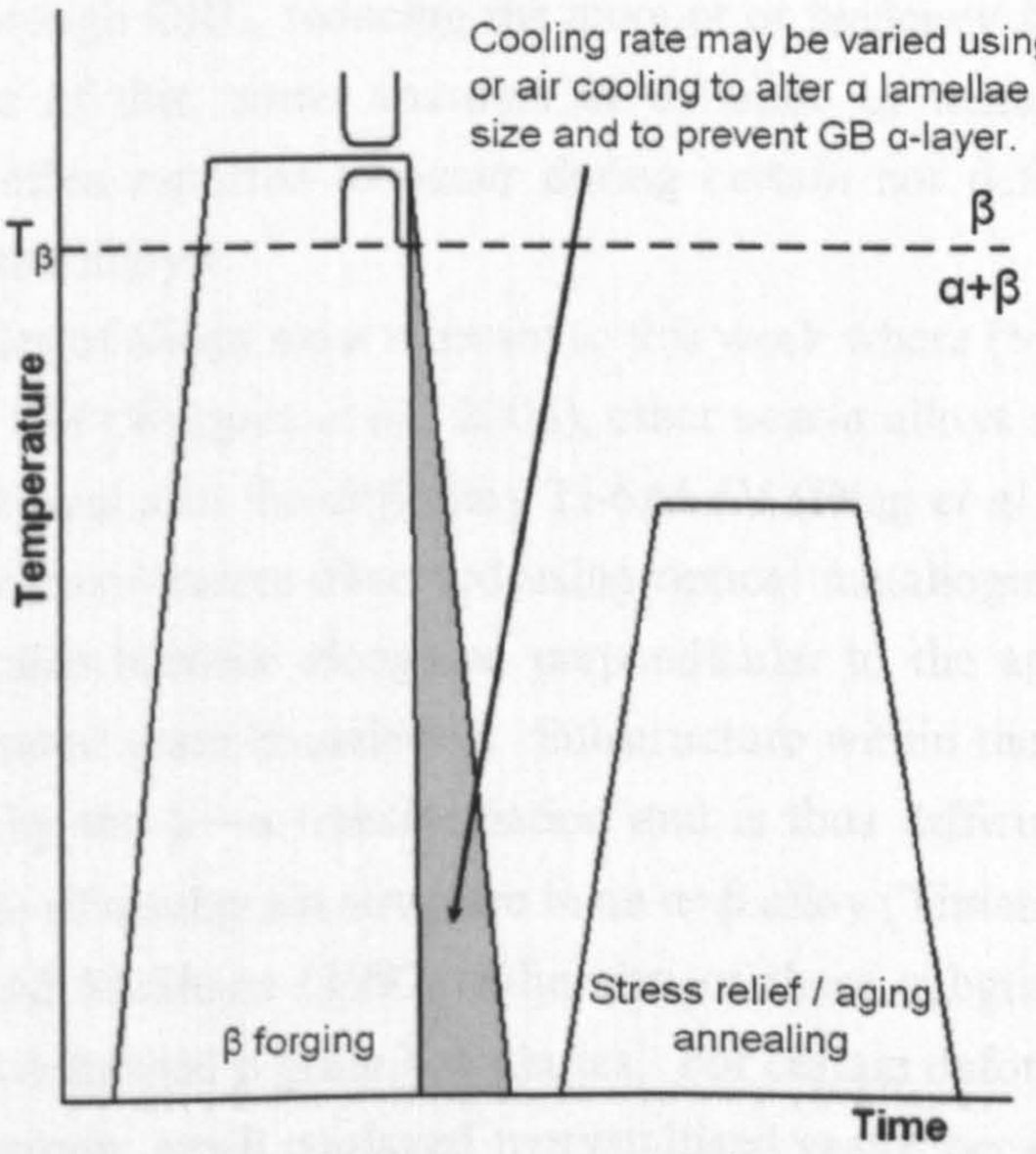

Fig. 2.17 Typical β secondary working and heat treatment to produce a fully lamellar microstructure.

2.4.4 Microstructural Evolution in the β Phase During Thermomechanical Processing.

Understanding the microstructural evolution in the β phase in near-α and α+β alloys is hampered by the β→α transformation on cooling, since this prevents direct study of the β microstructure in deformed and quenched specimens. Despite this, it is often possible to identify prior β grain boundaries using standard etching and optical metallography procedures. The use of EBSD β reconstruction techniques to enable a more detailed and quantitative study of β microstructures do not appear to have been used greatly. Insight may also be gained by studies on more heavily β-stabilised alloys in which the β phase does not transform on cooling. As the β microstructures in these alloys can be studied directly after quenching, there is more information available in the literature.

2.4.4.1 Processing in the β Phase Field

Most studies of microstructural evolution in titanium alloys have concluded from flow stress data and/or microstructural observations that dynamic restoration above the β transus is mostly controlled by dynamic recovery (DRE). In material undergoing DRE, the rate of hardening by generation of dislocations is balanced by the rate of softening due to dislocation annihilation resulting in constant flow stress deformation (Weiss and Semiatin, 1998). The difficulty in inducing dynamic recrystallisation (DRX) in the β phase field has been attributed to a medium to high stacking fault energy and the high self diffusivity of titanium in the β phase. This assists dislocation movements and decreases stored energy through DRE, reducing the amount or tendency for DRX (Guo and Baker, 1992). In spite of this, some amounts of dynamic or metadynamic recrystallisation ((M)DRX) are often reported to occur during certain hot deformation conditions in a number of titanium alloys.

Some examples of alloys most relevant to this work where (M)DRX has been observed include Timetal 834 (Wanjara *et al.*, 2006), other near-α alloys such as Timetal 685 (Guo and Baker, 1992) and also the α+β alloy Ti-6Al-4V (Ding *et al.*, 2002). In these studies, the deformed microstructures observed using optical metallography appear similar. The large prior β grains become elongated perpendicular to the applied strain and develop increasingly serrated grain boundaries. Substructure within the deformed β grains tends to be obscured by the β→α transformation and is thus difficult to observe. However, residual evidence of a subgrain structure in an α+β alloy (Timetal 550) has been observed by Robertson and McShane (1997a); the size of these subgrains corresponding to the serrations in the deformed β grain boundaries. For certain deformation conditions, after a certain level of strain, small equiaxed recrystallised grains became visible in the vicinity of the deformed β grain boundaries (e.g. Fig. 2.18). The amount of recrystallisation increases with increasing strain, strain rate and temperature. At low strain rates and

temperatures, the microstructure is dominated by the deformed β grains, with the recrystallised grains only a small fraction or absent altogether. At higher strain rates and temperatures, the microstructures tend to be only selectively recrystallised, resulting in mixed grain structures of small and large grains. For example, in Timetal 685 (β transus ~1020°C), deformed between 1025-1075°C, no recrystallisation was observed for strain rates below $0.09s^{-1}$ (Liu and Baker, 1995), while only limited amounts were observed in tests at strains rates of $0.5s^{-1}$ and $1.0s^{-1}$ (Guo and Baker, 1992). Recrystallisation was also limited in Timetal 834 (β transus ~1045°C), such that for deformation at 1050°C, a relatively high strain rate of $1s^{-1}$ and a high strain of 1.2 were required to achieve just over 50% recrystallisation (Wanjara *et al.*, 2006). Similarly, in Ti-6Al-4V (β transus ~1000°C), recrystallised volume fractions of less than 30% were found for deformation between 1000-1050°C and strain rates of $0.05\text{-}1s^{-1}$ (Ding *et al.*, 2002).

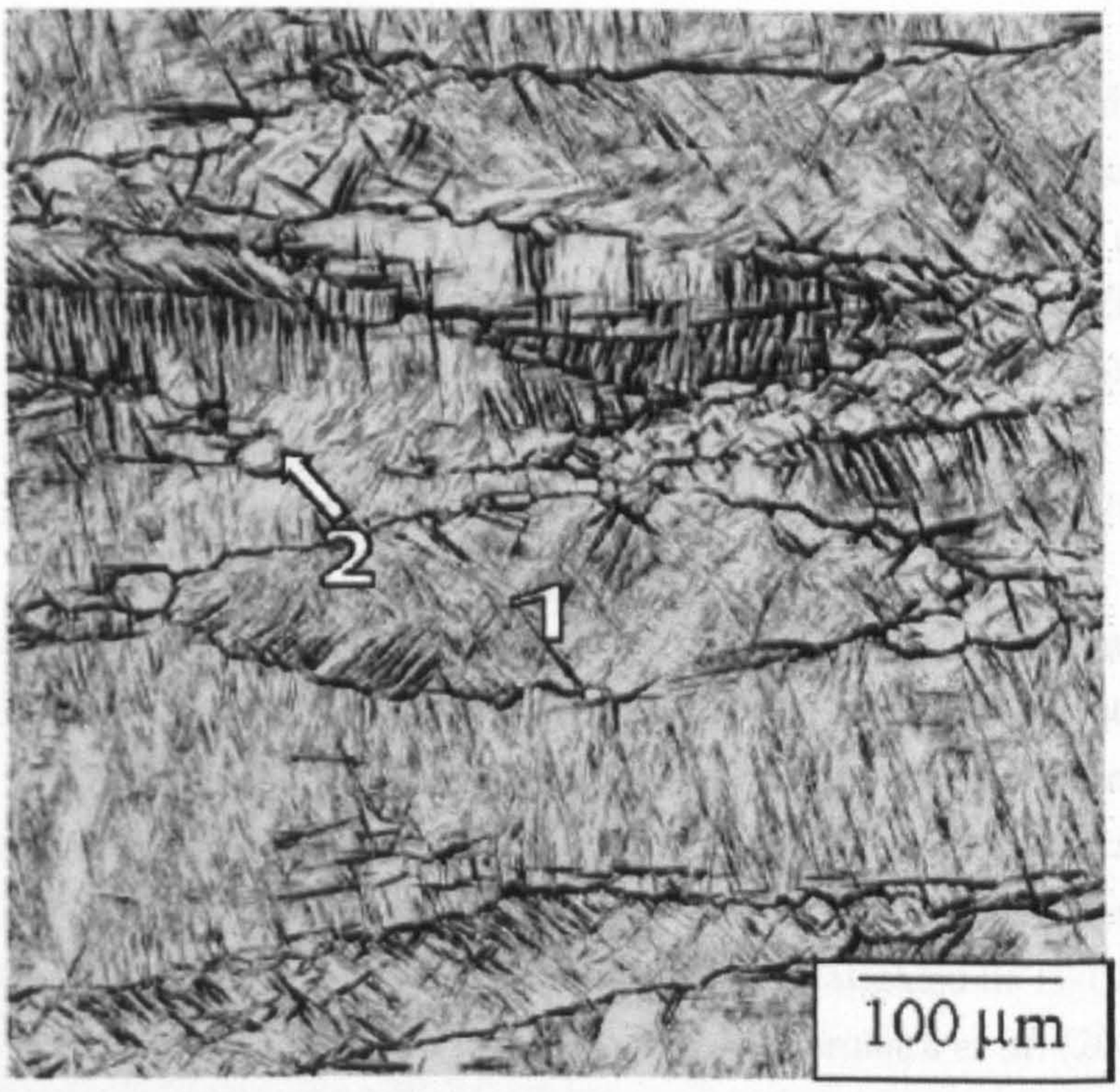

Fig. 2.18 Microstructure of Timetal 834 deformed at 1050°C (single phase β region) at a strain rate of $1s^{-1}$ to a strain of 0.8 followed by water quenching. (1) Deformed prior β grain. (2) Equiaxed recrystallised grain (Wanjara *et al.*, 2006).

In near-α and α+β alloys, where the β phase transforms to α on cooling, more detailed study of the deformed microstructures in the β phase is difficult. Substructure in the deformed β grains is largely obscured by the transformation and it is not possible to make direct measurements of misorientations within the β phase using techniques such as EBSD and TEM. As a result, information in the literature is limited. Reconstruction of β grain orientation maps from EBSD data for the transformed α phase could be a useful

technique for investigating microstructural evolution in the β phase. The only known use of β reconstruction to study the deformed microstructure is by Germain (2005) in Timetal 834. This was carried out on a small area of a sample from the previously mentioned work by Wanjara *et al.* (2006), for which the optical microstructure was shown in Fig. 2.18. Although the area analysed was small and contained only a few deformed and recrystallised β grains, the analysis revealed the following information. The deformed β grains studied were mainly orientated with either <111> or <100> parallel to the compression direction. The deformed β grains contained low angle subgrain boundaries due to DRE, which resulted in considerable orientation spread within each deformed β grain. The reconstructed map contained two small recrystallised grains. These were found to be misorientated from the neighbouring deformed β grains on all sides by at least 15°, confirming their high angle character. One recrystallised grain had <111> quite close to the compression axis, and the other <100>, suggesting that there may be similar textures in the deformed and recrystallised grains.

The similarity in the observed microstructures in Timetal 834 and the other near-α and α+β alloys mentioned strongly suggests that the (M)DRX mechanism is the same in each case. The origin of the recrystallised grains and the precise details of this mechanism do not appear to have been resolved conclusively due to the experimental difficulties posed by the β→α transformation. Wanjara *et al.* (2006) and Germain (2005) liken the observed microstructures to a special case of DRX, referred to as necklace recrystallisation, since the recrystallisation concentrates at the deformed β grain boundaries.

Additional insight into the microstructural evolution in the β phase may be gained through studies of more heavily β stabilized alloys where this phase is retained at room temperature. Thermomechanical processing of β alloys was the subject of a review by Weiss and Semiatin (1998). In this review, observations of microstructural evolution in the β alloys Ti-10V-2Fe-3Al (Weiss and Froes, 1984) and β-CEZ (Chaussy and Driver, 1994) were discussed. Hot deformation has also been investigated in Ti-10V-2Fe-3Al by Robertson and McShane (1997b) and more recently by Furuhara *et al.* (2003, 2007). As in the case of the near-α and α+β alloys discussed above, microstructures in the hot deformed β alloys were dominated by the large deformed β grains but also showed some amounts of (M)DRX under certain conditions. Deformed β boundaries were again observed to become serrated with increasing strain, and within the deformed β grains there was clear evidence of a well developed subgrain structure due to DRE. The size of these subgrains increases, as the strain rate decreases and the deformation temperature increases. The observations of (M)DRX are in general similar to the near-α and α+β alloys, with small equiaxed recrystallised grains observed at the deformed β boundaries. In most cases, these recrystallised grains appear to be of a similar size to the subgrains.

Although there are clear similarities in the observed (M)DRX between all of the alloys

discussed, there are differences in the reported recrystallisation mechanism. In the study of Ti-10V-2Fe-3Al by Weiss and Froes (1984), they described the mechanism of (M)DRX as "continuous dynamic recrystallisation also referred to as necklace recrystallisation". They also commented that upon static annealing for a short time, new recrystallised grains also formed by strain induced boundary migration (SIBM), which grow to consume recovered regions. In the study of β-CEZ by Chaussy and Driver (1994), an early use of EBSD enabled an analysis of misorientations in the deformed β grains at intermediate strains (Fig. 2.19). They concluded that the development of medium and high angle boundaries was a continuous process controlled by dynamic recovery. However, the growth process of these high angle boundaries during or after deformation is analogous to metadynamic recrystallisation. From these studies, Weiss and Semiatin (1998) concluded in their review that the recrystallisation process for the β phase above the β transus is not typical dynamic recrystallisation in which nucleation and growth of new recrystallised grains are taking place during hot deformation of low stacking fault materials. In their study of Ti-10V-2Fe-3Al, Robertson and McShane (1997) considered that the level of strain at which the recrystallised grains were first observed (20% reduction) was insufficient to initiate DRX and therefore concluded that they were formed by static recrystallisation. They also highlighted instances of apparent SIBM occurring in subgrains at deformed β grain boundaries. In the study of Ti-10V-2Fe-3Al by Furuhara (2003, 2007), the recrystallisation is described as discontinuous DRX.

To conclude this section, there is broad agreement in the literature, that the main restoration mechanism during deformation in the β phase field is DRE. This is clear from the constant flow stress deformation and the continued presence of the original β grains in the microstructure, which become deformed and have a well developed substructure. Selective recrystallisation also occurs for certain conditions, for which there is less agreement on the mechanisms. There appears to be fairly good evidence that recrystallised grains may form from subgrains whose misorientations develop gradually into high angle grain boundaries with increasing strain i.e. continuously. However these high angle grains only develop at the deformed β boundaries and as a result of this selective recrystallisation, may then proceed to grow into and consume the recovered micostructure metadynamically, thus also having characteristics of discontinuous recrystallisation. Other mechanisms such as SIBM may also operate.

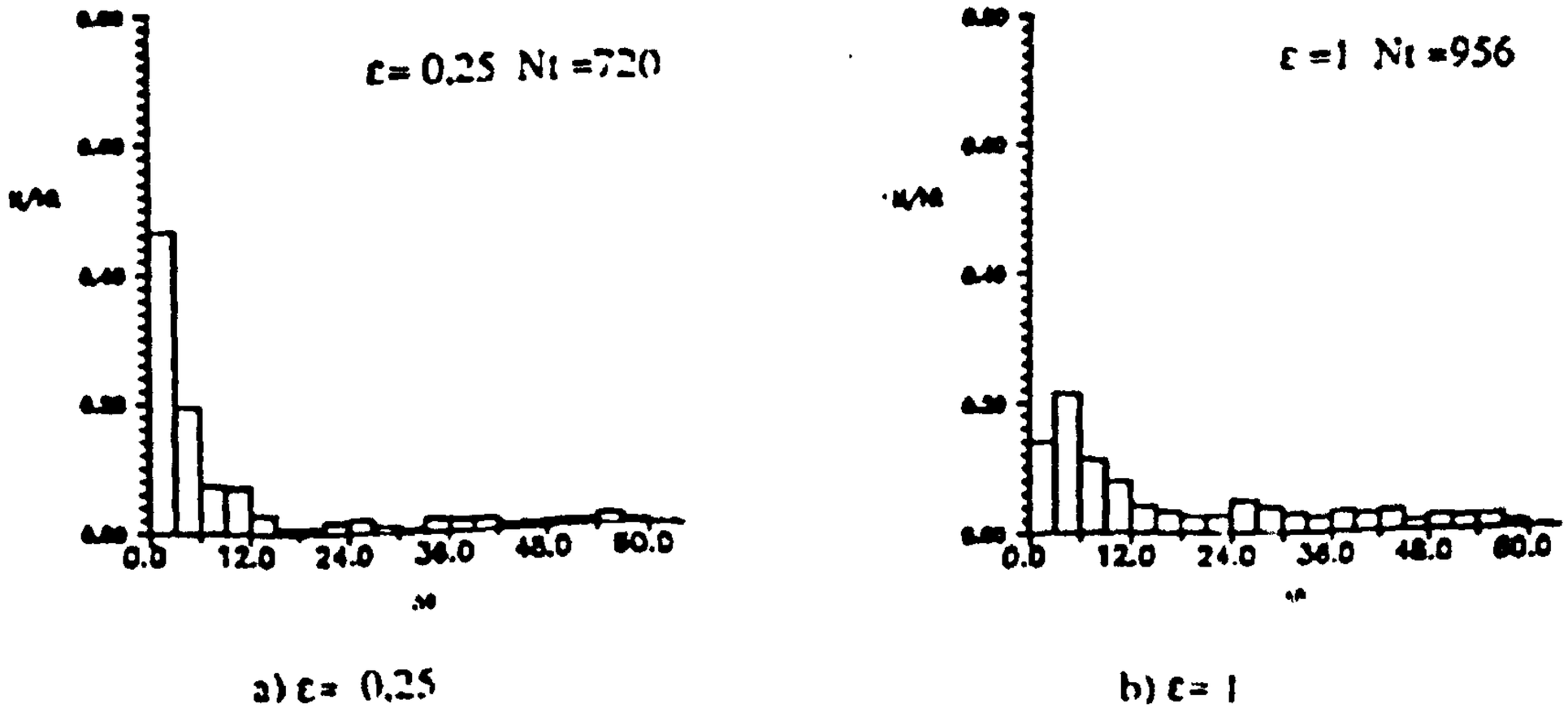

a) ε= 0.25 b) ε= 1

Fig. 2.19 Subgrain misorientation distribution in β CEZ hot deformed in the β phase field to a strain of (a) 0.25 and (b) 1.0 (Chaussy *et al.*, 1994 in: Weiss and Semiation, 1998).

2.4.4.2 Processing in the α+β Phase Field

Here, we will focus on temperatures in the upper α+β phase field, where β is the major phase and an equilibrium volume fraction of α is developed by a solution heat treatment for sufficient time prior to hot deformation. This α phase can be present in different forms depending on the initial condition of the material and the heat treatment used and this must be considered as it can affect both the flow behaviour and microstructural evolution in both phases. For the review of the literature, it is helpful to consider two types of microstructure. The first is formed when the material has been previously β heat treated and is then solution treated in the α+β phase field prior to deformation. In this case, the α phase will be present in the form of high aspect ratio laths, lamellae or platelets and there may also be allotriomorphic α at the β grain boundaries. This is the type of α+β microstructure that exits prior to the final α+β forging step in the primary working of billets and can be referred to as non-globular. α+β deformation of this microstructure tends to modify the α phase through the process of globularisation. The second type of microstructure is formed when the material was previously deformed in the α+β phase field and is then solution treated in the α+β phase field prior to further deformation. In this case, the α phase will be present in the form of globularised α_p grains in a continuous matrix of β. This is the type of α+β microstructure which exists prior to secondary working and can be referred to as globular.

The effect of the two types of microstructure on flow was discussed by Weiss and Semiatin (1998). Compared to deformation in the β phase field, both α+β microstructures tend to show larger amounts of flow softening. Higher flow stresses and more gradual flow softening are observed for the non-globular microstructure as compared to those for a globular morphology. However, at large strains, the flow curves for the two

microstructures approach each other and reach a steady state. There is similar agreement in flow curves for Ti-10V-2Fe-3Al for the two conditions by Robertson and McShane (1997b) and near-α alloys such as Timetal 834 (Vo *et al.*, 2007). In most cases, similar flow stresses and a near steady state are reached after strains of approximately 0.7. The differences in the flow behaviour for the two conditions has largely been ascribed to dynamic microstructure or texture changes in the α phase with some flow softening due to deformation heating at higher strain rates (Weiss and Semiatin, 1998). This indicates that it is difficult to use flow curves from α+β deformation to infer microstructural processes happening in the β phase because the flow behaviour may be heavily affected by the morphology and volume fraction of the α phase.

In some flow curves, sharp yield points followed by a sharp yield drop have been reported during the early stages of deformation in a range of alloys, particularly for higher strain rates and higher temperatures. Examples where this yield drop phenomenon has been observed are in β alloys such as Ti-6.8Mo-4.5Fe-1.5Al (Philippart and Rack, 1998), Ti-10V-2Fe-3Al (Robertson and McShane, 1997b), and Ti-10V-4.5Fe-1.5Al (Balassubrahmanyam and Prasad, 2002); α+β alloys such as Timetal 550 (Robertson and McShane, 1997a); and near-α alloys such as Timetal 834 (Wanjara *et al.*, 2005). However, other studies sometimes in the same alloys do not show this sharp yield drop phenomenon. For example, there does not appear to be a sharp yield drop in the flow curves for Timetal 834 by Bate *et al.* (1989). Where the yield drop phenomenon has been reported, it has been attributed to yielding behaviour caused by the generation of mobile dislocations from the grain boundaries (Philippart and Rack, 1998).

Most studies of microstructural evolution in the α+β phase field have concluded that, as for the single β phase field, dynamic restoration is controlled by dynamic recovery (DRE). Where there are reports of recrystallisation in the β phase at higher strains, it has in most cases been attributed to continuous DRX by the gradual increase in the misorientation of subgrain boundaries. The majority of studies have been for non-globular starting microstructures. It is worth noting that there can be a notable change in scale associated with α+β microstructures as compared to fully β microstructures because the dispersion of α particles tends to refine the β grains to a size comparable to the α particle spacing or less. This means that using optical metallography, it is not possible to detect microstructural features such as subgrains and grain boundaries as readily, particularly for alloys in which the β phase transforms on cooling.

Focussing initially on near-α and α+β alloys most relevant to this work; in studies restricted to optical metallography and where the β phase had transformed on cooling, Guo and Baker (1992) for Timetal 685 and Ding *et al.* (2002) for Ti-6Al-4V reported that there was no DRX for deformation of non globular microstructures below the β transus. In contrast, in a similar study (i.e. non globular starting microstructure and optical metallography) for Timetal 834, Wanjara *et al.* (2006) reported limited amounts of

recrystallisation in the β phase. The observed recrystallisation was similar to that observed in the same study for deformation above the β transus. The initial β grains became elongated and small equiaxed grains were observed at the β grain boundaries. However, the amount of recrystallisation was less than above the β transus, resulting in only a limited necklace structure of fine grains at the deformed β boundaries. Recrystallisation was only observed for strain rates above $0.01s^{-1}$ at 1000°C and above $0.001s^{-1}$ at 1030°C. Fig. 2.20 shows two micrographs from this study. Although the smaller equiaxed grains were referred to as recrystallised, the nature of the grain boundaries, whether high or low angle was not determined. In another study of Timetal 834, Germain (2005) used an EBSD β reconstruction technique, allowing more insight into the β microstructure prior to the transformation. The starting microstructure was non-globular and consisted of α colonies within larger mm sized β grains. Reconstruction of the β phase after deformation to a strain of 1.4 at 1000°C and $1s^{-1}$ revealed the following information. As was the case for deformation in the single β phase field, the deformed β phase was mainly orientated with either <111> or <100> parallel to the compression direction. Areas of β phase which didn't correspond to these orientations were also observed, mostly at the edges of α the colonies. The β phase between α colonies of different orientation and direction deformed differently, resulting in fragmentation of the prior β grains. In the β phase between an individual colony's α lamellae, subgrain boundaries developed, resulting in equiaxed β subgrains. Some of these subboundaries had developed into high angle grain boundaries. The observations of Germain suggests that the β phase undergoes DRE with the formation of high angle grain boundaries at large strains due to continuous DRX.

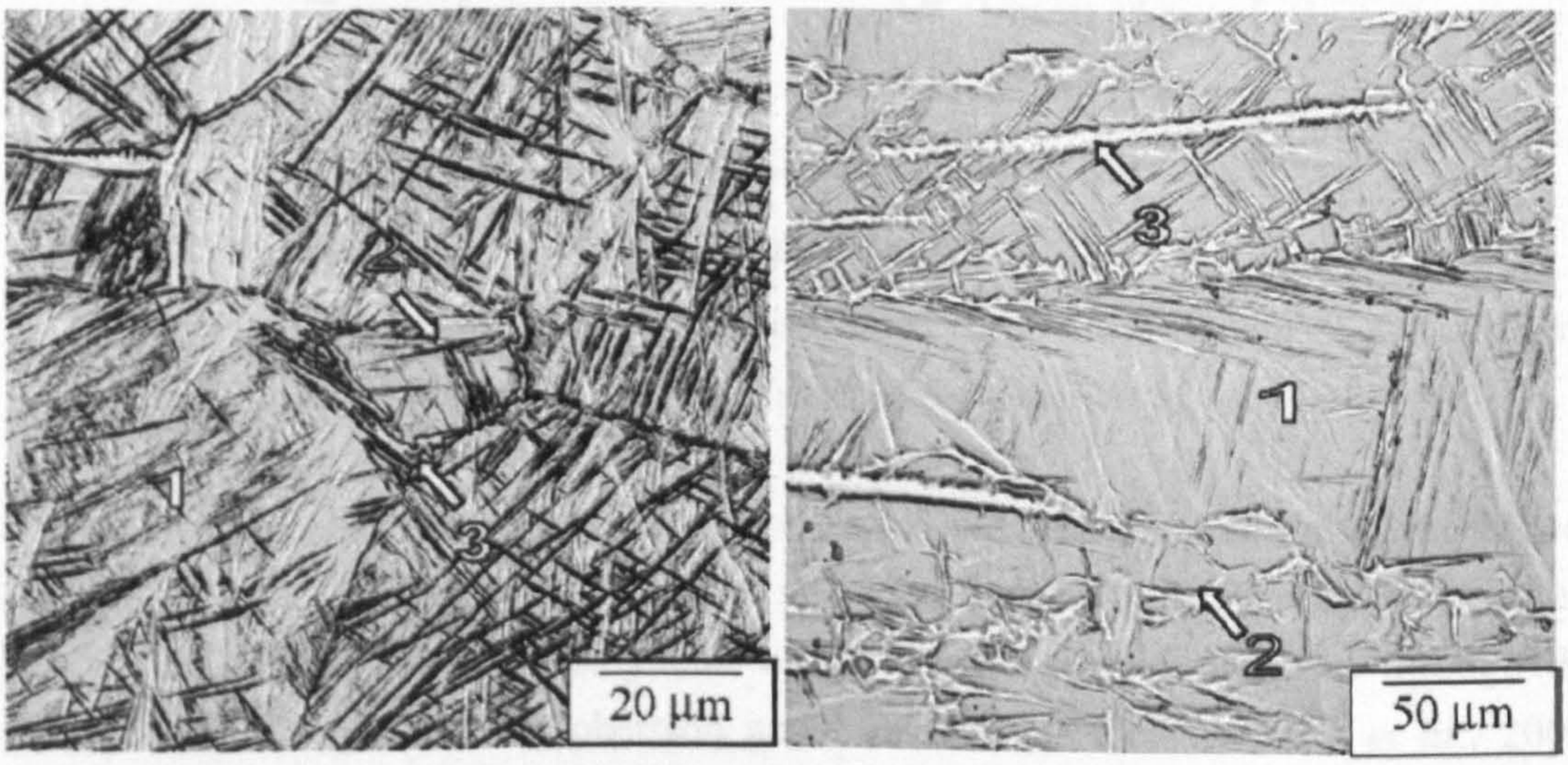

Fig. 2.20 Microstructure of Timetal 834 deformed at 1000°C (upper α+β region with a non-globular starting microstructure) at a strain rate of $1s^{-1}$ to a strain of (a) 0.2 and (b) 0.8, followed by water quenching. (1) Deformed prior β grain. (2) Equiaxed recrystallised grain. (3) α at β grain boundaries (Wanjara *et al.*, 2006).

Additional insight into the microstructural evolution in the β phase may be gained by examining studies of more heavily β stabilized alloys where this phase is retained at room temperature. In the review by Weiss and Semiatin (1998), deformation of β alloys in the α+β phase field was discussed. Due to the considerably higher hardness of the α phase, the behaviour of α_p grains during α+β processing of a globular microstructure was likened to a dispersion of hard particles in a soft matrix, an analogy which has also been used by Flower (1990). Weiss and Semiatin give examples of studies which show that the strain in the α phase is typically between two and four tenths of the nominal strain (e.g. Fig. 2.21). This means strain concentrations develop in the β phase in the vicinity of α_p grains, leading to the formation of smaller high misorientation subgrains in comparison to subgrains produced in the remainder of the β matrix. (Fig. 2.22). Weiss and Semiatin then state that the β matrix also undergoes microstructural changes associated with grain elongation and formation of subboundaries that increase their misorientation continuously, thus creating small recrystallised grains surrounded by high angle boundaries in the vicinity of the highly deformed β grain boundaries. No references or figures are provided to support this last statement, but this mechanism of continuous DRX is the same as that described for hot deformation above the β transus.

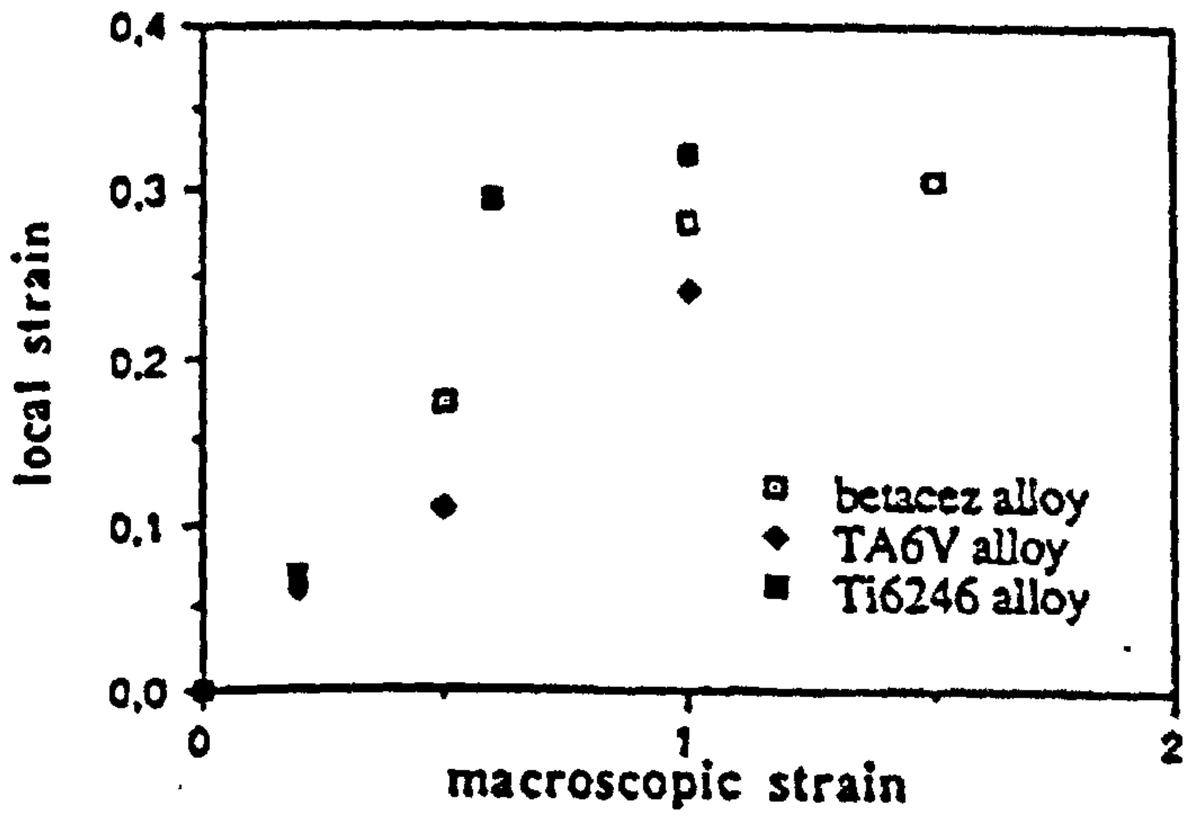

Fig. 2.21 Strain in α phase as a function of nominal strain for different titanium alloys (Chaze and Montheillet, 1994 in: Weiss and Semiatin, 1998).

Other more recent studies in β alloys also support the view that the β phase undergoes DRE leading to a well developed subgrain structure, and that with increasing strain this may gradually lead to the development of high angle grain boundaries through the process of continuous DRX (Robertson and McShane, 1997b. Jackson *et al.*, 2000. Furuhara *et al.*, 2003). The work of Jackson *et al.* (2000) and Furuhara *et al.* (2003) suggests that the development of high angle grain boundaries between the β subgrains (i.e. continuous DRX) occurs more readily for lower temperatures and higher strain rates.

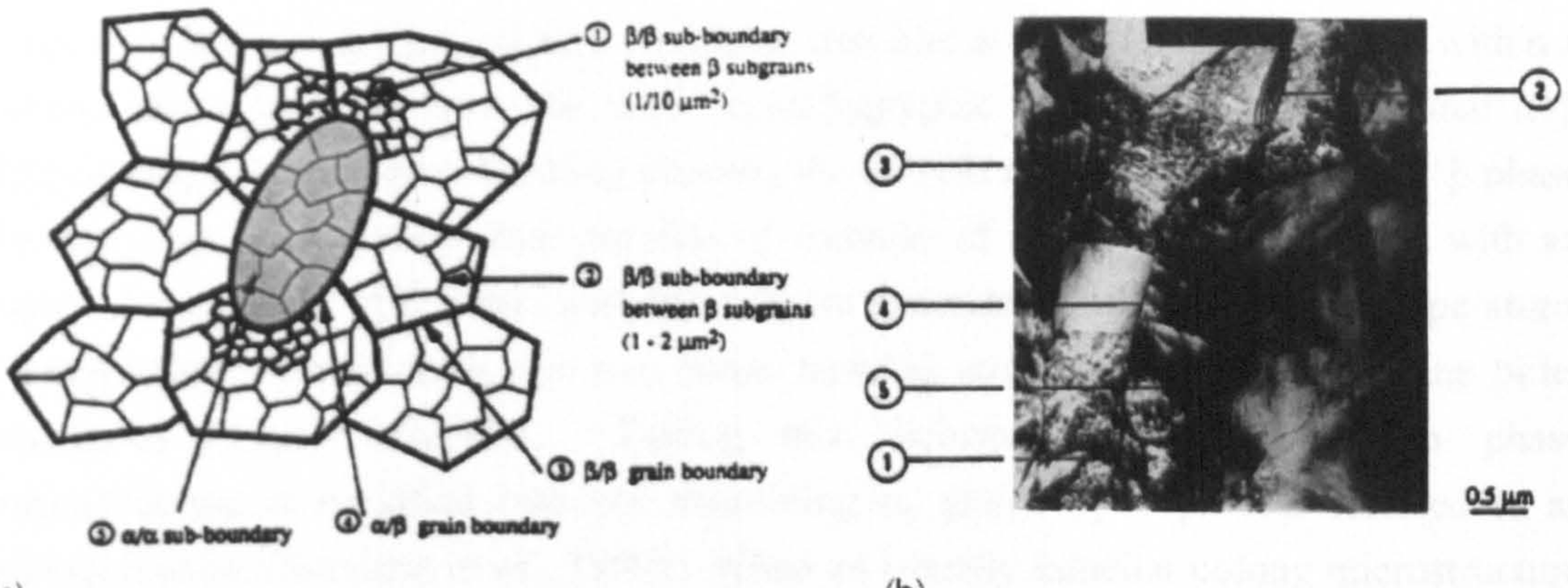

(a) (b)

Fig. 2.22 Formation of substructure in the alpha and β phases during deformation of Ti–5Al–2Sn–2Cr–4Mo–4Zr–1Fe (β CEZ) at a temperature of 840°C and strain rate of 0.3 s^{-1} (Chaze and Montheillet, 1994 in: Weiss and Semiatin, 1998).

To conclude this section, there is broad agreement in the literature, that the main restoration mechanism during deformation in the β phase field is DRE. This leads to the formation of a subgrain structure in the β phase between the α precipitates. Under certain conditions (lower temperature and higher strain rates), there is evidence for continuous DRX by the gradual increase in subboundary misorientations. Strains are higher in the β phase in the vicinity of the harder α phase due to accommodation. This modifies the subgrain structure in these regions (smaller, higher misorientation subgrains) and may also result in orientations other than the expected deformation texture.

2.4.5 Microstructural Evolution in the α Phase During Thermomechanical Processing.

The most important step in the industrial process route for a bimodal microstructure in terms of the α_p phase is the final α+β forging step during primary working, in which globularisation of an initially lamellar microstructure occurs. There is a large body of literature on this important process. By comparison, there is less information on microstructural changes in the globularised α_p grains during secondary working in the α+β phase field.

2.4.5.1 Globularisation of the α Phase During Primary Working

During primary working, the penultimate forging step takes place above the β transus in the single β phase field. As a result of the deformation, the microstructure consists of large β grains elongated along the billet axis. When the ingot is cooled to room temperature, the large β grains transform into colonies of coarse α lamellae. Only a small

amount of β phase is retained between the α lamellae at room temperature, and within a colony, the α lamellae have the same crystallographic orientation. For the final α+β forging step of the primary working process, the billet is reheated into the dual α+β phase field, so that the microstructure consists of colonies of α lamellae interspersed with an equilibrium amount of β phase, with this amount dependent on the reheating temperature. During subsequent working, the two phase lamellar structure is deformed as the billet undergoes further reduction. During this deformation, the lamellar α phase microstructure is modified into one containing α_p grains by a process referred to as globularisation (Semiatin *et al.*, 1999). When an initially lamellar colony microstructure undergoes globularisation, the orientations of the colonies persist, resulting in regions of closely aligned α_p grains. This suggests that dynamic globularisation does not involve recrystallisation of the α phase (Ari-Gur and Semiatin, 1998).

Globularisation is a direct result of the amount of deformation, the working temperature and the mode of deformation (Weiss *et al.*, 1986a). The first two parameters influence microstructure and texture, while the deformation mode mainly effects texture development. While globularisation can occur during deformation, a more complete separation into equiaxed α_p grains can be achieved by post deformation annealing.

Studies have shown that the globularisation process is characterised by a critical strain for its initiation (Semiatin *et al.*, 1999. Weiss *et al.*, 1986a. Poths *et al.*, 2004). This strain depends on the initial microstructure, deformation conditions and strain path (Semiatin *et al.*, 1999. Poths *et al.*, 2004). At strains below the initiation strain there is a realignment of the lamellar structure. Weiss *et al.* (1986a) showed that large uniaxial forging strains (20% and 80% reduction) caused the α plates to align themselves towards a direction perpendicular to the forging axis on experimentally forged Ti-6Al-4V plate with a lamellar microstructure. Semiatin *et al.* (1999) demonstrated the same trend more quantitatively by measuring the trace of packets of platelets with respect to the compression axis. He showed that substantial changes in the orientation distribution of the packets occurred at relatively low strains (of the order of 0.50) and that at the larger strains, the distribution around 90° with respect to the compression axis merely became sharper. The realignment of the lamellar microstructure was accompanied by large changes in crystallographic texture indicating that the platelets had rotated under the applied strain. Microstructures suggested that bending and kinking of the lamellae played a large part in these platelet rotations. Moril *et al.* (1986a) also observed regions with strongly bent and curled lamellae in hot rolled Ti-6Al-4V.

The flow behaviour of lamellar microstructures differs significantly from equiaxed microstructures, with lamellar microstructures generally showing much larger degrees of flow softening than the globular α+β stress-strain curves, particularly at lower test temperatures (Semiatin and Lahoti, 1981). Semiatin *et al.* (1999) observed this flow softening during the hot deformation of Ti-6Al-4V with a lamellar structure and while

some of the softening was attributed to deformation heating, it was concluded that there was also a microstructure-related contribution to the overall flow softening. It was argued that the microstructure related softening, which was observed at strains prior to globularisation was related to the realignment of the lamellar microstructure. It was postulated that the bending and kinking of the α platelets during the platelet rotations was a form of plastic buckling analogous to that which occurs during the compression of a slender beam, and it was this that led to flow softening.

The mechanisms behind the globularisation process, which initiates after the realignment of the α lamellae, have received considerable attention from Weiss and his co-workers (Weiss *et al.*, 1986a). In lamellar structures with relatively thin α plate thicknesses (~3.4μm), Weiss *et al.* (1986a) proposed that the mechanism for globularisation was the break up of the α lamellae by a two step process. The first step is the formation of low and high angle α/α boundaries or intense shear bands across the α plates during deformation; this is followed by surface tension driven penetration of the α plates by the β phase to complete the separation during deformation or on subsequent annealing. In the same work, lamellar structures with thicker α lamellae (~6μm) globularised less for a given strain; in this thicker plate morphology, the α/α interfaces formed during deformation were less easily penetrated by the β phase, which resulted in a morphology of necklace-like α grains in place of the original α lamellae. In other work by Weiss and co-workers (Weiss *et al.* 1986b) on material containing much coarser α lamellae (30 to 40μm thickness), classical recrystallisation was also observed because of the greatly increased thickness.

2.4.5.2 Microstructural Evolution in Globularised α_p Grains During Secondary Working

As discussed in section 2.3.4.2, the higher hardness of the α_p grains compared to the softer β matrix means that the strain in the α phase is less than the nominal strain. At temperatures in the upper α+β phase field, where β is the continuous phase, most studies of the deformed α_p grains report dislocations and subboundary formation, indicating that the grains deform by slip and that dynamic recovery (DRE) operates. In Ti-6Al-4V, after deformation followed by quenching, Robertson and McShane (1997b) observed heavily dislocated α_p grains and subboundary formation in progress for all strain rates in the examined range of $4.2\text{x}10^{-4}$ s^{-1} to $4.2\text{x}10^{-2}$ s^{-1}. More subboundaries were observed at the slower strain rates, suggesting a greater degree of recovery. A TEM study of deformed α_p grains in Ti-6Al-4V by Sastry *et al.* (1980) revealed hexagonal networks of dislocations. Flower (1990) used back scattered electron imaging to reveal the subgrain structure in the α_p grains of Timetal 834 compressed to a strain of 0.5 at 1025°C and a strain rate of $5\text{x}10^{-4}$ s^{-1}. More recently deformed α_p grains in specimens deformed to a range of strains at a temperature of 1010°C and a strain rate of $2s^{-1}$, were investigated by Thomas (2007)

using high resolution EBSD. This revealed the development of accumulated misorientations and subgrain boundaries. Often the interior of the α_p grains contained fewer boundaries, which were more linear, whereas a higher density of subboundaries with a more equiaxed structure was observed at the grain edges. Single surface trace analysis on the more linear boundaries for the likely slip systems together with a calculation of their Schmid factors, indicated that grains probably deformed by a mixture of <a> and <c+a> slip. Deformation twins were also observed very infrequently in some α_p grains. Two examples of deformation twins were analysed by single surface slip trace analysis. One was found to coincide with a $\{10\bar{1}2\}\langle\bar{1}2\bar{1}0\rangle$ type tensile twin; a common twinning mode in titanium alloys. The second type of twin did not coincide with any of the commonly reported twinning modes. The lowest index plane shared by twin and matrix that showed a close correspondence to the twin trace on the map was found to $\{13\bar{4}1\}$. Two further $\{10\bar{1}2\}\langle\bar{1}2\bar{1}0\rangle$ type twins were reported in a specimen deformed at a higher strain rate of $20s^{-1}$ but no twins were observed at a lower strain rate of $0.2s^{-1}$. In the other studies mentioned, strain rates were below $2s^{-1}$, which may explain why deformation twinning was not reported in these cases.

In most previous studies, no recrystallisation is reported to occur in the α_p phase. However, it has been reported in some cases, suggesting that recrystallisation may be possible for certain processing conditions. Small equiaxed grains were observed around the larger α_p grains in isothermally forged Ti-6Al-4V using optical microscopy by Chen and Coyne (1976). However, forging temperatures were much lower in the $\alpha+\beta$ phase field such that the volume fraction of α_p was much higher (~80%). This microstructure was more pronounced at lower temperatures and slower strain rates. The specimens were air cooled following deformation, so any recrystallisation may have been either static or dynamic. Recrystallisation was also reported in Ti-6Al-4V by Sastry *et al.* (1980) but again this was at lower temperatures in the $\alpha+\beta$ phase field. The few reports for recrystallisation of the globular α_p phase, suggests that it is not a significant restoration mechanism, at least in the upper $\alpha+\beta$ phase field.

2.4.6 Texture Development in Hot Deformed $\alpha+\beta$ Microstructures

The textures which develop in the α phase during the hot deformation of two phase ($\alpha+\beta$) titanium alloys, depend strongly on the volume fraction and geometrical arrangement of the constituent phases (Moril *et al.*, 1986a, 1986b. Lebensohn and Canova, 1997). Since the volume fraction of α phase depends on the temperature, Morii *et al.* (1986b) distinguished three typical temperature regimes for deformation of a titanium alloy in the $\alpha+\beta$ phase field: (1) At low temperatures, where the volume fraction of α is very high, the material deforms like a single phase consisting of α with the hcp structure. (2) At

intermediate temperatures, the structure consists of α and β, with sufficient β so that it strongly influences the deformation modes of the α phase. (3) At high temperatures, where the volume fraction of β exceeds that of the α phase, slip in the β phase controls the deformation behaviour of the alloy.

The influence of the geometrical arrangement of the phases on the texture development means that different textures develop for globular and lamellar microstructures (Moril *et al.*, 1986a). In the former, the grains of both phases are approximately equiaxed and when fully globularised, there is no correlation between the orientations of two neighbouring α and β grains. In the latter, the α and β lamellae have a highly elongated morphology and within each colony, a regular alternating spatial arrangement. Furthermore, the orientations between neighbouring α and β lamellae within a colony are correlated by means of the Burgers relationship given in equation 2.3 and from which other relationships follow, such as:

$$\begin{aligned} &\{10\bar{1}0\}_\alpha \,//\, \{112\}_\beta \\ &\langle 1\bar{2}10\rangle_\alpha \,//\, \langle 111\rangle_\beta \end{aligned} \qquad (2.4)$$

The habit plane between phases is given by Ankem and Margolin (1986) as $\{5\text{-}1\text{-}40\}_\alpha$, which is near to $\{10\bar{1}0\}_\alpha$. Lütjering and Williams (2003) give the habit plane as $\{10\,1\,0\}_\alpha$ and $\{11\,2\}_\beta$. Fig. 2.23 shows the arrangement of the phases schematically. These correlations in morphology and orientation between the α and β phases in lamellar structures have an effect on the local plastic behaviour of each phase and hence the texture development.

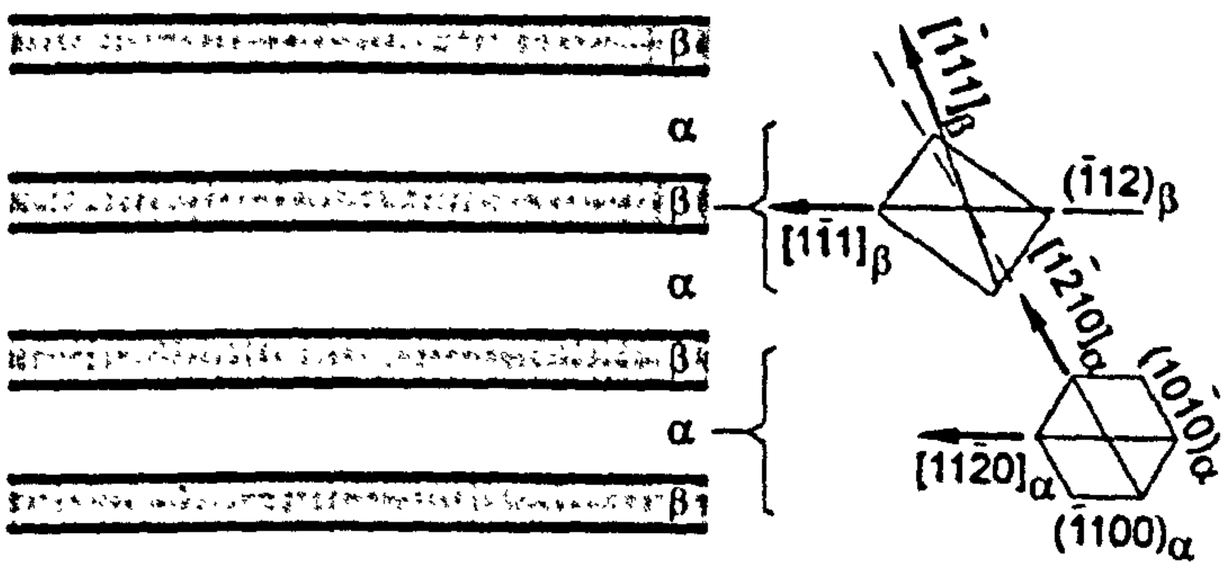

Fig. 2.23 Schematic representation of the crystallographic orientation relation between the α plates and the β matrix in α+β lamellar colonies (Lütjering and Williams, 2003).

Moril *et al.* (1986b) investigated the effect of microstructure and temperature on the texture development of Ti-6Al-4V after hot rolling. In the case of lamellar structures, hot rolling developed textures with a strong $\{1\bar{2}10\}\langle 10\bar{1}0\rangle$ component which gives a basal

maximum in the transverse direction (TD). At 1073K, there was also a rather large fibre like scatter around RD whereas at 1173K, the texture was dominated by the single $\{1\bar{2}10\}<10\bar{1}0>$ component with fluctuations of about 30° around ND and RD. In contrast, for the globular structure at 1073K, a rather smooth $<10\bar{1}0>$ fibre around RD formed. The texture formed at 1173K was similar but with a preference for the $\{1\bar{2}10\}<10\bar{1}0>$ component. Textures which resulted from hot rolling of lamellar microstructures in Ti-6Al-4V can also be seen in work by Ari-Gur and Semiatin (1998). These are broadly in agreement with Moril *et al.* (1986a) except that at the higher temperatures, in addition to the $\{1\bar{2}10\}<10\bar{1}0>$ component, there also a $\{1\bar{2}10\}<0002>$ component. It was speculated that this second RD component, which diminished in sharpness with increasing levels of strain, was associated with lamellar plate kinking and bending.

It is generally believed that the available slip systems in titanium alloys are: prismatic $\{0\bar{1}10\}<\bar{2}110>$, pyramidal $\{0\bar{1}11\}<\bar{2}110>$ and basal systems $\{0001\}<\bar{2}110>$ all having the <a> slip directions and the pyramidal systems $\{0\bar{1}11\}<11\bar{2}3>$ with <c+a> slip directions (Partridge, 1967). At low temperatures, twinning systems are also active but their contribution to the total strain becomes negligible at high solute additions and/or at higher temperature (Moril *et* al., 1986b). The <a> slip systems mentioned only provide four independent slip systems. Since five systems are required for an arbitrary shape change, exclusively <a> type slip is insufficient for deformation of a single phase hcp polycrystalline material (Von Mises and Angew, 1928. Taylor, 1938). Hence, in a single phase α titanium alloy, large plastic deformation demands <c+a> type slip in addition to <a> slip. In two phase α+β alloys however, the presence of β means that deformation of the rather anisotropic α phase no longer requires five independent slip systems, since incompatibilities can be accommodated easily by strains in the more isotropic β. This mechanism explains why the α textures in 2 phase alloys are quite different to those in single phase alloys. If slip occurs on all four <a> type slip systems with equal probability, a fibre texture of the type reported for globular structures at 1073K develops. In the lamellar structure, the correlations in crystallographic orientation and morphology between the alternate α and β lamellae favours the prismatic slip system, since this does not give rise to a shear of the large interface. An increase of the relative activity of prismatic slip is known to be associated with the formation of a TD maximum of the α texture.

Texture development in the β phase is only weakly affected by microstructure and texture (Moril *et al.*, 1986a). Moril *et al.* (1986a) found that the texture in the β could be described by components that are usually observed in rolled bcc materials, namely {001}<110>, {211}<011>, {111}<011>. They noted that the β textures were less sharp than those normally observed in bcc materials, particularly so for the lamellar case with a low volume fraction of β, where the effect of the accommodation strains from the α was

particularly strong. This is similar to the findings of Germain (2005), except the {211}<011> component was not reported.

2.4.7 Dwell Sensitive Fatigue in Near-α and α+β Titanium Alloys

It has been shown that a number of near-α and α+β titanium alloys can display a significant reduction in fatigue life when the fatigue cycle contains a dwell period at peak stress. Dwell sensitive fatigue has resulted in compromise and conservatism in alloy selection and design and in determining the service life of parts for the aerospace industry. Understanding the origins of dwell sensitive fatigue has therefore been the focus of many investigations during the last 30 years. The subject was recently reviewed by Bache (2003).

Fracture surface studies have shown that initiation sites in dwell fatigue failures are sub-surface and are characterised by the presence of quasi-cleavage facets. The facets form on the basal plane of the α phase and are predominantly aligned perpendicular to the principal stress direction. The facets are believed to form by the gradual separation of slip damage concentrated within a persistent planar slip band (Evans and Bache, 1994). It was argued that for the facets to form, slip must occur on the basal plane even though it may not be favourably orientated with respect to planes of maximum shear. Evans and Bache (1994) therefore proposed a modified Stroh pile-up model, to account for the transfer of a shear stress onto the unfavourably orientated planes (Fig. 2.24). This would introduce a tensile stress component, which in conjunction with the applied stress causes a crack to develop within the resultant slip band. In simple terms, stress is redistributed from favourably orientated or 'weak' grains onto 'hard' grains with their basal planes perpendicular to the applied stress. The dwell period at peak stress assists this process by encouraging bulk strain accumulation through ambient temperature creep, to which titanium alloys are susceptible (Bache, 2003).

The proposed model for dwell sensitivity suggests that microtexture i.e. both the microstructure and the local orientation distribution, will play a significant role in determining the dwell sensitivity of a particular part. In β processed near-α alloys, more slowly cooled microstructures consisting of large colonies of aligned α plates with the same crystallographic orientation have been shown to be the most susceptible to dwell. The basketweave structure, which tends to be produced at higher cooling rates, is less susceptible (Woodfield *et al.*, 1995). Timetal 685 (Evans and Bache, 1994) and 829 are examples of near-α alloys that are designed to be β heat treated and show these effects.

It would seem logical to expect α+β processed alloys to show low susceptibility to dwell as they do not contain large aligned α colonies. However, this is not the case, α+β processed Ti-6242 has been shown to be sensitive to dwell (Woodfield *et al.*, 1995), as

has Timetal 834 (Bache *et al.*, 1997). Woodfield *et al.* (1995) using EBSD showed that in α+β forgings, aligned α colonies that formed during the intermediate stages of billet processing can survive subsequent α+β processing and heat treatment even though the α plates undergo globularisation into α_p grains. Forgings containing the regions of aligned α_p grains showed significant life reductions when subjected to cyclic loading with a dwell period. In Timetal 834, Bache *et al.* (1997) found that specimens extracted from an isothermal disc forging were also dwell sensitive. This was again attributed to microstructural anisotropy; the microstructure contained agglomerations of elongated α_p grains with common basal plane orientations. In contrast, dwell sensitivity was not significant in specimens taken from small diameter bar stock, which was attributed to the larger amount of α+β working and a final solution heat treatment that resulted in the recommended 15% volume fraction of well distributed equiaxed α_p grains (Fig. 2.25).

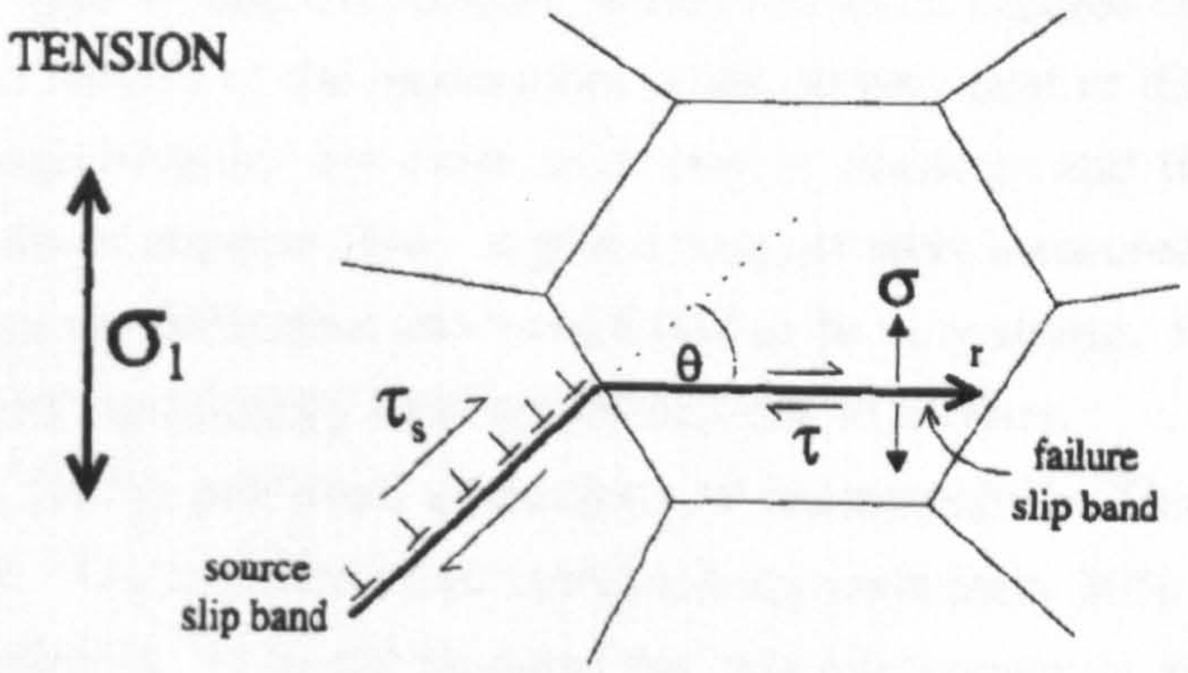

Fig. 2.24 The Stroh type model used to explain basal facet formation (Evans and Bache, 1994).

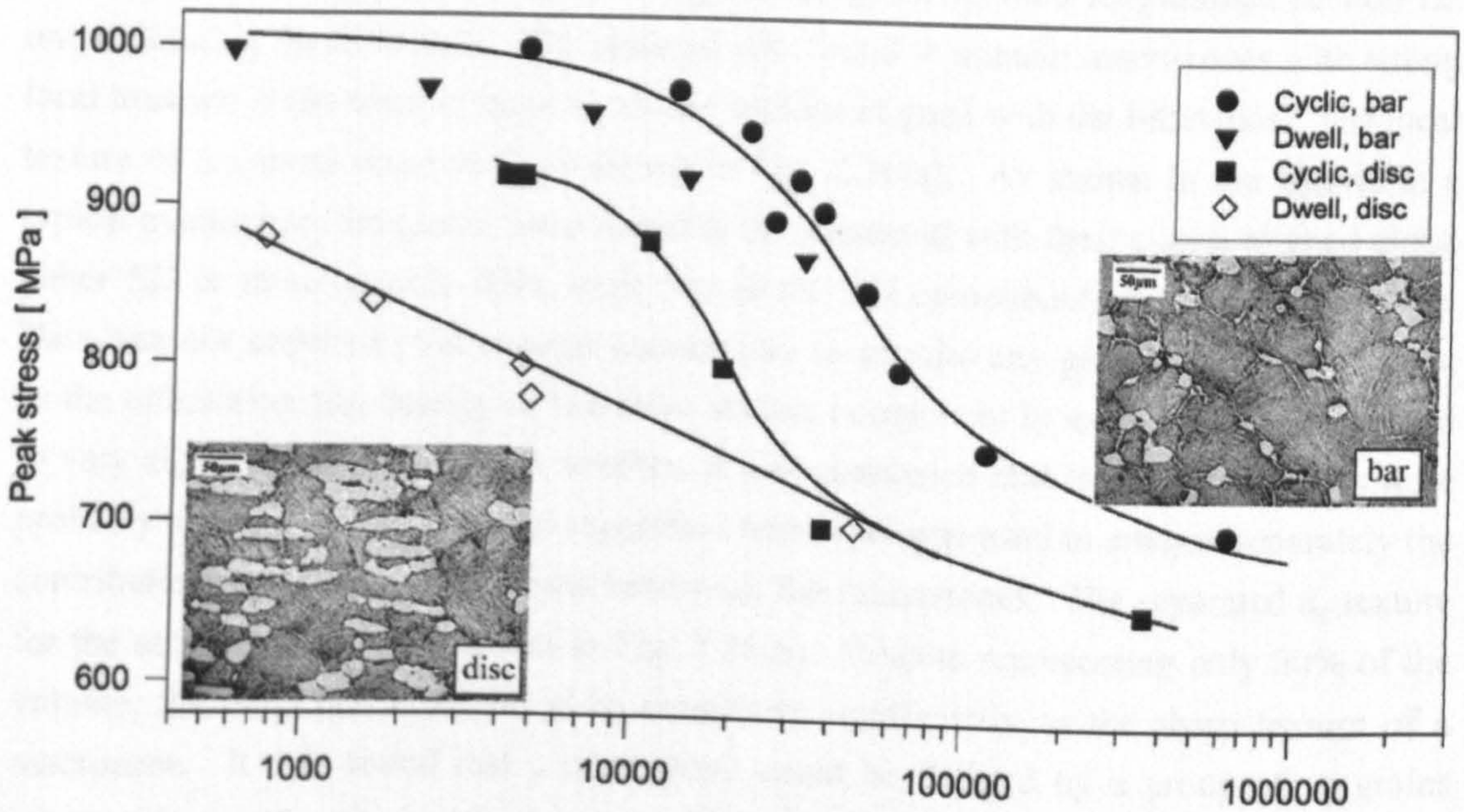

Fig. 2.25 Cyclic and dwell fatigue response of Timetal 834 in bar and forged disc conditions (Bache *et al.*, 1997).

2.4.8 Microtexture Development in Hot Deformed α+β Microstructures

The regions of aligned α_p grains and how they form during manufacture have been investigated in several studies. Ari-Gur and Semiatin (1997) investigated their evolution in Ti-6Al-4V during hot rolling. Regions with strong local textures, caused by aligned α_p grains, were present after hot rolling in material which consisted initially of lamellar colonies, but were not present when the initial microstructure was basketweave / acicular. It was concluded from this study that the textured regions were related to the prior colonies rather than the prior β grains.

Le Biavant *et al.* (2002) reported their presence in a bimodal Ti-6Al-4V alloy billet. The regions were revealed by macroetching and found to be roughly 100 times the apparent α_p grain size when viewed in the transverse plane of the billet. The regions of aligned α_p grains were termed macrozones, which has since become commonly used. It was found that the borders of the macrozones could be very neat or diffuse. The size of the macrozones was irregular but close to 1 mm in diameter and they seemed to be aligned in directions of material flow. α phase textures were measured inside individual macrozones using x-ray diffraction and were found to be very strong. Furthermore, the α phase textures varied significantly from one macrozone to another.

Germain *et al.* (2005) published an analysis of macrozones in Timetal 834 material described as billet. The microstructure contained approximately 30% α_p surrounded by finer lamellar α_s colonies. It should be noted that this microstructure differs from typical Timet supplied billets for this alloy, which tend to contain a much higher fraction of α_p and coarser α_s. The material was investigated using EBSD on a longitudinal section i.e. one containing the billet axis. The material was found to contain macrozones with strong local textures in the form of large band-like regions aligned with the billet axis. The local texture of a typical macrozone is shown in Fig. 2.26(a). As shown in the figure, in a typical macrozone, the grains were found to be orientated with their c-axes aligned along either ED or three specific RDs, with one of the RD components tending to dominate. Data was not acquired over enough macrozones to acquire any global billet textures but as the orientation and density of the main texture component in each macrozone seemed to vary significantly from one to another, it was concluded that the global textures were probably not very sharp. A phase separation technique was used to analyse separately the contribution of α_p and α_s to the local texture of the macrozones. The separated α_p texture for the same macrozone is shown in Fig. 2.26(b). Despite representing only 30% of the volume, the α_p grains were found to contribute significantly to the sharp texture of a macrozone. It was found that a macrozone could be defined by a group of α_p grains orientated around a single texture component with about 20° of spread. The orientation of the single α_p texture component corresponded to the dominant RD component in the combined macrozone texture (Fig. 2.26(a)). The separated α_s texture for the macrozone

is shown in Fig. 2.26(c). The α_s was responsible for the remaining textures components seen in the combined macrozone texture (Fig. 2.26(a)). Differences in the pole intensities of these components indicated that variant selection occurs in the $\beta \rightarrow \alpha_s$ phase transformation. Variants having on average their c-axes in the same macroscopic direction as those of the α_p grains are favoured. Consequently, the sharp local texture of the combined macrozone was found to be due to the overlapping of the single α_p component and the main α_s component.

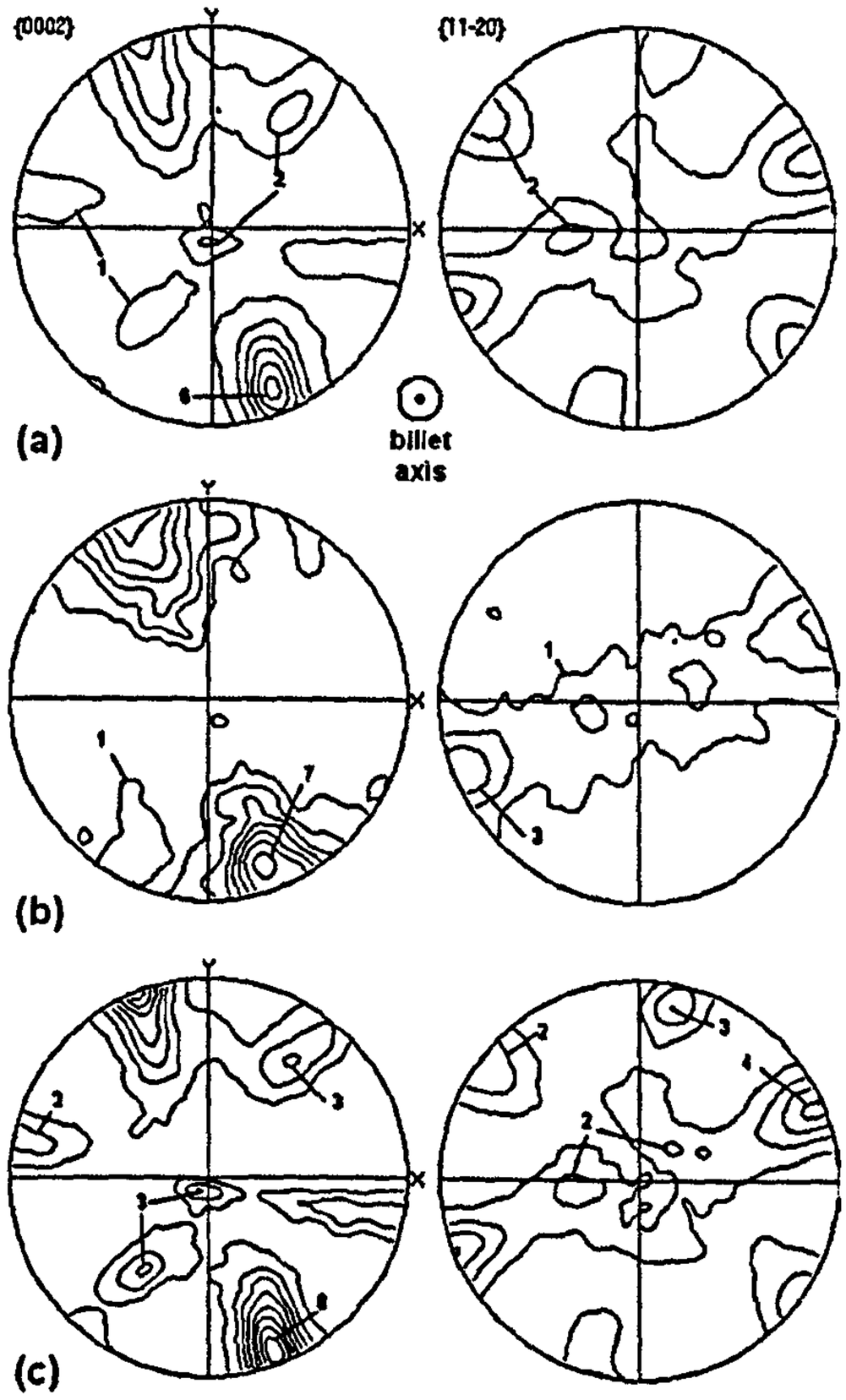

Fig. 2.26 (a) Overall α texture of a macrozone, (b) the separated α_p texture, (c) the separated α_s texture (Germain *et al.*, 2005).

Bantounas *et al.* (2007) characterised macrozones in Ti-6Al-4V forged bar, unidirectional rolled plate and cross-rolled plate product forms as part of an investigation into the effect of microtexture on fatigue cracking. The bar was found to be composed of columnar macrozones 50-70μm in width and elongated along the bar axis. In agreement with Germain (2005), the macrozones were orientated with their c-axes in radial directions i.e. perpendicular to the bar axis. It was also noted that each macrozone, in turn consisted of smaller bands, within which the misorientations were small. The

unidirectional rolled plate contained two macrozone orientations, one having the c-axes aligned with TD and the other aligned with RD. The TD macrozones occupied a greater portion of the scanned region and were approximately 70 μm in width, while the RD macrozones were approximately 25 μm in width. In the cross-rolled plate, macrozones were in the form of thins bands, a few grains in thickness.

Macrozones in a billet of Timetal 834 were investigated by Thomas (2007). The material investigated originated from the mid-radius of a 200 mm diameter billet. The macrozones had diameters in the transverse plane which ranged from 200-800 μm. The textures of the macrozones consisted of a single hcp component with varying degrees of spread. This differs from the previously mentioned macrozone textures reported by Germain *et al.* (2005), which contained additional secondary components attributed to the α_s phase. The absence of these secondary components in the work of Thomas can be explained by the much lower volume fraction of α_s in his billet (only 30% α_s). Textures were measured from 12 separate macrozones. In 11 of the macrozones, the c-axes of the grains were orientated in radial directions and in the majority of these 'radial' macrozones, a $\{10\bar{1}0\}$ plane lay parallel to the transverse plane of the billet. In 1 of the macrozones, the c-axes of the grains were orientated along the billet axis.

Germain *et al.* (2008) published a further paper on macrozones in Timetal 834. In this work, cylindrical specimens with an initially coarse lamellar microstructure were heated to 1000°C and deformed in axi-symmetric compression to simulate the final α+β deformation step occurring in primary working. The resulting microstructures were investigated using EBSD and found to contain macrozones. The grains within a macrozone were found to have their c-axes parallel to a common radial direction of the cylindrical specimen and a $\{11\bar{2}0\}$ pole parallel to the compression direction. The radial c-axis direction varied from one macrozone to the other, so that the global texture consisted of a rather inhomogeneous $\{11\bar{2}0\}$ fibre parallel to the compression direction. It was shown that all lamellae of a colony tended to deform in the same way, which meant the α colony size directly influenced the macrozone size. However, it was also argued that neighbouring colonies with different orientations, whether inherited from the same parent β grain or not, could rotate toward the same texture component, leading to an extension of macrozone size beyond the prior colony size. As in the earlier work, it was found that the α_s colonies were often orientated close to the main α_p texture component in a macrozone. This was explained by variant selection and additionally, in the case of particularly strongly textured macrozones, the fact that the β phase was found to still be close to a Burgers relation with the α_p grains despite the deformation.

In the studies of macrozones mentioned above, EBSD has been used to study relatively small areas of material and thus the number of macrozones studied in each case has been fairly limited. The work has shown that macrozones clearly have certain preferred orientations in different product forms but many more macrozones would need to be

studied in order to gather statistically representative data on these preferred orientations. Furthermore, no information has been published on how the macrozones and their orientations vary depending on the location in products such as billet.

Various studies have demonstrated that ultrasonic inspection is a technique capable of detecting the presence of macrozones in titanium alloys (Han and Thompson, 1997. Gigliotti *et al.*, 2000. Bescond *et al.*, 2004. Thompson *et al.*, 2007). Gigliotti *et al.* (2000) showed that blocks of Ti-6242 material with a fine, uniform, texture-free microstructure, had a significantly greater signal-to-noise ratio than equivalent blocks with a microstructure consisting of macrozones. Bescond *et al.* (2004) developed a numerical focusing technique that revealed differences in the backscattered noise due to variations in the size shape and orientations of the macrozones (Fig. 2.27). When inspecting a titanium alloy billet, a low backscattered noise level was observed for incident acoustic waves along the billet axis, while higher noise levels were observed in radial directions. This was believed to be due to the primary alignment of the macrostructure along the billet axis i.e. the billet contained columnar macrozones elongated along the billet axis. Additionally, in the radial directions the noise level was found to have an angular dependence. Four high-noise bands separated by 90° were observed, which was taken to be evidence of a secondary alignment of the macrostructure in the transverse plane. The symmetry of the four high noise bands separated by 90° was explained by the fact that the billet was forged from an intermediate square cross-section to a circular one. A final forged part was also examined using the technique. This produced more complex images for the backscattered noise since the macrozones have more complex orientations following the forging flow lines. However, the angular dependence of the billet could still be seen in regions of the forging receiving moderate deformation.

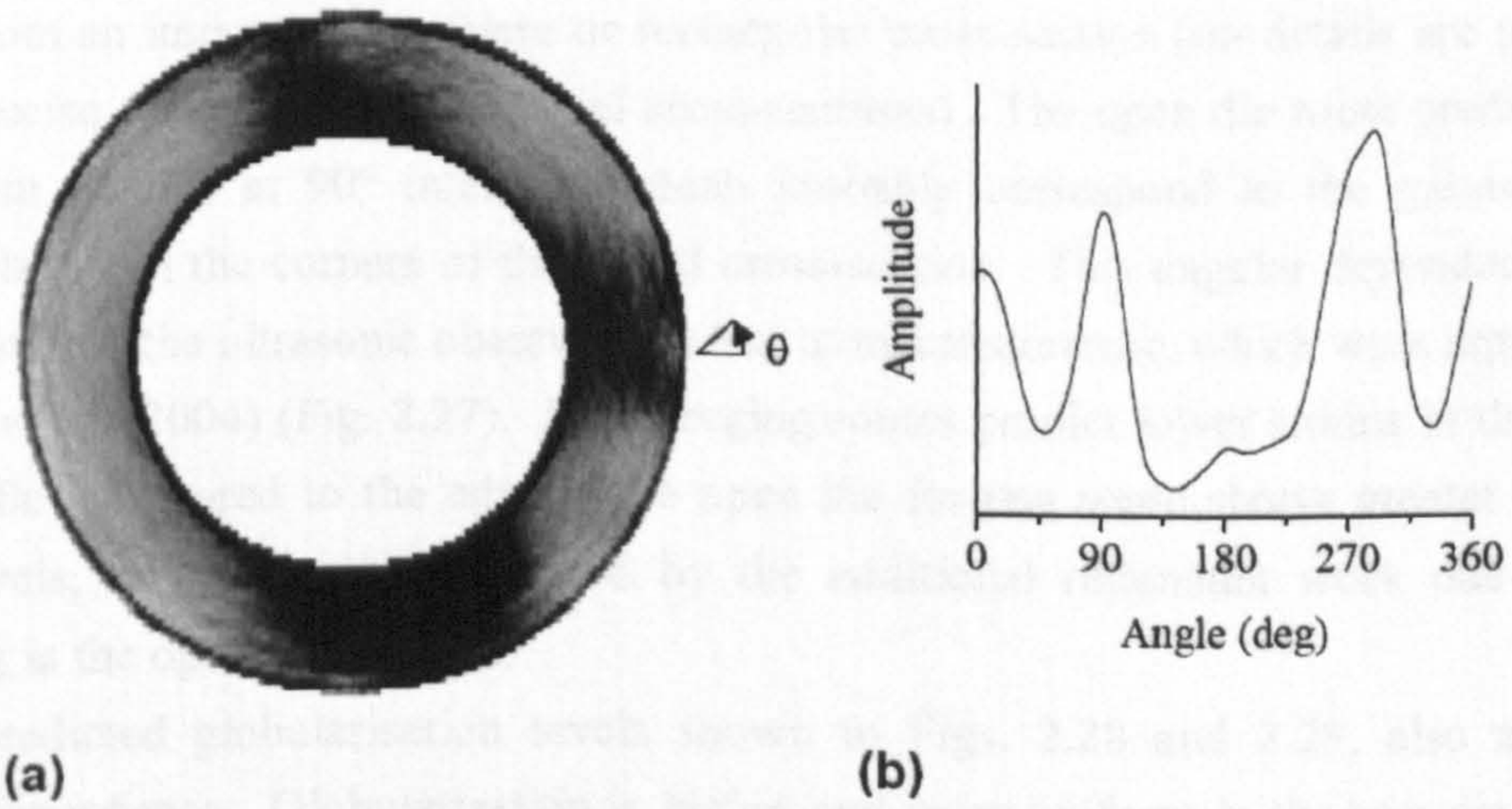

Fig. 2.27 (a) Image of the ultrasonic backscattered noise in radial directions in a titanium billet. (b) Angular dependence of the back scattered noise averaged along the radial direction (Bescond *et al.*, 2004).

2.4.9 Modelling of the Billet Forging Process

Compared to computer modelling of closed die forging, the application of modelling to the billet forging process is less well developed (Fox and Neal, 1995). Most of the published work has focused on Ti-6Al-4V and microstructure predictions have not been extended to the prediction of microtexture and macrozones. Two-dimensional plane strain approaches have been applied to the billet forging process and have been found to give useful semi-quantitative information on the strain distribution through the cross-section (Dumas *et al.*, 1995) and near surface stresses and strains that can lead to surface cracking (Fox and Neal, 1995). Dumas *et al.* (1995) developed a 2-d finite element model for the billet forging of Ti-6Al-4V. The influence of the thickness of the billet and the bite and depth of the forging pass on local strain distribution across sections of the billet was investigated. The results showed that the deformation was more localised at the surface for thicker billets. Increasing the bite leads to more deformation at the centre of the billet and the formation of a 'dead zone' beneath the die. Increasing the depth i.e. the applied strain, did not have a substantial effect on the strain distribution but increased the general intensity of the equivalent strain.

Forging billets using an open die forge induces 3 dimensional metal flow, where both side-spread and extension of the bar are significant. Therefore, to improve accuracy, more recent models have employed a 3D finite element approach (Wilson *et al.*, 2003). Wilson *et al.* predicted strain distributions and the volume fraction of globularised α_p in Ti-6Al-4V billet forged using both open die forging and four die radial forging routes (Figs. 2.28 and 2.29). The model predictions were supported by microstructural findings from forged bars produced by these routes. It can be seen in Figs. 2.28 and 2.29 that the predicted strain distributions have an angular dependence due to fact that the billets are forged from an intermediate square or rectangular cross-section (no details are provided on the precise dimensions of the initial cross-sections). The open die route predicts four high strain regions at 90° intervals, which probably correspond to the greater strain imposed between the corners of the initial cross-section. This angular dependence is in agreement with the ultrasonic observations due to macrostructure, which were reported by Bescond *et al.* (2004) (Fig. 2.27). Both forging routes predict lower strains in the centre of the billet compared to the edge. The open die forging route shows greater average strain levels, which can be explained by the additional redundant work due to side spreading in the open die process.

The predicted globularisation levels shown in Figs. 2.28 and 2.29, also show an angular dependence. Globularisation is higher and more uniform in the two die process due to the greater average strain levels and a greater number of reheats (time at temperature) used in the two die forging route. For both routes, globularisation is lower in the centre of the billet compared to the edge. Although microtexture is not discussed in

the work of Wilson *et al.* (2003), it is logical to conclude from the predicted variations in strain and globularisation that there may also be significant variations in microtexture through the billet cross-section.

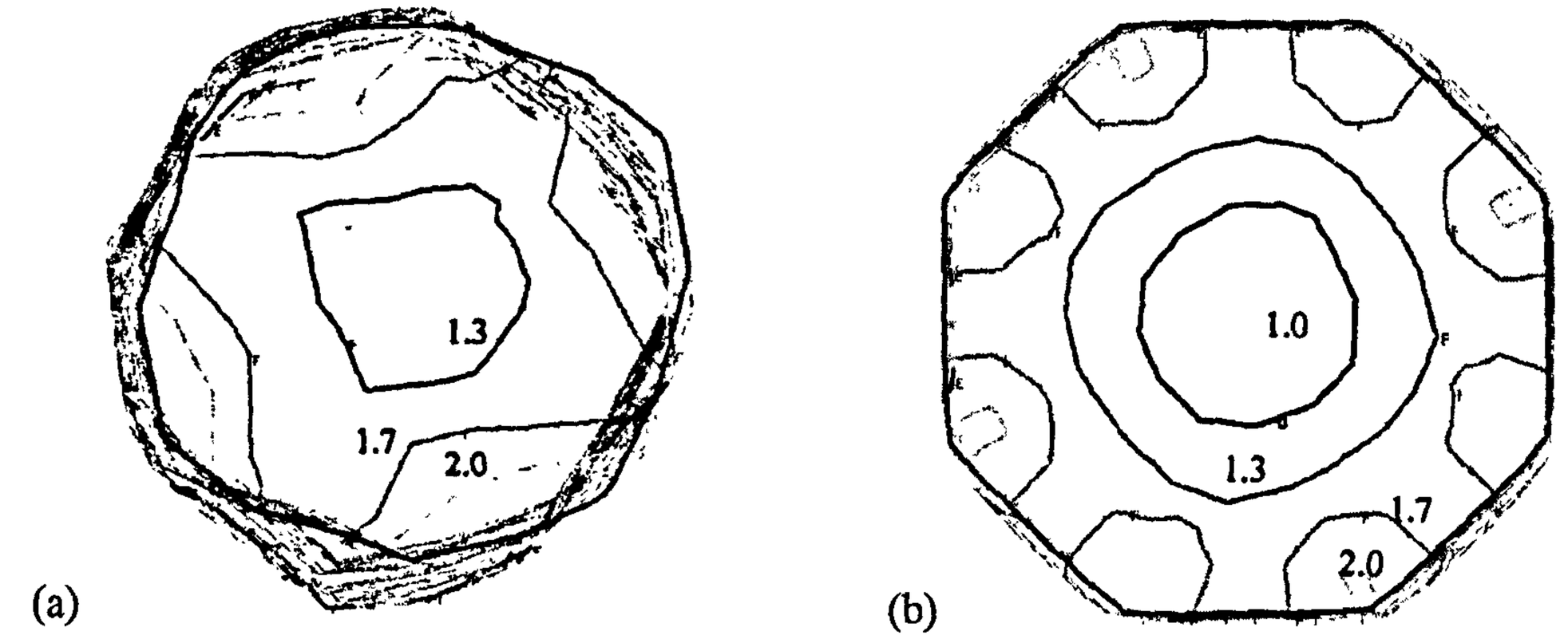

Fig. 2.28 Transverse slice showing predicted strain distribution in (a) open die forging press and (b) four die radial forging routes, following final α+β forging (Wilson *et al.*, 2003).

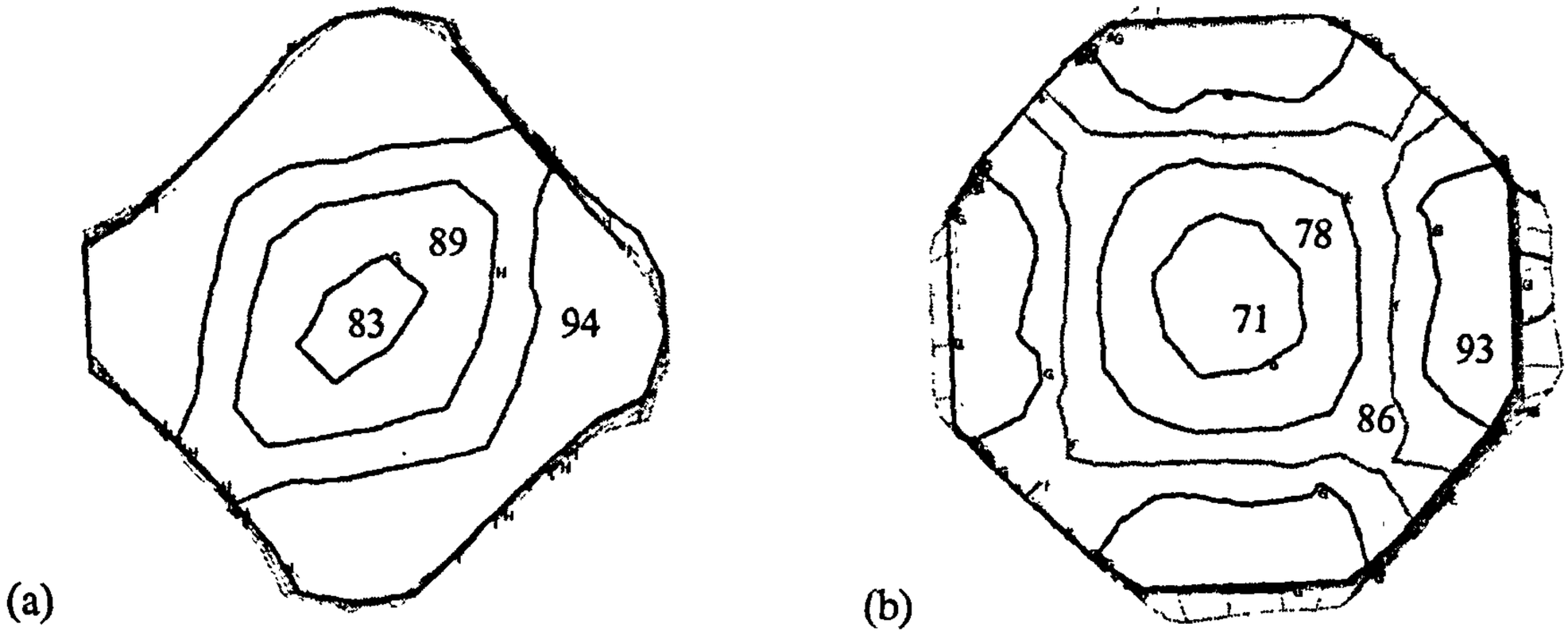

Fig. 2.29 Transverse slice showing predicted volume fraction of globularised α distribution in (a) open die forging press and (b) four die radial forging routes, following final α+β forging and heat treatment (Wilson *et al.*, 2003).

2.5 Texture Analysis and EBSD Post-processing Techniques

2.5.1 Orientation

In this section, aspects of orientation and texture relevant to the EBSD post-processing work are introduced. For a thorough background to orientation and textures in materials science, the reader is referred to books by Randle and Engler (2000), Bunge (1982), and Kocks *et al*. (2000). The term *orientation* in materials science refers to how the atomic planes in a volume of crystalline material are positioned relative to a fixed reference frame. In order to describe an orientation it is necessary to define two coordinate systems, the *specimen coordinate system* and the *crystal coordinate system*. The orientation then becomes a description of the transformation between these two coordinate systems.

2.5.1.1 Coordinate Systems

Both coordinate systems are Cartesian and preferably right-handed (Randle and Engler, 2000). The axes of the specimen coordinate system are usually chosen according to important directions which relate to the external form of the specimen and in the case of a fabricated material, the processing geometry. A rolled product is a common example (Fig. 2.30(a)). Here, the axes of the specimen coordinate system are the rolling direction (RD), the direction normal to the rolling plane (ND) and the transverse direction (TD). These axes also apply to the plane strain compression test, which is a key part of this work. The other type of specimen in this work originates from a round billet, which has only uniaxial symmetry. Here, only one axis has to be specified in the specimen coordinate system and the other two axes can be chosen arbitrarily, as shown in Fig. 2.30(b).

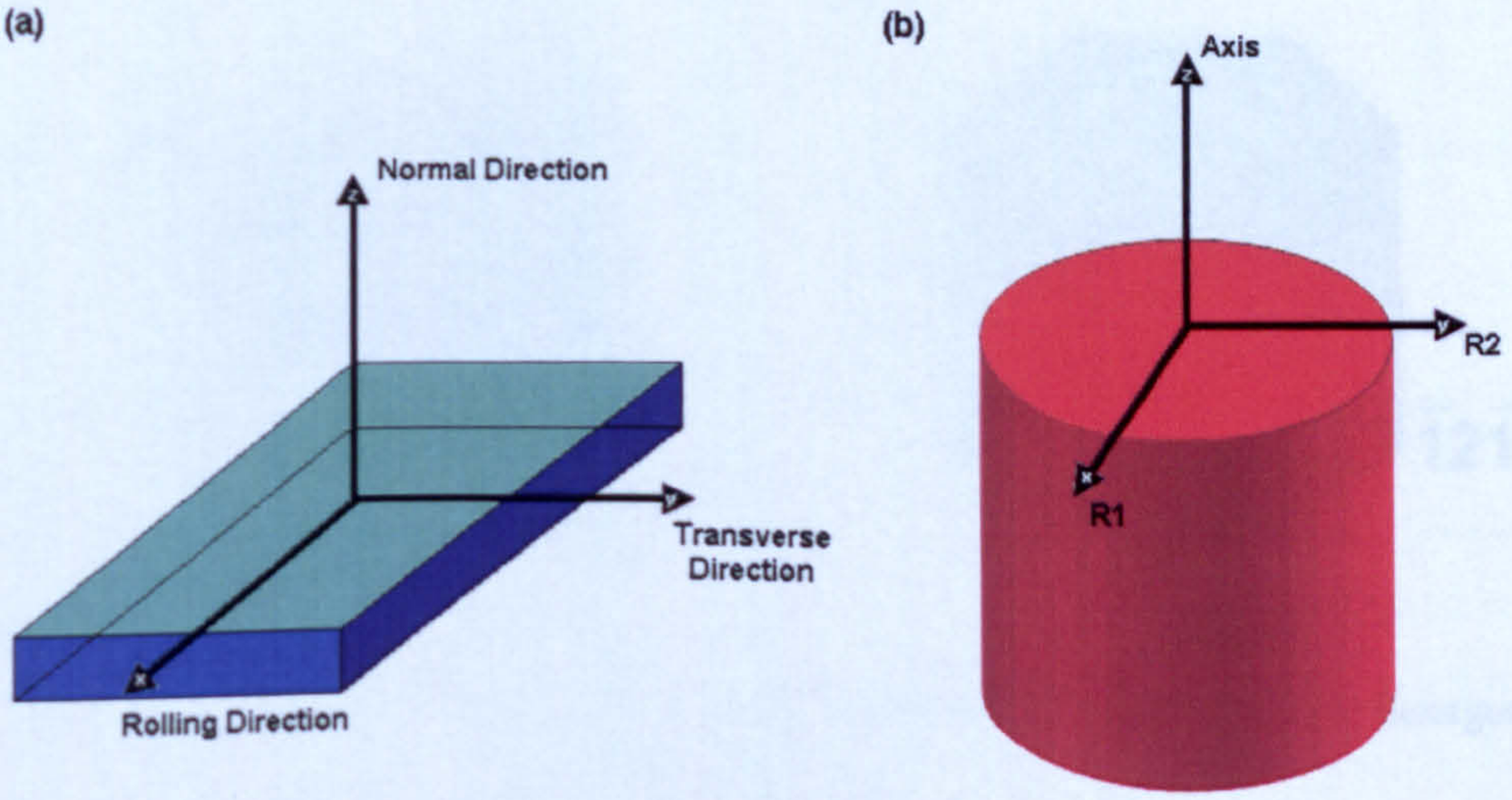

Fig. 2.30 Specimen coordinate systems for (a) a rolled product and (b) a uniaxial product.

The crystal coordinate system is specified by directions in the crystal. It is convenient to adapt the coordinate system to the crystal symmetry. For crystals with orthogonal symmetry (cubic, tetragonal, orthorhombic), the axes [100], [010] and [001] already form an orthogonal frame, which is adopted as the crystal coordinate system, as shown in Fig. 2.31(a) (Randle and Engler, 2000). This crystal coordinate system is used for the β phase of titanium, which has the body centred cubic (bcc) crystal structure. For crystals with hexagonal symmetry, such as the α phase of titanium, which has the hexagonal close-packed (hcp) crystal structure, the most common choice for the crystal coordinate system is (Randle and Engler, 2000):

$$X = [10\bar{1}0], \quad Y = [\bar{1}2\bar{1}0], \quad Z = [0001] \tag{2.5}$$

These crystal axes must be normalised so that they are all the same length (i.e. orthonormal). This normalisation procedure is carried out by pre-multiplying a zone axis, referenced to the crystal coordinate system, by a transformation matrix L. For hexagonal crystals, this transformation matrix L is given by (Randle and Engler, 2000):

$$L = \begin{pmatrix} a & -a/2 & 0 \\ 0 & (a\sqrt{3})/2 & 0 \\ 0 & 0 & c \end{pmatrix} \tag{2.6}$$

where a and c are the unit cell parameters. To transform back from orthonormal coordinates to the crystal reference system, one must premultiply by the inverse of the transformation matrix L^{-1}. The crystal coordinate system for hexagonal symmetry is shown in Fig. 2.31(b).

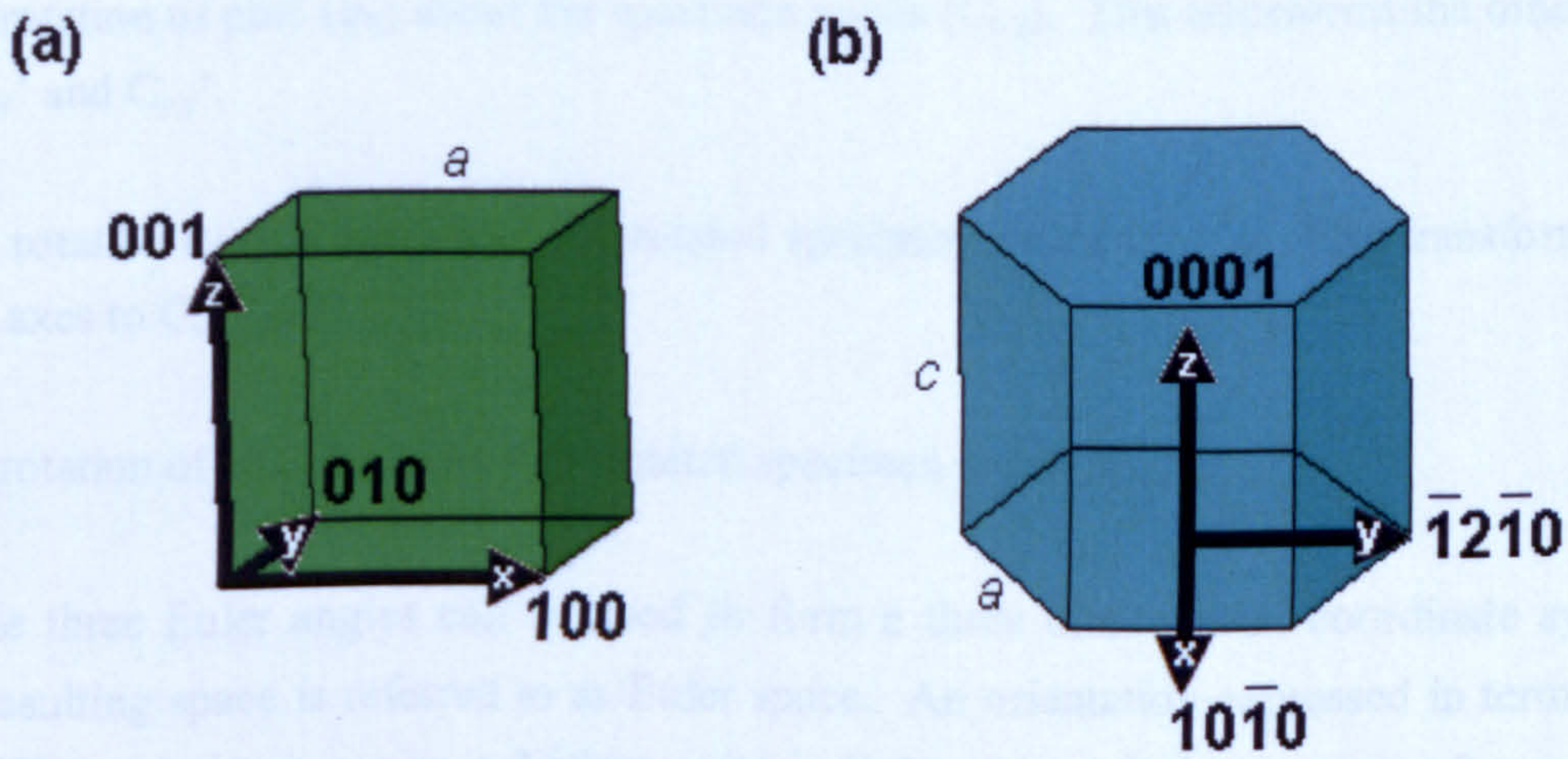

Fig. 2.31 Orthonormalised crystal coordinate systems for (a) cubic and (b) hexagonal symmetries.

2.5.1.2 Descriptors of Orientation

Having defined the coordinate systems for the specimen and the crystal, the orientation can be defined as (Randle and Engler, 2000):

$$C_c = g \cdot C_s \tag{2.7}$$

Where C_c and C_s are the crystal and specimen coordinate systems respectively and g is the orientation. Using this description, g describes the rotation from the specimen coordinates onto the crystal coordinates. There are several different methods for describing the orientation g, each having there own advantages for processing and representing different aspects of orientation measurements. Four such descriptors, which will be introduced here are: Euler angles, the orientation matrix, the Angle/axis pair and the quaternion.

Euler Angles

The minimum number of variables needed to completely define an orientation is three. The most common method of describing an orientation using only three variables is using Euler Angles. The three Euler Angles describe a sequence of rotations of the specimen coordinate system about various axes until it comes into coincidence with the crystal coordinate system. There are various conventions regarding the choice of axes and the order of operation. One of the most common and the one which is used by the Channel 5 EBSD software is the Bunge convention (Bunge, 1982). The effect of the operation sequence can be seen in Fig. 2.32. The sequence of rotations are:

1. A rotation of phi1 (ϕ_1) about the specimen z-axis (C_{sz}). This transforms the other axes to C_{sx}' and C_{sy}'.

2. A rotation of PHI (Φ) about the rotated specimen x-axis (C_{sx}'). This transforms the other axes to C_{sy}'' and C_{sz}'.

3. A rotation of phi2 (ϕ_2) about the rotated specimen z-axis (C_{sz}').

The three Euler angles can be used to form a three dimensional coordinate system. The resulting space is referred to as Euler space. An orientation expressed in terms of a set of Euler angles occupies a distinct point in Euler space. Euler space is often used to present orientation distribution functions (ODFs), which are a means of describing textures.

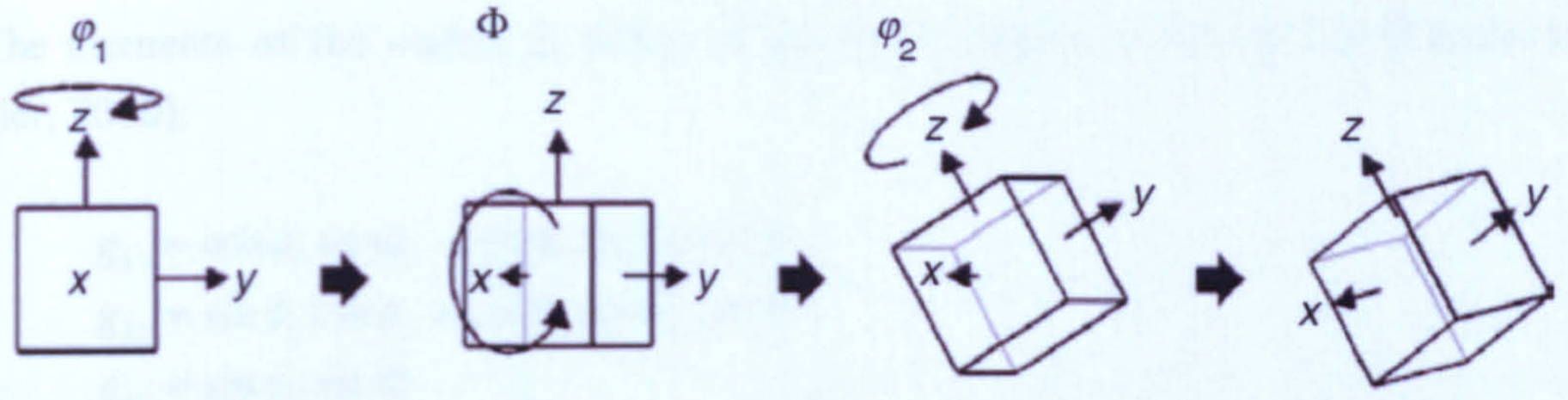

Fig. 2.32 Diagram showing the rotation of a specimen through the Euler angles ϕ_1, Φ and ϕ_2 (HKL Channel 5, 2006).

Orientation Matrix

The orientation matrix is a square 3x3 matrix that describes the rotation g. The elements of the matrix can be obtained as follows (Randle and Engler, 2000): The first row of the matrix is given by the cosines of the angles between the first crystal axis, $C_{c\,x}$ and each of the three specimen axes, $C_{s\,x}$, $C_{s\,y}$, $C_{s\,z}$, in turn. These three angles are labelled as α_1, β_1, γ_1, in Fig. 2.33. Similarly, the second row is given by the cosines of the angles α_2, β_2, γ_2, between the second crystal axis $C_{c\,y}$ and each of the three specimen axes, $C_{s\,x}$, $C_{s\,y}$, $C_{s\,z}$, in turn. Finally, the third row is given by the cosines of the angles α_3, β_3, γ_3, between $C_{c\,z}$ and each of the three specimen axes, $C_{s\,x}$, $C_{s\,y}$, $C_{s\,z}$, in turn. Hence, the complete matrix can be written as:

$$g = \begin{pmatrix} g_{11} & g_{12} & g_{13} \\ g_{21} & g_{22} & g_{23} \\ g_{31} & g_{32} & g_{33} \end{pmatrix} = \begin{pmatrix} \cos\alpha_1 & \cos\beta_1 & \cos\gamma_1 \\ \cos\alpha_2 & \cos\beta_2 & \cos\gamma_2 \\ \cos\alpha_3 & \cos\beta_3 & \cos\gamma_3 \end{pmatrix} \tag{2.8}$$

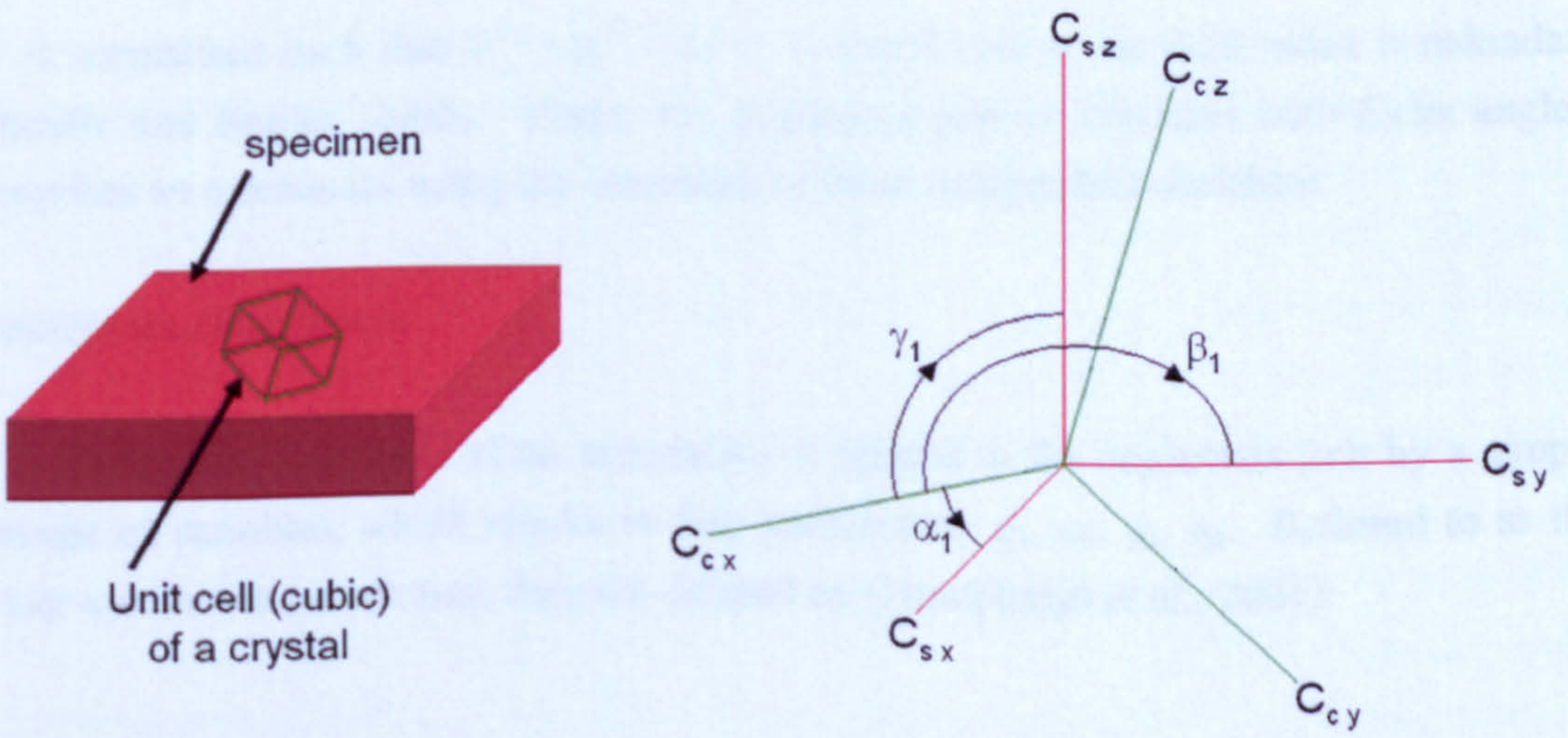

Fig. 2.33 An illustration of the orientation of a crystal with respect to a specimen. The cosines of the angles α_1, β_1, γ_1 give the first row of the orientation matrix.

The elements of the matrix in terms of the Euler Angles are given by (Randle and Engler, 2000):

$$\begin{aligned}
g_{11} &= \cos\phi_1 \cos\phi_2 - \sin\phi_1 \sin\phi_2 \cos\Phi \\
g_{12} &= \sin\phi_1 \cos\phi_2 + \cos\phi_1 \sin\phi_2 \cos\Phi \\
g_{13} &= \sin\phi_2 \sin\Phi \\
g_{21} &= -\cos\phi_1 \sin\phi_2 - \sin\phi_1 \cos\phi_2 \cos\Phi \\
g_{22} &= -\sin\phi_1 \sin\phi_2 + \cos\phi_1 \cos\phi_2 \cos\Phi \\
g_{23} &= \cos\phi_2 \sin\Phi \\
g_{31} &= \sin\phi_1 \sin\Phi \\
g_{32} &= -\cos\phi_1 \sin\Phi \\
g_{33} &= \cos\Phi
\end{aligned} \tag{2.9}$$

Angle/axis Pair

The same transformation described by the three Euler angles can be described by a single rotation if this rotation takes place about a specific axis. The angle θ and axis $\vec{d}$ can be calculated from the orientation matrix g as follows (Randle and Engler, 2000. Germain, 2005a):

$$\cos\theta = (g_{11} + g_{22} + g_{33} - 1)/2 \tag{2.10}$$

$$\vec{d} = \begin{pmatrix} d_1 \\ d_2 \\ d_3 \end{pmatrix}, \text{ where: } \begin{aligned} d_1 &= g_{23} - g_{32} \\ d_2 &= g_{31} - g_{13} \\ d_3 &= g_{12} - g_{21} \end{aligned} \tag{2.11}$$

$\vec{d}$ is normalised such that $d_1^2 + d_2^2 + d_3^2 = 1$, which means the third index is redundant (Randle and Engler, 2000). Hence the angle/axis pair in common with Euler angles, describes an orientation using the minimum of three independent variables.

Quaternion Description

The quaternion descriptor of an orientation is related to the angle/axis pair by a simple change of variables, which results in four parameters: q_1, q_2, q_3, q_4. Referred to as the Euler-symmetric parameters, they are defined by (Humphreys *et al.*, 2001):

$$\begin{aligned} q_1 &= d_1 \sin(\theta/2) \\ q_2 &= d_2 \sin(\theta/2) \\ q_3 &= d_3 \sin(\theta/2) \\ q_4 &= \cos(\theta/2) \end{aligned} \tag{2.12}$$

where d_1, d_2, d_3, is the normalised axis of rotation and θ is the angle of rotation about the axis that together make up the angle/axis pair. The norm of the four parameters is unity, i.e. they satisfy the equation (Kocks *et al.*, 2000):

$$\left[q_1^2 + q_2^2 + q_3^2 + q_4^2\right]^{1/2} = 1 \tag{2.13}$$

The four parameters with a norm of one can be regarded as the components of a unit quaternion. A quaternion consists of a real scalar part (q_4) and a hyper-imaginary 3 vector part (q_1, q_2, q_3) defined as (Zombeck, 2007):

$$\mathbf{q} = q_4 + iq_1 + jq_2 + kq_3 \tag{2.14}$$

where

$$i^2 = k^2 = j^2 = -1 \tag{2.15}$$

and

$$\begin{aligned} ij &= -ji = k \\ jk &= -kj = i \\ ki &= -ik = j \end{aligned} \tag{2.16}$$

Rotations described by quaternions may be efficiently combined and manipulated using quaternion algebra. For a comprehensive background on quaternions and their algebra, the reader is referred to the book by Kuipers (1999). The properties of quaternions and their connection to matrices and Euler angles have also been reviewed by Morawiec and Pospiech (1989). Ways in which quaternions may be applied to the analysis of orientation data have been described by Harauz (1990), Humbert *et al.* (1996), Humpreys *et al.* (2001) and Glez and Driver (2001).

When described in terms of unit quaternions, every orientation is represented by a point on the surface of the upper half of a sphere in four-dimensional Euclidean space (Humphreys *et al.*, 2001). Although this physical interpretation of quaternions is less intuitive than the Euler angle or angle/axis descriptors, quaternions offer a number of

advantages when analysing and processing orientation data. They are particularly useful for interpolating rotations e.g. when calculating the average or spread of a cloud of orientations (Humphreys *et al.*, 2001. Harauz, 1990. Humbert *et al.*, 1996). Such operations are required when analysing large numbers of orientation measurements such as EBSD datasets. The commonly used three parameter descriptors such as Euler angles and angle/axis pair prove unsatisfactory for these types of operation because the orientation spaces associated with these descriptors are very distorted and generally not closed (Humphreys *et al.*, 2001). As a result, distances between orientations in them can differ greatly from the misorientation angle, whereas the quaternion elements vary continuously over the unit hypersphere as the orientation changes. Also, quaternions are one of the most computationally efficient ways of combining and manipulating rotations, since the calculations generally require fewer floating point operations and transcendental functions compared to the equivalent calculations using the other common descriptors (Rollet, 2005).

Addition for quaternions is defined by adding the corresponding parameters. For example, the sum of two quaternions **p** and **q** is given by (Kuipers, 1999):

$$\mathbf{p}+\mathbf{q}=(p_4+q_4)+i(p_1+q_1)+j(p_2+q_2)+k(p_3+q_3) \tag{2.17}$$

Quaternion multiplication is non commutative. The parameters of the quaternion product, **r**, of two quaternions, **pq** is given by (Kuipers, 1999):

$$\mathbf{r}=\mathbf{pq}$$

$$\begin{aligned} r_4 &= p_4q_4 - p_1q_1 - p_2q_2 - p_3q_3 \\ r_1 &= p_4q_1 + p_1q_4 + p_2q_3 - p_3q_2 \\ r_2 &= p_4q_2 - p_1q_3 + p_2q_4 + p_3q_1 \\ r_3 &= p_4q_3 + p_1q_2 - p_2q_1 + p_3q_4 \end{aligned} \tag{2.18}$$

The inverse of a unit quaternion **q** is the same as the complex conjugate, denoted $\mathbf{q}^*$. The parameters of $\mathbf{q}^*$ are defined by (Kuipers, 1999):

$$\begin{aligned} q^*4 &= q_4 \\ q^*1 &= -q_1 \\ q^*2 &= -q_2 \\ q^*3 &= -q_3 \end{aligned} \tag{2.19}$$

The negative of a quaternion **q** is given by:

$$-q = -q_4 - iq_1 - jq_2 - kq_3 \tag{2.20}$$

2.5.1.3 Crystallographically Related Solutions

An orientation, *g*, has been defined as the rotation from the specimen coordinate system onto the crystal coordinate system and 4 possible descriptors of this rotation have been introduced. However, this rotation is not usually unique; meaning a number of *crystallographically-related solutions* can exist depending on the symmetry of the crystal system (Randle and Engler, 2000). For a crystal with cubic symmetry, there are 24 different ways in which the crystal can be arranged. As a result, there are 24 *crystallographically-related solutions* which describe the orientation of a cubic crystal. Similarly, there are 12 *crystallographically-related solutions* to describe the orientation of a hexagonal crystal. For a given orientation g, the full set of solutions are obtained by

$$\{S_i \cdot g\} \tag{2.21}$$

where S_i are the symmetry operators for the crystal symmetry in question. The symmetry operators for the cubic and hexagonal crystal systems (i.e. in titanium alloys, the β and α phase respectively) are given below. The first symmetry operator, which contains ones on the main diagonal and zeros elsewhere, is known as the identity matrix and is often denoted by the symbol *E*. Premultiplying an orientation by the identity matrix returns the same orientation (Kocks *et al.*, 2000).

The 24 symmetry operators, S_i, for cubic symmetry are:

E	${}^{c}C_{2e}$	${}^{c}C_{4y}^{-}$	${}^{c}C_{2y}$	${}^{c}C_{4y}^{+}$	${}^{c}C_{4x}^{+}$	${}^{c}C_{2x}$	${}^{c}C_{4x}^{-}$
1 0 0	0 0 $\bar{1}$	0 0 $\bar{1}$	$\bar{1}$ 0 0	0 0 1	1 0 0	1 0 0	1 0 0
0 1 0	0 $\bar{1}$ 0	0 1 0	0 1 0	0 1 0	0 0 $\bar{1}$	0 $\bar{1}$ 0	0 0 1
0 0 1	$\bar{1}$ 0 0	1 0 0	0 0 $\bar{1}$	$\bar{1}$ 0 0	0 1 0	0 0 $\bar{1}$	0 $\bar{1}$ 0

${}^{c}C_{4z}^{+}$	${}^{c}C_{2z}$	${}^{c}C_{4z}^{-}$	${}^{c}C_{31}^{+}$	${}^{c}C_{31}^{-}$	${}^{c}C_{33}^{+}$	${}^{c}C_{33}^{-}$	${}^{c}C_{32}^{-}$
0 $\bar{1}$ 0	$\bar{1}$ 0 0	0 1 0	0 0 1	0 1 0	0 0 $\bar{1}$	0 $\bar{1}$ 0	0 1 0
1 0 0	0 $\bar{1}$ 0	$\bar{1}$ 0 0	1 0 0	0 0 1	$\bar{1}$ 0 0	0 0 1	0 0 $\bar{1}$
0 0 1	0 0 1	0 0 1	0 1 0	1 0 0	0 1 0	$\bar{1}$ 0 0	$\bar{1}$ 0 0

${}^{c}C_{32}^{+}$	${}^{c}C_{34}^{+}$	${}^{c}C_{34}^{-}$	${}^{c}C_{2a}$	${}^{c}C_{2d}$	${}^{c}C_{2c}$	${}^{c}C_{2b}$	${}^{c}C_{2f}$
0 0 $\bar{1}$	0 0 1	0 $\bar{1}$ 0	0 1 0	$\bar{1}$ 0 0	0 0 1	0 $\bar{1}$ 0	$\bar{1}$ 0 0
1 0 0	$\bar{1}$ 0 0	0 0 $\bar{1}$	1 0 0	0 0 1	0 $\bar{1}$ 0	$\bar{1}$ 0 0	0 0 $\bar{1}$
0 $\bar{1}$ 0	0 $\bar{1}$ 0	1 0 0	0 0 $\bar{1}$	0 1 0	1 0 0	0 0 $\bar{1}$	0 $\bar{1}$ 0

The 12 symmetry operators, S_i, for hexagonal symmetry are:

$$E = \begin{matrix} 1 & 0 & 0 \\ 0 & 1 & 0 \\ 0 & 0 & 1 \end{matrix} \qquad {}^{H}C_{6z}^{-} = \begin{matrix} 0.5 & \sqrt{3}/2 & 0 \\ -\sqrt{3}/2 & 0.5 & 0 \\ 0 & 0 & 1 \end{matrix} \qquad {}^{H}C_{3z}^{-} = \begin{matrix} -0.5 & \sqrt{3}/2 & 0 \\ -\sqrt{3}/2 & -0.5 & 0 \\ 0 & 0 & 1 \end{matrix} \qquad {}^{H}C_{2z} = \begin{matrix} -1 & 0 & 0 \\ 0 & -1 & 0 \\ 0 & 0 & 1 \end{matrix}$$

$$ {}^{H}C_{3z}^{+} = \begin{matrix} -0.5 & -\sqrt{3}/2 & 0 \\ \sqrt{3}/2 & -0.5 & 0 \\ 0 & 0 & 1 \end{matrix} \qquad {}^{H}C_{6z}^{+} = \begin{matrix} 0.5 & -\sqrt{3}/2 & 0 \\ \sqrt{3}/2 & 0.5 & 0 \\ 0 & 0 & 1 \end{matrix} \qquad {}^{H}C_{21}^{"} = \begin{matrix} 1 & 0 & 0 \\ 0 & -1 & 0 \\ 0 & 0 & -1 \end{matrix} \qquad {}^{H}C_{23}^{'} = \begin{matrix} 0.5 & \sqrt{3}/2 & 0 \\ \sqrt{3}/2 & -0.5 & 0 \\ 0 & 0 & -1 \end{matrix}$$

$$ {}^{H}C_{22}^{"} = \begin{matrix} -0.5 & \sqrt{3}/2 & 0 \\ \sqrt{3}/2 & 0.5 & 0 \\ 0 & 0 & -1 \end{matrix} \qquad {}^{H}C_{21}^{'} = \begin{matrix} -1 & 0 & 0 \\ 0 & 1 & 0 \\ 0 & 0 & -1 \end{matrix} \qquad {}^{H}C_{23}^{"} = \begin{matrix} -0.5 & -\sqrt{3}/2 & 0 \\ -\sqrt{3}/2 & 0.5 & 0 \\ 0 & 0 & -1 \end{matrix} \qquad {}^{H}C_{22}^{'} = \begin{matrix} 0.5 & -\sqrt{3}/2 & 0 \\ -\sqrt{3}/2 & -0.5 & 0 \\ 0 & 0 & -1 \end{matrix}$$

2.5.1.4 Misorientations

A misorientation describes the rotation from one crystallographic orientation to another; for example, when describing the misorientation between neighbouring grains in a specimen. The different descriptors used to describe an orientation can be applied to misorientations in the same way. The misorientation matrix is calculated from the orientations of grain A and grain B by (Kocks *et al.*, 2000):

$$\Delta g = g_B g_A^{-1} \tag{2.22}$$

where Δg is the matrix which describes the rotation from g_A to g_B, with g_A having been arbitrarily chosen as the reference orientation. Fig. 2.34 illustrates how equation 2.22 is simply a compound of the two rotations which describe the orientations of grain A and grain B, to arrive at the net rotation between them.

The angle/axis pair for the misorientation is found using equations 2.9 and 2.10, substituting the elements of the misorientation matrix Δg for those of the orientation matrix g.

Since there are usually a number of crystallographically related solutions for each orientation, it follows that there will be many equivalent ways of describing a misorientation. When considering the misorientation between two grains with cubic symmetry, each orientation can be described by 24 equivalent rotations. Therefore, there are 576 (= 24 x 24) equivalent rotations for the misorientation. However, if we also

consider that the misorientation and the inverse misorientation are equivalent, this switching symmetry doubles the number of symmetrically equivalent misorientations for two cubic crystals to 1152 (= 2 x 24 x 24). Similarly, for two hexagonal crystals, there are 288 (= 2 x 12 x 12) symmetrically equivalent misorientations (Kocks *et al.*, 2000).

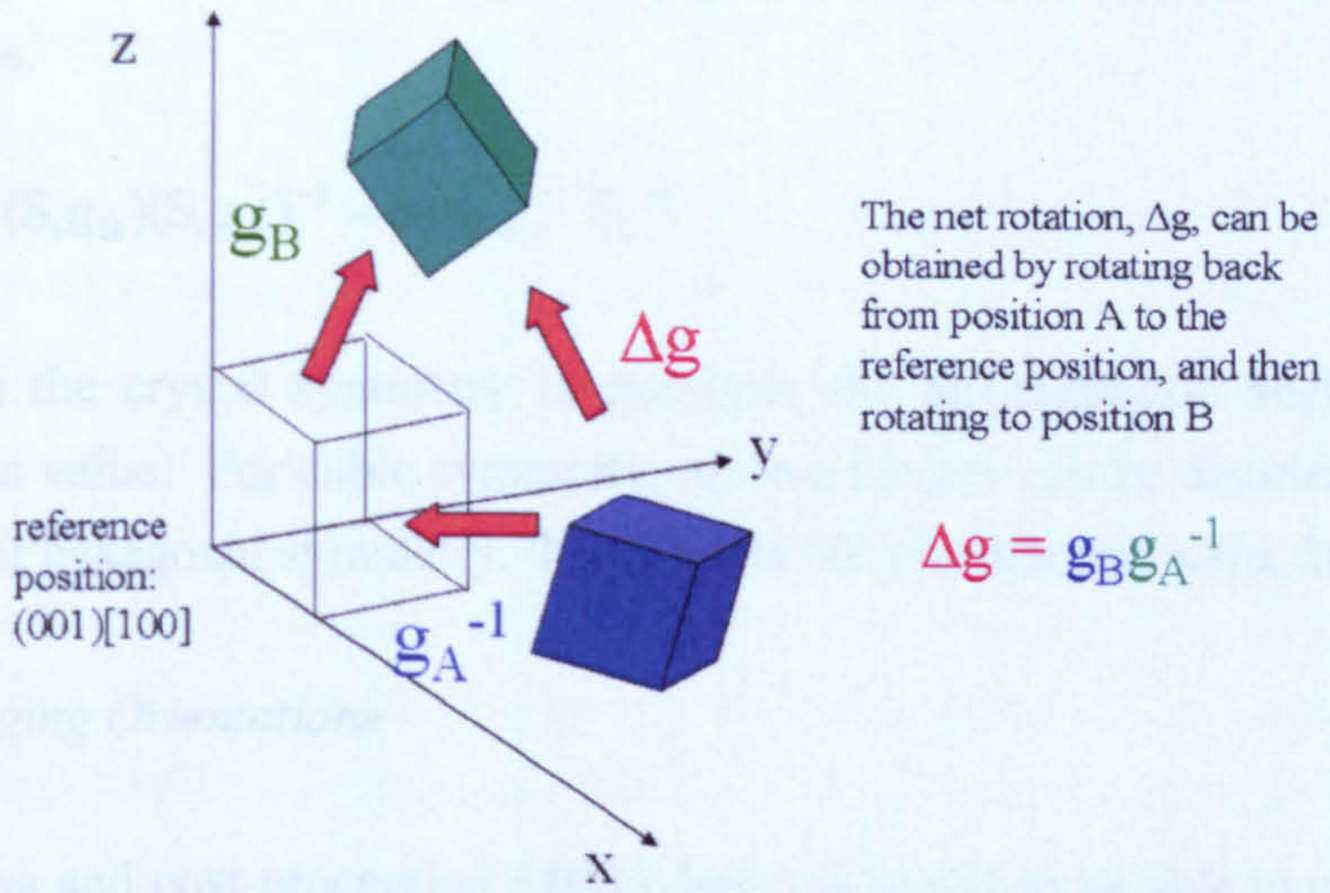

Fig. 2.34 The calculation of the misorientation from the orientations of grain A and grain B (adapted from Rollet and Kalu, 2005).

Of the many equivalent misorientations, it is often useful to select the one having the minimum rotation angle between the two lattices. This is often referred to as the *disorientation* (Rollet and Kalu, 2005). If the angle is the only criterion of interest, then only one set of symmetry operators has to be applied and the *disorientation* is found as follows:

- Calculate the 3x3 orientation matrix for each orientation, g_A and g_B, and then form the misorientation matrix, Δg, using $\Delta g = g_B g_A^{-1}$ (equation 2.21).

- From the misorientation matrix, calculate the rotation angle using:

$$\theta = \cos^{-1}\left[\left(\Delta g_{11} + \Delta g_{22} + \Delta g_{33} - 1\right)/2\right] \tag{2.23}$$

- To find the one with the smallest rotation angle i.e. the disorientation, apply the crystal symmetry operators, S_i, to the misorientation matrix:

$$\{S_i \cdot \Delta g\} \tag{2.24}$$

- In each case, recalculate the rotation angle and select the one with the smallest absolute value.

The *full disorientation* has the minimum rotation angle and in addition the rotation axis is located in the standard stereographic triangle i.e. $d_1 \geq d_2 \geq d_3 \geq 0$. In order to find the *full disorientation*, the symmetry operators must be applied twice, using the order of multiplication shown in equation 2.25, and to account for switching symmetry, the order of the two crystals reversed, thus generating the full set of symmetrically equivalent misorientations.

$$\Delta g = (S_i g_B)(S_i g_A)^{-1} = S_i g_B g_A^{-1} S_i^{-1} \tag{2.25}$$

Depending on the crystal symmetry in question, the disorientation angle always falls below a certain value. For cubic symmetry, no two lattices can be disorientated by more than 62.8°. For hexagonal symmetry, this value is 90° (Rollett and Kalu, 2005).

2.5.1.5 Averaging Orientations

When analysing and post-processing EBSD data it is useful to be able to obtain the mean orientation from a set of orientation measurements. Orientation averaging may be used as a means to improve the angular precision of EBSD maps (Humphreys *et al.*, 2001), for procedures to analyse the orientation distribution in grains and sub grains (Glez and Driver, 2001), or may be used as part of the method to reconstruct the orientation of a parent β grain from the orientations of an inherited α_s phase (Humbert and Gey, 2002. Gey and Humbert, 2003).

Orientation averaging is not a straightforward matter because accurate estimates of the average cannot be made using the commonly used three parameter descriptors of orientation such as Euler angles or angle/axis pair. Spaces using these parameters tend to be very distorted and not closed, and distances between orientations in them can differ greatly from the misorientation angle. Krieger Lassen *et al.* (1994) showed by way of an example that simply taking the arithmetic mean of Euler angles as a measure of an average orientation is not to be recommended. Several authors have now shown that the quaternion descriptor of orientation offers perhaps the most efficient and accurate means to determine a mean orientation (Humphreys *et al.*, 2001. Glez and Driver, 2001. Krieger Lassen *et al.*, 1994. Humbert *et al.*, 1996).

For a set of orientations described in quaternion form, $\mathbf{q}_N$, a quaternion associated with the average orientation, $\tilde{\mathbf{q}}$, can be obtained by the sum of the quaternions in the set divided by the norm of the sum (Humbert *et al.*, 1996):

$$\tilde{\mathbf{q}} = \frac{(\mathbf{q}_1 + \mathbf{q}_2 + \ldots + \mathbf{q}_N)}{\|\mathbf{q}_1 + \mathbf{q}_2 + \ldots + \mathbf{q}_N\|} \tag{2.26}$$

From the definition of quaternion addition (equation 2.16), this means that each parameter of the average quaternion is found by adding the corresponding parameter from each quaternion in the set and dividing the result by the norm. For example, $\tilde{q}_1$, is given by:

$$\tilde{q}_1 = \frac{(q_{11} + q_{12} + \ldots + q_{1N})}{\left[(q_{11} + q_{12} + \ldots + q_{1N})^2 + (q_{21} + q_{22} + \ldots + q_{2N})^2 + (q_{31} + q_{32} + \ldots + q_{3N})^2 + (q_{41} + q_{42} + \ldots + q_{4N})^2\right]^{1/2}} \quad (2.27)$$

Humphreys *et al.* (2001) and Glez and Driver (2001) discuss further practical issues concerning crystal symmetry and orientation spreads, which must be considered to avoid ambiguities when averaging orientation sets. Depending on the crystal symmetry, each orientation can be represented by a number of equivalent rotations (e.g. 24 for cubic and 12 for hexagonal). Each of these crystallographically-related solutions lies within a delimited zone in orientation space. All zones have the same size and shape and each one is centred on one of the symmetry operators, S_i, for the crystal symmetry in question (Glez and Driver, 2001). Orientations which are in fact close can appear to be highly misorientated if they lie within different zones. Therefore, before an orientation set is averaged, each orientation must be transformed by appropriate symmetry operators to give the smallest misorientation (i.e. the disorientation) with respect to a reference orientation, in order to bring all of the orientations into the same zone. If the chosen reference orientation is the identity matrix, E (S_1), then the orientations are said to be brought into the *fundamental zone* (Glez and Driver, 2001). While the above method alone is sufficient for individual orientation measurements, it is not always adequate to treat a set of orientations that have a spread because of the so-called "Umklapp" effect, shown in Fig. 2.35 (Glez and Driver, 2001).

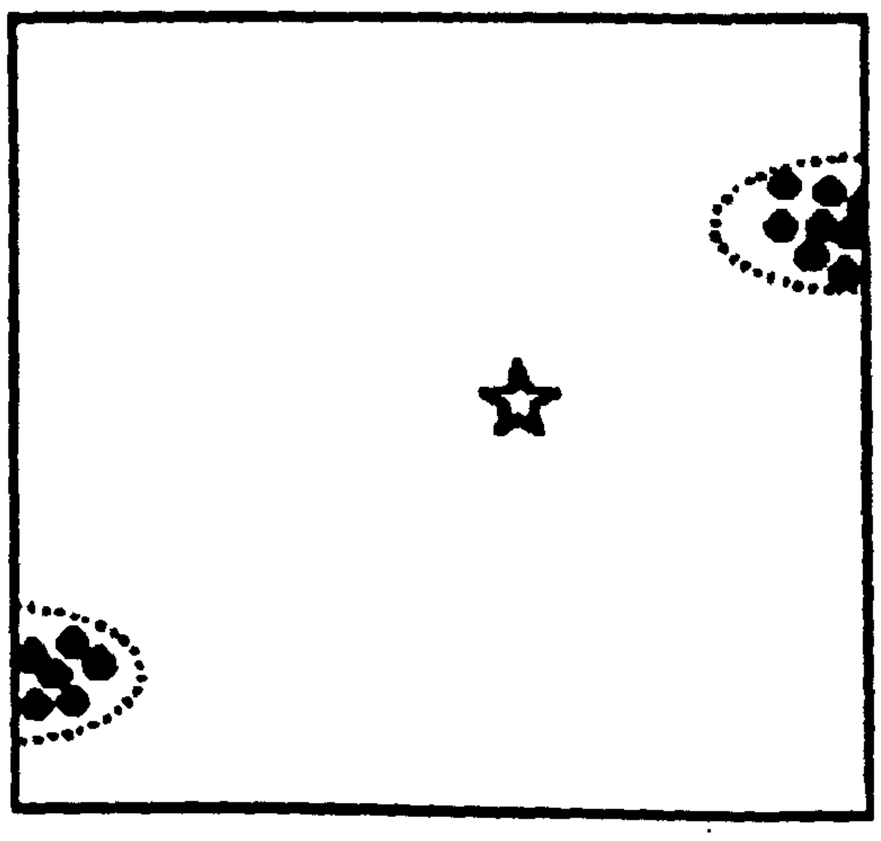

Fig. 2.35 Two-dimensional schematic of the "Umklapp" effect. A spread of orientations is located across the border of the fundamental zone, resulting in a mean orientation at the location of the star (Glez and Driver, 2001).

When an orientation spread is located across the border of the fundamental zone, it will be split into two spreads at opposite sides of the zone and hence far from each other in terms of Euclidean distance. An average of this orientation data would result in an ambiguity. The "Umklapp" effect can be eliminated by changing the reference frame so that the orientation spread lies near the centre of the fundamental zone. For small orientation spreads, the reference frame can be any one of the orientations in the set. The mean orientation for the spread can then be calculated in the new reference frame avoiding problems with crystal symmetry and the "Umklapp" effect.

In summary, sets of orientation measurements may be averaged using the following procedure:

- For each quaternion in a set of quaternion orientations, $\mathbf{q}_N$, calculate a new quaternion, $\mathbf{q}_{i1}$ by premultiplying by the inverse of the first quaternion orientation in the set, $\mathbf{q}_1^*$, and then postmultiplying the result by each quaternion symmetry operator, $\mathbf{s}_j$, and selecting the quaternion product with the minimum angle of rotation. For cubic symmetry this equation is

$$\mathbf{q}_{i1} = \left(\mathbf{q}_1^* \times \mathbf{q}_i \times \mathbf{s}_j\right)_{\min, 1 \le j \le 24} \tag{2.28}$$

  where x denotes the quaternion product (equation 2.18) and * denotes the quaternion conjugate i.e. the inverse of a unit quaternion (equation 2.19).

- Find the mean of the new set of quaternions, $\tilde{\mathbf{q}}_1$, using equation 2.26.

- To find the mean with respect to the initial reference frame, premultiply by $\mathbf{q}_1$:

$$\tilde{\mathbf{q}} = \mathbf{q}_1 \times \tilde{\mathbf{q}}_1 \tag{2.29}$$

2.5.2 Applying Orientation Averaging to EBSD Datasets

The simplest way to apply orientation averaging to EBSD data would be to obtain new orientation estimates by averaging over a set of values centred on each grid point in turn. However, such a simple approach tends to smooth features in the microstructure such as grain and subgrain boundaries. For this reason, Humphreys *et al.* (2001) suggested the use of a Kuwahara image filter which preserves boundaries. This procedure consists of subdividing an array of pixels surrounding the central point into several smaller zones; the central point is then given the mean orientation of the zone with the lowest spread of

orientations. A simple Kuwahara smoothing strategy using a 5x5 region divided into 4 3x3 sub regions is illustrated in Fig. 2.36. When applying the filter to each successive point in a map, the original orientation data should be used for each point, so as not to introduce 'marching errors'.

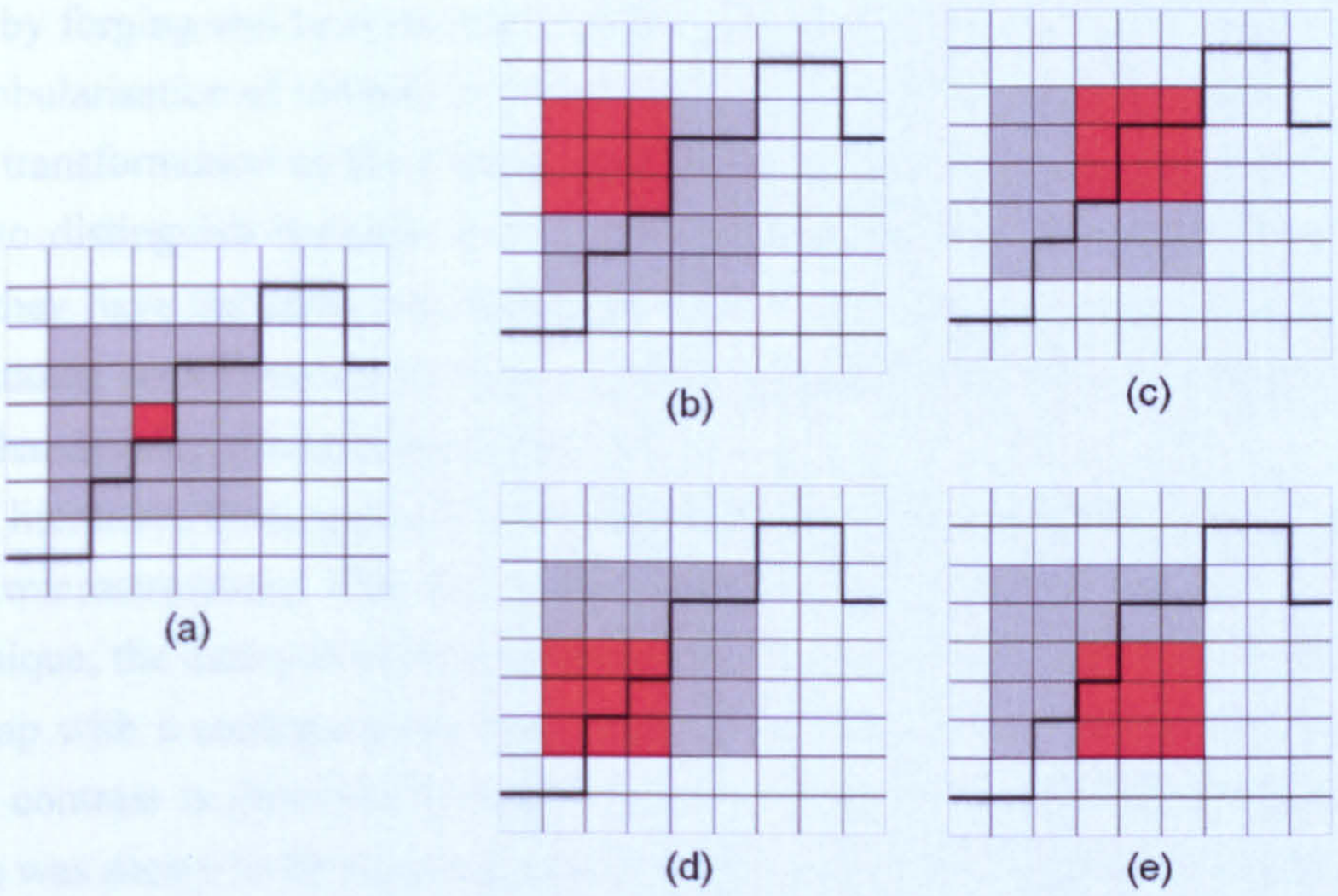

Fig. 2.36 A simple Kuwahara smoothing strategy using a 5x5 array of points surrounding the central point to be averaged. The value assigned to the central point is the average orientation of the sub zone with least variance. In this case, due to the presence of the grain boundary indicated by the black line, the sub zone with least variance is likely to be the one shown in (b).

Humphreys *et al.* (2001) found that increasing the number of sub regions e.g. eight blocks of 3x3 in the 5x5 region gives better edge preservation at corners. They also suggest that the filter is modified so as to abort the averaging procedure for a particular point if the block with the least variance contains a pixel misorientated to the central pixel by more than a set minimum value, typically 3°. This modification prevents spurious orientations being introduced at grain boundary corners, when the least variance block can sometimes contain points from different grains.

Several passes of the smoothing procedure may be performed to give an incremental reduction in the orientation noise. After approximately 4 passes however, further passes become ineffective because the data becomes organised into stable blocks separated by low misorientations. It is important to recognise that these blocks are a feature of the smoothing and should not be interpreted as microstructural features (Humphreys *et al.*, 2001).

2.5.3 Separation of the α_p and α_s Phases in Bimodal EBSD Datasets

Near-α and α+β alloys used for aero engine components are often thermomechanically processed to produce a bi-modal microstructure. Such a microstructure consists of equiaxed α_p grains surrounded by Widmanstätten α_s. Bimodal microstructures are obtained by forging and heat treatment in the α+β phase field. The α_p grains are formed by the globularisation of initially coarse α lamellae whereas the α_s phase forms on cooling from the transformation of the β phase which was present at high temperature. It is not possible to distinguish between the α_p and α_s phases during a standard EBSD analysis because they have the same hcp crystal structure. Methods to separate these phases in EBSD datasets are of interest as they can allow greater insight into the microtexture and textures that develop during processing.

In the literature, three methods have been described for separating the two phases in bi-modal microstructures. The first method was presented by Germain *et al.* (2005b). In this technique, the data points belonging to each phase are dissociated by correlating the EBSD map with a corresponding back scattered electron (BSE) image, in which a high chemical contrast is observed between the α_p and the α_s (+ residual β) phases. This technique was shown to be successful but is fairly time consuming to perform because the EBSD data is collected with the sample tilted at 70°, while the best chemical contrast in the BSE image is obtained with the sample tilted at 0° and may require the insertion of the BSE detector as this is often withdrawn from the chamber for EBSD acquisition. Furthermore, the BSE image must be image processed to obtain the best contrast and then modified using rotations, translations, shearing and scaling operations to obtain the best pixel to pixel correspondence between the two images.

A method was proposed by Glavicic *et al.* (2005) for separating the α_p and α_s textures measured by X-ray diffraction analysis. This was based on the texture analysis of samples in two different heat treatment conditions, the starting (bimodal) condition and the corresponding condition heat treated so as to dissolve the α_s and to grow the α_p under near equilibrium conditions. This technique worked well for microstructures containing coarse α_s lamellae, where it was claimed the BSE image technique may be less successful. However, the technique is again time consuming and most importantly, while it can separate the textures measured by EBSD or X-ray diffraction, it cannot be used dissociate the pixels in an EBSD map i.e. it can separate textures but not microtextures.

An alternative method which could separate the microtextures was proposed by Thomas *et al.* (2005). In this method, the EBSD map was correlated with an optical micrograph of the same area. It was found that the area analysed by EBSD analysis could be easily located when the specimen was subsequently etched due to carbon contamination in the electron microscope. Once an etched image of the area was obtained, the α_p and α_s phases were separated in the micrograph by the light contrast

obtained between the two phases. In much the same way as Germain *et al.* (2005b), rotations, translations, shearing and scaling operations were then required to obtain the best pixel to pixel correspondence with the EBSD map.

2.5.4 Reconstruction of the High Temperature β Phase in EBSD Datasets

Titanium and its alloys exhibit between 900°C and 1000°C an α→β phase transformation on heating and a β→α transformation on cooling. In near-α alloys the amount of β phase retained at room temperature is very low and it is normally not possible to index this phase reliably using EBSD. As a result, a standard EBSD analysis usually only allows the characterisation of the microtexture of the α phases, which can be either α_p, which is α that was present at high temperature, or α_s which forms when the β phase present at high temperature transforms on cooling.

Additional information regarding the microtexture of the high temperature β phase may be obtained from the data recorded during the standard EBSD analysis because the β→α_s phase transformation very often obeys the Burgers orientation relation, given in equation 2.3 (Burgers, 1934).

Methods of deducing the microtexture of the high temperature β phase from the room temperature inherited α_s phase are of great interest because most industrial processing steps take place within the β or α+β phase fields where β is the dominant phase. The texture evolution of the β phase during plastic deformation and the texture evolution resulting from phase transformation play a large role in determining the final microstructure and properties of titanium alloys.

Taking into account the Burgers relation and the symmetries of the two phases, it can be shown that the transformation of a parent β grain can give rise to 12 distinct α_s orientations, named 'variants' (Humbert *et al.*, 1994, 1995). Conversely, for an α_s orientation resulting from a β→α transformation, it can be shown that there are six potential cubic orientations for the parent β grain. In order to find a unique solution for the orientation of the parent β grain, it is necessary to compare more than one inherited α_s orientation. Humbert *et al.* (1994, 1995) proposed a scheme to obtain the parent β grain orientation from a small number of inherited α_s variants in cases where there is a close adherence to the Burgers orientation relation. In this case, it was stated that the number of different α_s orientations required to obtain a unique solution depends on which variants are chosen, being three in the less favourable case but reduced to two in the most favourable case. The paper lists 11 unique misorientations that can exist between different variants inherited from the same parent β grain. 8 out of these 11 misorientations are the aforementioned favourable case, which leads to a unique solution without reference to a third variant. In conclusion, the paper mentions the potential

application of the method to the orientation data collected by EBSD analysis.

This method was later applied in the work of Moustahfid *et al.* (1997a, 1997b) to studies of variant selection in Ti-6Al-4V using EBSD. At this stage, the reconstruction was limited to deducing single parent β orientations for approximately 100 grains from triplets of variants. The data was used to calculate ODFs. The procedure was no doubt time consuming and furthermore, it was necessary for the user to manually identify the prior β grains in the microstructure in order to find three variants originating from the same parent grain and where this proved difficult, the efficiency of the reconstruction method proved rather weak. Thus at this stage, the reconstruction of an orientation image map of the high temperature β phase was not practical.

In a later paper, Humbert and Gey (2002) proposed a new approach to their reconstruction procedure, where the number of variants used in the evaluation of the parent was no longer limited to three as in the first method. This approach was found to be more efficient in cases where the adherence to the Burgers orientation relation is less strict or when the orientations of the inherited volumes vary slightly at different locations of the variant. The basis of the method is to deduce all of the six potential parent orientations for each inherited variant orientation using the Burgers relation and the cubic and hexagonal symmetries. In each case, one of the six potential cubic parent orientations will be close to the rotation matrix characterising the true parent orientation. Thus, when several variants are analysed, there will be a cluster of potential parent orientations close to the true parent orientation. The parent orientation is evaluated by averaging this group of close potential parent orientations using quaternions or polar decomposition of matrices. The principal of this method is illustrated schematically in Fig. 2.37.

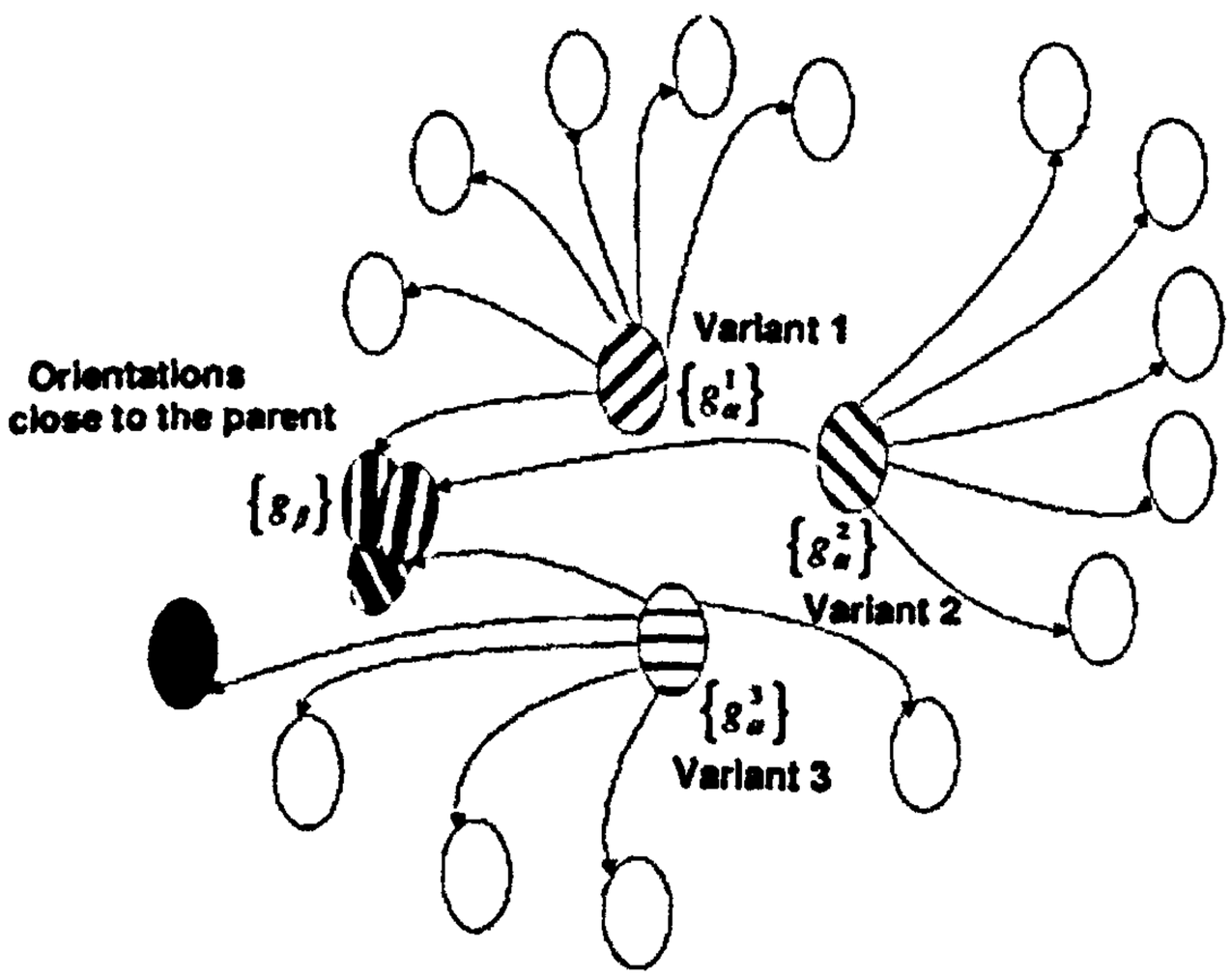

Fig. 2.37 Principle of the method proposed by Humbert and Gey to determine the cubic parent orientation from a limited number of variants when the transformation does not strictly obey the Burgers orientation relation (Humbert and Gey, 2002).

The accuracy of the method was demonstrated in the paper by evaluating the parent β orientation from variant orientations which had been calculated from an initial β orientation with small Gaussian variations of the Burgers relation. In a second numerical example, the average orientation of a single parent β grain in a sample of Zircaloy 4 was calculated from an analysis of the orientations of 5 inherited variants. Stereographic projections were used to show that the poles of variants calculated from the evaluated parent β orientation matched very well the observed variants. It appears that at this time, a procedure based on this method would still be reliant on the manual identification of prior β grains.

Details of a method that could automatically reconstruct orientation image maps of the high temperature β phase containing many prior β grains was subsequently published by Gey and Humbert (2003). To overcome the problem of identifying α_s variants inherited from the same parent β grain, an initial step in the reconstruction procedure was introduced to systematically identify these variants on the α_s map by considering the misorientation angles and axes between adjacent measurements. The α_s variants inherited from the same parent β grain are characterised by specific misorientations linked to the Burgers orientation relation. If the misorientation having the minimum rotation angle i.e. the disorientation, and its corresponding axis is chosen to characterise the misorientation, one obtains 5 possible misorientation types between variants inherited from the same parent grain (Table 2.5).

Table 2.5 Specific misorientations between α colonies inherited from the same β grain (axis $\vec{n}$ corresponds to one of the symmetrically equivalent rotation axes) (Gey and Humbert, 2003).

ω	$\vec{n}$
10.529°	$\vec{c} = [00.1]$
60°	$\vec{a}_2 = [\bar{1}2.0]$
60.832°	$\vec{d}_1$ at 80.97° from $\vec{c}$ in $(\vec{d}_3, \vec{c})$ plane
63.262°	$\vec{d}_2$ at 72.73° from $\vec{c}$ in $(\vec{a}_2, \vec{c})$ plane
90°	$\vec{d}_3$ at 5.26° from $\vec{a}_2$ in basal plane

If the experimental misorientations between neighbouring pixels in the map are above a certain value (3° is suggested), they are deemed to be belong to different variants. In this case, the misorientation is compared to the theoretical misorientations in Table 2.5. When the experimental misorientation angle is within a certain tolerance of one of these theoretical misorientations (suggested tolerance of 5°), the pixels are deemed to belong to different variants but inherited from the same parent β grain. In this way, the traces of variant and non variant i.e. prior β boundaries can be traced on the α_s map and as a result,

the outlines of the prior β grains are easily seen. To automate this procedure for identifying parent grains, this specific misorientation analysis is incorporated into a standard grain boundary reconstruction procedure such as that described by Humphreys (2004). An initial point is selected and the grain to which it belongs is built up by examining neighbouring pixels, which are assigned to the same grain if the neighbour to neighbour misorientations are within the specified limit. This procedure continues until a complete 'parent grain' has been defined. A new reference point that has not already been assigned to a grain is then selected and the process repeated until all the data in the map have been assigned to parent grains. Gey and Humbert mention that sometimes the entire contour of the parent β grain is not traced because two neighbouring β grains will sometimes have a specific misorientation that results in inherited variants with a misorientation that coincides with one of the theoretical misorientations in Table 2.5. In the grain reconstruction procedure, this would result in two prior β grains being incorrectly unified and as a result, the subsequent procedure to calculate the β orientation would fail. The variation of the tolerance angle can somewhat modify the reconstruction but cannot completely eradicate this problem. Therefore to tackle the problem, a manual procedure was incorporated whereby the user could select the α_s colonies assumed to be inherited from the same parent grain and check that there orientations are related to a unique β orientation.

The next stage in the procedure is the determination of the parent β orientations. This is based on the method in the aforementioned paper by Humbert and Gey (2002). If more than 3 variants are identified inside a parent β grain, all possible combinations of 3 variants can be considered. Each orientation triplet then leads to a calculated parent orientation. The set of resulting β orientations can show some spread, either because the Burgers orientation relation is not strict or due to the error in the orientation measurements. In such a case, an evaluation of the parent orientation is obtained by averaging the calculated orientations. This averaging approach is a good way of reconstructing β orientations in cases where the Burgers relation is not strictly observed. However, such an approach is less useful if the β grains contain significant orientation perturbations due to deformation as it will not reveal any information about these intragrain misorientations.

An alternative method for automatically reconstructing orientation image maps of a high temperature phase having undergone a Burgers type phase transformation is given in the work of Glavicic *et al.* (2003a, 2003b, 2004). This method uses a Monte-Carlo global minimisation approach, which avoids the need for any manual selection of colonies or laths. The implementation of this approach comprises the following steps:

1) A unique grain identification number (GID) is assigned to the sets of Euler angles in the data set that are likely to belong to the same α_s variant by examining neighbour to

neighbour misorientations. Neighbouring points are deemed to belong to the same variant if they are misoriented by less than a certain value.

2) The connectivity of the identified α_s variants is examined to establish which GIDs are adjacent. This connectivity is stored in a 2-dimensional array, AD(*i,j*) in which *i* and *j* run from 1 to the maximum GID. Each element (*i,j*) is either 1 if GIDs *i* and *j* are adjacent or 0 if they are not.
3) A Monte-Carlo technique together with the connectivity array is used to select 'random' pairs of points from adjacent GIDs. For these pairs of points, an approximate β orientation for each point is found by calculating the possible β orientations and selecting those with the minimum β phase misorientation. Based on this misorientation, a probability number is assigned based on the likelihood that the two variants came from the same β grain. After many Monte-Carlo iterations approximate β orientations and probability numbers for most GID pairs are determined.
4) Two minimisation of misorientation steps are carried out for every GID in the data set. The misorientations between a given GID and every adjacent GID for which the probability number suggests they could be from the same parent grain are summed, and the β phase misorientation which minimises the sum is selected for all points sharing that selected GID.
5) A final minimisation of misorientation step is applied which evaluates the possible β orientations for adjacent GIDs for which the probability number suggests it is highly likely that they were from the same parent grain.

This was the first work to present actual reconstructed orientation image maps, albeit relatively small, of the high temperature β phase, an example of which is shown in Fig. 2.38.

Glavicic *et al.* (2004) validated the technique by correctly deducing the texture and average grain size of the β phase measured previously using X-ray diffraction and metallographic techniques, respectively. However, it can be clearly seem from Fig. 2.38 that there are some errors in the reconstructed IPF map, where α_s variants within β grains have been incorrectly reconstructed. This shows that the technique does not have the ability to restore the parent microtexture with complete reliability. However, as the errors are clearly a relatively small fraction of the reconstructed maps, they are unlikely to significantly affect the texture and are easily excluded when measuring the prior β grain size. No mention is made of the underlying reasons for these errors and how they could be eradicated or reduced. One of the points to note about the method of Glavicic *et al.* compared to that proposed by Gey and Humbert, is that the latter will not provide a solution when the α_s variants cannot provide one without ambiguity, whereas the former will give one of the multiple solutions, which can be incorrect.

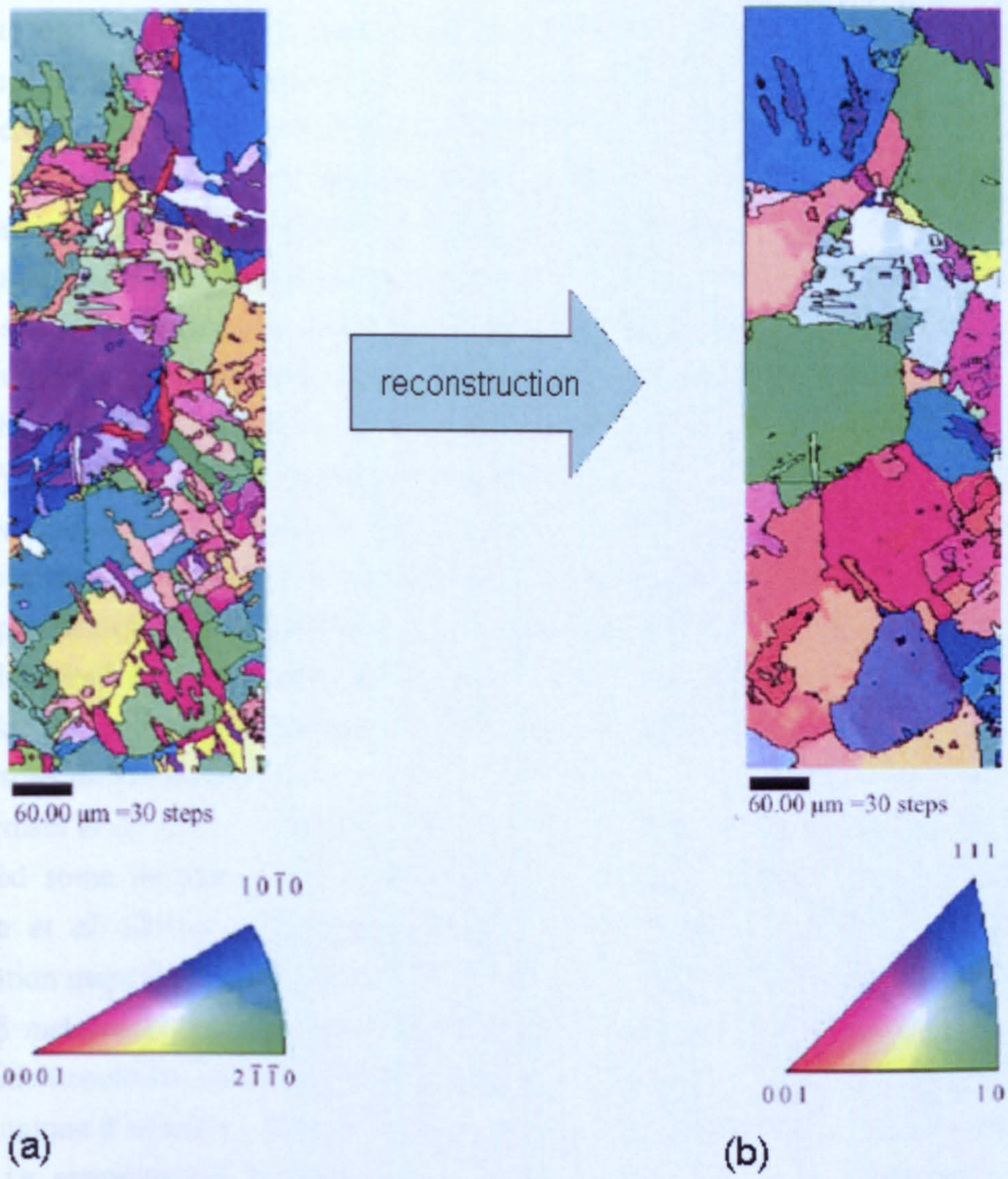

Fig. 2.38 EBSD inverse pole Fig. maps for (a) Ti-6Al-4V with a colony α_s microstructure and (b) the corresponding β phase determined by a Monte-Carlo global minimisation method (Glavicic *et al.*, 2004).

An alternative algebraic approach to dealing with the crystallography of phase transformations was applied by Cayron (2006) and Cayron *et al.* (2006) based on the theoretical groupoid structure formed by the variants and their operators. In this work, it was pointed out that where Humbert *et al.* (1995) had found that at maximum 3 α_s variants are required to determine without ambiguity the β parent orientation, actually 4 variants are needed because in a special case, 3 α_s variants can give rise to 2 possible parent β solutions, where one is a twin of the other through the $(1\,\bar{1}\,1)$ mirror plane. In the second of the two papers, Cayron *et al.* (2006) examined the problem of incorrectly unified grains during the neighbour to neighbour grain reconstruction step used in Gey and Humbert's (2003) method in detail. Random orientations were generated to deduce

the probability that two randomly orientated crystals are linked by a rotation accidentally close to one of the specific misorientations within an angular interval lower than the tolerance angle. It was found that for the tolerance angle of 5° suggested by Gey and Humbert, the probability to wrongly suppose that two grains are inherited from the same parent crystal is 12% for a Burgers transformation. Cayron *et al.* concluded that β reconstruction using the neighbour to neighbour method works satisfactorily for Ti alloys but would not be suitable for martensitically transformed steels due to the larger number of possible variants and the fact that the martensitic transformation in steel can lead to high intragrain misorientations due to the very high stresses and deformations that result from the transformation itself. An alternative to the neighbour to neighbour approach for identifying which variants belonged to which parent grain was described, which it was claimed could be applied more successfully to a wider range of materials and phase transformations, including the reconstruction of austenitic grains in martensitic steels. This approach checks the coherency of all possible triplets between variants to recognise those inherited from the same parent grain. This is accomplished using a composition table for the relevant groupoid and a "nucleation/propagation" method to progressively reconstruct the parent grains.

Germain *et al.* (2007) published a further paper on their reconstruction technique that included some modifications which address the points raised by Cayron (2006) and Cayron *et al.* (2006). The paper discusses the reliability of their reconstructed β orientation maps and a comparison is made between a measured and reconstructed β map for a β metastable titanium alloy, which contained enough retained β phase so that its orientation could be measured directly by EBSD. The authors calculated the probability that a unique β solution could be found from a set of n variants selected randomly from the 12 i.e. assuming that the variants arise independently with no variant selection. These results are shown in Table 2.6 below.

Table 2.6 Probability, P_n, that a unique solution for the parent β orientation can be found for *n* variants. From (Germain *et al.*, 2007).

n	P_n (%)
1	0
2	72.72
3	98.18
4 and more	100

This shows that although 4 variants are strictly needed to find a unique solution without ambiguity and not 3 as was originally stated by Humbert *et al* (1995), in the vast majority

of cases, 3 variants will give a unique solution, while in nearly 73% of cases, only 2 variants are required. The authors modified their procedure for identifying which α_s variants belonged to which parent grain to reduce the problem of incorrectly unified grains when 2 variants from neighbouring β grains have a misorientation which coincides with one of the specific misorientations between inherited variants. It was argued that the approach by Cayron *et al.* (2006), which checks all possible misorientation combinations between variants is rather time consuming. Instead, they proposed a faster alternative. To reconstruct a parent grain, a reference grain is first chosen. Then, the variants are considered to have the same parent as that of the reference variant if they fulfil two conditions:

- To be adjacent to a variant already collected (i.e. possibly inherited from the same parent as the reference variant) and to have a misorientation with the adjacent variant that is within a defined tolerance of one of the specific misorientations that exist between inherited variants.
- And also to have a misorientation with the reference variant that is within the defined tolerance of one of the specific misorientations.

The previous neighbour to neighbour approach is illustrated in Fig. 2.39(a). An incorrectly unified grain using this approach is shown in Fig. 2.39(b). The new strategy incorporating a reference grain is shown in Fig. 2.39(c). Fig. 2.39(d) shows that the choice of reference grain can slightly influence the variant identification but it is argued that the influence on the restored β grain boundaries is relatively insignificant and wrongly gathered variants can be easily identified and removed from the set used to calculate the parent orientation.

The accuracy of the recalculated orientations was assessed by comparing pixel to pixel the recalculated and measured β orientations (the small areas where the prior β boundaries were not well reconstructed were not considered). The mean angle difference calculated on the whole map was less than 1°, which demonstrated the ability of the method to accurately determine the parent β orientations. It was shown that the few areas where the β boundaries were not well reconstructed were due to α_s colonies with close orientations, which had developed on either side of a former β/β boundary. As a result, these colonies could not be distinguished using a misorientation criterion. For similarly orientated α_s colonies to result from different β grains, implies that there must be specific misorientations between the β grains when this occurs. These specific misorientations were determined and are summarised in Table 2.7.

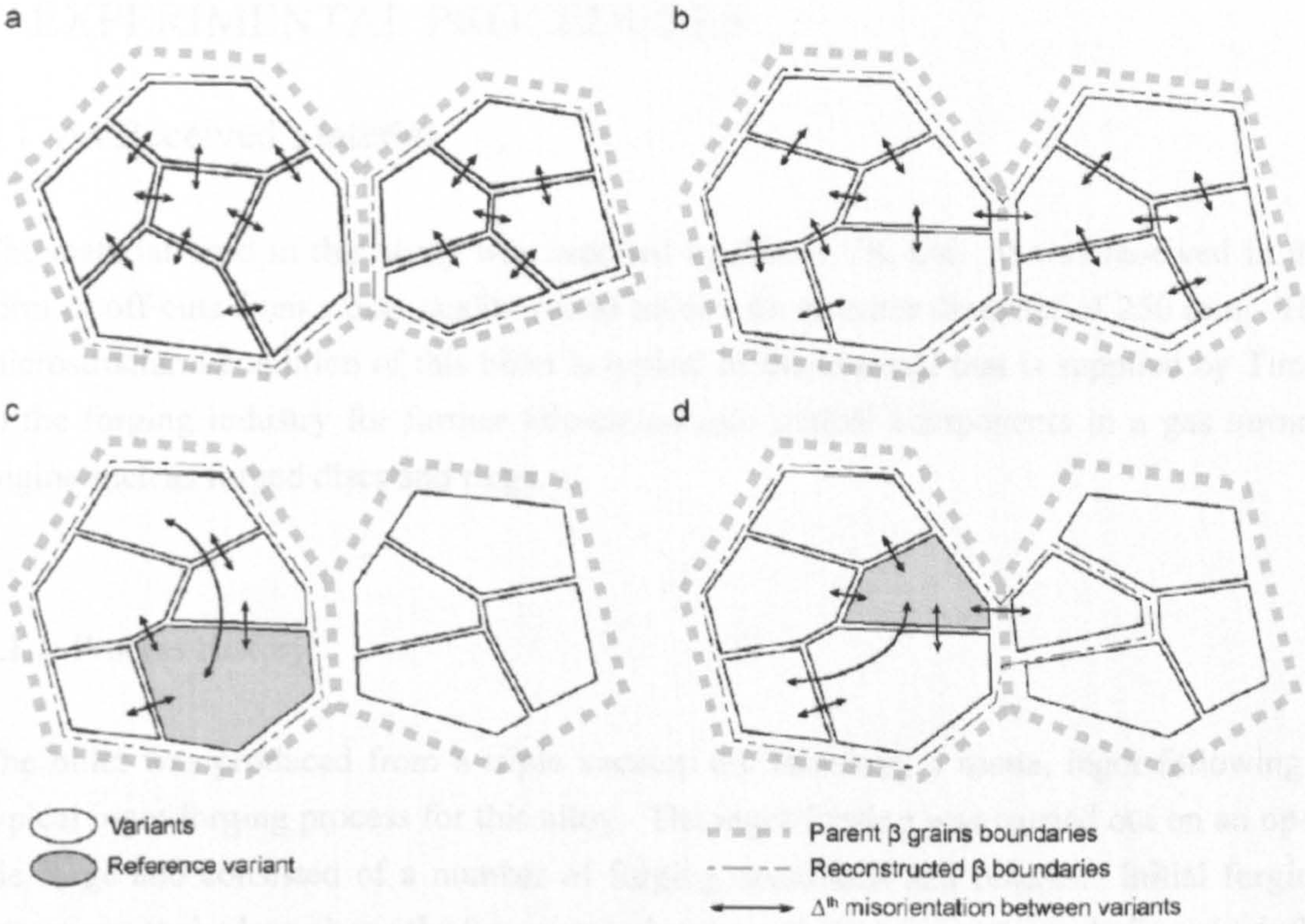

Fig. 2.39 Different strategies to gather variants inherited from the same parent grain and an illustration of specific situations where errors can arise. (a) A simple neighbour to neighbour approach. (b) Two incorrectly unified β grains where the β/β misorientation coincides with one of the specific misorientations between inherited variants. (c) A neighbour to neighbour approach incorporating an additional reference variant. (d) Same as in (c) but using a different reference variant, which results in one variant being incorrectly assigned. From Germain *et al*. (2007).

Table 2.7 Specific misorientations between adjacent β grains able to share a common variant. From Germain *et al*. (2007).

ω	$\vec{n}$
10.5°	$[110]_\beta$
49.5°	$[110]_\beta$
60°	$[110]_\beta$
60°	$[111]_\beta$

3 EXPERIMENTAL PROCEDURES

3.1 As Received Material

The material used in this study was supplied by Timet UK Ltd. It was received in the form of off-cuts from a disc quality round billet with an outer diameter of 250 mm. The microstructural condition of this billet is typical of the material that is supplied by Timet to the forging industry for further fabrication into critical components in a gas turbine engine such as forged discs and rings.

3.1.1 Process History

The billet was produced from a triple vacuum arc remelted, 3 tonne, ingot following a typical ingot forging process for this alloy. The ingot forging was carried out on an open die forge and consisted of a number of forging operations and reheats. Initial forging operations took place above the β transus to break up the ingot structure, during which the round ingot was forged to a rectangular billet. Secondary forging took place below the β transus within the α+β phase field, during which the rectangular billet was forged to a 270 mm diameter round billet. After forging, the alpha case on the surface of the billet was removed by grinding, reducing the diameter to 250 mm. The steps in the ingot forging process are summarised in Fig. 3.1. Precise forging temperatures and dimensions of the billet at the intermediate stages of the process have not been given as this is proprietary information.

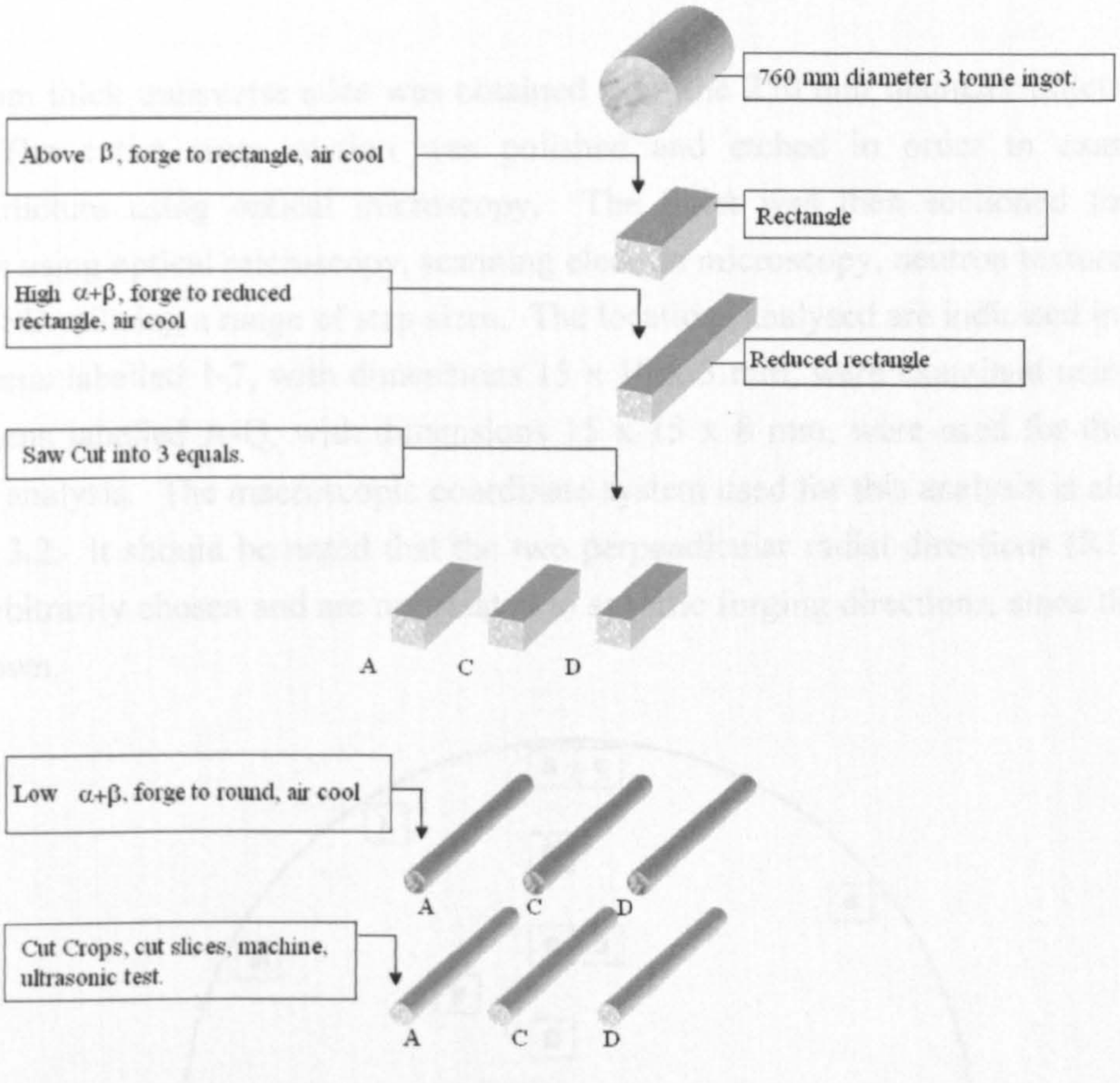

Fig. 3.1 Timet UK Ltd standard route for 250 mm disc quality Timetal 834 billet.

3.1.2 Chemical Composition

Compositional analysis of the as-received billet material was provided by Dr Andrew Wilson of Timet UK. The amounts of the elements: Al, Sn, Zr, Nb, Mo, Si and Fe were measured using x-ray fluorescence (XRF) spectroscopy. The amounts of the interstitial elements O and N were measured by combustion analysis. The amount of C was not determined. The chemical composition of the billet was measured at the centre and the edge. There was no significant difference in the composition between the two measurements. The average composition is given in Table 3.1.

Table 3.1 Billet composition (wt%).

Al	Sn	Zr	Nb	Mo	Si	Fe	O	N	C	Ti
5.90	4.00	3.54	0.69	0.50	0.33	0.006	0.1028	0.0025	Not measured	Balance

3.2 Characterisation of the Timetal 834 Billet

An 8 mm thick transverse slice was obtained from the 250 mm diameter billet of Timet 834. The entire cross section was polished and etched in order to examine the microstructure using optical microscopy. The billet was then sectioned for further analysis using optical microscopy, scanning electron microscopy, neutron texture analysis and EBSD utilising a range of step sizes. The locations analysed are indicated in Fig. 3.2. Specimens labelled 1-7, with dimensions 15 x 10 x 3 mm, were examined using EBSD. Specimens labelled A-Q, with dimensions 15 x 15 x 8 mm, were used for the neutron texture analysis. The macroscopic coordinate system used for this analysis is also shown in Fig. 3.2. It should be noted that the two perpendicular radial directions (R1 and R2) were arbitrarily chosen and are not related to specific forging directions, since these were not known.

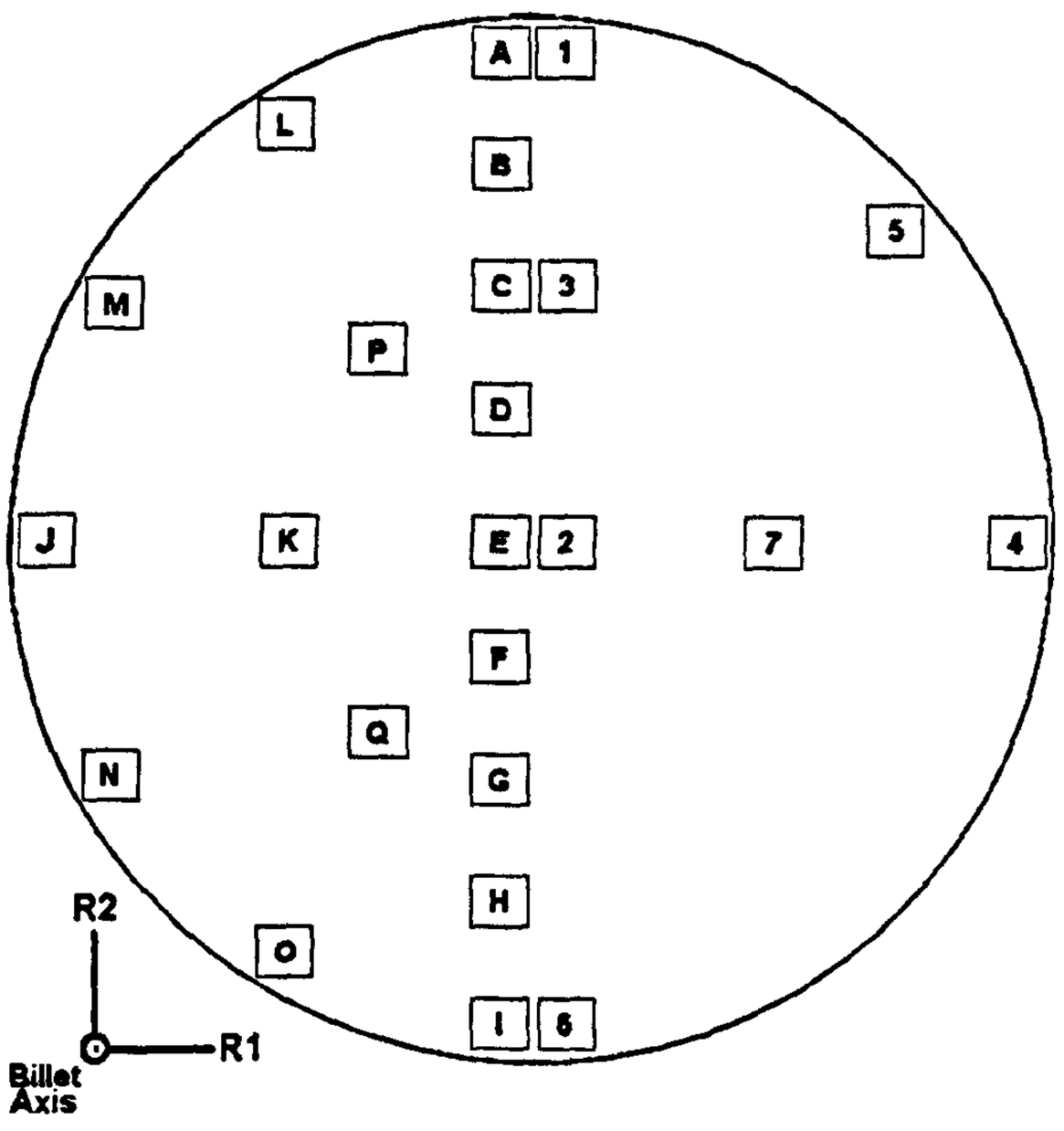

Fig. 3.2 Specimen positions and macroscopic coordinates for the billet characterisation.

3.3 β Approach Curve Determination

The first stage of the microstructural evolution study was to determine the β approach curve for the billet material provided by Timet. This was achieved by the solution heat treatment of small specimens of the billet at a range of temperatures in the α+β phase field followed by water quenching to preserve the volume fraction of α_p present at the

solution heat treatment temperature. The heat treated specimens were prepared for optical metallography and etched so that the volume fraction of α_p could be measured using image analysis software on a computer linked to an optical microscope.

3.3.1 Specimens

Cube shaped specimens measuring 10x10x10 mm^3 were cut from near the mid radius of the billet using a water cooled silicon carbide cut-off wheel. A 1.1 mm diameter hole was drilled in each specimen, at the centre of one face to a depth of 5mm in order to accommodate a thermocouple (Fig. 3.3).

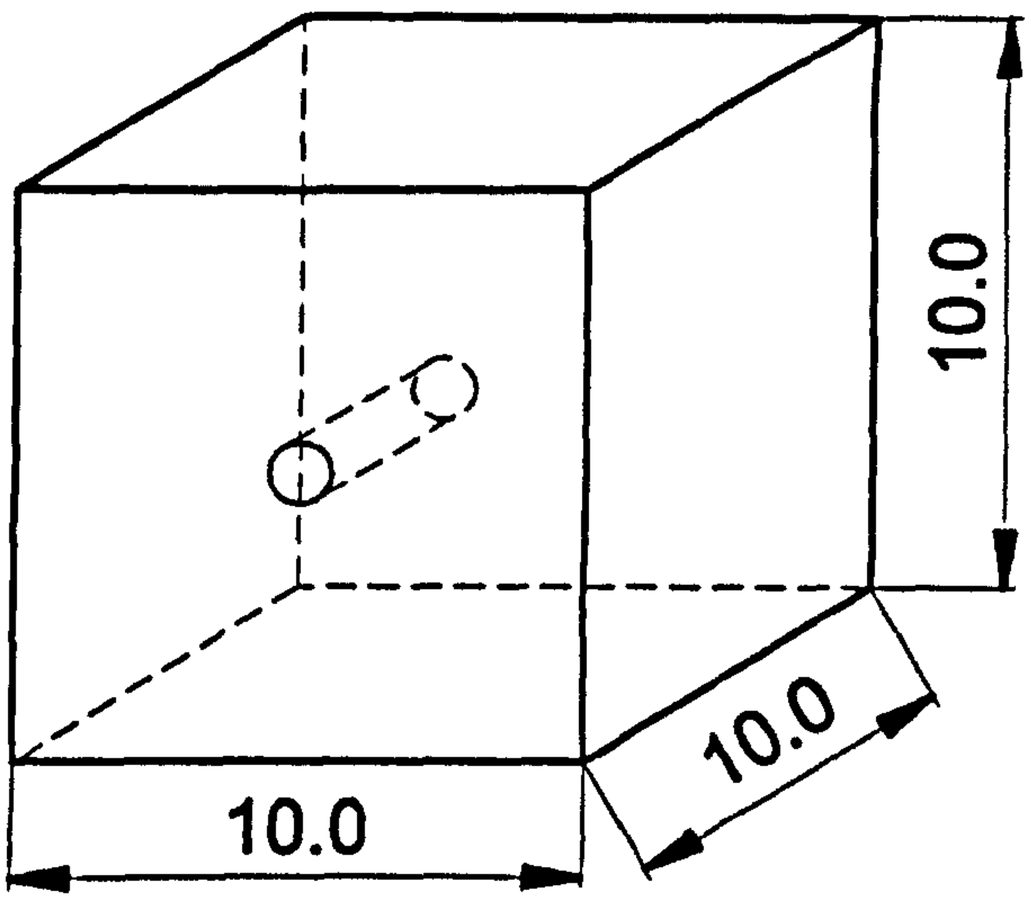

Fig. 3.3 Specimens for the β approach curve determination (dimensions in mm).

3.3.2 Test Details

The specimens were individually solution heat treated at a range of temperatures within the α+β phase field using the induction heating facility on the Thermomechanical Compression (TMC) Machine. The operation of this machine is described in section 3.5. In all, eight specimens were heat treated to a range of temperatures between 960°C and 1050°C in order to obtain sufficient points for the β approach curve to be determined (Table 3.2). In each case, the specimens were heated to the required temperature at a rate of 5°C s^{-1}, held at the required temperature for 600s in order to obtain phase equilibrium and then water quenched to room temperature. The heat treatment profile for a test at 1010°C is shown in Fig. 3.4.

The hold time of 600s was selected after carrying out initial tests at 1010°C, using the same heating rate but different hold times. The billet microstructure prior to testing contained approximately 70% α_p. After holding for 30s, the α_p volume fraction had reduced to 45%. For hold times of 300, 600 and 900s, the α_p volume fraction was similar at approximately 25%. This shows that phase equilibrium for the samples is obtained within a few minutes at a test temperature of 1010°C. Based on these results, a standard hold time of 600s was adopted for both the heat treatment specimens used here and for the larger plane strain specimens used elsewhere in this work. This gave a good compromise between ensuring phase and temperature equilibrium in the temperature range of interest, whilst minimising the thickness of the α case which develops at the surface of the specimens.

Table 3.2 Temperatures used to determine the β approach curve.

Sample	Temperature (°C)
A	1050
B	1040
C	1030
D	1020
E	1010
F	1000
G	990
H	960

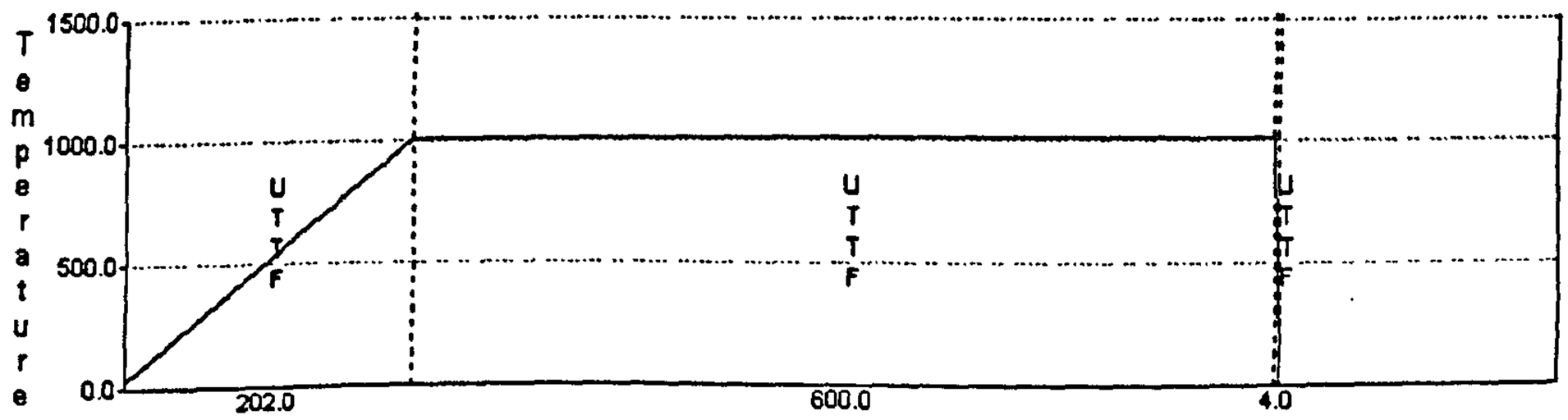

Fig. 3.4 Heat treatment for β approach curve determination.

3.3.3 Metallography

The heat treated specimens were cut in half and one half was mounted and metallographically prepared using the standard techniques outlined in section 3.6.1. The specimens were then etched using Weck's reagent. Optical micrographs were acquired from near the centre of the specimens at 100x magnification. Image analysis software was then used to determine the area fraction of α_p phase in each image by a light threshold technique. The etch provided by the Weck's reagent resulted in an excellent and consistently reproducible contrast in reflected light between the light α_p phase and the darker transformed β. This proved to be a much faster technique for measuring volume fraction compared to a traditional point counting approach. For each specimen, 3 separate images were analysed to obtain an average value for the volume fraction of α_p. Fig. 3.5 shows a typical micrograph obtained using Weck's reagent and the corresponding analysed image with the detected α_p phase assigned colours.

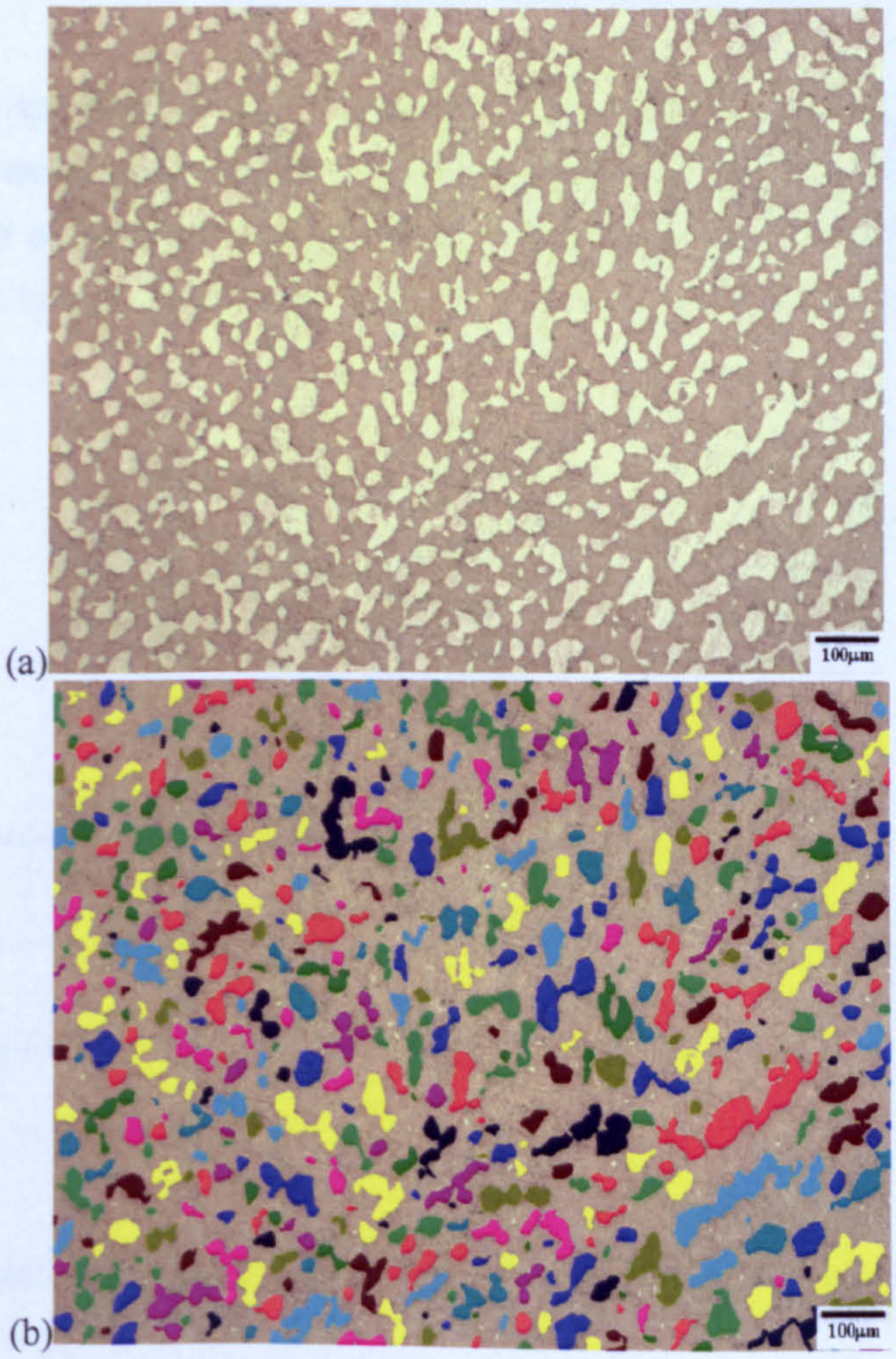

Fig. 3.5 (a) Billet specimen solution treated at 1000°C and water quenched, (b) α_p phase detected through contrast in reflected light after etching with Weck's reagent.

3.4 Phase Transformations During Cooling

An investigation was conducted to examine the effects of cooling rate on the β→α phase transformation in Timetal 834. The experimental procedure was based on the work of Ahmed and Rack (1998), who conducted a similar investigation on Ti-6Al-4V by adapting the end quench Jominy procedure (ASTM, 1995), normally used for assessing the hardenability of ferrous alloys. In this modified procedure, the Jominy end quench bar was circumferentially insulated and instrumented with thermocouples in order to obtain time-temperature profiles during cooling at locations along the bar length, providing a complete thermal history. The resulting microstructures were investigated using a combination of optical microscopy, scanning electron microscopy and EBSD. Microhardness testing was also carried out.

3.4.1 Specimens

A standard Jominy specimen (Fig. 3.6) was fabricated from the mid-radial position of the Timet billet. Into each specimen, four 1.1 mm diameter holes were drilled to a depth of 11 mm in order to accommodate four n-type thermocouples. The thermocouple holes were located 3mm, 15mm, 35mm and 65mm from the quenched end respectively.

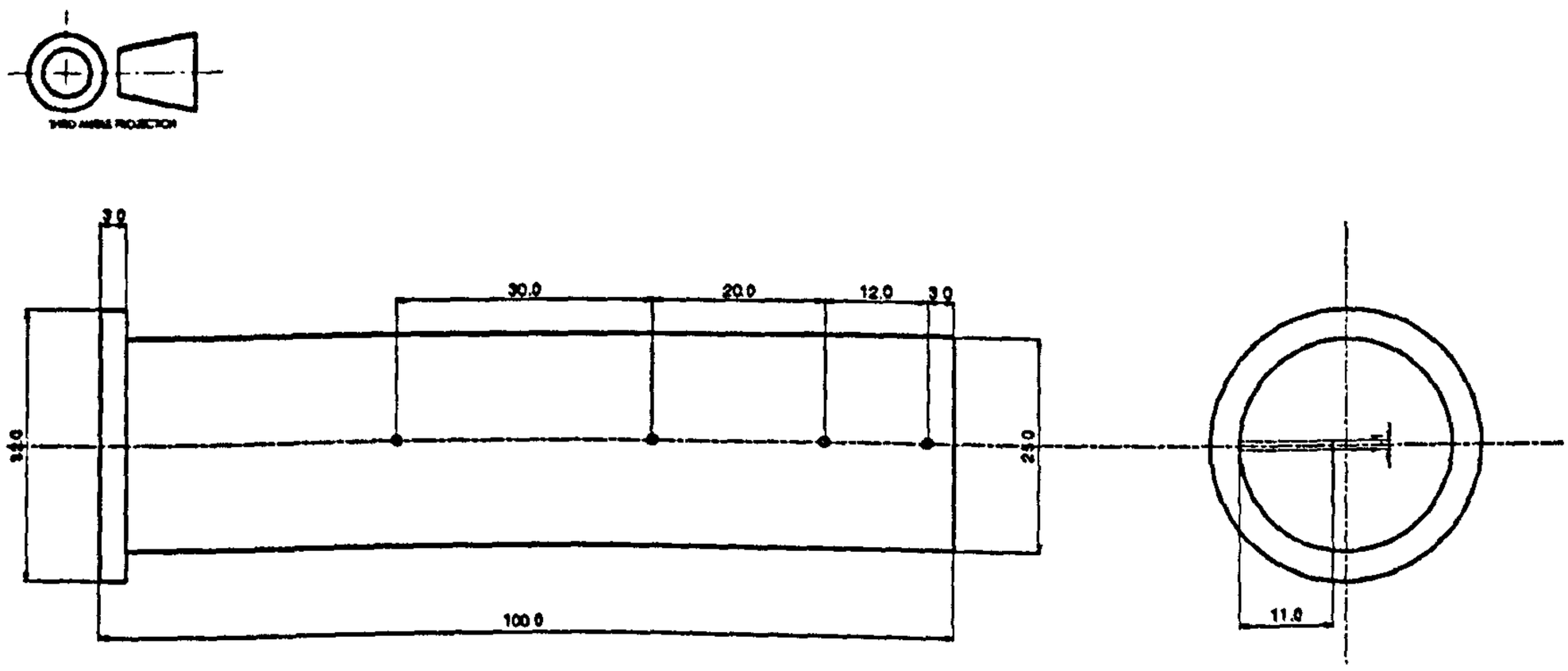

Fig. 3.6 Jominy end quench specimen with thermocouple holes (dimensions in mm).

3.4.2 Test Details

After fitting the thermocouples, the specimen was insulated with a Kaowool insulating barrier to ensure one-dimensional heat flow during subsequent cooling. The specimen was placed in the centre of a preheated furnace set to a nominal temperature of 1010°C. After 30 minutes, the specimen temperature as indicated by the four thermocouples had reached approximately 990°C. The furnace set temperature was then gradually increased until a specimen temperature of 1010°C was reached after approximately 65 minutes. The specimen was then transferred to a stand where water cooling was applied to the end of the specimen (Fig. 3.7).

The complete time-temperature history for the four thermocouples is shown in Fig. 3.8 and in greater detail during the cooling period in Fig. 3.9. It can be seen from Fig. 3.9, that some cooling of the specimen occurred between the opening of the furnace at t = 0s and the onset of rapid cooling due to the application of the water quench. This effect was most pronounced close to the quenched end. For example, for the thermocouple 3mm from the quenched end, the temperature dropped from 1009°C at t = 0s to 960°C at t = 15s (i.e. a cooling rate of approximately 3.3°C s^{-1}), after which rapid cooling took place at approximately 100°C s^{-1}. The effect of this interim cooling on the microstructure must be considered when interpreting the results of the test.

In Fig. 3.10, the mean cooling rate between 990°C and 500°C and the instantaneous cooling rate at 900°C (CR_{900}) is plotted against distance from the quenched end for the four thermocouples. The instantaneous cooling rate at 900°C is perhaps the more useful measure of cooling rate as the phase transformations which take place during cooling take place in the temperature range between 800 and 1000°C. It can be seen from Fig. 3.10 that the variation in cooling rates along the bar obeyed a power law type relationship. This relationship was subsequently used to estimate the cooling rates for any distance, from the quenched end. The instantaneous cooling rate at 900°C varied from 1.7°C s^{-1} for the thermocouple located 65mm from the quenched end, to 100°C s^{-1} for the thermocouple 3mm from the quenched end. Using the fitted curve to extrapolate closer to the quenched end, an estimate of around 300°C s^{-1} is obtained for a distance of 1.5mm from the quenched end. Beyond this point, it is clearly not possible to estimate the cooling rates with any accuracy, suffice to say that it is likely to be in excess of many hundreds of degrees per second.

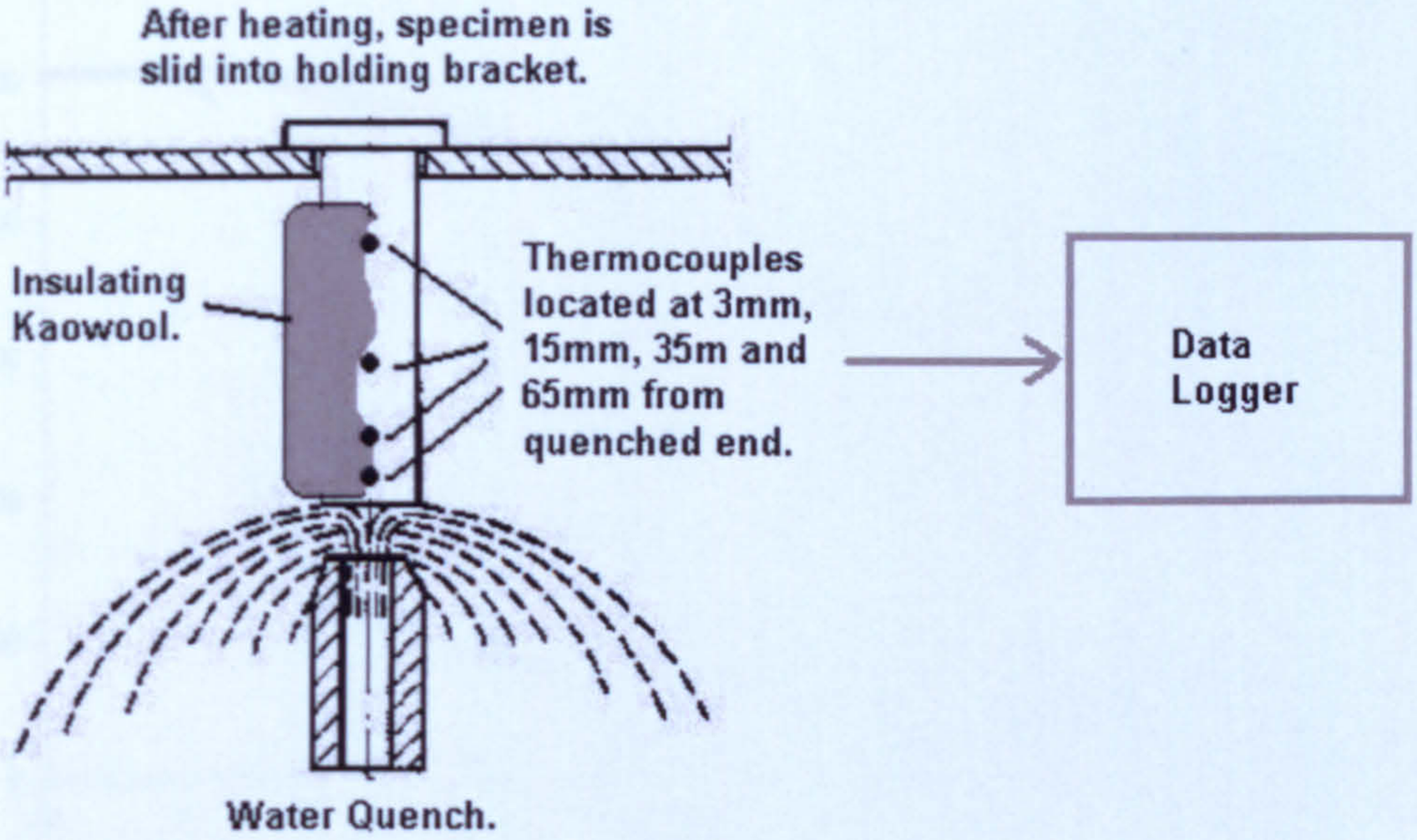

Fig. 3.7 Jominy test set-up.

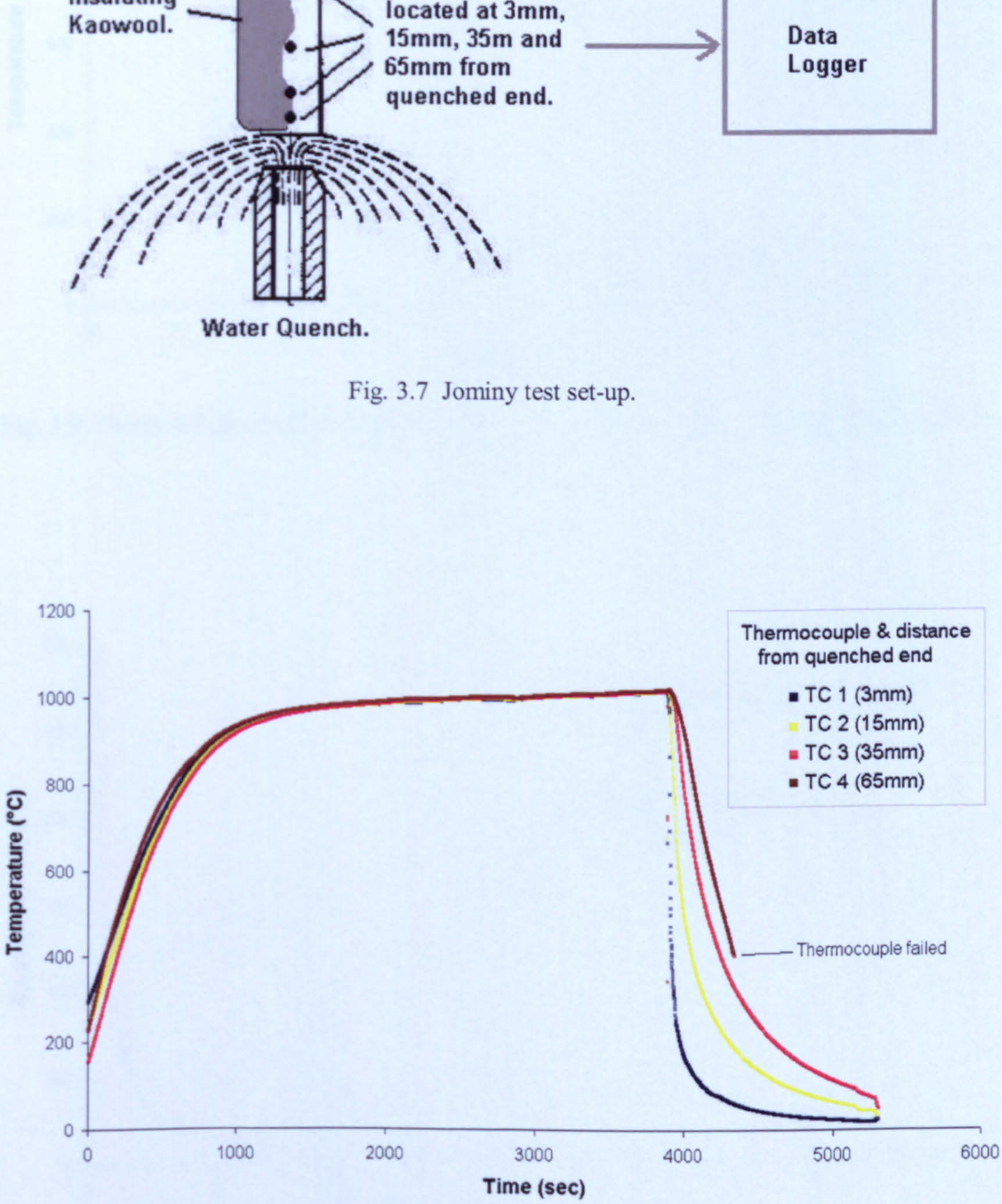

Fig. 3.8 Thermocouple time-temperature history for Timetal 834 Jominy specimen heat treated to 1010°C and water quenched.

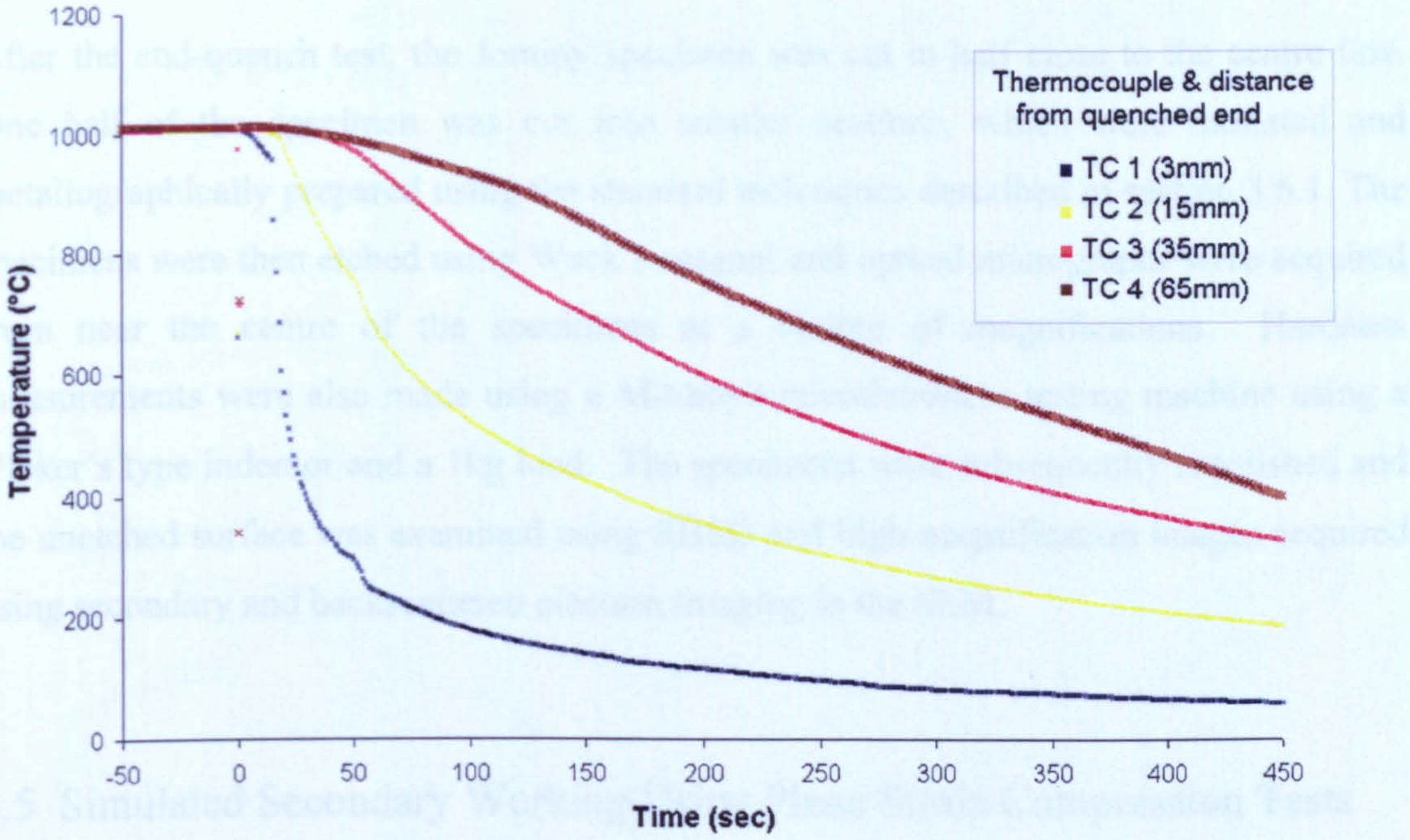

Fig. 3.9 Thermocouple cooling curves for Timetal 834 Jominy specimen water quenched from 1010°C.

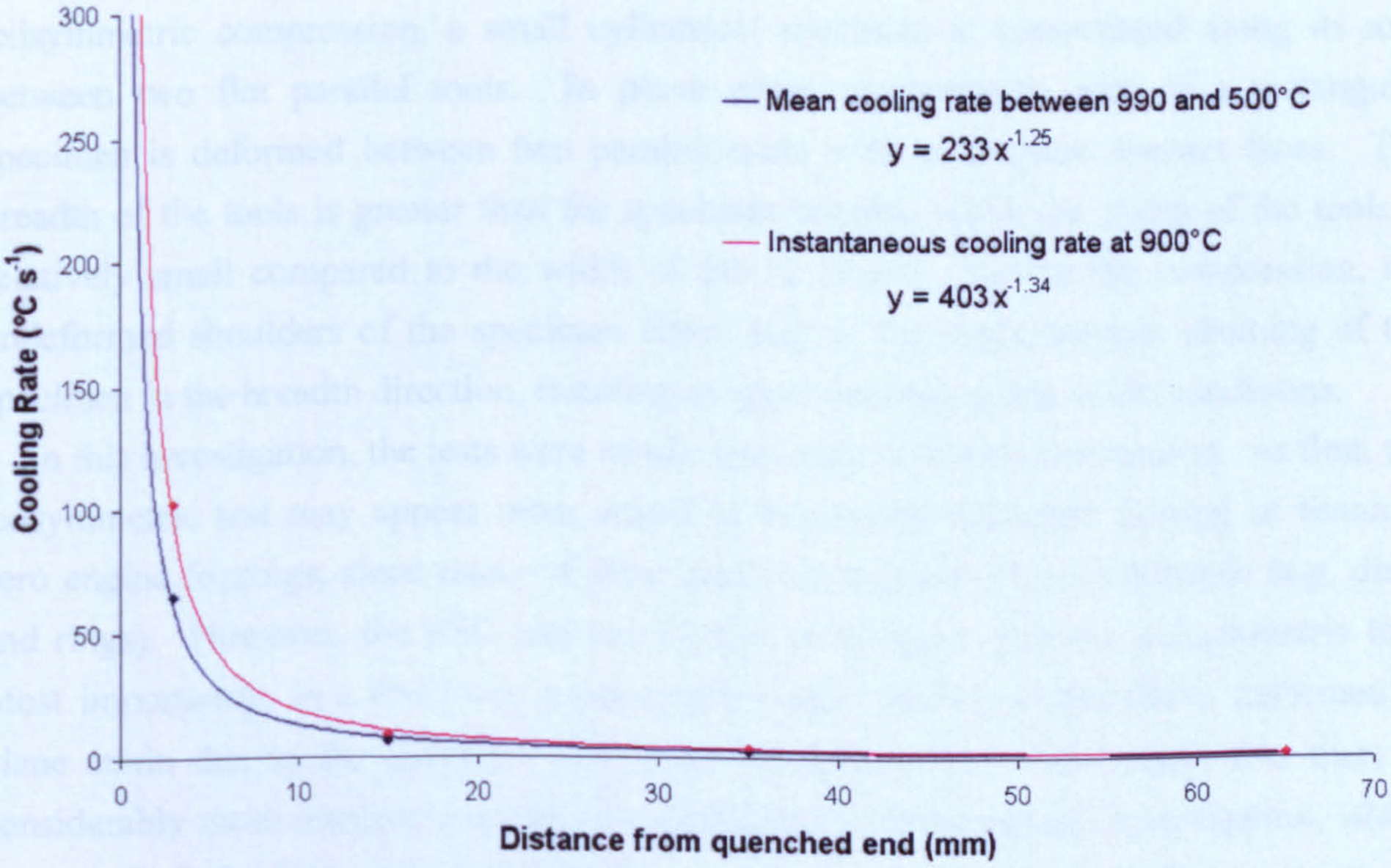

Fig. 3.10 Cooling rate versus distance from quenched end. Blue line shows the mean cooling rate between 990°C and 500°C, while the red line shows the instantaneous cooling rate at 900°C (CR_{900}).

3.4.3 Metallography

After the end-quench test, the Jominy specimen was cut in half close to the centre line. One half of the specimen was cut into smaller sections, which were mounted and metallographically prepared using the standard techniques described in section 3.6.1. The specimens were then etched using Weck's reagent and optical micrographs were acquired from near the centre of the specimens at a variety of magnifications. Hardness measurements were also made using a Mitutoyo microhardness testing machine using a Vicker's type indentor and a 1kg load. The specimens were subsequently repolished and the unetched surface was examined using EBSD and high magnification images acquired using secondary and backscattered electron imaging in the SEM.

3.5 Simulated Secondary Working Using Plane Strain Compression Tests

Hot compression tests were used to investigate microstructural development during thermomechanical processing. The tests were conducted on The University of Sheffield's Thermomechanical Compression (TMC) Machine. This machine can operate in two modes: axisymmetric compression and plane strain compression (PSC). The tool and specimen geometries for these two types of test are shown schematically in Fig. 3.11. In axisymmetric compression, a small cylindrical specimen is compressed along its axis between two flat parallel tools. In plane strain compression, part of a rectangular specimen is deformed between two parallel tools with rectangular contact faces. The breadth of the tools is greater than the specimen breadth, while the width of the tools is relatively small compared to the width of the specimen. During the compression, the undeformed shoulders of the specimen either side of the tools restricts straining of the specimen in the breadth direction, resulting in approximately plane strain conditions.

In this investigation, the tests were conducted in plane strain compression. At first, the axisymmetric test may appear more suited to simulating industrial forging of titanium aero engine forgings, since many of these parts are themselves axisymmetric (e.g. discs and rings). However, the PSC test has several advantages over the axisymmetric test. Most importantly, in a PSC test, a reasonably large volume of material is deformed in plane strain due to the geometry and larger specimen size. This means that there is considerably more material available for subsequent microstructural investigation, which is a particularly important consideration when several analysis techniques are to be performed on the same deformed specimen. In the case of axisymmetric specimens, not only are they much smaller in size but one must also be much more critical as to where in

the deformed volume the material is sectioned since there is greater local variation in the strain, strain rate and temperature distribution in a test specimen. The PSC test is also more suited to investigations in which high strains are generated because axisymmetric testing becomes limited by barrelling of the specimen.

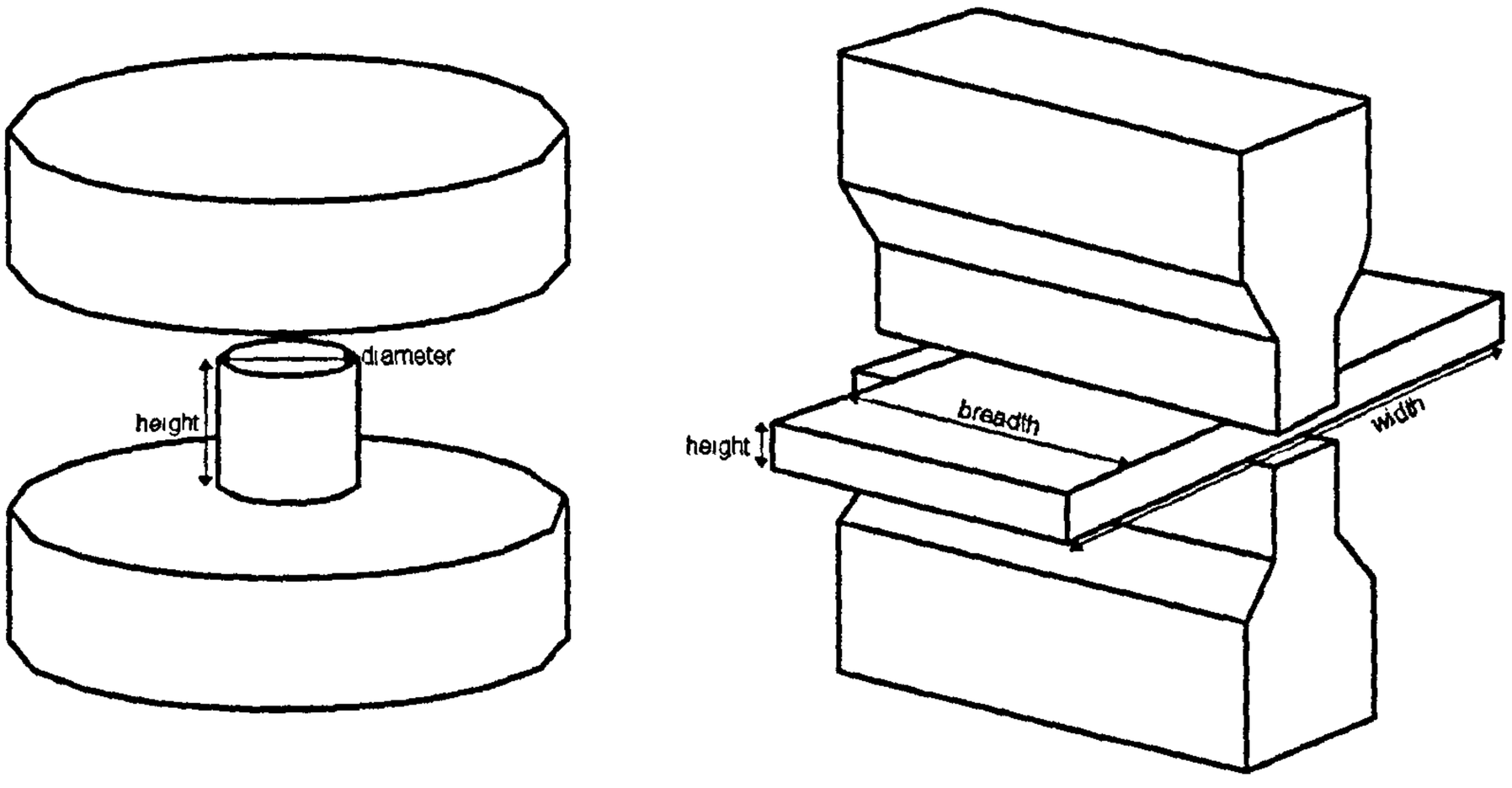

Fig. 3.11 Schematic diagrams of the two testing modes: (a) axisymmetric, (b) plane strain compression (PSC).

3.5.1 Equipment Description

The TMC machine was developed by Servotest Ltd, Feltham in conjunction with The University of Sheffield and was built specifically for conducting research into thermomechanical processing. The apparatus consists of two main components; a deformation furnace containing the forging tools and a fast thermal treatment unit (FTTU) used for conducting complex thermal treatments. There are also two additional furnaces, which may be used for more conventional heat treatments such as soaking prior to deformation and post deformation annealing. The specimen is held by a robotic arm, which moves between the various components. The machine is operated from a computer using purpose written software. The software is used to pre-program a complete thermomechanical test, so that during the test, the machine operates automatically. The key components of the TMC machine are shown in Fig. 3.12

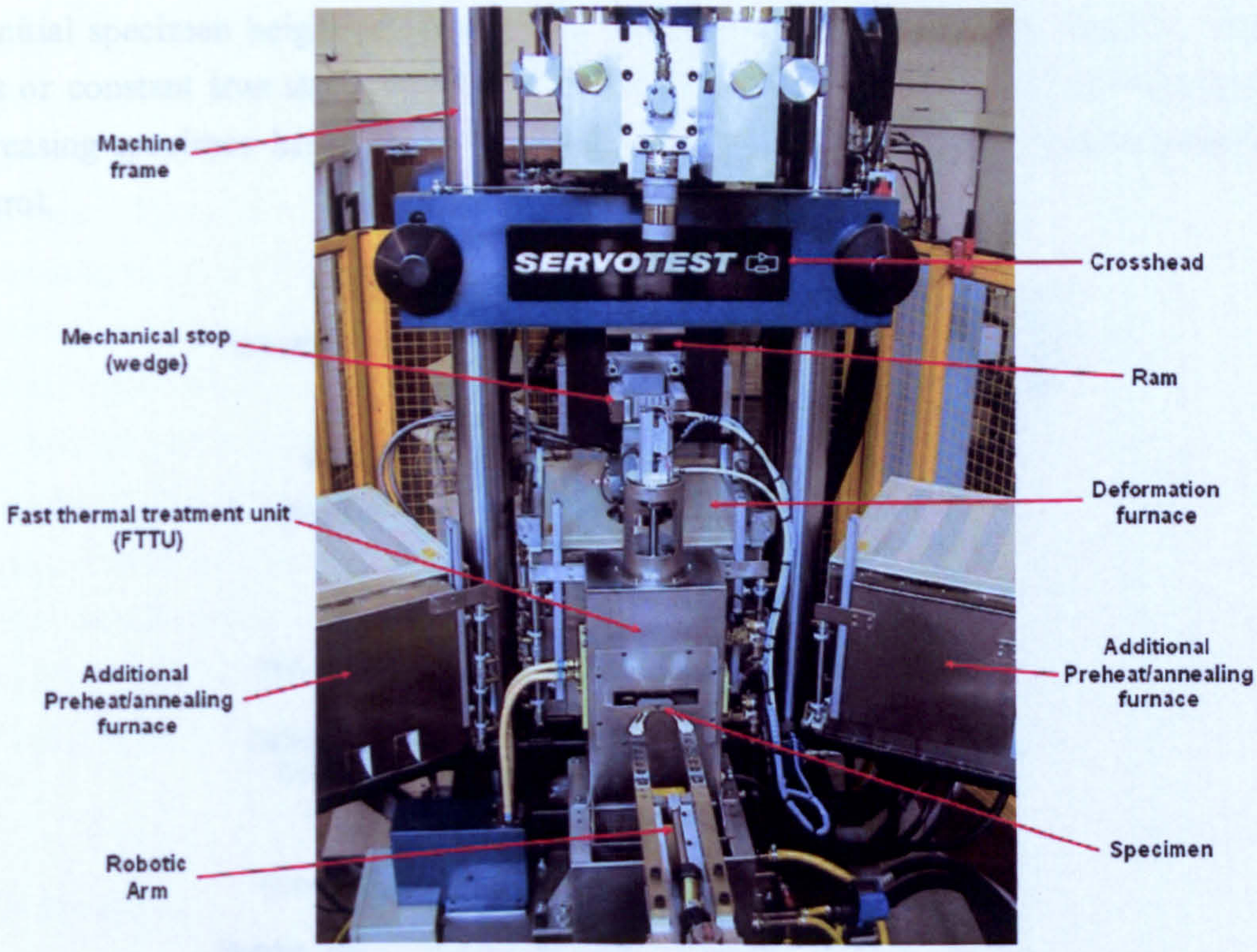

Fig. 3.12 The University of Sheffield's Thermomechanical Compression (TMC) Machine.

The construction of the machine frame and forging apparatus are shown schematically in Fig. 3.13. The machine frame consists of four stainless steel columns mounted on a steel framework base, which provides a rigid structure to support the forging tools. The lower forging tool is fixed and is attached to the machine frame via a tool post containing a load cell. The upper tool is attached to another tool post, which is in turn mounted onto a ram which can move in the vertical plane, thus allowing a specimen placed between the tools to be deformed by the downward motion of the ram. The ram is controlled by a servo-hydraulic system and transducers which monitor its displacement and velocity. In order to achieve acceptable control in the total applied strain and an abrupt stop in the strain rate at the end of an applied deformation, a movable wedge is used to provide a mechanical stop for the ram at the desired displacement. The top and bottom tools are contained within the deformation furnace, which has holes in the top and bottom to permit entry of the tool posts. In addition to the temperature control afforded by the deformation furnace, there are also independent tool heaters within the top and bottom tool posts to allow greater control of the temperature of the tools. There is a door in the front of the deformation furnace that opens just before a deformation is scheduled to take place to allow entry of the specimen. The ram can generate a maximum force of 500kN and has a maximum velocity of $3.0ms^{-1}$ under zero load, which drops to around $1.6ms^{-1}$ at a load of 400kN. This results in a maximum controllable strain rate of around $200s^{-1}$ for

an initial specimen height of 10mm. The machine can conduct either constant velocity tests or constant true strain rate tests, which require a linear decrease in velocity with decreasing specimen height. The machine also has the capability to operate under load control.

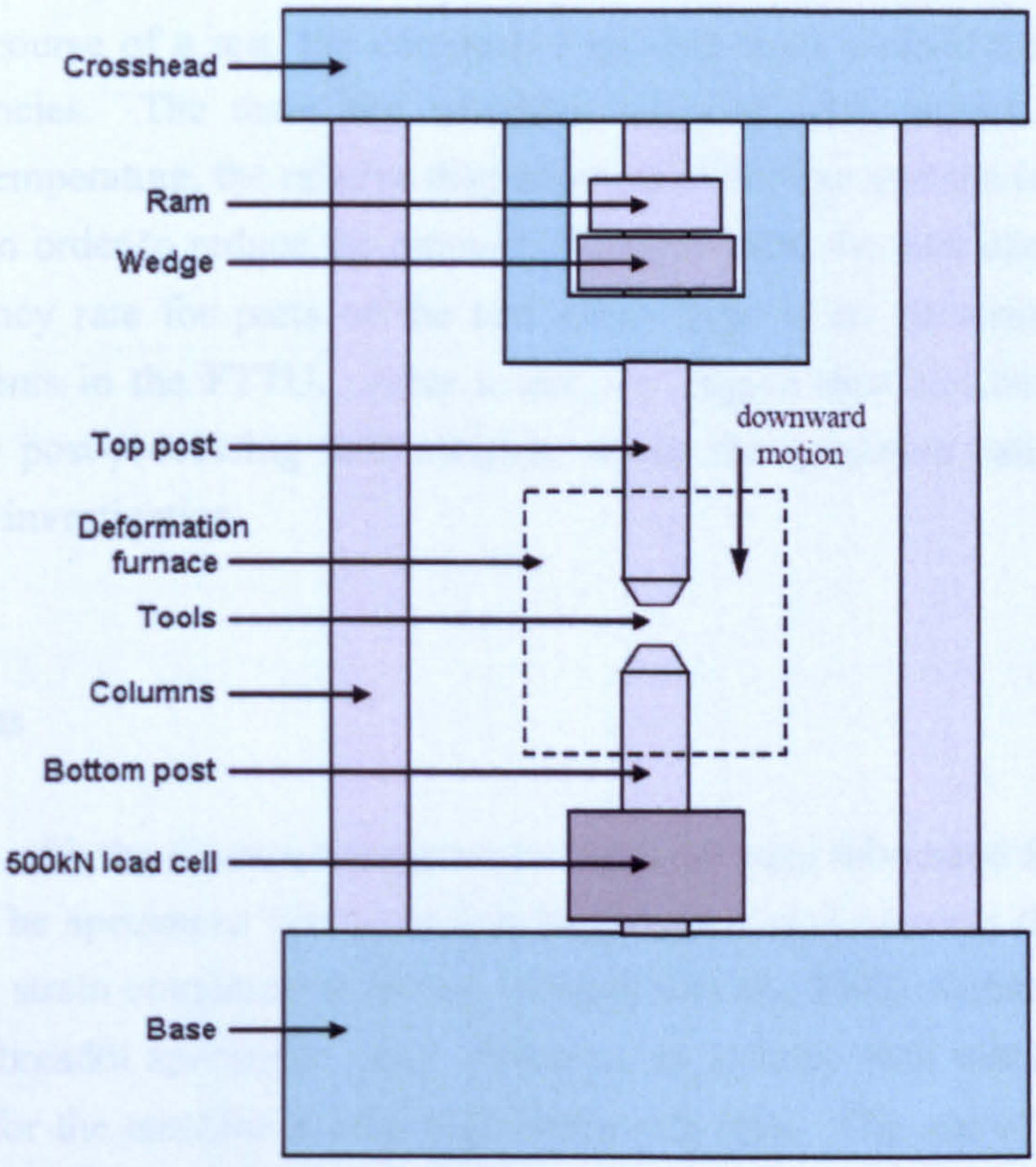

Fig. 3.13 Schematic diagram of the TMC machine frame and forging apparatus (Hinton, 2006).

The forging tools for plane strain compression have a rectangular contact face with a width of 15mm and a breadth of 100mm. The tools are manufactured from a nickel-based superalloy with the nominal composition shown in Table 3.3. The tools are periodically redressed to maintain a consistent ground surface finish.

Table 3.3. Nominal composition of alloy used for the PSC forging tools (wt%).

Ni	W	Cr	Al	Ta	Mo	Zn	C
71	11	6	6	3	2	0.6	0.13

The fast thermal treatment unit (FTTU) provides controlled specimen heating through an induction coil and controlled cooling by spraying either air, water, or mist. The FTTU is located directly in front of the deformation furnace, to enable rapid transfer of the

specimen between these locations (less than 1s). This is particularly important when a rapid quench is desired after deformation. Specimen temperature is monitored and controlled by an n-type thermocouple, which is usually inserted into a hole drilled into the specimen. There is also the provision for monitoring the temperatures of two extra thermocouples during the course of a test.

During the course of a test, the computer logs data from various transducers at user defined frequencies. The three key variables recorded with respect to time are the thermocouple temperature, the relative displacement of the ram and the load registered by the load cell. In order to reduce the amount of logged data, the user can specify a lower logging frequency rate for parts of the test when there is no deformation e.g. during thermal treatments in the FTTU. After a test, the logged data can be transferred to a spreadsheet for post-processing and analysis, whilst the specimen can be retained for microstructural investigation.

3.5.2 Specimens

PSC specimens with the dimensions shown in Fig. 3.14 were fabricated from the supplied Timet billet. The specimens had a breadth/height ratio of 3 whereas the good practice guide for plane strain compression testing (Roebuck *et al.*, 2002) recommends a ratio of 6. These half breadth specimens were chosen so as to keep well within the maximum specified load for the machine during high strain rate tests. The use of reduced breadth specimens means that corrections must be made for breadth spreading when analyzing the test data. The PSC specimen axes are labelled in this research using the convention for rolling i.e. rolling direction (RD), transverse direction (TD) and normal direction (ND). The specimens were fabricated such that the normal direction (ND) was parallel with the billet axis as shown in Fig. 3.15. It should be noted that the two perpendicular radial directions in the billet (R1 and R2) were arbitrarily chosen and are not related to specific ingot forging directions, since these were not known. Into each specimen, a thermocouple hole was drilled into the centre of the RD/ND face to a depth of 10 mm in order to accommodate an n-type thermocouple.

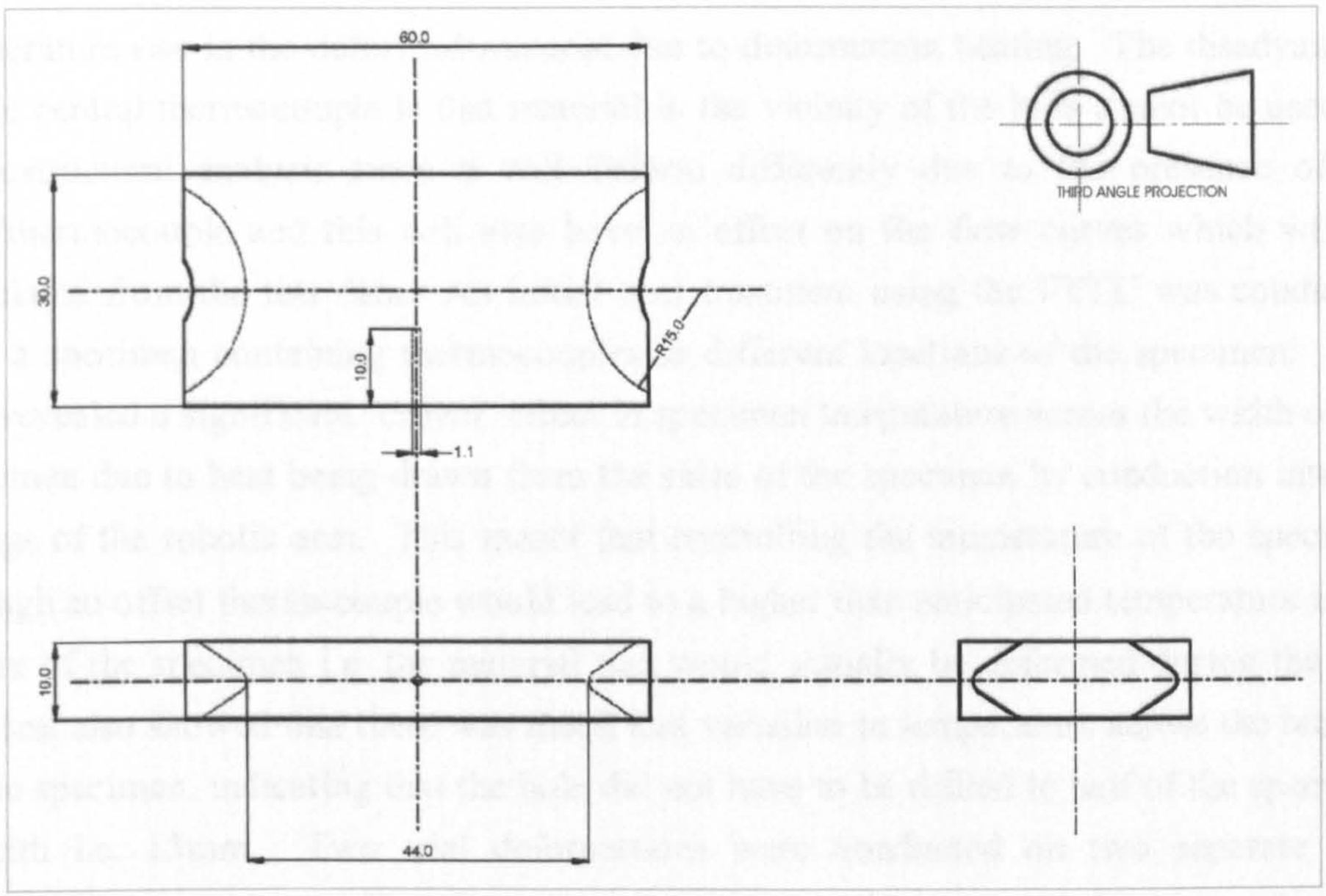

Fig. 3.14 Plane strain compression specimen (dimensions in mm).

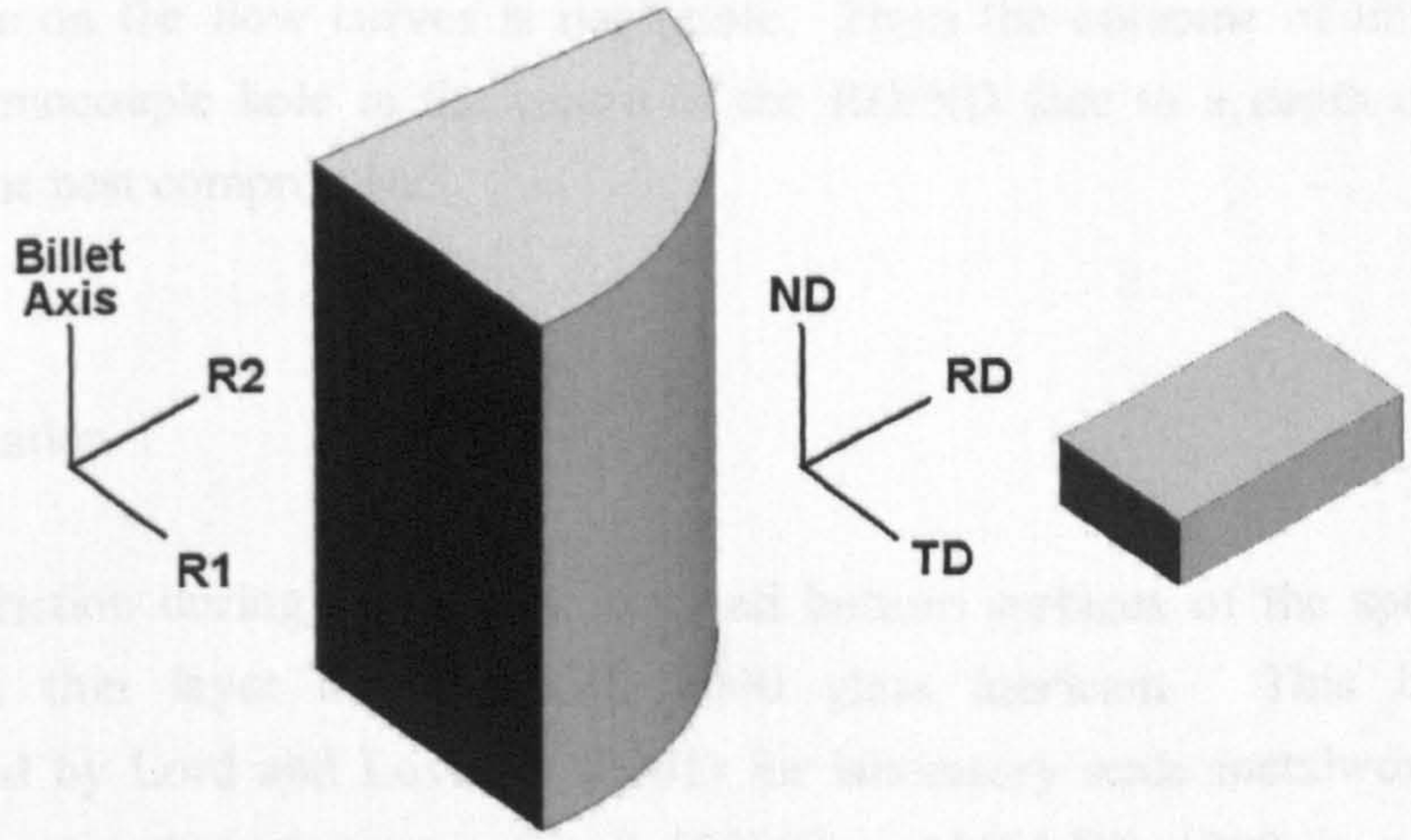

Fig. 3.15 Orientation of the PSC specimens with respect to the billet. The directions of the perpendicular radial directions R1 and R2 were arbitrary.

3.5.3 Thermocouple Position

In choosing the best position for the location of the thermocouple, one must choose between a position in the centre of the specimen or one that is offset from the centre line, so that it lies to one side of the intended deformation zone. The advantage of locating the thermocouple in the centre is that it provides the best measurement of the temperature of the material that is to be deformed and also provides a much better assessment of the

temperature rise in the deformed material due to deformation heating. The disadvantage of the central thermocouple is that material in the vicinity of the hole cannot be used for microstructural analysis since it will deform differently due to the presence of the hole/thermocouple and this will also have an effect on the flow curves which will be calculated from the test data. An initial heat treatment using the FTTU was conducted with a specimen containing thermocouples in different locations of the specimen. This trial revealed a significant 'crown' effect in specimen temperature across the width of the specimen due to heat being drawn from the sides of the specimen by conduction into the prongs of the robotic arm. This meant that controlling the temperature of the specimen through an offset thermocouple would lead to a higher than anticipated temperature in the centre of the specimen i.e. the material that would actually be deformed during the test. The test also showed that there was much less variation in temperature across the breadth of the specimen, indicating that the hole did not have to be drilled to half of the specimen breadth i.e. 15mm. Two trial deformations were conducted on two separate steel specimens, one with an offset thermocouple and one with a central thermocouple, both drilled to a depth of 10mm. An examination of the raw load displacement data for these tests revealed no significant differences, suggesting that the effect of the central thermocouple on the flow curves is negligible. From the outcome of this preliminary work, a thermocouple hole in the centre of the RD/ND face to a depth of 10mm was selected as the best compromise.

3.5.4 Lubrication

To reduce friction during testing, the top and bottom surfaces of the specimens were coated in a thin layer of AMLUBE 1000 glass lubricant. This lubricant was recommended by Lord and Loveday (2001) for laboratory scale metalworking tests on titanium alloys at temperatures around 1000°C. AMLUBE 1000 is a water-based, unleaded glass precoat. When the specimen is heated, the glass frit fuses and forms a continuous, viscous fluid film, which insulates, protects, and lubricates the specimen during testing.

3.5.5 Conducting a Test

Before any testing can take place, various preliminary activities must be carried out. The deformation furnace is switched on approximately 2 hours before testing to allow the furnace environment including the forging tools and tool posts to reach thermal equilibrium at the desired furnace temperature. The thermocouples that are used to

monitor and control the temperature of the specimens are checked for accuracy by comparing them with a reference thermocouple in a calibrated furnace. A thermocouple is deemed acceptable if it records a temperature within +/- 2°C of the reference. The specimens that are to be tested are individually marked for identification purposes and their dimensions measured in the locations indicated in Fig. 3.16 to establish the initial specimen dimensions. The AMLUBE 1000 Lubricant is then applied to the entire top and bottom surface of each specimen using a brush and allowed to dry.

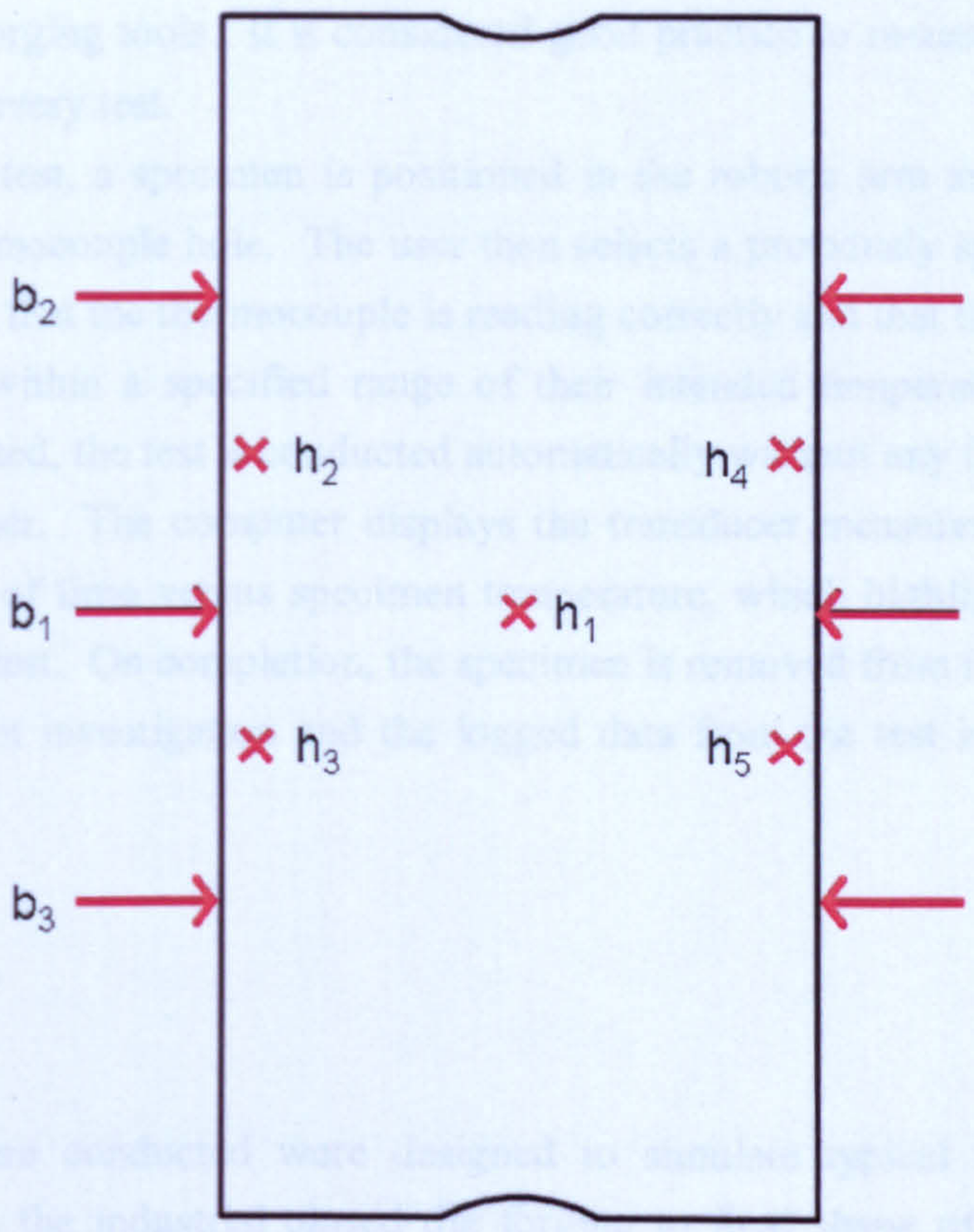

Fig. 3.16 Measuring locations for height (h_1 to h_5) and breadth (b_1 to b_3) on an initial PSC specimen prior to testing.

Before each test, the TMC machine software is used to specify the test details. In order to do this, the tests are broken down into a number of smaller segments. For example, for a heat treatment segment using the FTTU, the user would choose the FTTU as the specimen position, which in turn allows the user to select a variety of heating or cooling options e.g. controlled heating using the induction coil. Similarly, for a deformation segment, the user would choose the deformation furnace as the specimen position, which then enables the user to select first the type of deformation (e.g. a constant strain rate deformation), followed by various parameters to further define this deformation e.g. strain rate, total strain etc. Once a test has been specified, the details of the test are saved for future use.

The next step is to adjust the robotic arm with a dummy specimen in place to ensure that the specimen is level and will be delivered centrally between the forging tools, leaving a clearance of approximately 2mm between the lower forging tool and the bottom of the specimen.

The final step before testing is to zero the displacement transducer. This is accomplished by bringing the forging tools into contact with each other by lowering the ram until a very small load of approximately 1kN is registered by the load cell. This position is then set to zero, so that the displacement transducer subsequently displays the gap between the forging tools. It is considered good practice to re-zero the displacement transducer before every test.

To carry out a test, a specimen is positioned in the robotic arm and a thermocouple fitted into the thermocouple hole. The user then selects a previously specified test and is prompted to check that the thermocouple is reading correctly and that the furnace and tool temperatures are within a specified range of their intended temperatures. Once these checks are completed, the test is conducted automatically without any further intervention required by the user. The computer displays the transducer measurements in real time and plots a graph of time versus specimen temperature, which highlights any problems arising during the test. On completion, the specimen is removed from the robotic arm and kept for subsequent investigation and the logged data from the test is saved for further analysis.

3.5.6 Test Details

The tests that were conducted were designed to simulate typical secondary forging conditions used in the industrial closed die forging to final shape of Timetal 834 aero engine components. Each test consisted of four distinct segments (Fig. 3.17). In the first segment, the specimen was transferred from an initial start position into the FTTU, where it was heated using the induction heater at a linear rate to the desired deformation temperature in a period of 202 seconds (i.e. approximately $5°Cs^{-1}$ for a temperature of 1010°C). In the second segment, the specimen remained in the FTTU and the specimen temperature was maintained by the induction heater at the desired deformation temperature for 600 seconds to allow for thermal homogenisation and phase equilibrium. In the third segment, the specimen was rapidly transferred to the deformation furnace and deformed in plane strain compression at the desired constant true strain rate to the desired total true strain. The time delay from the end of the second segment in the FTTU until the start of deformation in the deformation furnace was less than 1 second. In the fourth segment, immediately after deformation, the specimen was rapidly transferred to the FTTU and cooled at the fastest possible rate by quenching in a continuous supply of cold

water. The time taken to cool the specimen to below 500°C using this quench was less than 2.5 seconds from the end of deformation. A typical time-temperature profile for segments 3 and 4 for a test at 1010°C followed by a water quench is shown in Fig. 3.18. Details of the tests that were successfully carried out are given in Table 3.4. The specimens from these tests were investigated using optical microscopy, scanning electron microscopy and EBSD.

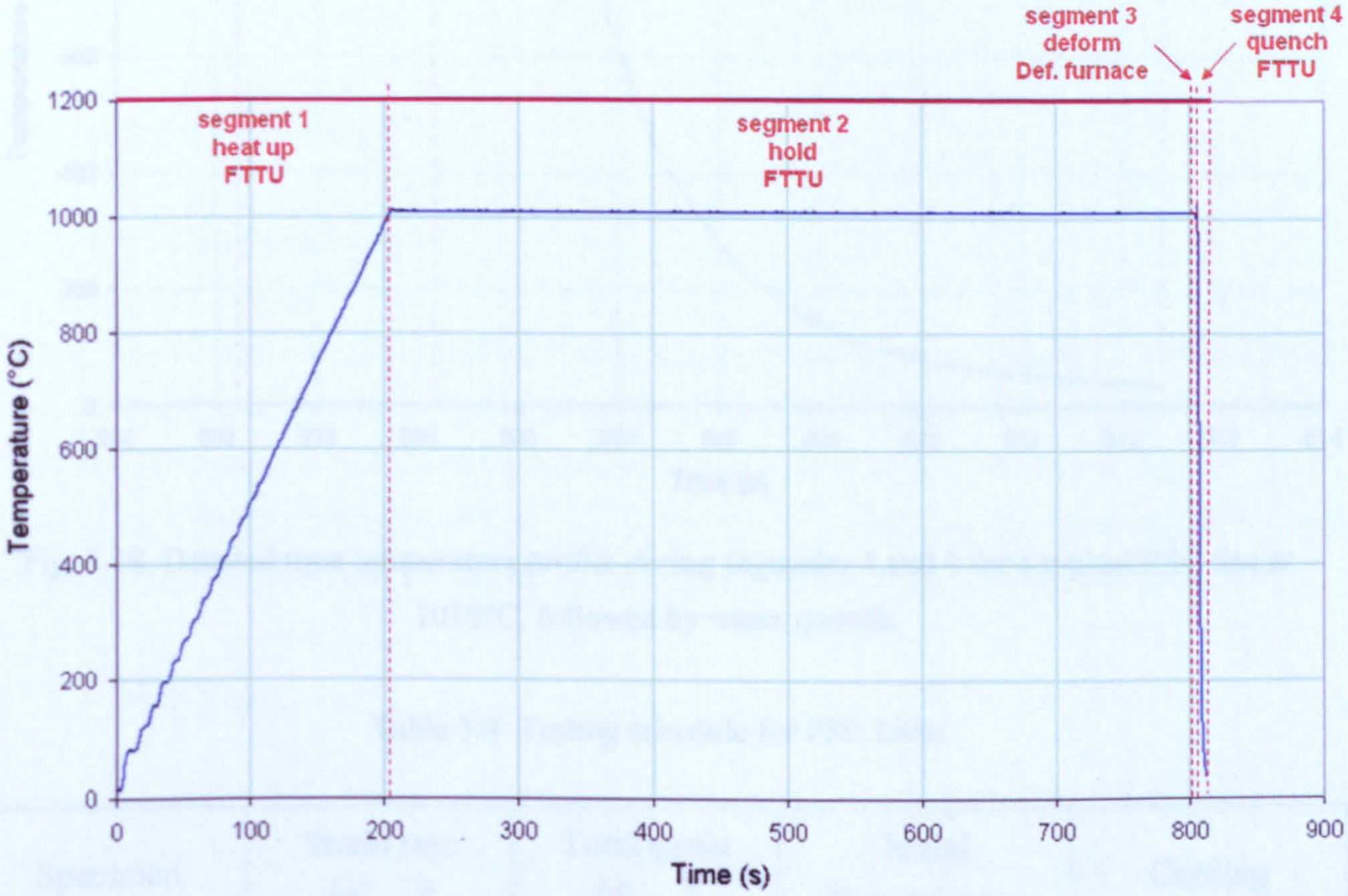

Fig. 3.17 Time-temperature profile of a specimen during a typical PSC test at 1010°C, followed by water quench.

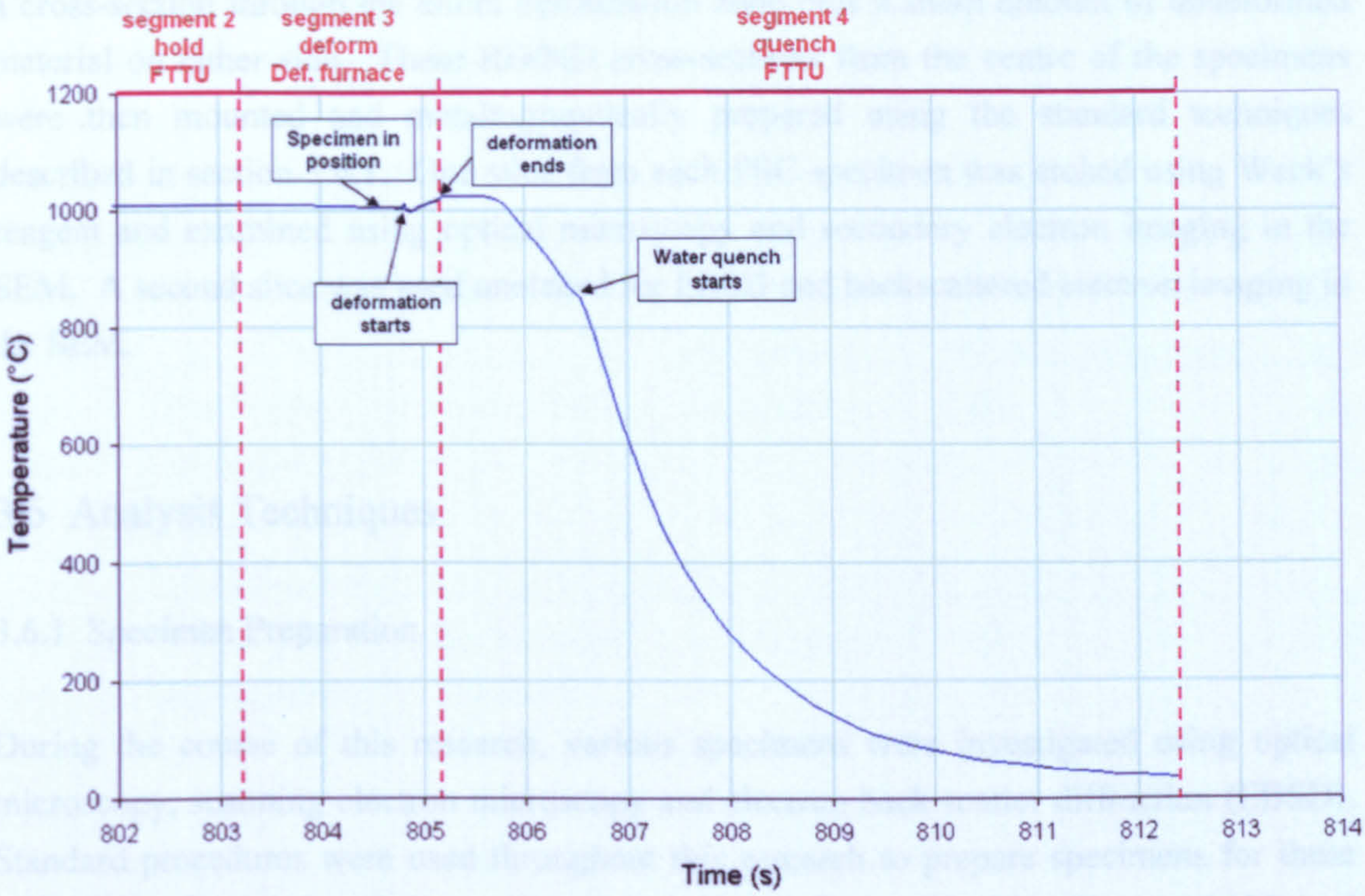

Fig. 3.18 Detailed time temperature profile during segments 3 and 4 for a typical PSC test at 1010°C, followed by water quench.

Table 3.4 Testing schedule for PSC tests.

Specimen	Strain rate (ε_{nom})	Total strain (ε_{nom})	Initial Temperature	Cooling
A	20 s^{-1}	0.69	1010 °C	WQ
B	2.0 s^{-1}	0.69	1010 °C	WQ
C	2.0 s^{-1}	1.39	1010 °C	WQ
D	0.2 s^{-1}	0.69	1010 °C	WQ
E	0.2 s^{-1}	0.69	1010 °C	WQ
F	0.02 s^{-1}	0.69	1010 °C	WQ
G	No deformation		1010 °C	WQ

3.5.7 Metallography

The specimens from successful plane strain compressions tests were cut in half along the centre of the specimen breadth. Thin parallel slices (approx 2mm thick) were then taken from the centre of the specimens and parallel to this initial cut such that they incorporated

a cross-section through the entire deformation zone plus a small amount of undeformed material on either side. These RD/ND cross-sections from the centre of the specimens were then mounted and metallographically prepared using the standard techniques described in section 3.6.1. One slice from each PSC specimen was etched using Weck's reagent and examined using optical microscopy and secondary electron imaging in the SEM. A second slice was used unetched for EBSD and backscattered electron imaging in the SEM.

3.6 Analysis Techniques

3.6.1 Specimen Preparation

During the course of this research, various specimens were investigated using optical microscopy, scanning electron microscopy and electron back scatter diffraction (EBSD). Standard procedures were used throughout this research to prepare specimens for these techniques. These procedures are based on the methods described by Thomas (2007) and on the guidelines provided by the materials preparation company Struers (Struers, 2005).

3.6.1.1 Sectioning

Specimens of the desired size were usually cut from a larger initial piece of metal. Initial sections were made using a manually operated Buelher Abrasimet silicon carbide cut-off saw, which enabled rapid sectioning. To reduce specimen heating during cutting, a liquid coolant was applied continuously to the specimen and the cutting wheel. In the later stages of sectioning, more care was required to ensure the correct specimen dimensions and to reduce the volume of material affected by the cutting procedure. For these cuts, a Struers Accutom fitted with a 0.5mm thick silicon carbide cutting wheel was used. The cutting operations on this machine are automated and can be positioned with an accuracy of 0.1mm. To minimise specimen heating, the cutting wheel was advanced with a low feed rate and a liquid coolant was applied continuously to the cutting wheel.

3.6.1.2 Surface Preparation

To prepare a specimen surface, the specimen was incorporated face down into a 30mm diameter Bakelite resin mount. The mounted specimen was then ground and polished in three stages using a Struers Abramin automatic polishing machine. In the first stage, the specimen was ground using a resin bonded diamond disc, followed by initial polishing

using a water based diamond suspension and then final polishing using colloidal silica. The details of these stages are given in Table 3.5.

Table 3.5 Metallographic preparation procedure.

Stage	Preparation surface	Additives	Specimen/surface relative rotation	Speed (RPM)	Force (N/specimen)	Time (mins)
1. Grind	Resin bonded diamond disc equivalent to 220 grit. (Struers MD-piano)	Water cooled	complimentary	300	5	Until planar
2. Initial polish	Composite disc (Struers MD-largo)	Water based 9μm Diamond suspension + lubricant	complimentary	150	5	10
3. Final polish	Porous neoprene disc (Struers MD-chem)	90% 0.05μm colloidal silica suspension + 10% laboratory reagent grade H_2O_2 (30% w/v)	complimentary	150	5	15

3.6.1.3 Etching

For certain techniques, the prepared surface was chemically etched to reveal the microstructure. Two fluorine based etchants were used during this research.

Kroll's reagent	1-3 ml HF 2-6 ml HNO_3 100 ml H_20	Immerse and agitate specimen for between 5 and 15s.
Weck's reagent	2g NH_4HF_2 100 ml H_2O	Ammonium hydrogen difluoride crystals dissolved in water. Immerse and agitate specimen for between 10 and 30s.

3.6.2 Optical Microscopy

Optical microscopy was carried under reflected light. The microscope was equipped with a video camera connected to a PC. The PC was equipped with image analysis software (Imaging Associates KS 400) which was used to capture still images from the camera and to perform image analysis procedures to quantify aspects of the microstructures. Pictures of a graticule were taken in tandem with micrographs to provide an accurate scale.

Some traditional quantitative metallography was also carried out using the point counting and linear intercept methods described by Higginson and Sellars (2003). This approach was necessary for quantifying aspects of billet microstructures, which contained coarse α_s within transformed β grains. The coarse nature of this phase made it difficult to distinguish between α_p grains and the coarse α_s using automated image analysis techniques. To measure the volume fraction of α_p using the point counting method, the user counts

n_α the number of points falling in α_p grains,
n_β the number of points falling in transformed β grains (α_s),
$n_{\alpha\beta}$ the number of points where it is uncertain in which type of grain they fall.

A Swift point counter was used for this purpose. The stage which holds the sample was moved a set 'jump' distance and at each jump, the position of the eyepiece crosshair on the microstructure determined which type of point was counted. The jump distance was adjusted so that the crosshair did not fall on the same α_p grain more than once. The volume fraction of α_p was determined from the point counts using the following expression:

$$X_v = \frac{n_\alpha + 0.5 n_{\alpha\beta}}{n_T} \tag{3.1}$$

where X_V is the volume fraction of α_p and n_T is the total number of points counted. The confidence limits were determined using the following expression for the relative error:

$$\left(\frac{\sigma_x}{X_v}\right)^2 = \frac{1 - X_v}{n_\alpha} \tag{3.2}$$

To measure grainsizes using the linear intercept method, the user calculates, $\overline{L}$, the average distance between grain boundaries along lines placed at random on the plane of

polish. To obtain an average over the directions in the plane of polish, a circular line of known length was used. $\overline{L}$ was determined from the following expression

$$\overline{L} = \frac{N}{l} \tag{3.3}$$

Where N is the number of boundaries and l is the length of the circular line.

3.6.3 Scanning Electron Microscopy (SEM)

To study microstructures at higher magnifications, SEM was carried out on polished and etched specimens. The majority of SEM imaging was carried out on a FEI Sirion field emission gun (FEG) SEM microscope operating at 15kV. Use was made of secondary and backscattered electron imaging modes.

3.6.4 Electron Back Scatter Diffraction (EBSD)

Extensive use was made of EBSD. The EBSD technique involves the acquisition and interpretation of Kikuchi patterns from backscattered electrons in an SEM, to provide information on the crystallographic orientation of a small region of a specimen's surface. On the simplest level, EBSD can be used to measure textures by acquiring orientation data from many regions on a specimen's surface. However, the technique is particularly powerful when the orientation and spatial data are combined to provide microtexture maps of a specimen's surface. EBSD was used in both of these ways for three main aspects of this research.

1. Investigating textures and microstructures in the as received billet.
2. Investigating the effect of cooling rate on microstructures via a Jominy end-quench test.
3. Investigating microstructural evolution during thermomechanical processing via plane strain compression tests.

In this third aspect of the work, EBSD analysis was carried out on hot deformed plane strain compression specimens, which had been quenched to room temperature immediately after the test. A standard EBSD analysis on these specimens enables the characterisation of the microtexture of the α_p phase but can only provide limited information about the β phase which existed during high temperature deformation

because this phase transforms on cooling to form an inherited α_s phase. An important part of this work concerns a computer program which has been written to reconstruct the high temperature β phase grain structure from a standard EBSD analysis of the room temperature transformed (α_s) microstructure. The details of this EBSD post-processing are discussed in detail in Chapter 4.

3.6.4.1 Equipment Description

The EBSD analysis was carried out on the same FEI Sirion FEG SEM that was used for conventional SEM imaging. The microscope is equipped with a HKL Technology EBSD analysis system. This system consists of a retractable Nordlys S detector fitted to the vacuum chamber of the microscope and an adjoining system PC, which runs the HKL Channel 5 imaging and acquisition software.

3.6.4.2 General Principles of the EBSD System

The principle components of the EBSD system are shown in Fig. 3.19. For EBSD, the specimen is placed in the specimen chamber of the microscope and then tilted to an angle of 70° from the horizontal. The detector, which is contained in a vacuum tight tube, is then inserted into the SEM chamber via an electric motor. The operating position of the detector is controlled by a handset. When a beam of electrons from the electron gun is directed at an area of interest on a tilted crystalline specimen, a fraction of the electrons are inelastically scattered by the atoms of the specimen, with a small energy loss, to form a divergent source of electrons close to the specimen surface. Some of these electrons are incident on atomic planes at angles which satisfy the Bragg equation

$$n\lambda = 2d\sin\theta \tag{3.4}$$

where n is an integer, λ is the wavelength of the electrons, d is the spacing of the diffracting planes and θ is the angle of incidence. The diffracted electrons form sets of paired large angle cones corresponding to each diffracting plane. Where the diffracted electrons strike the detector, they form a fluorescent pattern on the phosphor screen on the front of the detector. The pattern consists of characteristic Kickuchi bands due to the increased electron intensity between the diffracted cones. The electron back scatter pattern (EBSP) formed on the phosphor screen is characteristic of the crystal structure and the orientation of the crystalline region from which it was generated.

In order to analyse the EBSP pattern, it must be converted into a digital image. The EBSP is digitised using a charge coupled device (CCD) camera positioned behind the

phosphor screen, protected by a lead glass shield. At its highest resolution setting, the entire CCD array is used giving a maximum resolution of 1344x1024.

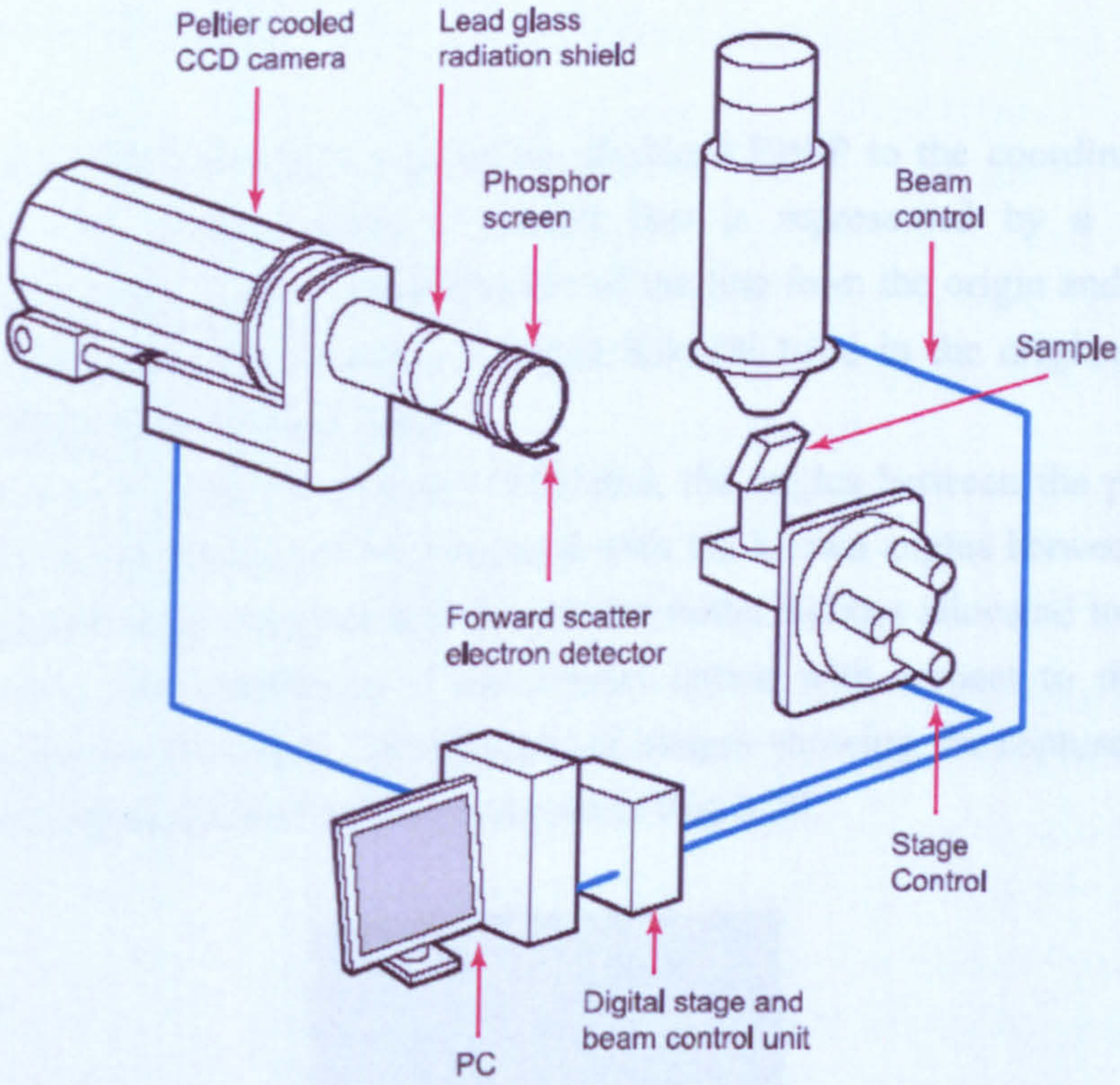

Fig. 3.19 Principle components of an EBSD system (Oxford Instruments, 2004).

Next, the clarity of the EBSP image is improved by two processing steps. The first is known as frame averaging. A single image captured by the CCD camera in a few milliseconds can often appear noisy. The clarity of the EBSP can be improved by capturing more than one frame and averaging them in order to reduce the noise in the image. The second method to improve the image is known as background correction. The Kikuchi bands in the initial image are often quite weak compared to other scattered electrons striking the phosphor and this background intensity varies depending on the position in the image. In order to remove this effect, an image of the background is subtracted (or divided) from the image. The background image is acquired during the set-up of an EBSD acquisition by collecting a CCD image while the microscope is operating in TV mode at a low magnification. Under these operating conditions, no Kikuchi bands are observed because the beam scans rapidly over a large area of the specimen. The result of the background subtraction is a clearer and more evenly illuminated EBSP.

The crystal orientation for the digitised EBSP is found from the positions of the Kikuchi bands. The positions of the bands are found by converting these linear features to single points in Hough space using the Hough transform

$$\rho = x\cos\theta + y\sin\theta \tag{3.5}$$

This transforms the coordinates (x,y) of the digitized EBSP to the coordinates (ρ,θ) in Hough space. In Hough space, a straight line is represented by a single point characterized by ρ, the perpendicular distance of the line from the origin and θ, the angle that the line makes with the x-axis. A bright Kikuchi band in the original EBSP will result in a bright point in Hough space.

When the EBSD system is properly calibrated, the angles between the planes which produced the Kikuchi bands can be compared with the known angles between planes for the crystal system being analysed and the correct miller indices allocated to each plane. In the final step, the orientation of the crystal lattice with respect to the specimen coordinate system is calculated. A sequence of images showing the capture, processing and analysis of a typical EBSP pattern is shown in Fig. 3.20.

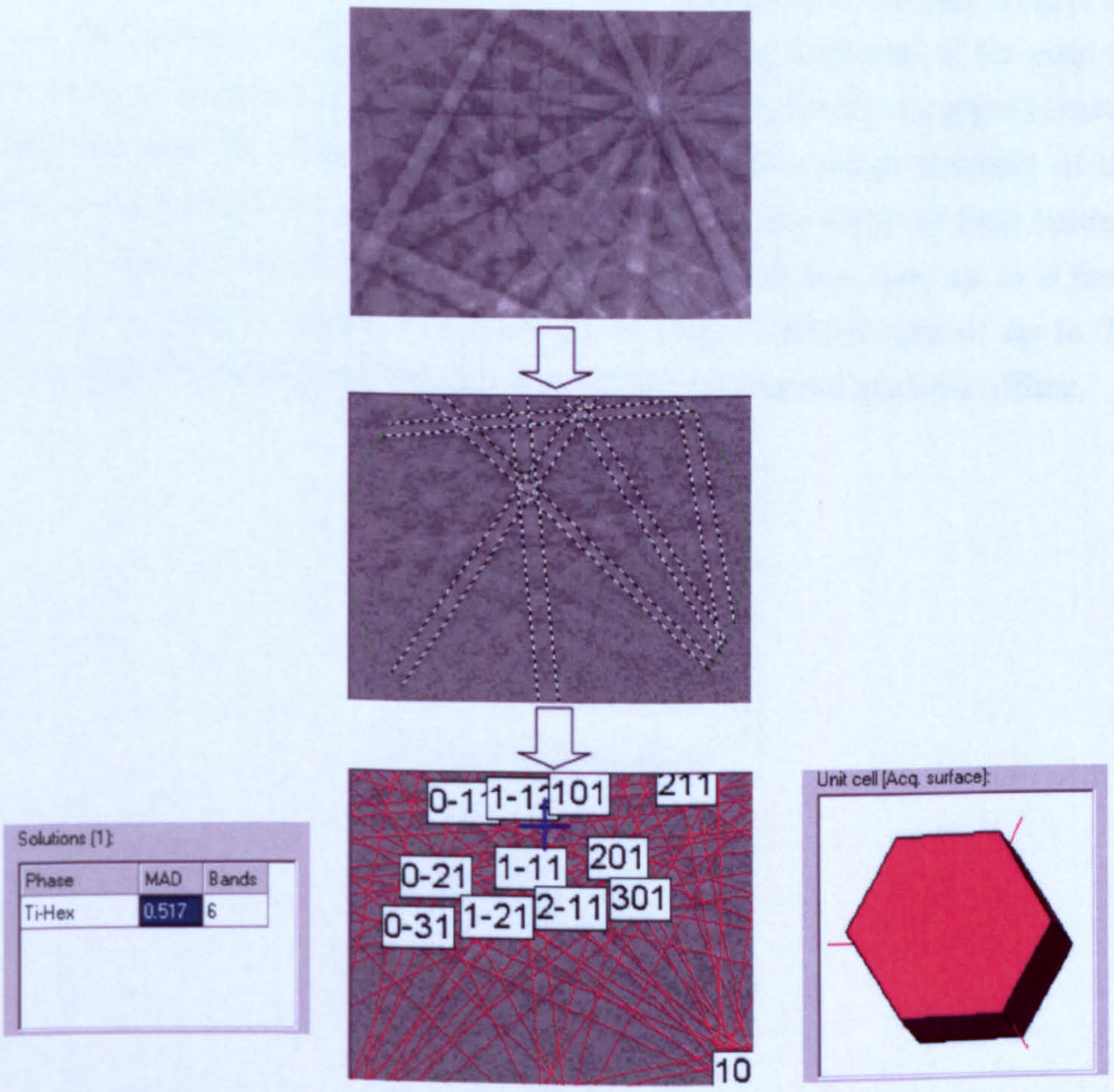

Fig. 3.20 The capture, processing and analysis of an EBSP.

The process of acquiring and then analyzing a single EBSP is typically of the order of a few milliseconds. This equates to tens of thousands of measurements per hour of analysis; thus by scanning the beam in a grid across the surface of a specimen, within a few hours a detailed microtexture map can be acquired. These beam scans, termed 'jobs', are set-up to run automatically using the Channel 5 acquisition program, enabling large maps to be acquired over many hours or even days. The maps acquired by scanning the beam are limited to a size of approximately 300x300μm on the specimen surface. For acquiring maps over larger areas, a series of overlapping beam jobs can be collected by moving the specimen stage by a controlled amount between each beam job. The individual maps can be joined together afterwards using a special offline 'mapstitcher' program, which is part of the Channel 5 suite of applications.

3.6.4.3 Typical Parameters for EBSD Analyses

The steps in planning and conducting a typical EBSD analysis are shown in Fig. 3.21. Prior knowledge of the microstructure gained through optical microscopy and prior knowledge of EBSD acquisition rates for the material in question are helpful in planning the analysis. The user must consider the required resolution of the map to give sufficient detail for the features of interest (e.g. grains) and the required area of the map to ensure that the information acquired is representative. This will dictate the approximate number of points that must be collected for the analysis. With a rough estimate of the likely acquisition rate for a given material, the user can choose the length of time needed for the experiment. EBSD runs are usually in the form of short day runs up to 6 hours long, overnight runs of up 16 hours long, through to long weekend runs of up to 70 hours. When the analysis is complete, the data is saved for subsequent analysis offline.

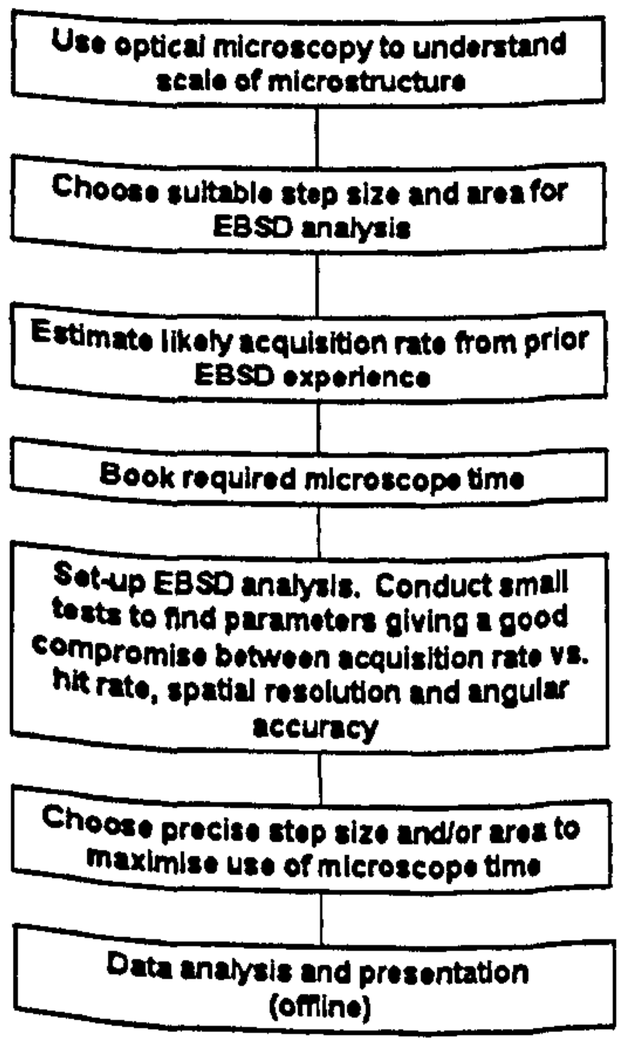

Fig. 3.21 Planning a typical EBSD experiment.

In the set-up stage, there are a number of parameters that the user must adjust in order to optimise the EBSD acquisition. By adjusting these parameters, the user aims to create a set-up that results in an acceptable hit rate (i.e. the percentage of patterns successfully solved), an acceptable angular accuracy (i.e. precision of the orientation measurements) and acceptable spatial resolution, whilst at the same time maintaining an acquisition rate that is high enough to collect the required data in the time available. The most important parameters and considerations are explained in Table 3.6 and some typical values that gave good results for the EBSD analysis of titanium alloys in this work are given.

Table 3.6 Effect of EBSD parameters and typical conditions used.

	Parameter	Comments	Typical Value
Specimen	Material	The backscattered electron signal and pattern quality increases with the atomic number (z) of the material (Humphreys, 2001). There is also an improvement in spatial resolution with increasing z.	Ti
	Condition / microstructure	Defects such as dislocations can cause the patterns to lose sharpness, therefore well annealed materials achieve higher hit rates, acquisition rates and angular accuracy. If the interaction volume of the beam contains a defect such as a grain boundary, the resulting EBSP may be diffuse or the product of two overlapping patterns from neighbouring grains, resulting in a zero or misindexed point. Therefore very fine grained microstructures will have decreased hit rates.	Coarse, well recovered (e.g. billet) through to very fine transformed microstructures resulting from water quenching.
	Specimen preparation	The metallographic preparation of the specimen is critical for producing good quality EBSPs. The pattern quality will be poor if mechanical damage from grinding, surface films or contamination is present. Good specimen preparation results in improved hit rate, angular accuracy and acquisition rate.	The specimens were carefully prepared for EBSD using the techniques outlined in 3.6.1. Where possible, specimens were prepared on the same day as the EBSD experiment as this was found to give noticeable improvements.

Microscope	Operating voltage	Increasing the accelerating voltage decreases the band width and increases contrast and sharpness in the patterns. This increases acquisition rates, hit rates and angular accuracy. However, spatial resolution is reduced at large voltages due to the larger interaction volume. Spatial resolution is also reduced at low voltages as pattern quality deteriorates. In practice voltages between 5 and 20kV are common for a FEGSEM EBSD system.	15kV
	Spot size	The spot size has a large effect on the spatial resolution of the EBSD system. If a specimen produces weak patterns, a larger spot size may improve the patterns. In practice, the smallest spot size consistent with acquiring solvable patterns should be selected (Rolland *et al.* 2002).	3
	Probe current	The probe current was not varied directly in this work although it changes with the spot size. Increasing the probe current can increase pattern quality and the intensity of the EBSP signal resulting in higher acquisition rates, higher hit rates and higher angular accuracy. However, at large probe currents, the spatial resolution decreases as a result of beam spread in the specimen due to the large beam size (Humphreys, 2001). Humphreys (2001) obtained an optimum spatial resolution for a FEGSEM EBSD system with a probe current of around 10nA.	Not varied directly
	Working distance	In this work, the working distance was always adjusted to achieve a focused beam at a working distance of 14mm. This working distance gave a good EBSP signal for the given detector position and specimen tilt.	14mm
	Magnification	This has no effect on acquisition rate but governs the area of the specimen that can be scanned using beam shift i.e. without moving the specimen stage. If the beam is shifted too far there may be a decrease in the hit rate and angular accuracy at the edges of the scanned area.	200x The size of the scanned area was limited to a maximum of ~300x300μm

	Microscope beam and imaging controls	It is important that the microscope is always corrected for gun tilt, lens alignment, astigmatism and is correctly focused. This will result in better patterns and optimises spatial resolution. The image, focusing and stage controls are automatically corrected for the specimen tilt.	Optimised
CCD Camera	Camera gain	Choose from high or low gain settings. High gain increases the sensitivity of the camera enabling a lower timing per frame. However, this may introduce more noise. Both settings should be tried to determine which one is best for a given material.	High
	Pixel binning	The camera has a high resolution, which enables high quality EBSPs to be collected. This is useful for phase identification or when high angular accuracy is paramount. However, by clustering together groups of pixels, it is possible to collect lower resolution EBSPs, which increases the acquisition rate at the expense of angular accuracy. The user can choose binning levels from: none, 2x2, 4x4, 8x8 and 8x8-superfast.	8x8
EBSP Enhancement	Timing per frame	This is the time in milliseconds used to acquire a frame. Lower timing results in a higher acquisition rate but in practise, this value should be adjusted to achieve an EBSP with the correct brightness. The EBSP should be neither too dark nor should it contain any saturated (white) areas in the image.	10-20ms
	Frame averaging	Increasing the number of frames increases the clarity of the pattern. This will increase the hit rate and angular accuracy at the expense of the acquisition rate.	3-10
Band Detection	Band centres vs. edges	The program can detect the centres or the edge of the Kikuchi bands. Selecting band centres can increase the acquisition rate at the expense of angular accuracy but indexing may be less reliable. Band centres can sometimes improve performance for specimens with narrow bands (high kV) or blurred bands (highly deformed or poorly prepared specimens).	Band edges

	Min/max number of bands	This changes the number of bands detected in the EBSP. Increasing these values can increase the reliability of indexing at the expense of acquisition rate but it may also decrease the hit rate.	4/6
	Hough resolution	This determines the resolution of the image when it is converted into Hough space. Typical resolutions vary from 40 to 60. A lower resolution increases the acquisition rate at the expense of angular accuracy.	60
	Calibration of projection parameters	During set-up, a standard calibration file is selected for the approximate accelerating voltage, spot size and working distance being used. This calibration is then further refined using the software. 3 projection parameters (working distance, detector distance and pattern centre), which reflect the exact EBSD geometry for the current set-up are adjusted in order to obtain a good fit between the EBSP and the simulated EBSP for the solved pattern. This calibration is then repeated for several good quality EBSPs and an average obtained. A good calibration increases angular accuracy, hit rate and acquisition rate and reduces misindexing.	Refined using calibration averaging
Acquisition	Step size	The step size is selected to acquire information on the area of interest in sufficient detail.	0.15-10μm
	Acquisition rate	A particular set-up for a given specimen results in an acquisition rate measured in points per second.	Up to 12 p/s

3.6.4.4 Presentation of EBSD Maps

The analysis and presentation of EBSD data was carried out offline using the Channel 5 suite of applications. Maps were generated and displayed using the HKL Tango application. Four main types of map are used in this work. In some cases, these types can be superimposed on a single map.

Band contrast

Band contrast maps are grey scale images which give a measure of the pattern quality for all the points in a map. A lighter shade of grey indicates a higher band contrast value and hence better EBSP quality. All points have a band contrast value even if they have not

been successfully indexed. The band contrast is influenced by a number of factors including local crystalline perfection, sample preparation, surface contamination and the phase and orientation being analysed. The band contrast map often resembles an etched micrograph, revealing features such as grains, grain boundaries and surface scratches. An example of a band contrast map is shown in Fig. 3.22.

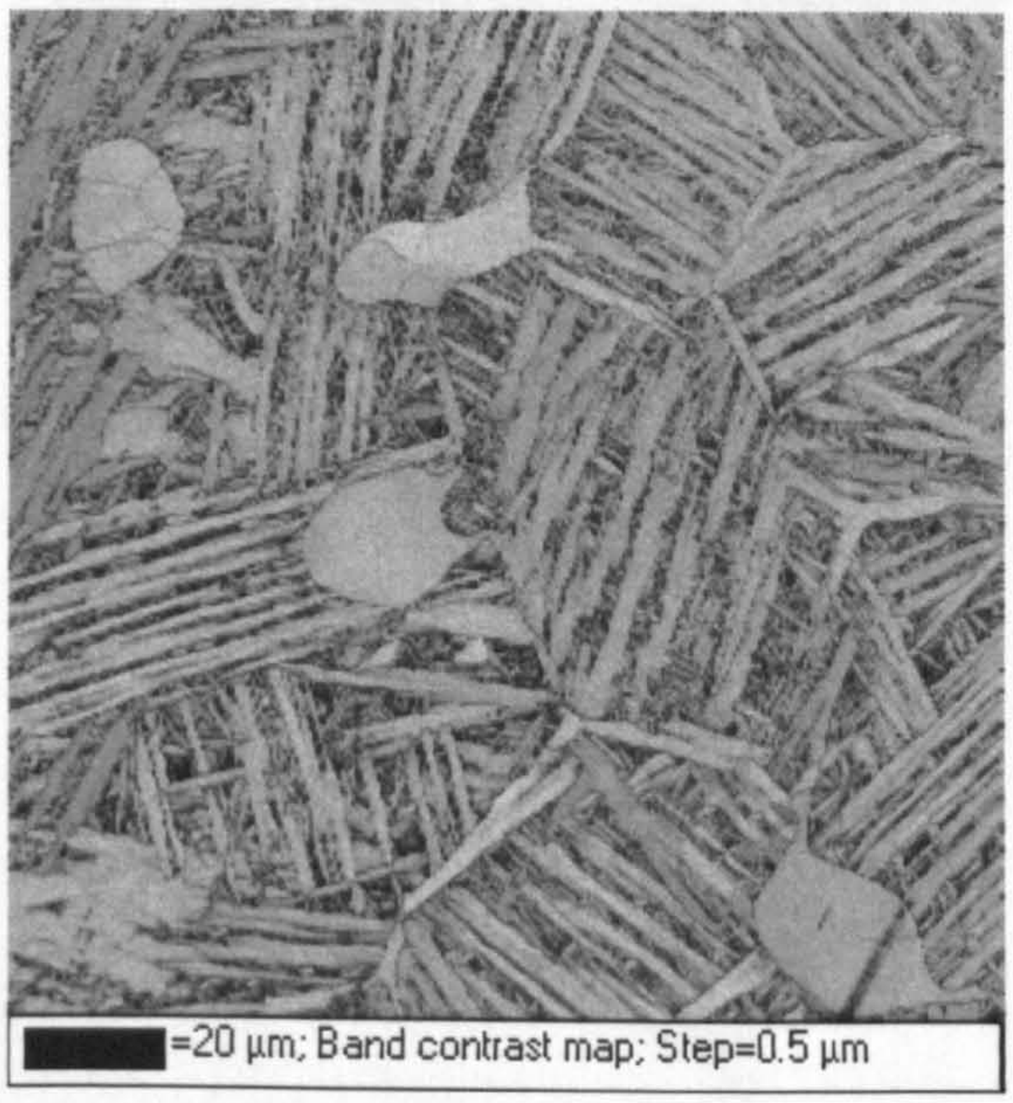

Fig. 3.22 Band contrast colouring.

Inverse pole figure (IPF) colouring

This colouring scheme enables crystallographic orientations to be quickly interpreted with respect to the specimen coordinate system. An example is shown in Fig. 3.23. The colours are assigned to each point using the colour key shown. In this work, unless stated otherwise, the colours indicate which crystallographic plane is parallel to the surface of the map/specimen i.e. a red colour indicates a basal (0002) plane parallel to the map/specimen surface. IPF colouring does not completely describe the orientation because it does not indicate the rotation of the plane about the normal to the map/specimen surface. For instance, two neighbouring pixels with the same plane parallel to the specimen surface but rotated about the normal to the surface by an angle x, would be assigned the same colour.

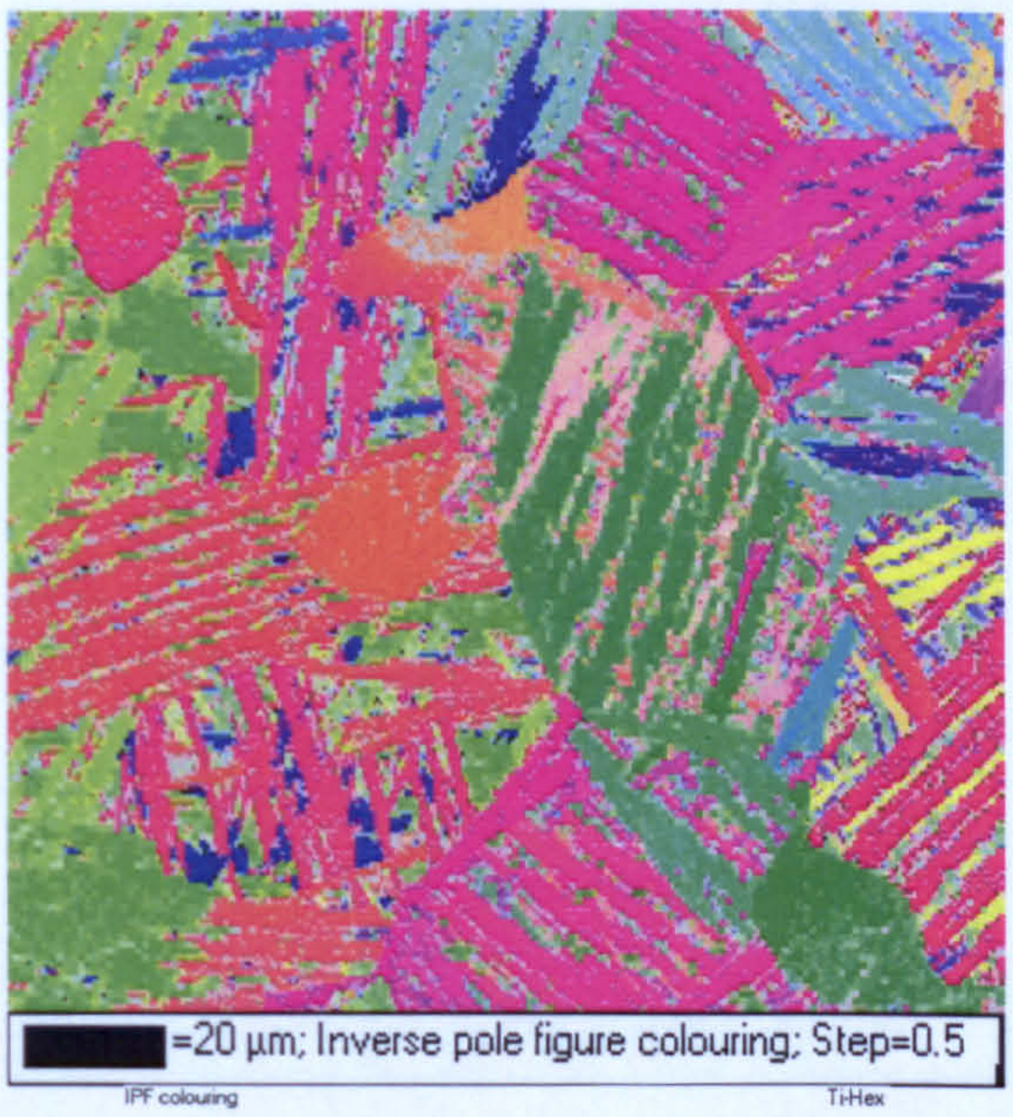

Fig. 3.23 Inverse pole figure (IPF) colouring with non indexed points coloured grey.

Euler colouring

Unlike IPF colouring, this colouring scheme displays a unique colour for each crystallographic orientation. However, the crystallographic orientations cannot be interpreted as easily from the colours. An example of Euler colouring is shown in Fig. 3.24. The colours are formed from red, blue and green values determined by the values of the three Euler angles, as shown in the map key. Because of the way that Euler angles are defined, they have wrap-around problems near their limits. This can produce sudden changes of colour that do not correspond to large changes in orientation. An example of this wrap around effect can be seen in the α_p grain indicated by an arrow in Fig. 3.24, where the colour changes from orange to pink.

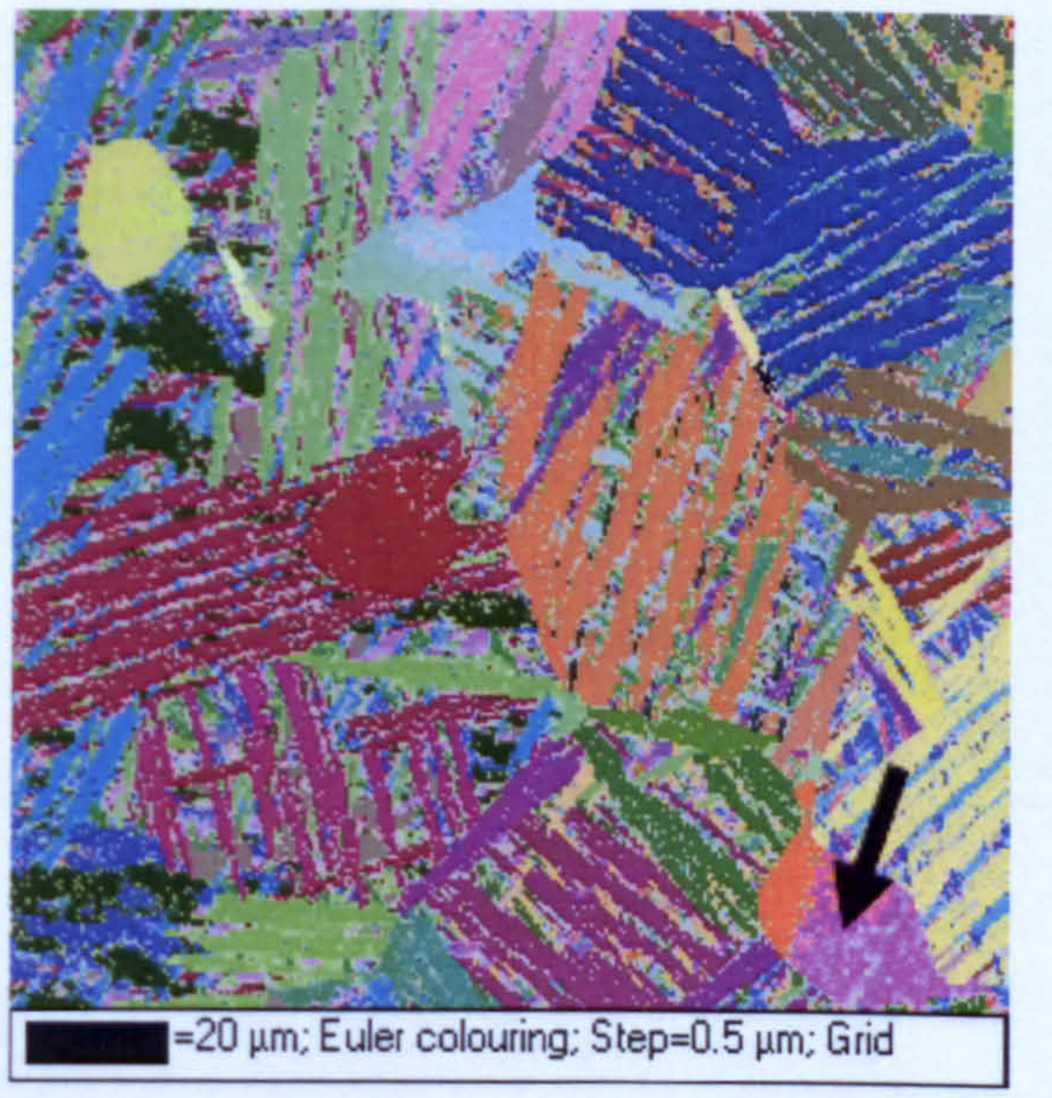

Fig. 3.24 Euler colouring with non indexed points coloured grey.

Misorientation maps

This colouring scheme colours the points based on the misorientation with neighbouring points according to a user defined colour scheme. An example is shown in Fig. 3.25, where misorientations between 2° and 15° are coloured grey and misorientations greater than 15° are coloured black. This type of map is useful for displaying grain boundaries based on the misorientation angle. The misorientations used are always for the lowest possible angular rotation for a given misorientation, which is also referred to as the disorientation angle.

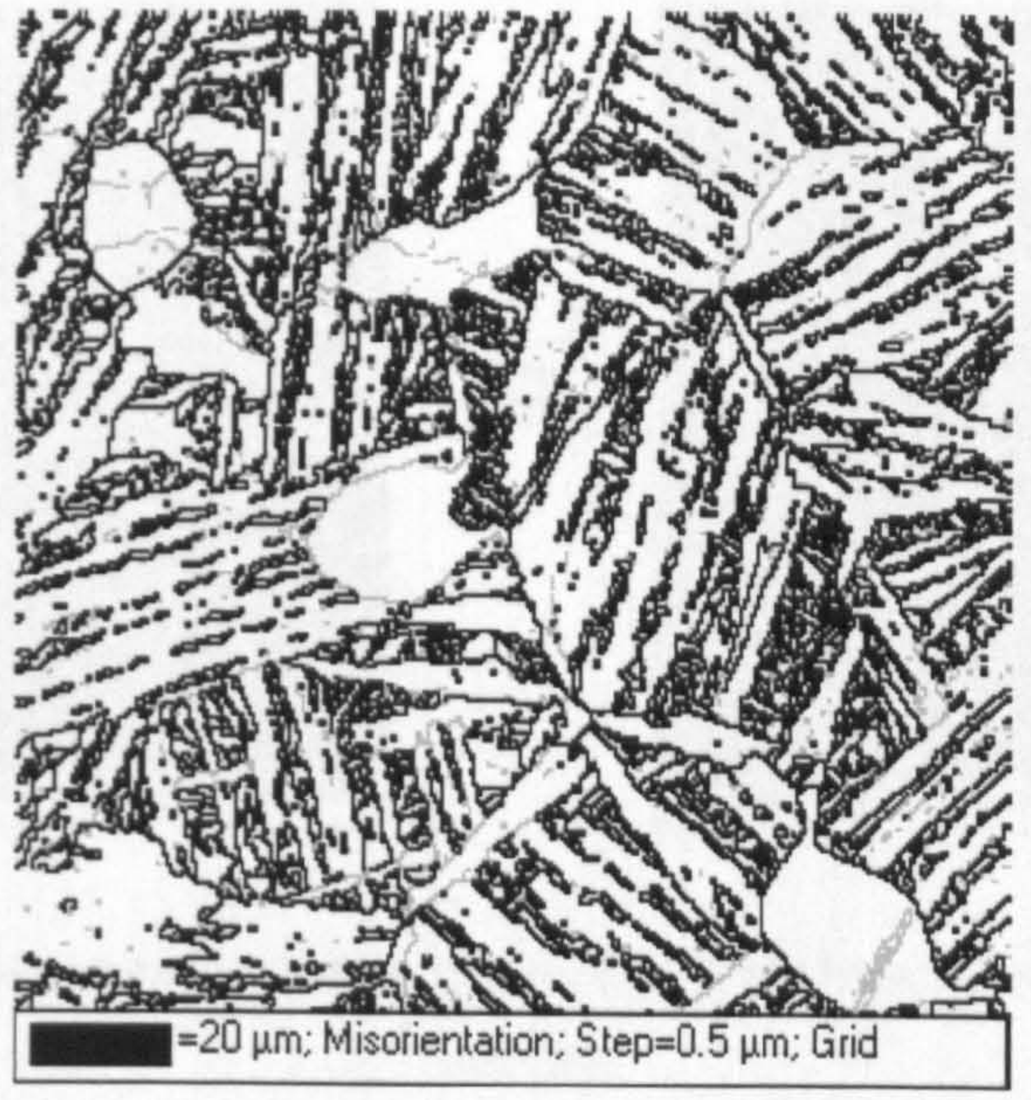

Fig. 3.25 Misorientation map with high angle grain boundaries coloured black and low angle boundaries coloured grey.

3.6.4.5 Noise Reduction

The noise reduction tools that are provided in the Tango program were used to clean maps by removing isolated misindexed points (wildspikes) and extrapolating data into areas which were not indexed. Normally, the wild spikes were removed first, followed by a medium level of zero solution extrapolation, which was repeated as necessary. Noise reduction should be used with caution because large regions of zero solutions can indicate the presence of unknown phases or contamination. In the results, the raw uncleaned data is always presented in addition to any maps which have been noise reduced. Fig. 3.26 shows the effect of complete noise reduction on an EBSD map.

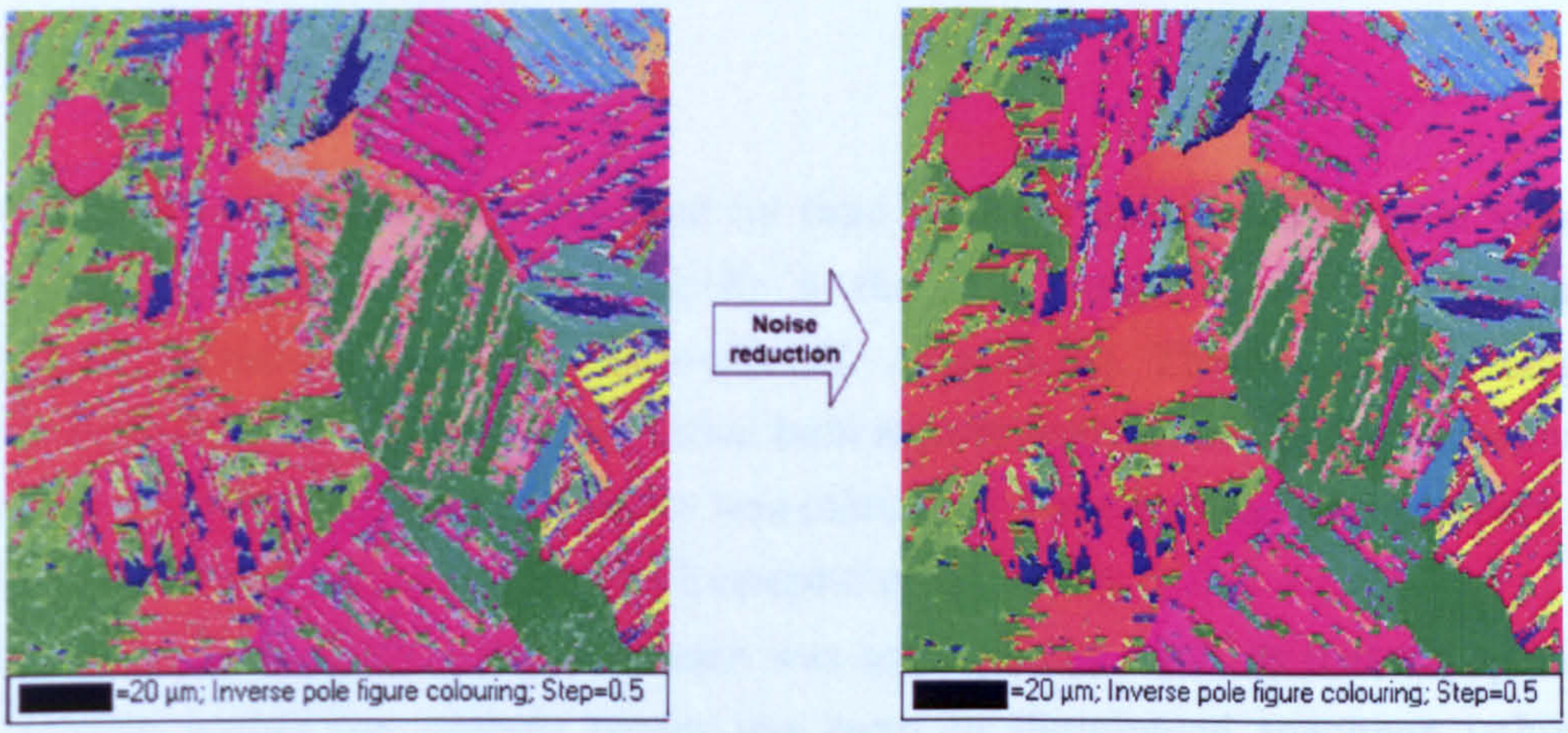

Fig. 3.26 The effect of complete noise reduction on an EBSD map which contained 17% zero solutions.

3.6.4.6 Presentation of Textures Determined by EBSD

Pole figures were generated and displayed using the HKL Mambo application. For textures in the α phase, two pole figures $\{0002\}$ and either $\{10\bar{1}0\}$ or $\{11\bar{2}0\}$ are used to present EBSD data. An accompanying key gives details of the projection method used. Unless stated otherwise, stereographic projections were used. Contouring was applied to the pole figures to show the strength of the clustering of poles, relative to that for a random distribution, i.e. in terms of multiples of random distribution (m.r.d.). Fig 3.27 shows pole figure data for the EBSD map used as an example in section 3.6.4.4.

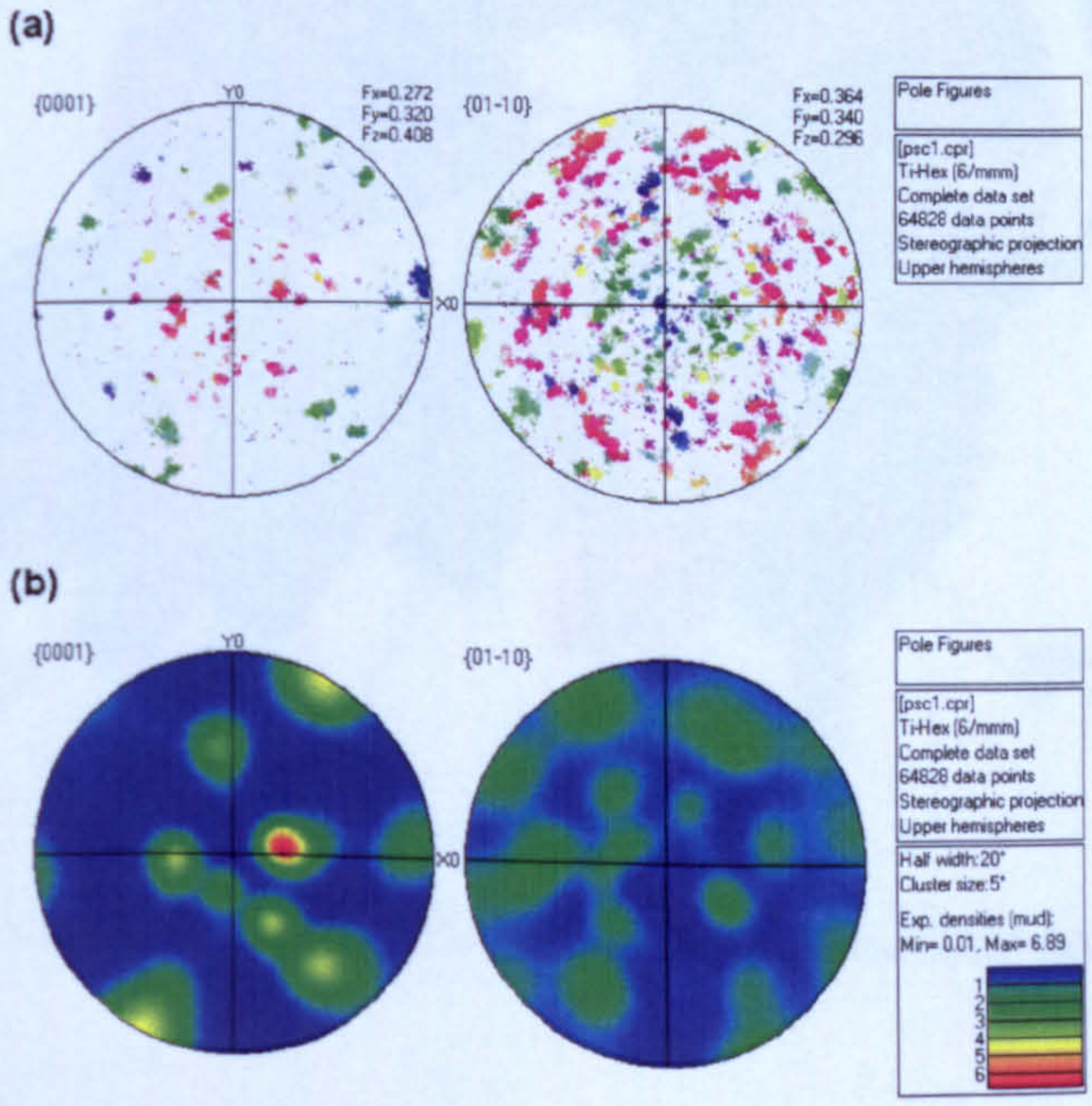

Fig. 3.27 (a) Pole figures for the EBSD map shown in section 3.6.4.4 using the IPF colouring key for each point. (b) Contouring applied to show clustering of poles relative to a uniform density.

3.6.5 Neutron Texture Analysis

Textures for the α phase were analysed by time of flight neutron diffraction using the General Materials Diffractometer (GEM) at the ISIS pulsed neutron source at the Rutherford Appleton Laboratory, Harwell, UK (Fig. 3.28). The detector coverage on GEM is sufficiently high that a quantitative bulk texture analysis can be performed with a single specimen orientation. The texture was calculated from the time of flight data using the MAUD Rietveld analysis software (Lutterotti *et* al., 1999).

The size of the incoming neutron beam was set at 20x20 mm^2, so that the specimens were entirely within the neutron beam; this gave an illuminated specimen volume of 1800 mm^3. Data were collected for 20 minutes per specimen. The data were normalised to the incident neutron flux distribution, corrected for detector efficiencies, and converted into 164 d-spacing patterns for each specimen corresponding to the texture detector grouping. 164 diffraction patterns were simultaneously Rietveld fitted in MAUD. Values of the ODF cells were extracted using the extended WIMV (E-WIMV) algorithm in the MAUD software. Reconstructed pole figures for the texture data were plotted using MAUD.

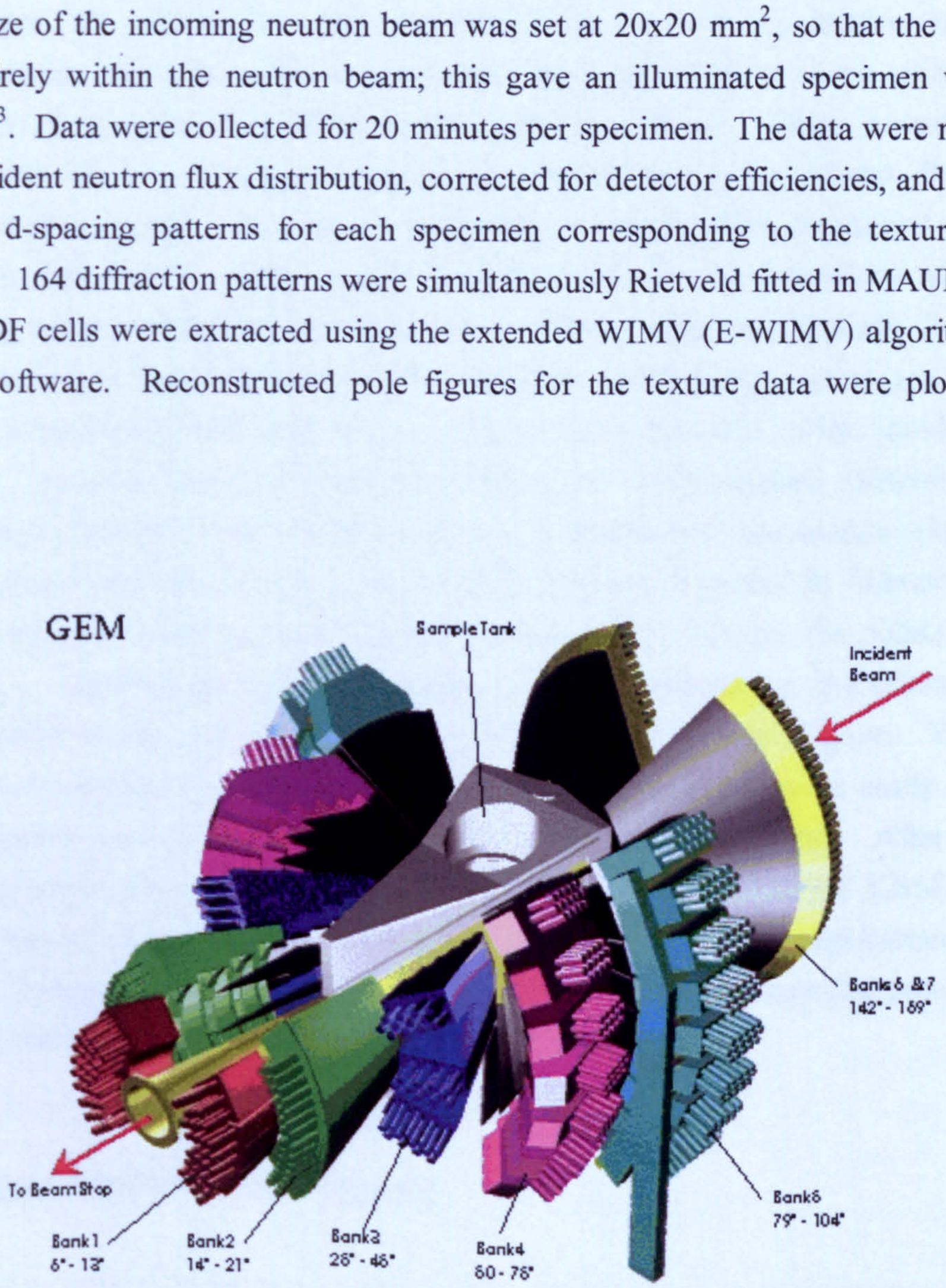

Fig. 3.28 A schematic layout of the detector banks of the GEM detector array.

4 EBSD POST-PROCESSING

4.1 Introduction

This chapter concerns work that was carried out to enable the post-processing of EBSD data in order to gain additional information that is not provided for in the standard software provided by HKL Technology. Three main post-processing procedures were developed: a Kuwahara type filter for the hexagonal phase for reducing orientation noise, a technique for identifying and separating the α_p and α_s phases in bimodal microstructures, and a technique to reconstruct the β microtexture which existed at high temperature from a standard EBSD analysis of the α_s phase. These procedures were incorporated into a standalone application written using the Visual Basic .NET programming language. As well as performing the three tasks mentioned above, the application can display various types of EBSD map, so that the effects of the post-processing can be visualised and understood. These map types include Euler maps, misorientation (i.e. grain boundary) maps and band contrast maps, which are commonly used for presenting EBSD data and as such are also available in the standard EBSD software. Two additional map types not provided for in the standard software were also developed as a better means of displaying misorientation and substructure within grains. One of these is termed 'relative Euler contrast' and was proposed by Humphreys *et al.* (2001), while the other, termed 'relative disorientation', colours the points in a map according to the disorientation from either a specific orientation, the orientation of a selected point on the map, or the average orientation of a selected grain. The smaller changes in orientation revealed by these additional map types are more easily seen when the orientation noise is reduced through use of the Kuwahara filter. After any post-processing steps using the application, the user can save the modified EBSD data in a form that can be viewed and presented using the standard suite of applications provided by HKL Technology. In the following chapter, these post-processing procedures are described and demonstrated.

4.2 General Aspects of the Program

Visual Basic .NET (VB.NET) is a fully object orientated computer language. Programs written in VB.NET are implemented on the Microsoft .NET framework. The post-processing application created in this work is a standalone executable application for Windows. The application can work with one EBSD dataset at any one time and has a multiple document interface (MDI) similar to many Windows applications, in which

windows for the different maps created reside under a single parent window. The map windows can be maximised, tiled or cascaded from a 'Window' menu (Fig. 4.1).

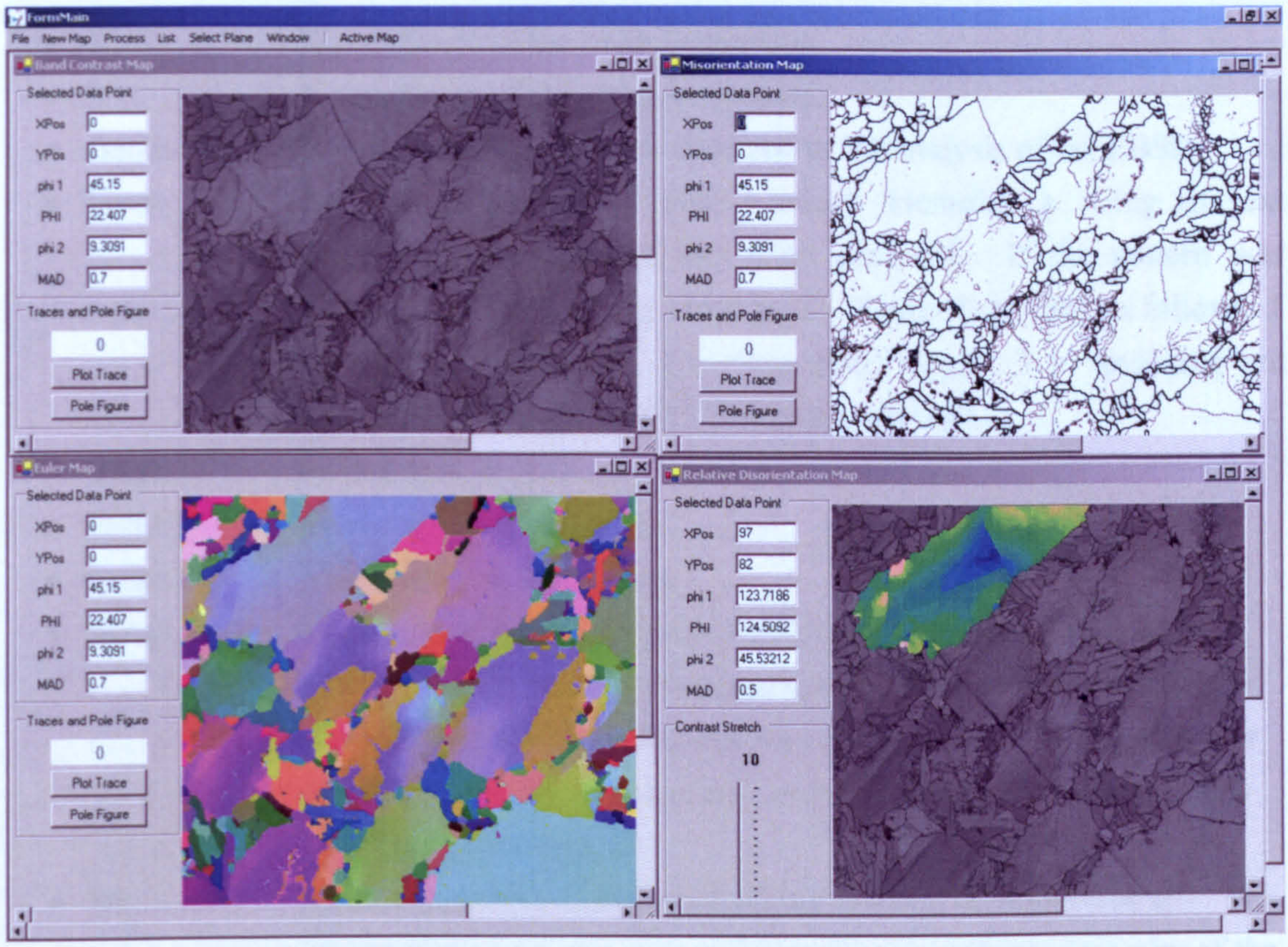

Fig. 4.1 A screenshot from the EBSD post-processing program with four different windows displaying different types of map for an EBSD dataset.

The application works with EBSD datasets acquired using HKL Technology EBSD systems. This data must be converted into a text file format using the HKL software before it can be opened in the application. The application saves processed data in this same text file format. To open these files again in the HKL software, the text files can be easily converted back to the standard HKL file format. An example of the text file format is shown in Fig. 4.2. The first 16 lines of the file contain general information about the EBSD analysis including: the number of data points analysed in the X and Y directions, the step size between each point, microscope settings and a line of information on the crystallography of each phase that was selected for the EBSD analysis. The remainder of the file is comprised of a line for each data point. Each line gives the following information:

- Phase — An integer identifying which of the selected phases the point was indexed as. If the point was not successfully indexed, this number is 0.
- X — X coordinate of the point in microns.
- Y — Y coordinate of the point in microns.
- Bands — Number of Kikuchi bands detected in the analysis of the EBSP.
- Error — An integer between 0 and 5 which identifies a string of text describing the status of the point analysed. If the pattern was successfully indexed, the error is '0'. Errors 1 to 5 are as follows: 1 = "low band contrast", 2 = "low band slope", 3 = "indexing not possible", 4 = "high MAD", 5 = "not analysed".
- Euler 1 — Euler angle, ϕ_1, in degrees.
- Euler 2 — Euler angle, Φ, in degrees.
- Euler 3 — Euler angle, ϕ_2, in degrees.
- MAD — The Mean Angular Deviation (MAD) is a measure of how well positions of the bands in the simulated EBSP match those in the actual EBSP. Given in degrees, the MAD gives the average angular misfit between the detected and simulated bands. A number below 1° is usually acceptable.
- BC — Band contrast is a measure of pattern quality. It is given as an integer between 0 and 255, and describes the average intensity of the bands with respect to the average intensity over the whole EBSP. The higher the number, the better the quality.
- BS — Band slope is also a measure of pattern quality. It is given as an integer between 0 and 255, and describes the maximum intensity gradient (i.e. sharpness) at the edges of the Kikuchi bands. The higher the number, the sharper the bands. If the EBSD analysis was configured to detect band centres as opposed to band edges, the band slope is not calculated and will be 0 by default.

```
Channel Text File
Prj     D:\My Documents\EBSD\programming\a7microclean.cpr
Author  [unknown]
JobMode Grid
XCells  600
YCells  600
XStep   0.3
YStep   0.3
AcqE1   0
AcqE2   0
AcqE3   0
Euler angles refer to Sample Coordinate system (CS0)!  Mag     400     Coverage        100     Device  0       KV      15      TiltAngle
Phases  2
2.954;2.954;4.729       90;90;120       Ti-Hex  9       0       3803863129_5.0.6.3      -2037178527     [Titanhex v3.cry]
3.192;3.192;3.192       90;90;90        Titanium cubic  11      229     3803863129_5.0.6.3      -1973751222     technique de l'ingenieur
Phase   X       Y       Bands   Error   Euler1  Euler2  Euler3  MAD     BC      BS
1       0.0000  0.0000  6       0       41.450  23.201  13.104  0.7000  73      0
1       0.3000  0.0000  0       3       44.340  22.265  9.5174  0.7000  80      0
1       0.6000  0.0000  6       0       43.204  23.745  11.744  0.6000  79      0
1       0.9000  0.0000  6       0       43.204  23.745  11.744  0.6000  82      0
1       1.2000  0.0000  6       0       32.069  31.793  24.350  0.5000  131     0
1       1.5000  0.0000  6       0       31.916  31.597  25.045  0.6000  130     0
1       1.8000  0.0000  6       0       32.705  31.511  24.276  0.4000  130     0
```

Fig. 4.2 The Channel Text File (*.ctf) format.

When an EBSD file is opened in the post-processing application, the general information contained in the first 16 lines is extracted and placed into an instance of a specially created class called EBSD_Data_Info. The information for each point is similarly extracted and placed into an instance of a specially created class called EBSD_Data_File(,). The EBSD_Data_File(,) is a two dimensional array, where the elements in the array correspond to the x,y coordinate of each data point. For each element, the values of all the variables for the corresponding data point in the channel text file are stored. In addition, the four Euler symmetric parameters for the quaternion descriptor of the orientation are calculated and stored to enable rapid averaging of orientations.

Many programming steps used to process and display the EBSD data require routine calculations and conversions between descriptors of orientation. Thus, for ease of programming, the program has a module containing various sub-routines for many of these frequently used calculations. These include:

matrix_mult	multiplies 2 orientation matrices
inverse_matrix	calculates the inverse of an orientation matrix
euler_to_matrix	calculates the matrix from Euler angles
matrix_to euler	calculates the Euler angles from a matrix.
hex_symm_mult	pre-multiplies a matrix by one of the 12 hexagonal symmetry operators in matrix form
cub_symm_mult	pre-multiplies a matrix by one of the 24 cubic symmetry operators in matrix form
quaternion_mult	calculates the product of 2 quaternions
inverse_quaternion	calculates the inverse of a quaternion
euler_to_quaternion	calculates the quaternion from Euler angles
quaternion_to_euler	calculates the Euler angles from a quaternion
quaternion_to_matrix	calculates the matrix from a quaternion
matrix_to_quaternion	calculates the quaternion from a matrix
quat_hex_symm_mult	post-multiplies a quaternion by one of the 12 hexagonal symmetry operators in quaternion form
quat_cub_symm_mult	post-multiplies a quaternion by one of the 24 cubic symmetry operators in quaternion form

4.3 The Kuwahara Filter

A Kuwahara filter for orientation averaging the hexagonal phase was incorporated into the program as a means of reducing the orientation noise in EBSD datasets. The filter

was based on the method described by Humphreys *et al.* (2001), which was described in the literature review. The smoothing strategy used an array of 5x5 points surrounding the point in question. This array was in turn divided into eight blocks of 3x3 as illustrated in Fig. 4.3. The central point was assigned the average of the 3x3 block having the least variance. Additionally, a cut off was incorporated whereby the averaging procedure was aborted if the 3x3 block with least variance contained a pixel misorientated from the central pixel by more than a chosen minimum value, which was typically set at 3°. This cut off prevents erroneous orientations being introduced when the averaging incorporates pixels from more than one grain, which can sometimes occur near grain boundary triple points. The averaging procedure was adjusted at the edge of the map, such that if the point to be smoothed lay within 2 pixels of the edge, the number of sub regions was reduced to those which still lay entirely within the map.

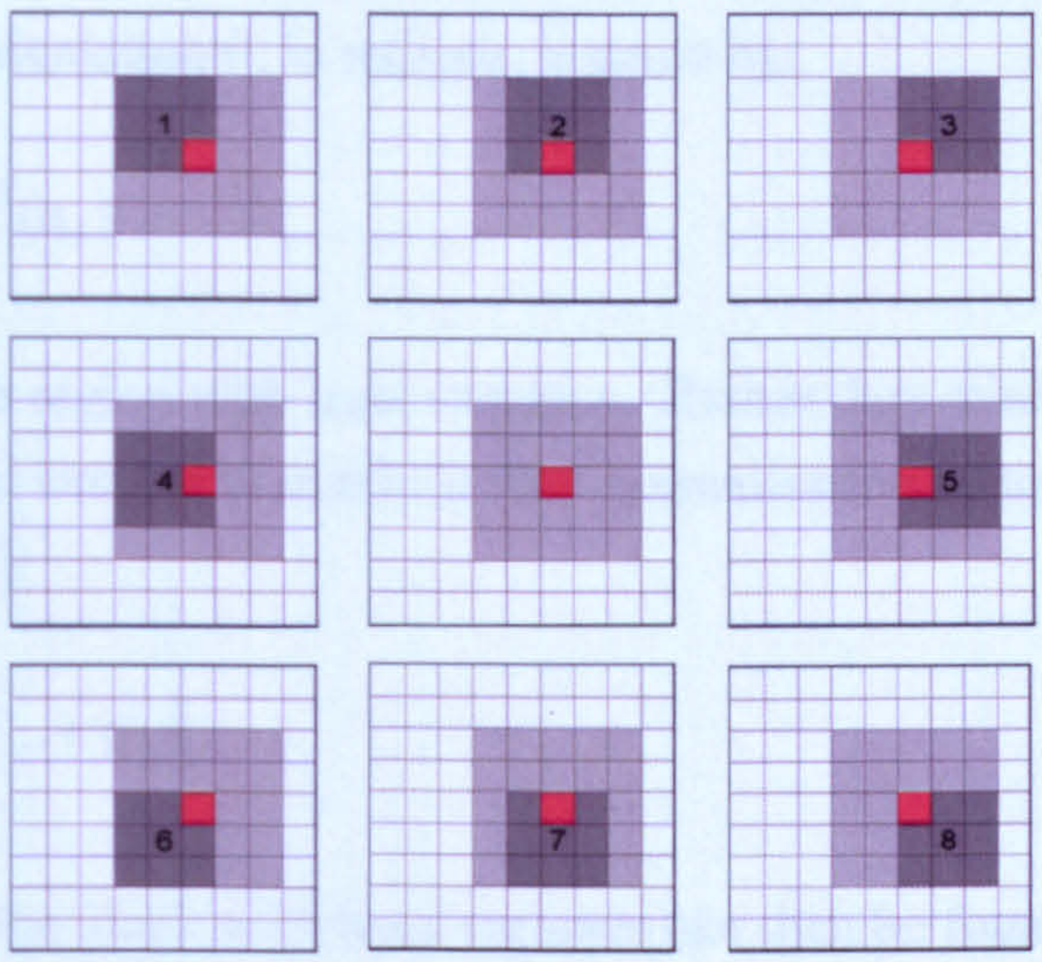

Fig. 4.3 The Kuwahara smoothing strategy using a 5x5 array containing 8 3x3 sub regions. The red point is assigned the average orientation of the 3x3 sub region with least variance.

All of the calculations in the code for the Kuwahara filter were performed using the Quaternion descriptor for orientation. For each point, prior to averaging, the orientations in the 5x5 array were transformed so that they lay within the *fundamental zone* in orientation space and so that the central point (i.e the point being averaged) was at the centre of this delimited zone. This accounts for the symmetry and "Umklapp" effects discussed in the literature review. The steps required to perform this transformation and the subsequent least variance and averaging calculation using quaternions are as follows:

1) Populate the 5x5 array of orientations surrounding the central point to be averaged.

2) Calculate the inverse of the central point using the "inverse_quaternion" sub-routine. This is now the "umklapp" rotation.

3) Premultiply each quaternion orientation in the array by the "Umklapp" rotation to turn the data towards the centre of the reduced zones in Euler space using the "quaternion_mult" sub-routine.

4) Post multiply the resulting quaternion from step 3 by each of the quaternion symmetry operators using the "quat_hex_sym_mult" sub-routine to generate the full set of crystallographically equivalent rotations.

5) From the set of quaternions generated in step 4, select the one with the smallest misorientation from the central point to select the one which lies in the *fundamental zone*. The misorientation θ, in radians, is given by:

$$\theta = 2\cos^{-1}(q_4) \tag{4.1}$$

6) Find the 3x3 sub region with least variance. Rather than minimising the variance, it is equivalent and simpler to maximise the normalisation factor (i.e. the denominator in equation 2.24):

$$\|q_1 + q_2 + ... + q_N\| \tag{4.2}$$

7) The average of the block with least variance can then be found using equation 2.25, which uses the normalisation factor already found in step 6.

8) Premultiply the average quaternion by the inverse of the "Umklapp" rotation (i.e. the original quaternion for the central point) to reverse the "Umklapp rotation". The result will become the new averaged quaternion for the central point in the filtered EBSD dataset.

9) Ensure the orientations in the filtered EBSD dataset are in the same reduced Euler space used by the EBSD software by calculating the set of crystallographically equivalent orientations for the average and selecting the one which has Euler angles in the range:

$$\phi_1 \leq 180°, \Phi \leq 180°, \phi_2 \leq 60°$$

The orientation noise present in a standard EBSD dataset is shown in Fig. 4.4 and the effect of successive passes of the Kuwahara filter on this orientation noise is shown in Fig. 4.5. The EBSD analysis in this example was performed on a specimen of billet, which had been heated to 1010°C and held at this temperature for 10 minutes to obtain a bimodal microstructure and then rapidly water quenched. The raw EBSD data (82% indexed) is shown using IPF colouring in Fig. 4.4(a). It can be seen that the isolated regions of α_p phase in this microstructure are composed of smaller grains and subgrains. This is apparent through changes in IPF colouring and by the presence of non indexed points along the grain and subgrain boundaries. Further boundaries with lower misorientations can be seen in the band contrast map, where they are revealed as dark lines within the lighter grains due to the poorer pattern quality (Fig. 4.4(b)). The boundaries can be highlighted in a quantitative manner by superimposing a misorientation map (Fig. 4.4(c)) In this map, if neighbouring pixels are misorientated by more than 2° and 15° a pixel is coloured silver and black respectively. The effect of orientation noise for highlighting the low angle boundaries of 2° or more is small. However, if the misorientation of the low angle boundaries is decreased to 0.5° as in Fig. 4.4(d), the boundaries tend to be obscured by the orientation noise.

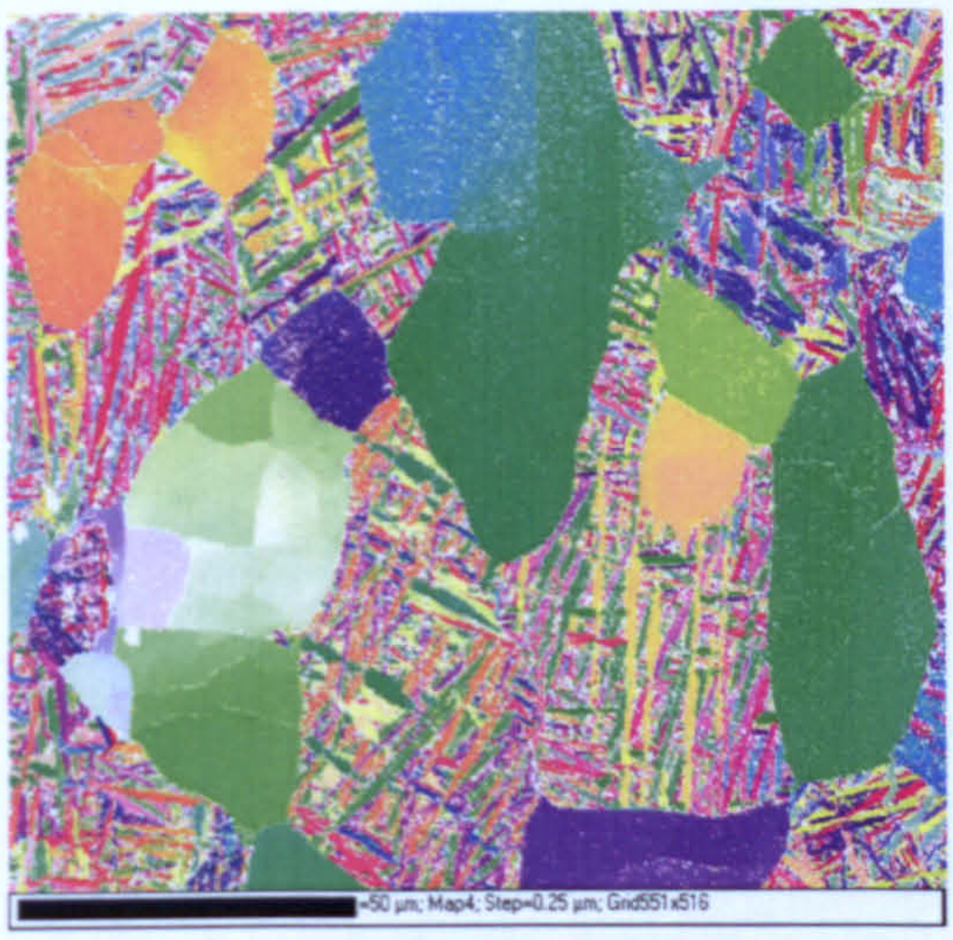

(a) IPF colouring, non indexed points shown in white.

(b) Band contrast map.

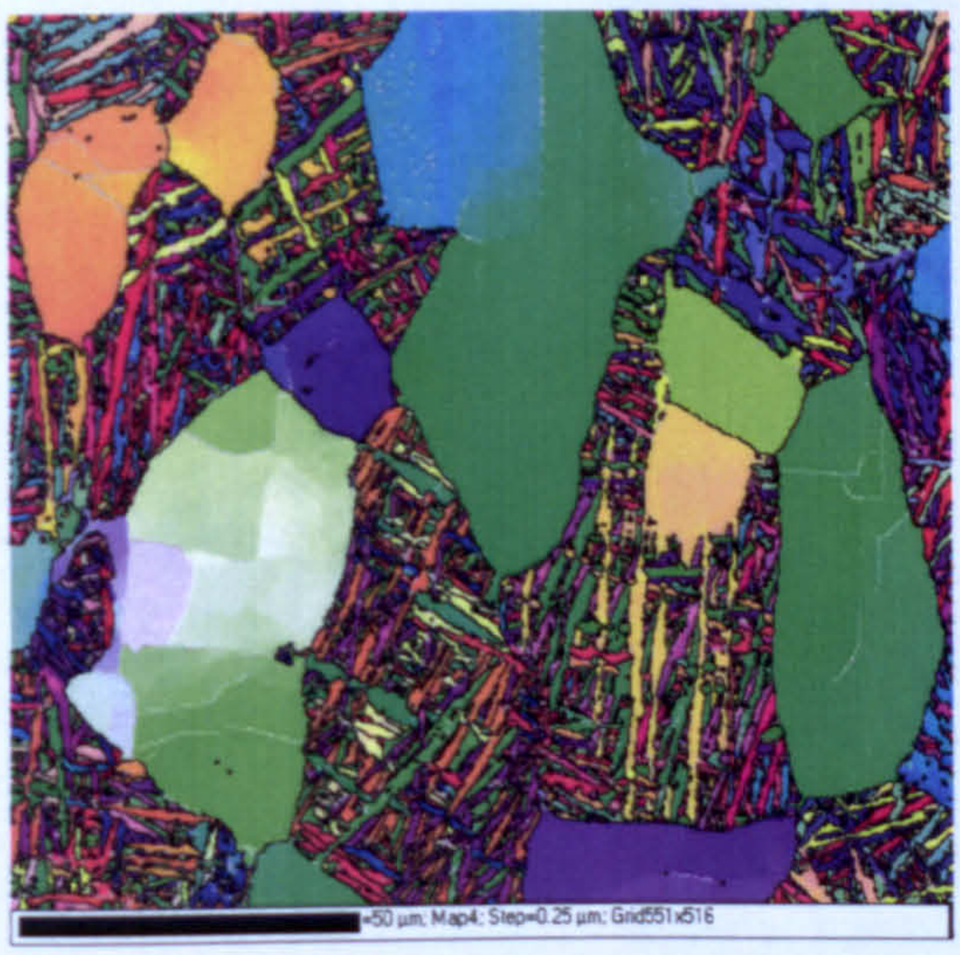

(c) Misorientation map (silver>2°, black>15°).

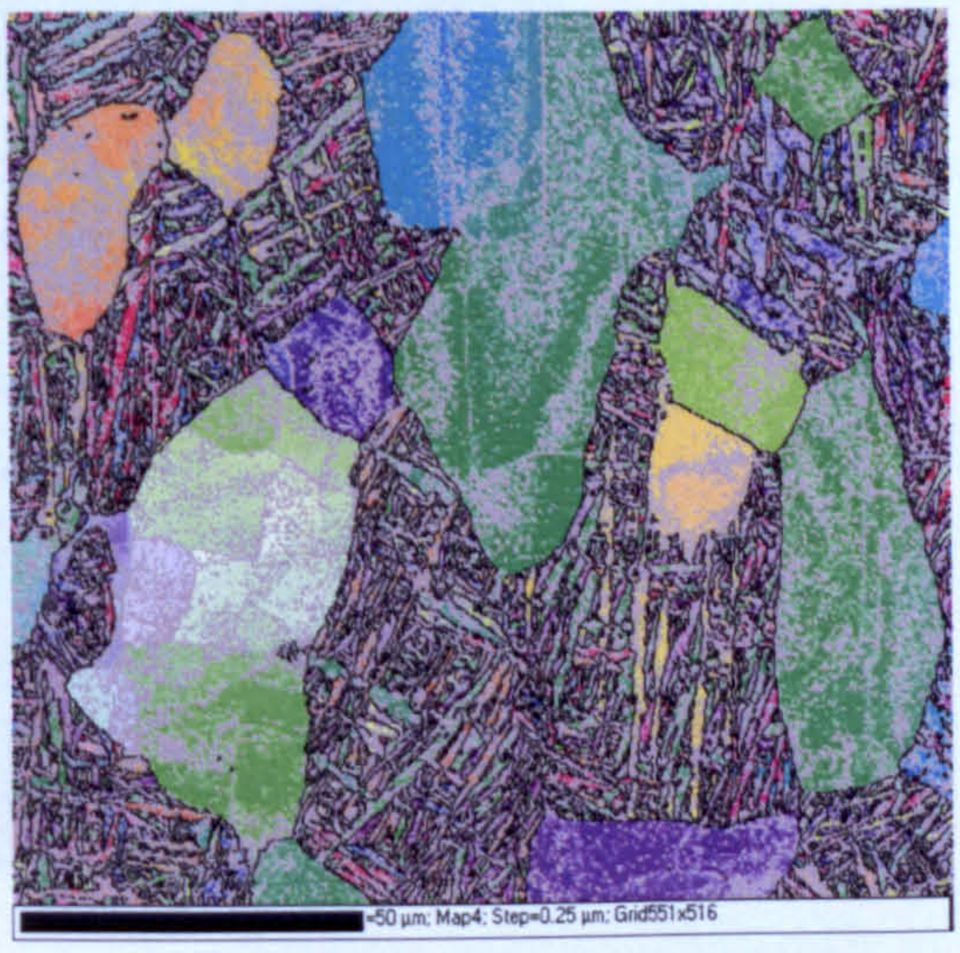

(d) Misorientation map (silver>0.5°, black>15°).

Fig. 4.4 The effect of orientation noise in resolving substructure in a standard EBSD dataset.

The effect of 1, 2 and 3 passes of the Kuwahara filter is shown in Fig. 4.5. It can be seen that 1 pass of the Kuwahara filter reduces the orientation noise to the extent that low angle boundaries of 0.5° are clearly resolved. The effect of further passes has only a relatively small effect. The effect of 1 pass on the orientation noise is also shown by way of a misorientation profile in Fig. 4.6. The line of this profile is shown with a red arrow in Fig. 4.5(a).

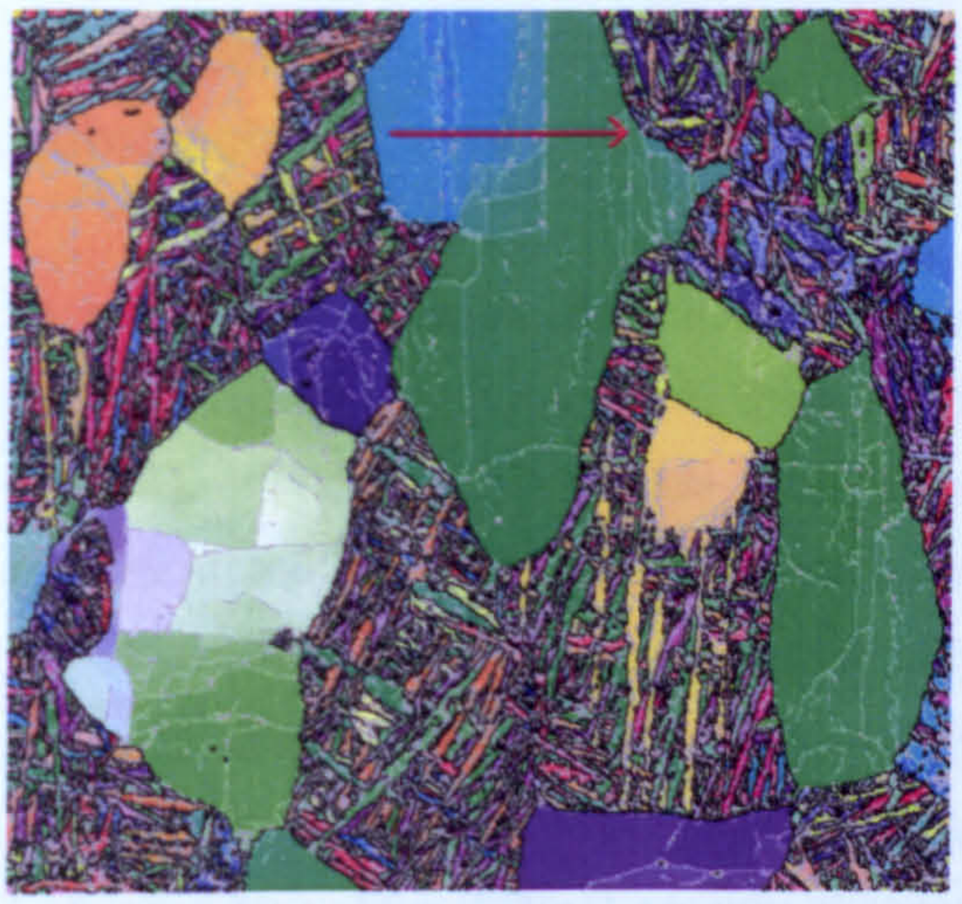

(a) After 1 pass (red arrow indicates location of misorientation profile in Fig. 4.6).

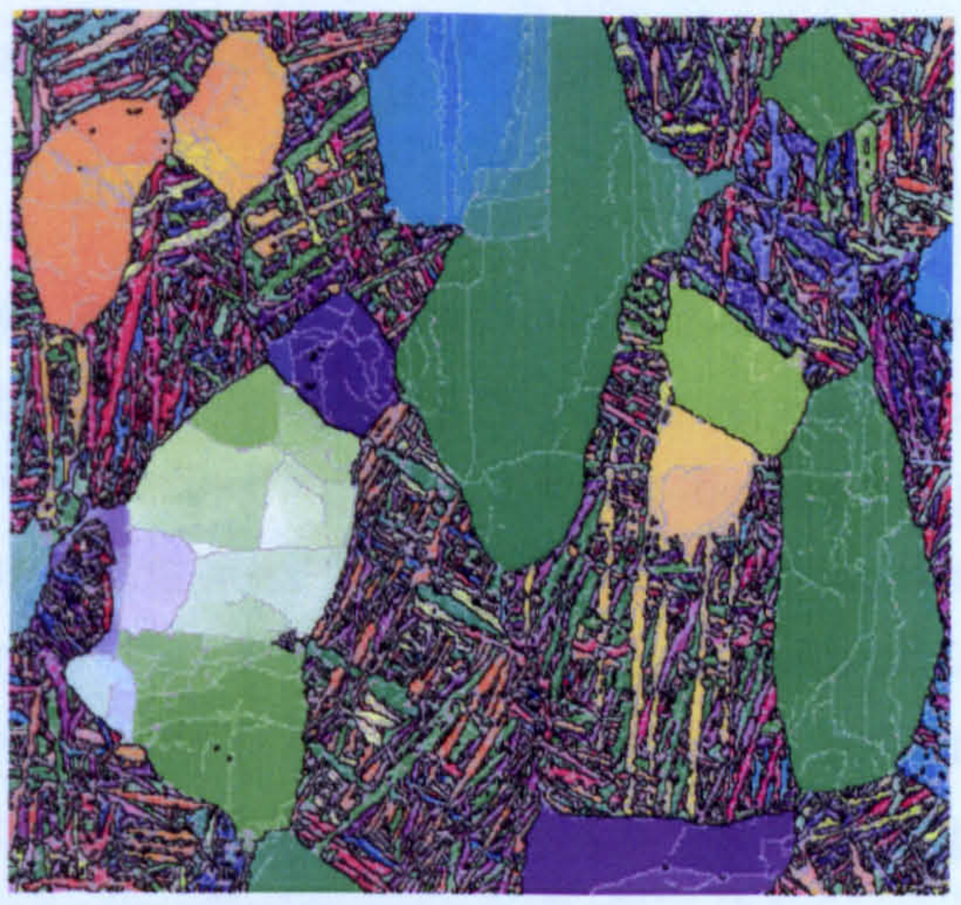

(b) After 2 passes.

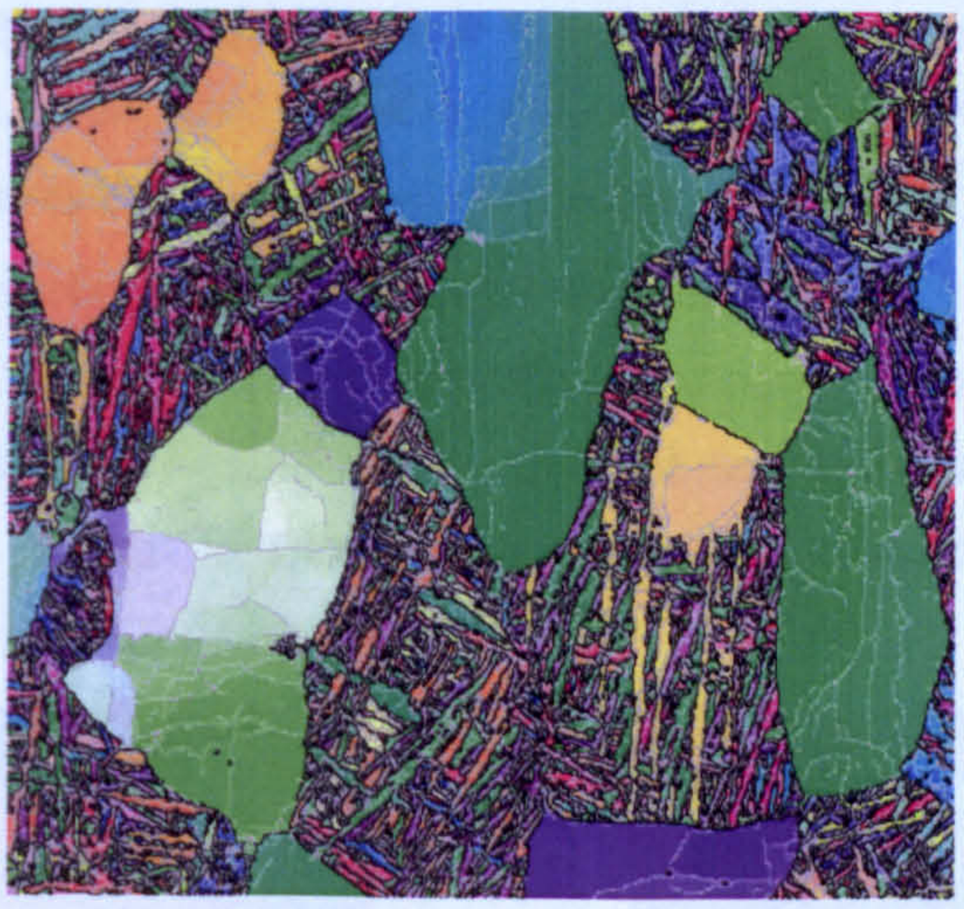

(c) After 3 passes.

Fig. 4.5 The effect of successive passes of the Kuwahara filter.

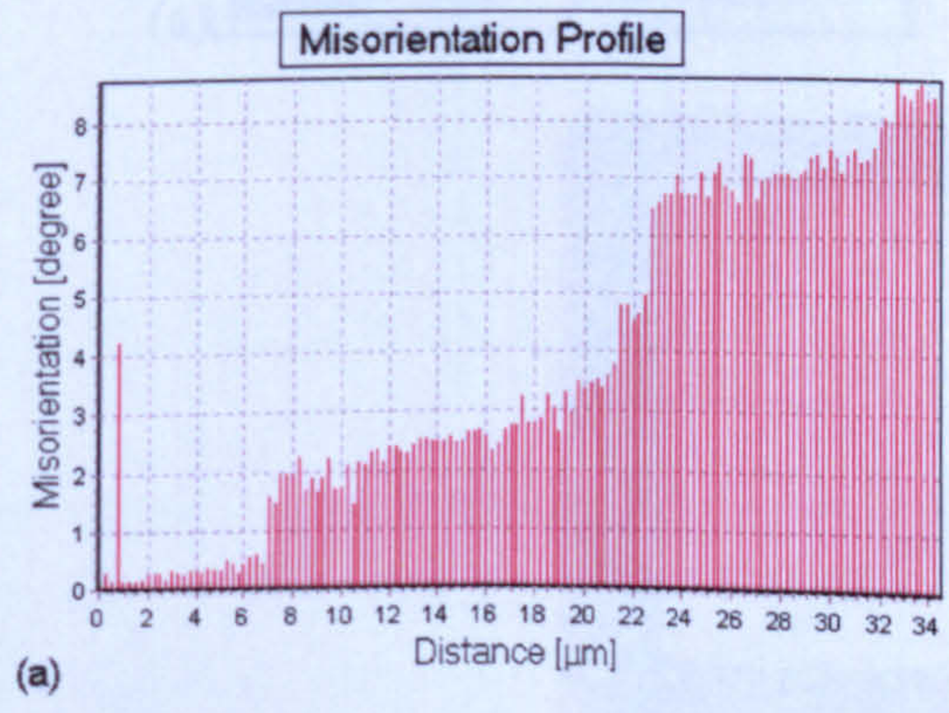

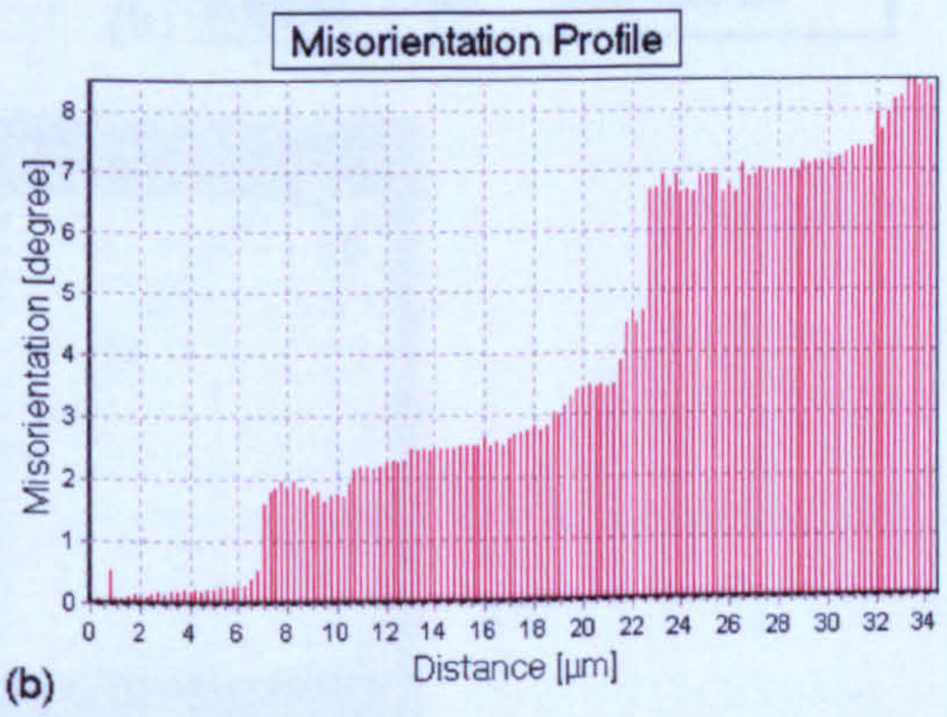

Fig. 4.6 The cumulative misorientation profile across an α_p grain (indicated by the red arrow in Fig. 4.5), showing the reduction in orientation noise as a result of orientation averaging. (a) The standard EBSD data and (b) after 1 pass of the Kuwahara filter.

4.4 Techniques for Showing Intra-grain Orientation Changes and Substructure

In plotting orientation data in EBSD maps, two methods that are commonly used to allocate colours to points in a map are Euler colouring and IPF colouring (see section 3.6.4.4). These methods are satisfactory for revealing the contrast between highly misorientated grains but are less suited to revealing more subtle orientation changes such as substructure within a grain. As an example, Fig. 4.7(a) shows an Euler map of an α_p grain surrounded by a finer structure composed of α_s variants. Using Euler colouring, contrast within the α_p grain is limited, yet a cumulative misorientation profile along the indicated line (Fig. 4.7(c)) clearly shows there are significant orientation changes within the grain. The same map using IPF colouring (Fig. 4.7(b)) shows greater contrast but the IPF colouring scheme can be misleading because the colours do not change evenly in the IPF key. Thus there can be very little contrast in grains which have orientations close to the corners of the key e.g. hexagonal α grains with orientations close to $\{0002\}$, $\{10\bar{1}0\}$ and $\{11\bar{2}0\}$, and furthermore, there is no contrast between orientations whose planes may be parallel to the viewing surface but are rotated differently about the plane normal.

To address this issue, the program incorporated two map types which are useful for revealing small differences in orientation and are not available in the standard EBSD software. Code was also written to allow one to plot orientation data onto pole figures and to plot the traces of selected planes onto the map.

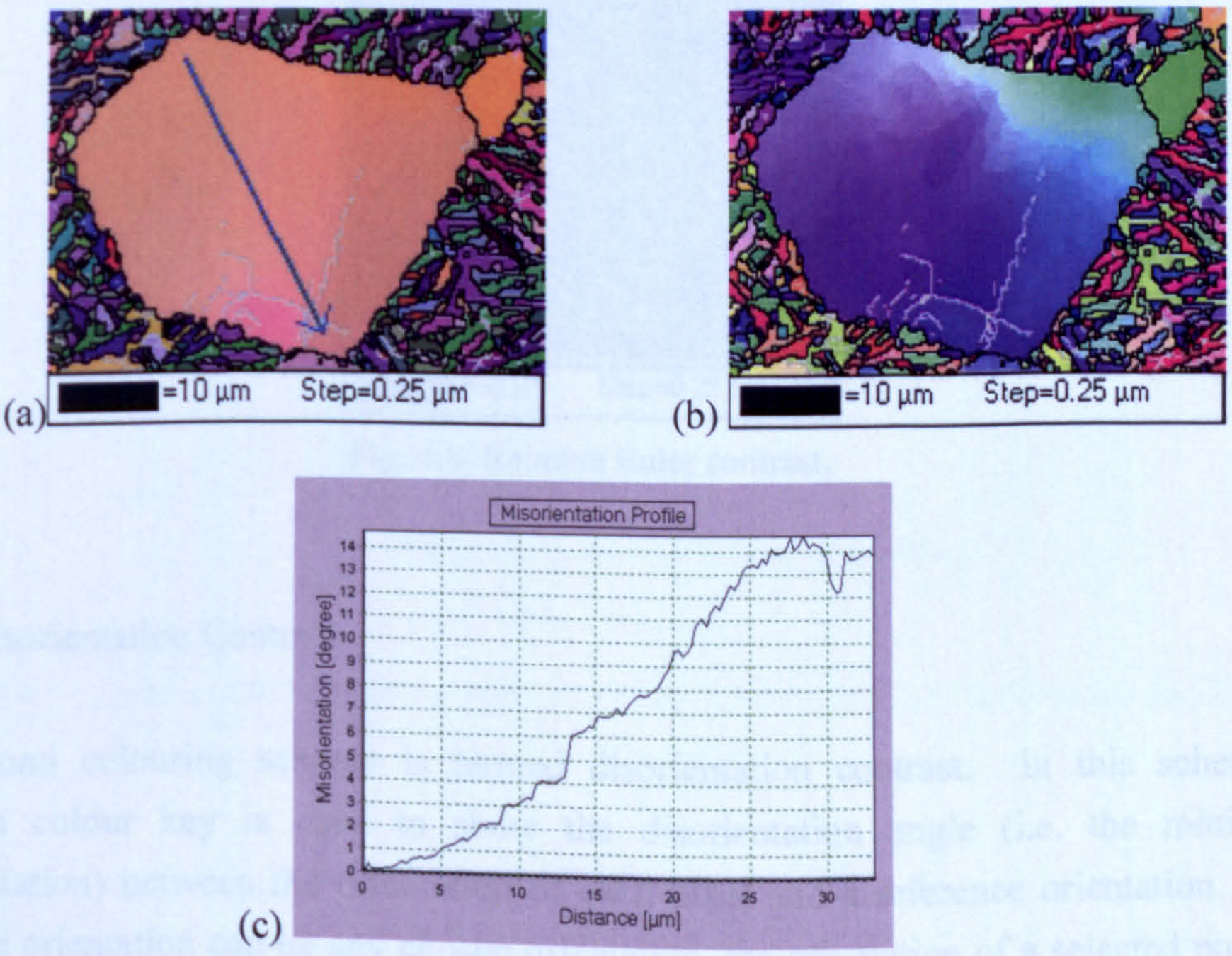

Fig. 4.7 Common EBSD map colouring schemes when used to show intragrain misorientations. (a) Euler colouring. (b) IPF colouring. (c) Cumulative misorientation profile across the α_p grain.

4.4.1 Relative Euler Contrast

The first colouring scheme incorporated into the program is termed relative Euler contrast and was first described by Humphreys *et al.* (2001). In this scheme, the RGB colour values for each point are proportional to the difference between the Euler angles for the point and a reference orientation. In the program, the reference orientation $\phi_1{}^0$, Φ^0 and $\phi_2{}^0$ can be any chosen orientation, the orientation of a selected point or the average orientation of a selected grain. For any point in the map with Euler angles ϕ_1, Φ and ϕ_2, the intensities of red, green and blue are given by

$$\begin{aligned} red &= \left(\phi_1{}^0 - \phi_1\right) \times S + 128 \\ green &= \left(\Phi^0 - \Phi\right) \times S + 128 \\ blue &= \left(\phi_2{}^0 - \phi_2\right) \times S + 128 \end{aligned} \tag{4.2}$$

The parameter *S*, which is set by the user, determines the contrast stretch and can be varied to provide the maximum contrast for a given misorientation spread whilst preventing a colour from becoming saturated (255) or falling to zero. If an orientation falls outside the 0-255 colour range, then that pixel is not coloured. Fig. 4.8 shows a relative Euler contrast map with the average orientation of the α_p grain as the reference orientation. The parameter S was adjusted to provide maximum contrast in the α_p grain.

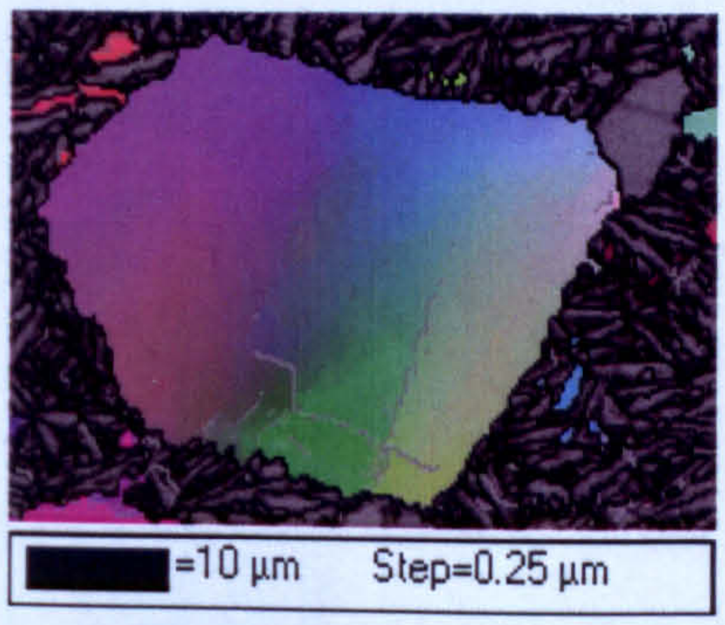

Fig. 4.8 Relative Euler contrast.

4.4.2 Disorientation Contrast

The second colouring scheme is termed disorientation contrast. In this scheme a spectrum colour key is used to show the disorientation angle (i.e. the minimum misorientation) between the orientation of each pixel and a reference orientation. The reference orientation can be any chosen orientation, the orientation of a selected point in the map or the average orientation of a selected grain. The contrast can be adjusted by

choosing the maximum disorientation for the colour range. If the disorientation of a point lies outside the maximum, then the pixel is not coloured. Fig. 4.9 shows a disorientation contrast map with the average orientation of the α_p grain as the reference orientation. The disorientation maximum was adjusted to 18° to provide maximum contrast in the α_p grain. As well as producing the map, the disorientation data for a grain can be copied and exported into a spreadsheet where a histogram can be constructed for the disorientation angle distribution (Fig. 4.10). It is interesting to note that in the example given, there are no disorientation angles within 5° of the average orientation. The reasons for this will become clear in the pole figure plots described in the next section.

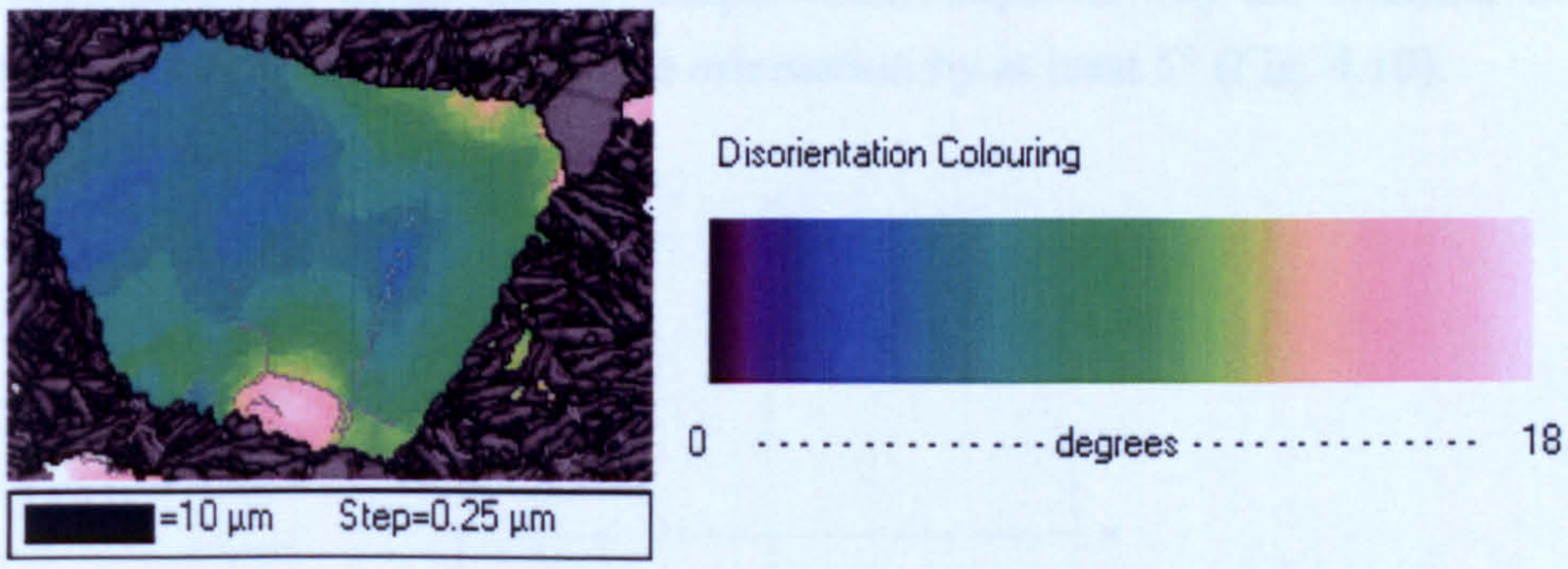

Fig. 4.9 Disorientation contrast. The points in the map are coloured according to their disorientation from the average orientation of the α_p grain.

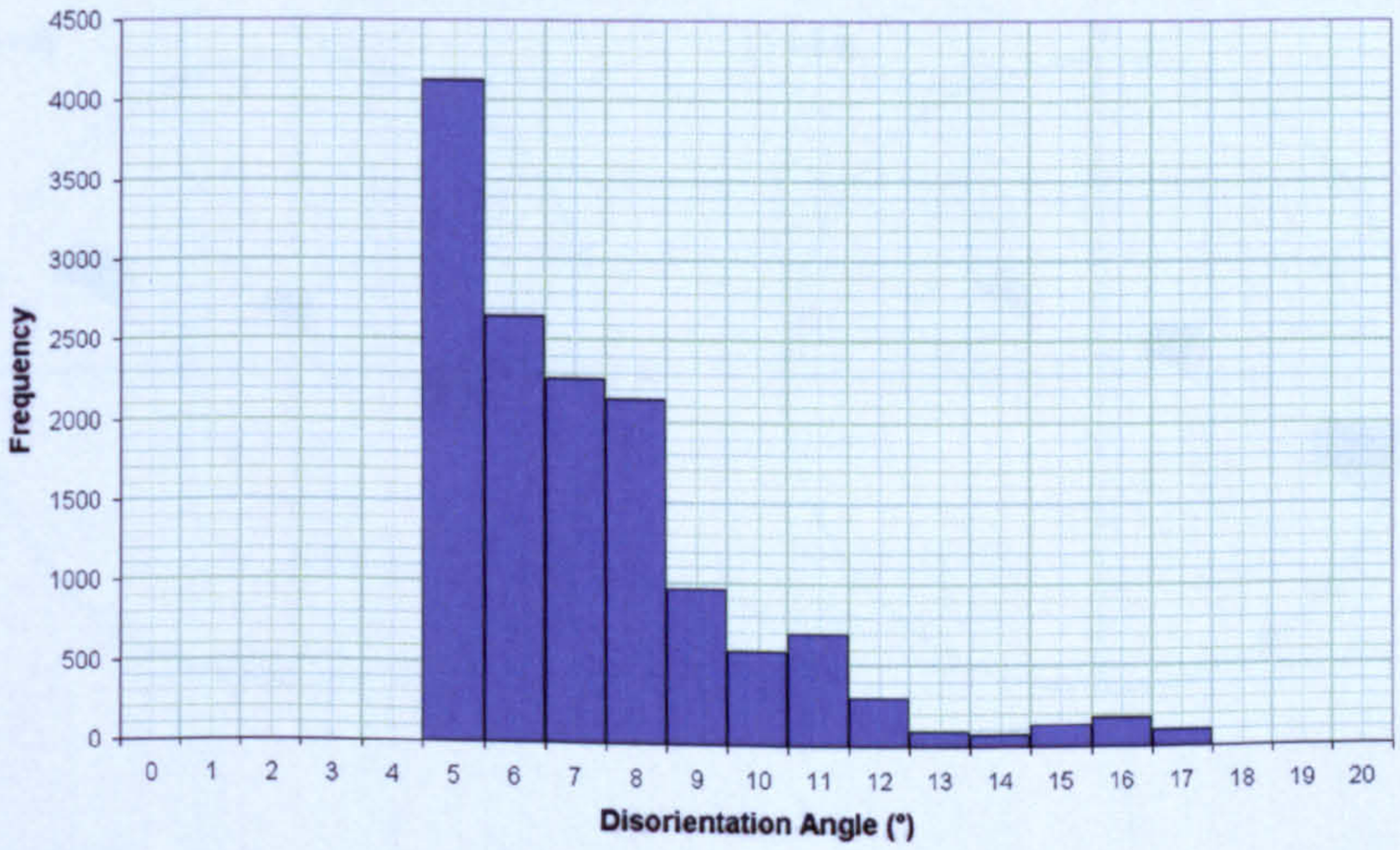

Fig. 4.10 Frequency distribution of disorientation angles from the mean orientation for the α_p grain in Fig. 4.9.

4.4.3 Pole Figure Plots

Code was written to allow orientations of selected points or grains to be plotted in the form of pole figures for any chosen crystallographic plane in stereographic projection. To demonstrate this feature, the orientation data for the α_p grain in Fig. 4.9 is plotted in $\{0001\}$, $\{10\bar{1}0\}$ and $\{11\bar{2}0\}$ pole figures in Fig. 4.11. Each point in the grain is plotted on the pole figures using the same disorientation colour used in Fig. 4.9 and the average orientation of the grain is indicated by a red point. It can be seen that in the $\{0001\}$ pole figure, the orientation data for the α_p grain form a 'c' shape in the projection. The average orientation lies inside this 'c' shape, which explains why the orientations in the grain are disorientrated from the average orientation by at least 5° (Fig. 4.10).

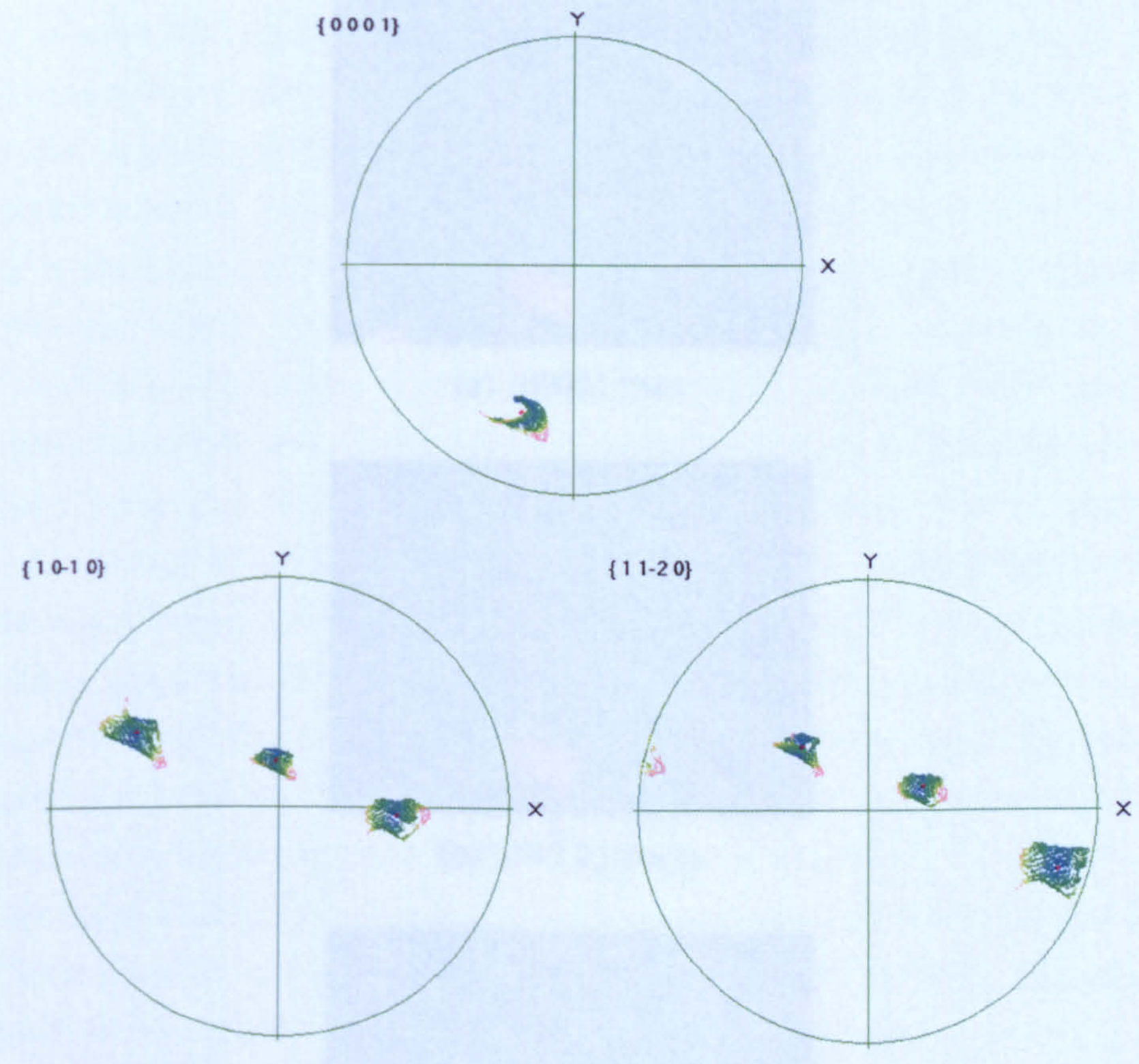

Fig. 4.11 Pole figures (stereographic projection) for the α_p grain in Fig. 4.9. The points are coloured according to their disorientation from the average orientation, which is shown by a red point.

4.4.4 Plane Trace Plots

A useful feature for investigating possible relationships between crystallography and substructure is the ability to plot the trace of where certain crystallographic planes intersect the plane of the map. Code was written so that the traces of a family of crystallographic planes could be plotted on the map for a chosen orientation, the orientation of a selected point or the average orientation of a selected grain. To demonstrate this feature, traces of the {0002}, {10$\bar{1}$0} and {11$\bar{2}$0} planes are plotted in Fig. 4.12(a), (b) and (c) respectively for the average orientation of the α_p grain. The trace of a plane should be perpendicular to a line drawn in the pole figure from the centre of the pole figure to plane's pole. A comparison with Fig. 4.11 shows this to be the case.

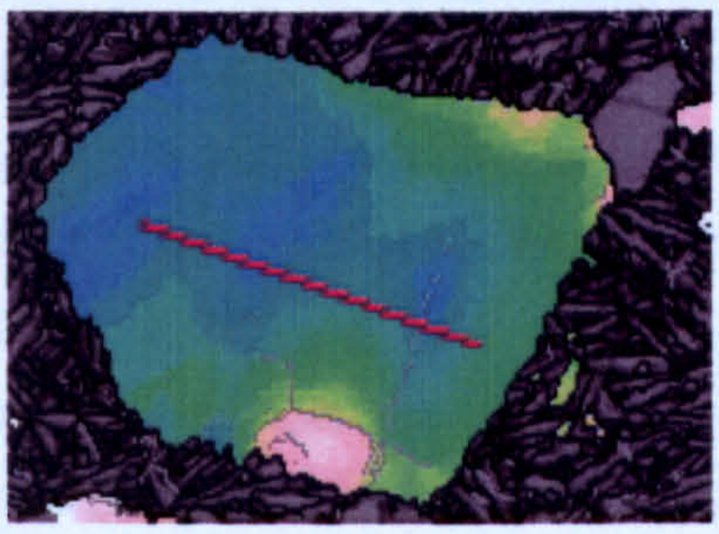

(a) {0002} trace

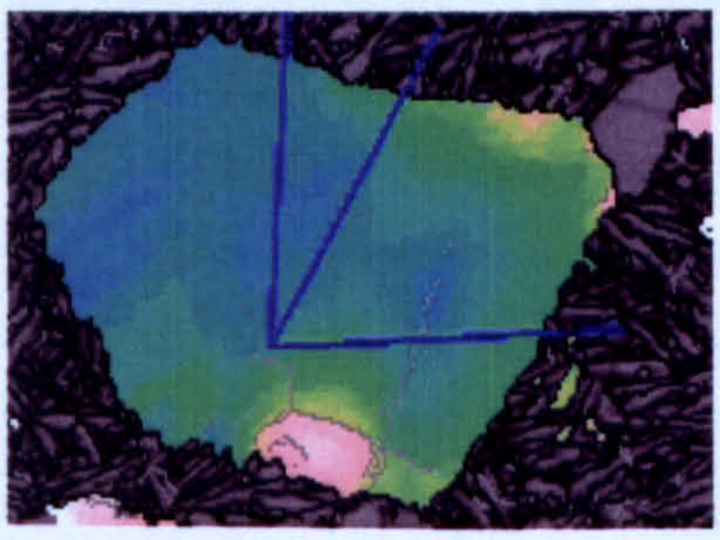

(b) {10$\bar{1}$0} traces

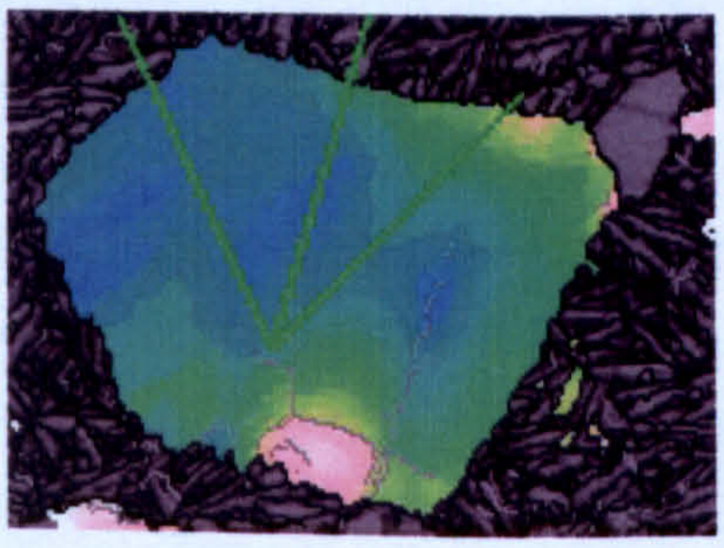

(c) {11$\bar{2}$0} traces

Fig. 4.12 The traces of intersections between crystallographic planes and the surface plane of the map.

4.5 The Direct Phase Separation Technique

A technique for separating the α_p and α_s phases was incorporated into the program. The separation of these phases cannot be accomplished during a standard EBSD analysis because they have the same hcp crystal structure. Separating these phases is useful in the study of texture evolution during thermomechanical processing. It is also an essential step in the reconstruction of the high temperature β phase from the inherited α_s phase because the α_p phase must be excluded from any reconstruction procedure.

The techniques of Germain *et al.* (2005b) and Thomas *et al.* (2005), which were described in the literature are possible separation methodologies but they are time consuming since they require one to obtain a separate back scattered electron image or an optical micrograph respectively. Their main disadvantage however is that they depend on obtaining an accurate correspondence between the EBSD map and the second image by rotating, translating, shearing and scaling operations. While the fit obtained may be adequate for separating the textures of two phases, it is less satisfactory for β reconstruction because small areas of α_p pixels wrongly assigned as α_s can lead to erroneous reconstructed β orientations and any α_s wrongly assigned as α_p will remain unreconstructed. Ideally, in the interests of time and accuracy, a separation technique is needed which is based directly on the information provided in the EBSD data. In this work, a direct technique was developed specifically for bimodal microstructures in which the α_s phase forms as a result of the transformation of the β phase under rapid cooling conditions i.e. water quenching. Under these conditions, the α_s phase tends to be either martensite or a fine basket weave Widmanstätten morphology. For these microstructures the technique gives excellent results for both high and low resolution maps and the accuracy of the separation is suitable for subsequent β reconstruction. The technique is less effective for separating α_s when it has formed at slower cooling rates but in many cases still provides sufficient accuracy for separating the textures.

The separation technique is a three step process. In the first two steps, differences in average band contrast and size between the α_p grains and α_s laths are exploited to distinguish between the two phases. The third step allows the user to manually select or deselect any remaining discrepancies thus achieving a very accurate separation of the phases. The separation strategy is illustrated in Fig. 4.13 using an area taken from a larger EBSD map. The EBSD analysis in this example was performed on a specimen of billet, which was heated to 1010°C and held at this temperature for 10 minutes to obtain a bimodal microstructure containing approximately 25% α_p. The specimen was rapidly water quenched so that the β grains transformed to a relatively fine basketweave, morphology. The map was acquired using a step size of 0.25 μm. Only the hexagonal α phases were indexed as any retained β in the microstructure is too fine to be indexed. The raw EBSD data is shown using Euler colouring in Fig. 4.13(a), with non indexed points

shown in white. The overall percentage of indexed points was 85%. It can be seen that α_p phase is indexed very well and that the majority of non indexed points lie in the α_s phase, mostly located at the α_s lath boundaries. Indexing is poor at these boundaries because the interaction volume of the electron beam in these areas will often contain regions of crystal from more than one α_s lath and also due to any retained β phase that may be present between the laths. This results in very poor pattern quality and/or overlapping patterns. The poor pattern quality in these non indexed areas can be seen in the band contrast map as very dark pixels (Fig. 4.13(b)). Fig 4.13(c) shows a map of average bad contrast for grains recognised using a misorientation criterion of 5°. It can be seen that this map results in good contrast between the predominantly light α_p grains and darker α_s laths. This contrast is improved further when the map is cleaned to extrapolate the non indexed points prior to the grain recognition procedure (Fig. 4.13(d)). With the zero solutions extrapolated, the recognised grains now include the formerly non indexed points which have low band contrasts. This further increases the contrast between the α_p grains and α_s laths in the average band contrast map.

For the phase separation technique, the user produces a map of average band contrast in the HKL Technology software and saves this file as a bitmap image. In doing this, the user must select the misorientation criterion used to recognise the grains (5° is recommended). Next, the user opens the EBSD dataset in the post-processing application and creates a new map of the type 'phase separation'. In this new window, the user is prompted to open the average band contrast bitmap image, which was saved previously. In the first separation step, a threshold grey value between 0 and 255 is chosen. Grains/laths with an average band contrast below this threshold will be removed from the map. The result of this first step is shown in Fig. 4.13(e), where a threshold value of 180 was used. It can be seen that with a suitable threshold level, the vast majority of α_s laths are successfully separated from the α_p grains. In this example, only one α_p grain (indicated with a star) was removed and this is due to a region of non indexed points within it that was most likely caused by contamination on the surface of the specimen. Of the remaining α_s laths in the image, it can be seen that they tend to be substantially smaller than the α_p grains. In the second separation step, the application finds the area of each remaining lath or grain. A size threshold in terms of number of pixels is then chosen to remove the majority of the remaining α_s laths. The result of this second step is shown in Fig. 4.13(f), where grains/laths containing fewer than 450 pixels were removed. After this step, it can be seen that a further α_p grain at the top edge of the map was removed and a small number of α_s laths remain. These laths may remain because they are abnormally large, but usually it is because they are adjacent to an α_p grain and share a similar orientation. They remain because they were recognised as part of the adjacent α_p grain because the misorientation between the them was less than the critical misorientation chosen in the initial grain recognition procedure. In the final step, laths or α_p grains can

be individually selected with a lower misorientation criterion and either added or removed from the separated α_p phase. The results of the final manual step are shown in Fig. 4.13(g) and (h). For a given microstructure and standard conditions of EBSD analysis, the first two steps can be performed extremely quickly since the same threshold values can be used once the optimum values have been established. For texture analysis, adequate separation of the textures can usually be achieved with these two steps alone. The third step can be used to give the best accuracy when subsequent reconstruction of the β microtexture is to be carried out. The time taken for this manual step depends on the map and microstructure in question. There is a certain level of subjectivity in this step as the user must decide from the Euler and band contrast maps what constitutes α_p and α_s.

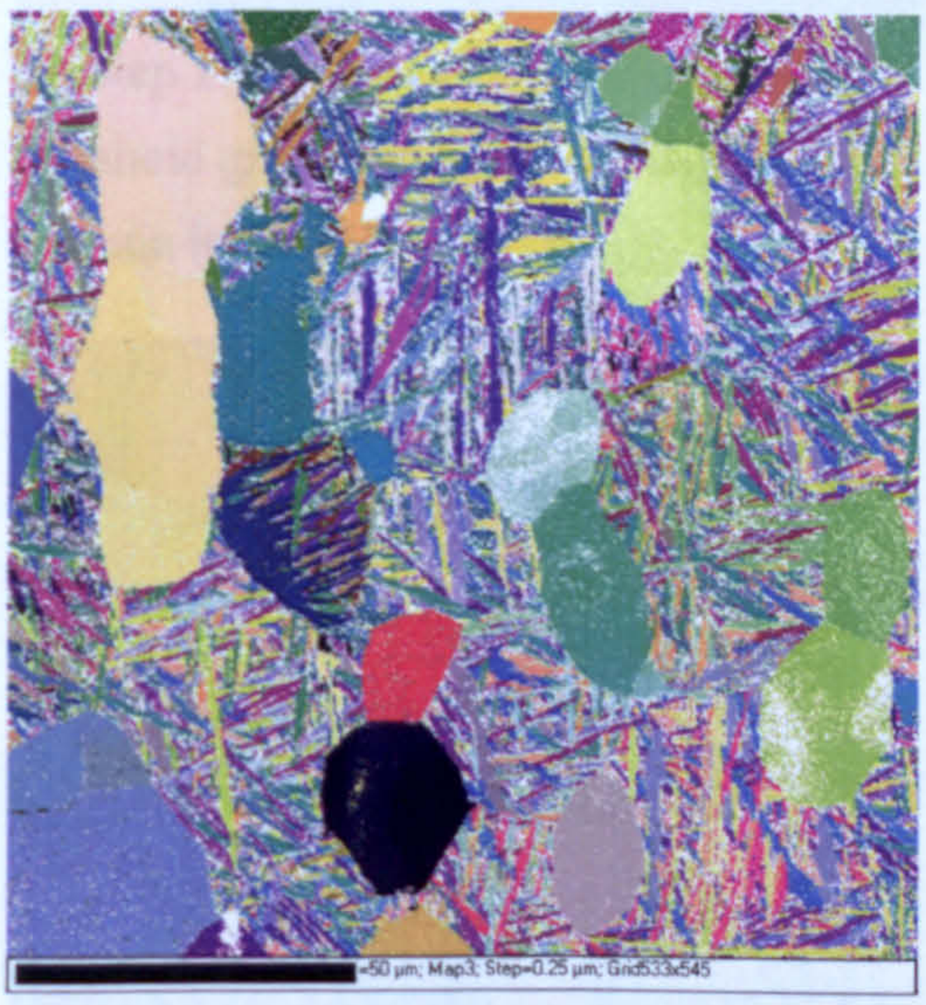

(a) Euler colouring, non indexed points shown in white.

(b) Band contrast image.

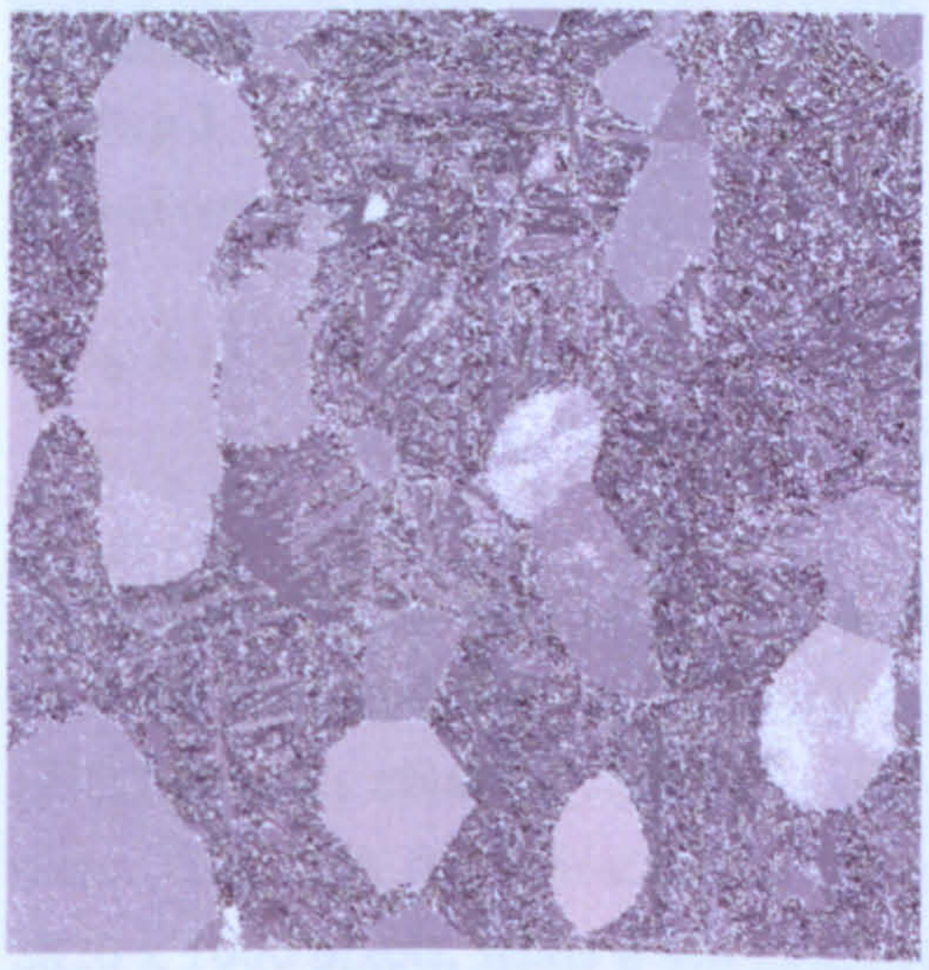

(c) Average band contrast of grains recognised with 5° misorientations. criterion.

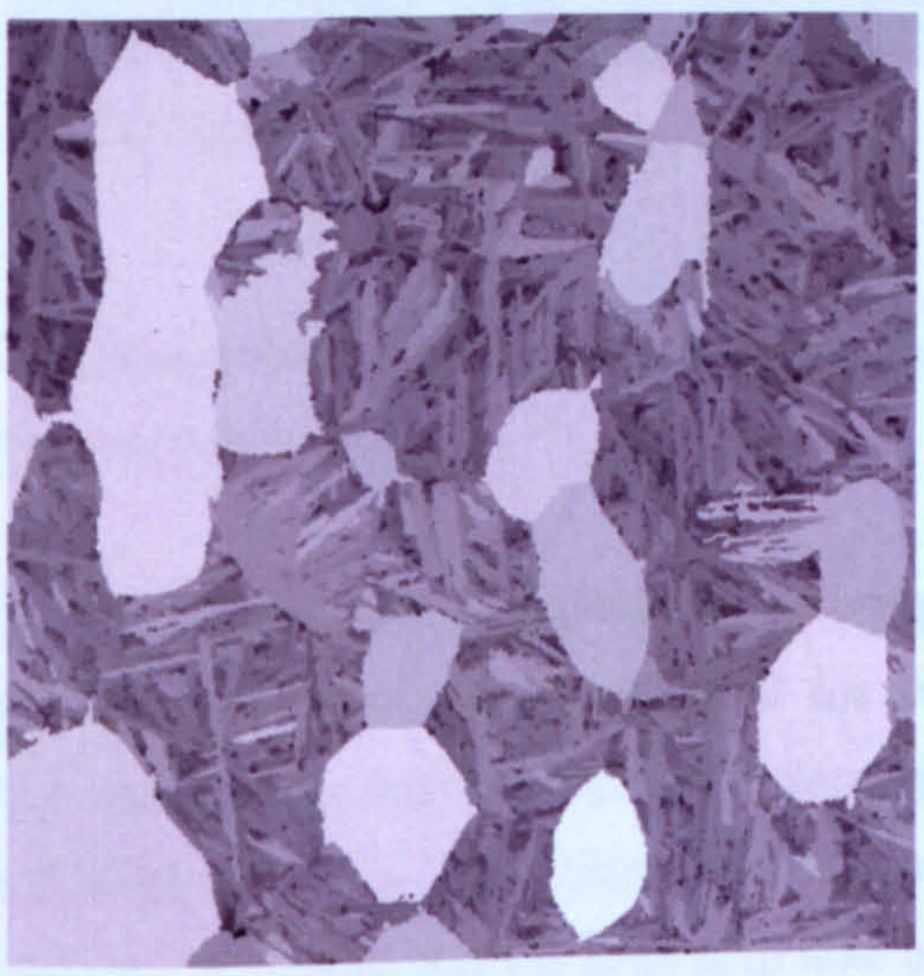

(d) Average band contrast of the same map after extrapolating the non indexed points.

(e) **Step 1**: removal of grains below a threshold gray level (180). Removed α_p grain indicated.

(f) **Step 2**: removal of grains below a threshold size level (450 pixels).

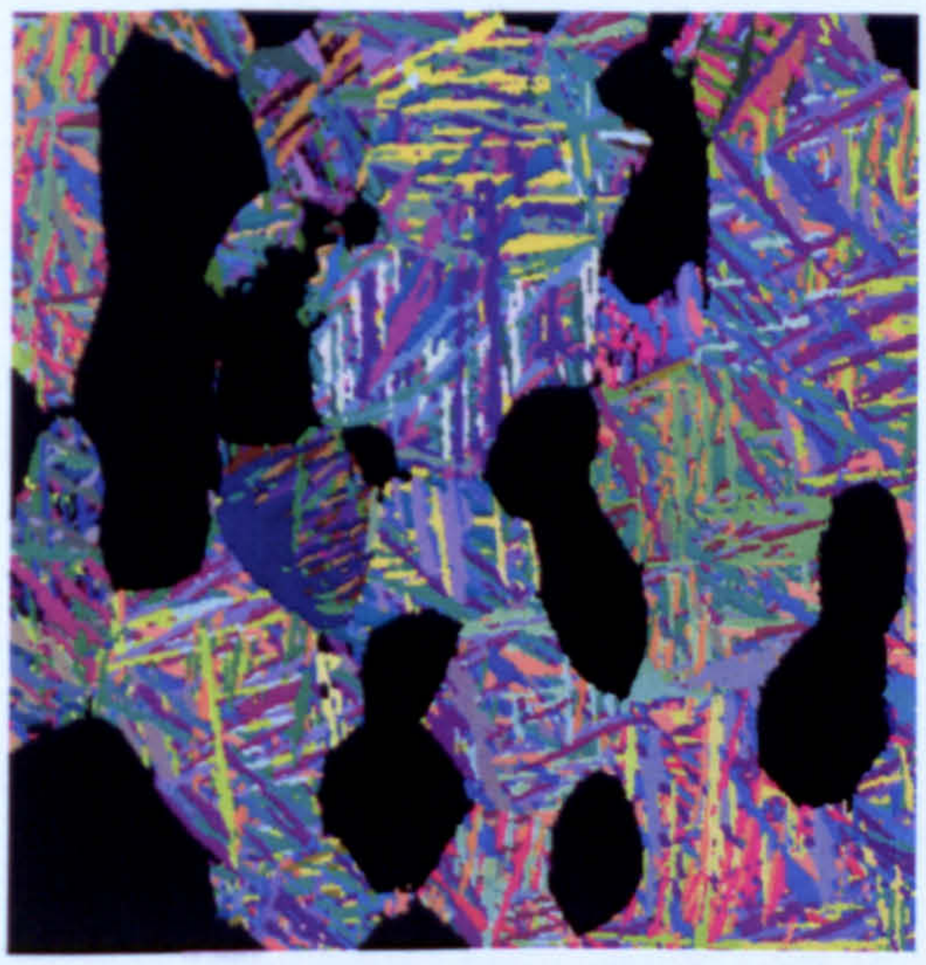

(g) **Step 3**: The separated α_s phase after manual correction.

(h) The separated α_p phase.

Fig. 4.13 A demonstration of the technique used to separate the α_p and α_s phases in a bimodal microstructure directly from the EBSD data.

To demonstrate the accuracy and suitability of the direct phase separation technique for both high and low resolution EBSD maps, the separation was performed for two EBSD datasets obtained from the same area of a specimen using two very different step sizes. The high resolution dataset was obtained with a 0.25μm step size and measured 2820 x 1000 pixels, while a low resolution dataset was obtained with a 3μm step size and measured 234 x 83 pixels. The cleaned high resolution map and the separated α_p and separated α_s phase are shown in Fig. 4.14 (a), (b) and (c) respectively. The separation

was made using an average band contrast threshold of 180, a size threshold of 450 pixels and manual correction of remaining discrepancies. The equivalent maps for the low resolution dataset are shown in Fig 4.15. The separation was made using an average band contrast threshold of 120, a size threshold of 10 pixels and a minor amount of manual corrections. The high resolution dataset fully resolves the transformed α_s phase, whereas the low resolution dataset does not, such that it can be regarded as more of a systematic sampling of this fine microstructure. Despite this, a comparison between the two figures shows good agreement in the separated phases. Pole figures showing the separated textures for the α_p and α_s phases for the high and low resolution datasets are shown in Figs. 4.16 and 4.17 respectively. A comparison shows that there is an excellent agreement in the separated textures for both step sizes.

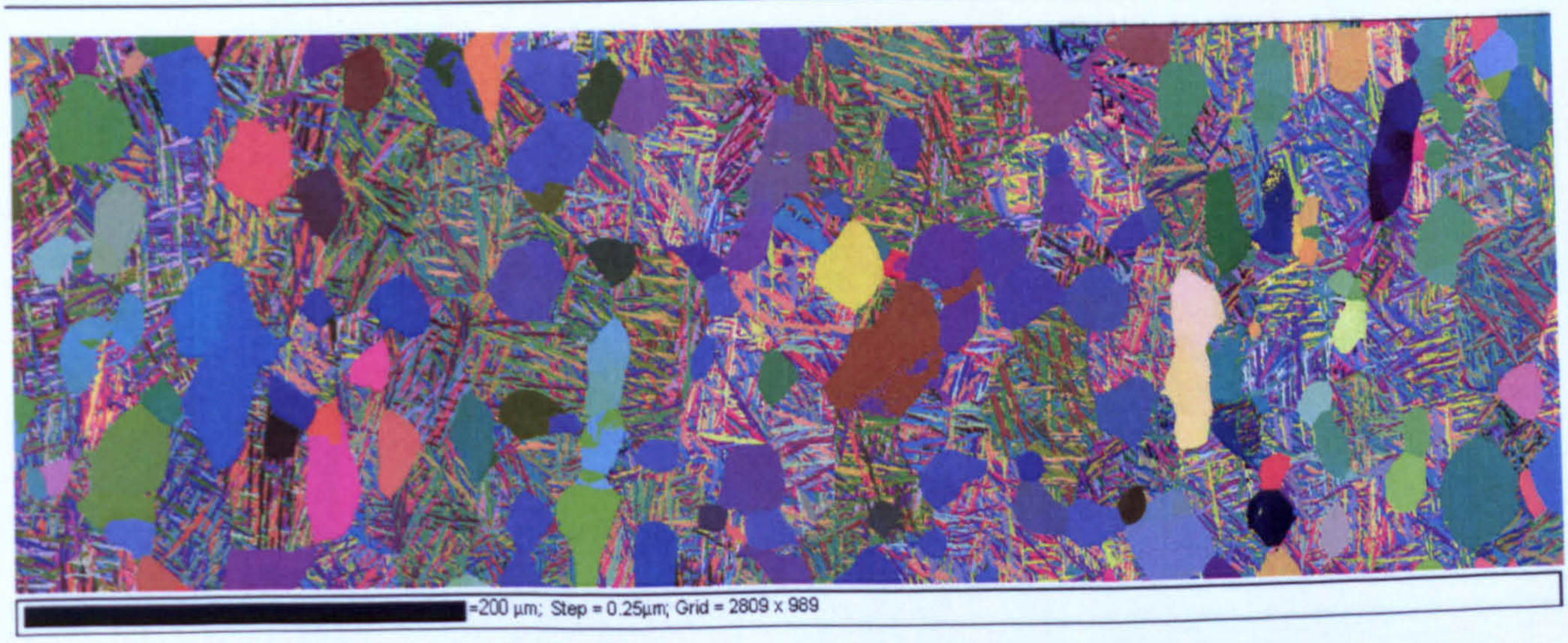

(a) Standard Euler map (cleaned).

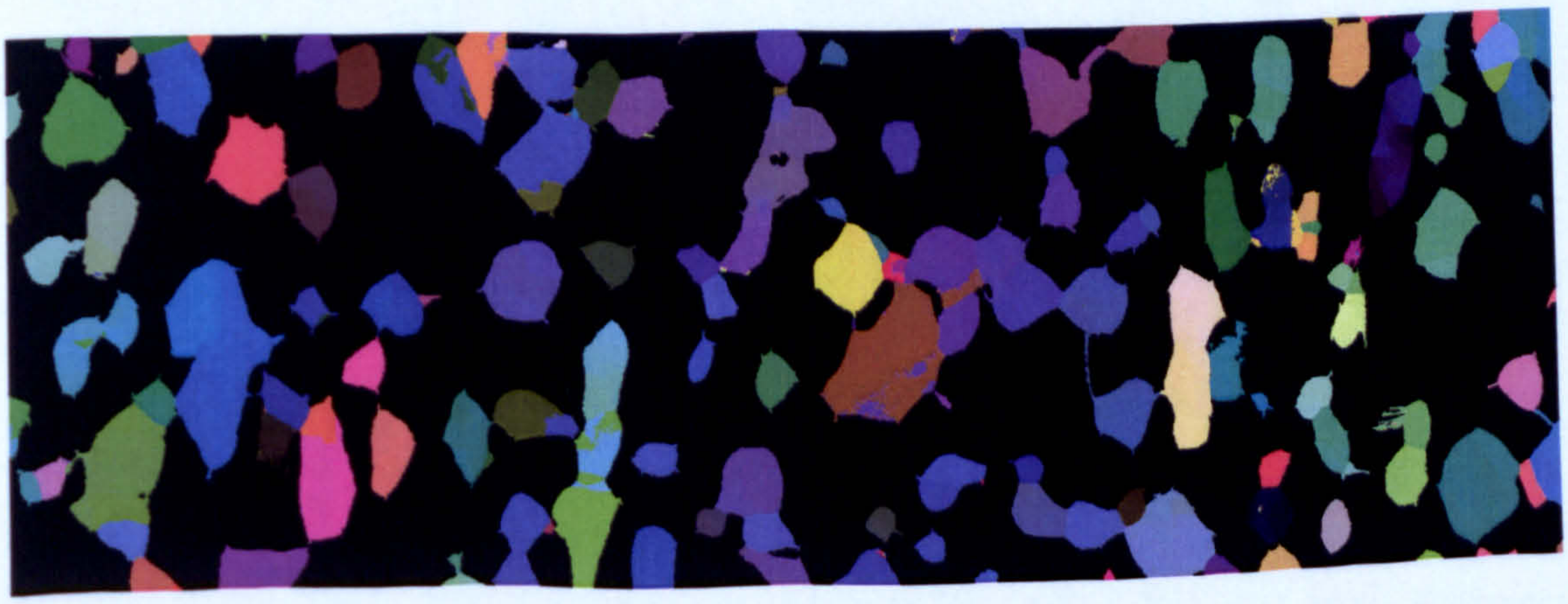

(b) The separated α_p phase.

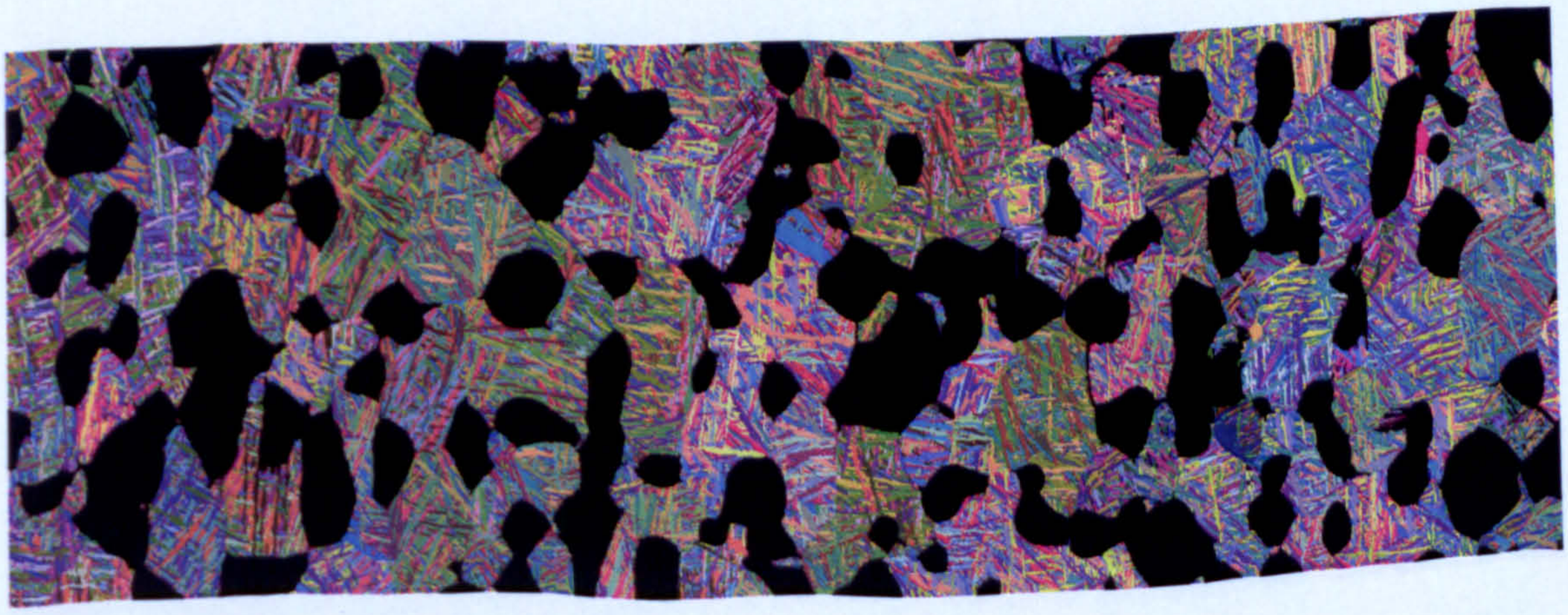

(c) The separated α_s phase.

Fig. 4.14 The direct phase separation technique for a high resolution (0.25µm step size) EBSD dataset.

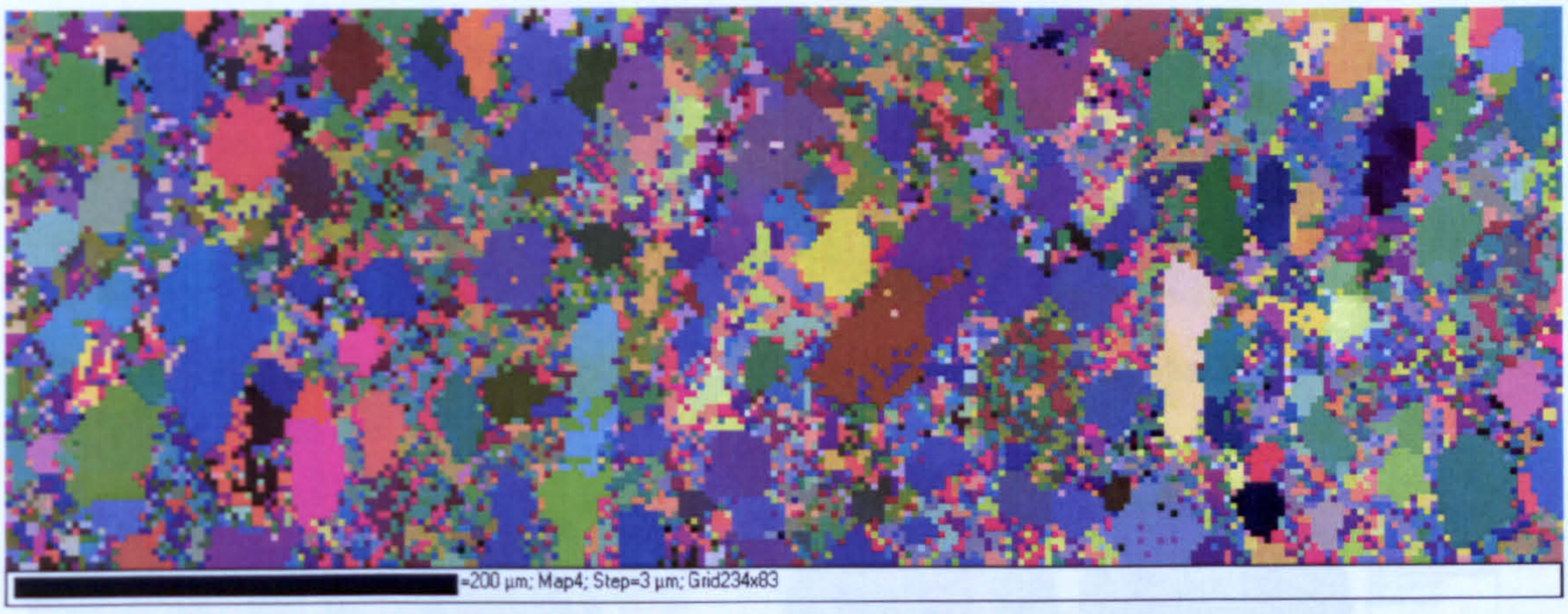

(a) Standard Euler map (cleaned).

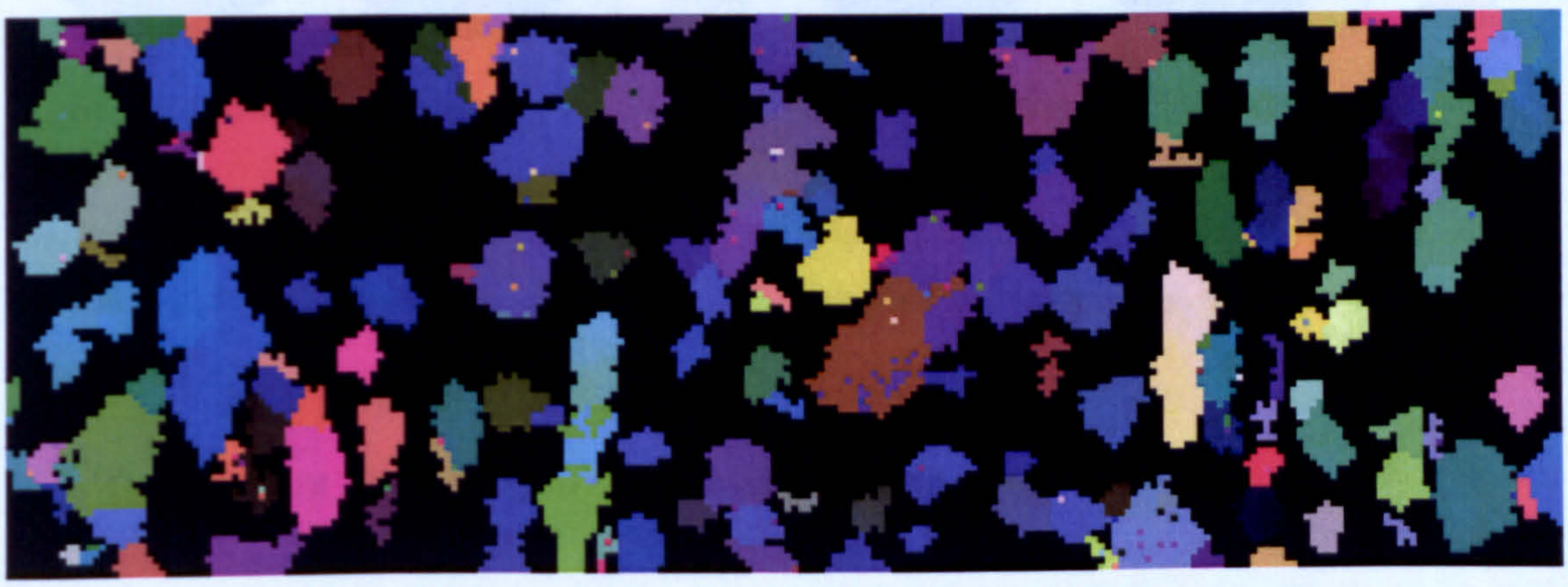

(b) The separated α_p phase.

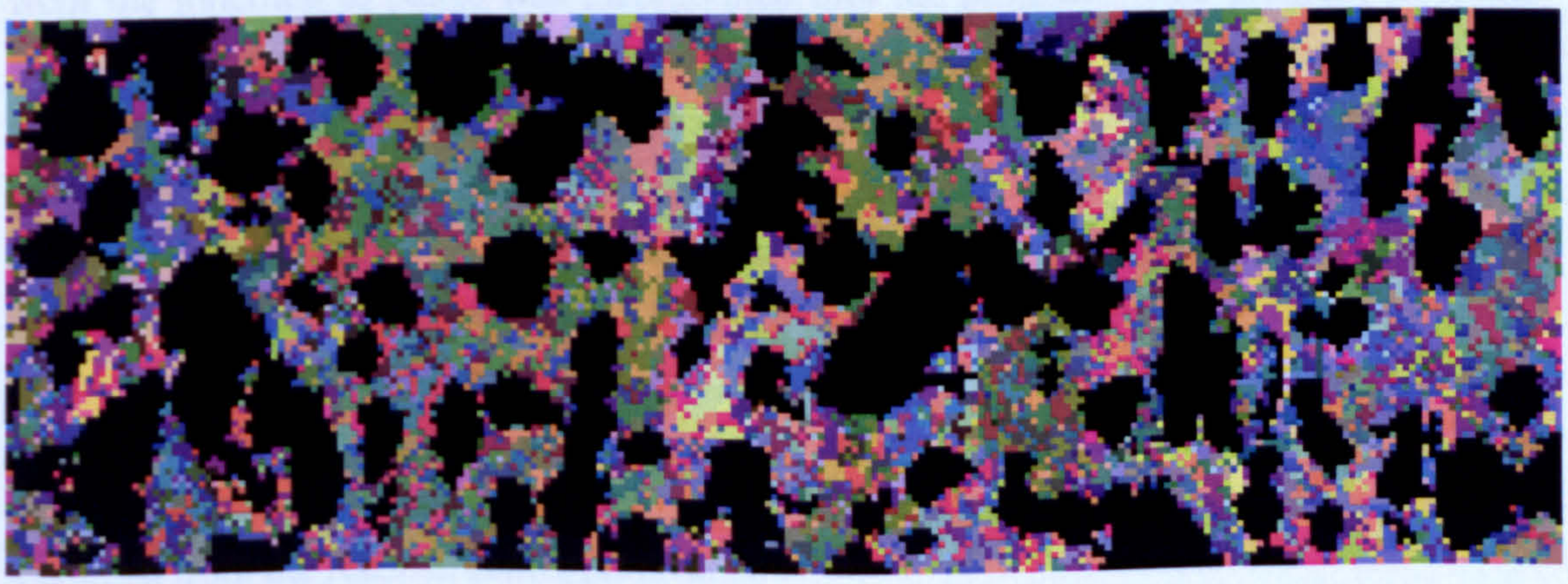

(c) The separated α_s phase.

Fig. 4.15 The direct phase separation technique for a low resolution (3µm step size) EBSD dataset obtained from the same area shown in Fig. 4.14.

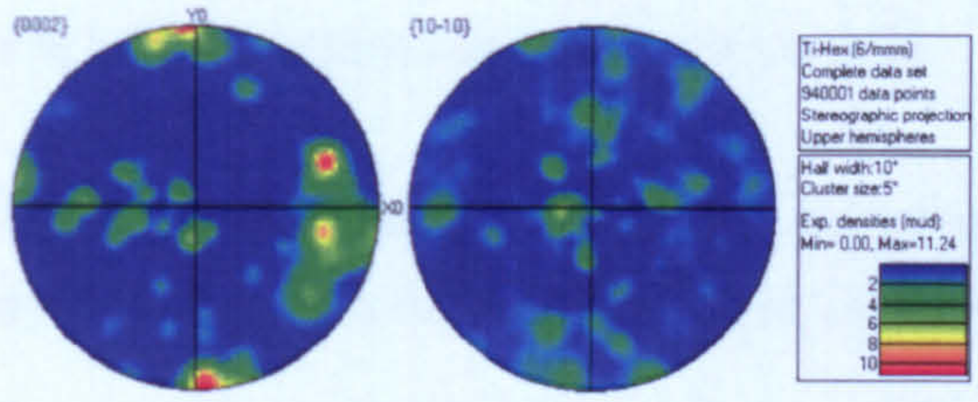

(a) The separated α_p phase.

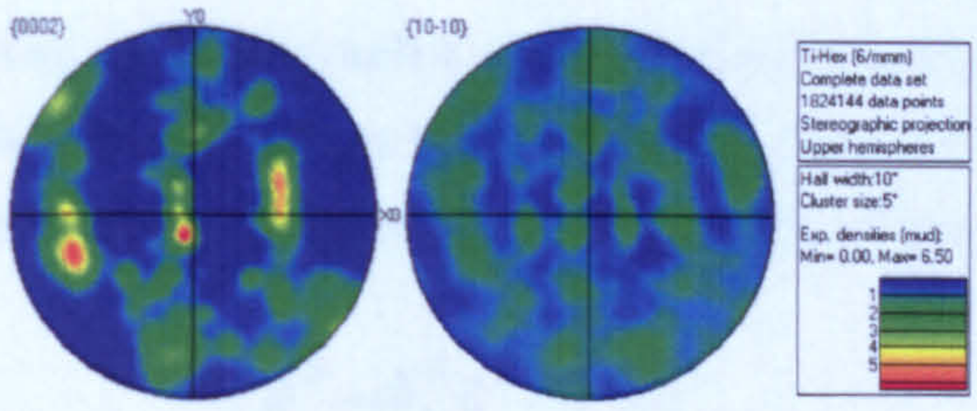

(b) The separated α_s phase.

Fig. 4.16 Separated textures for the high resolution dataset in Fig. 4.14.

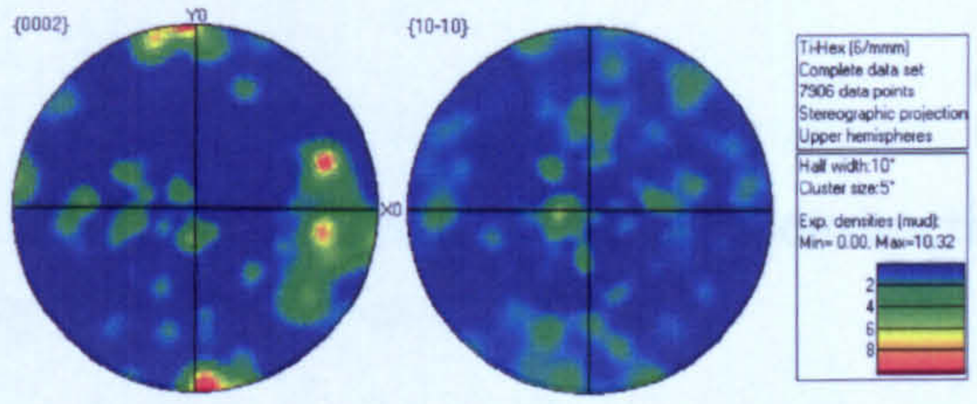

(a) The separated α_p phase.

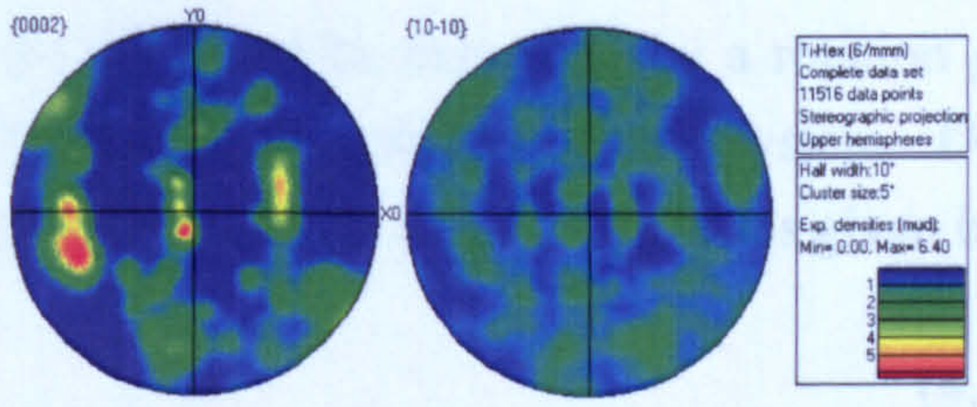

(b) The separated α_s phase.

Fig. 4.17 Separated textures for the low resolution dataset in Fig. 4.15.

4.6 The Variant Based β Reconstruction Technique

A technique for reconstructing orientation image maps of the high temperature β phase from the inherited α_s phase was incorporated into the program. The program finds the orientations of the parent grain for each α_s variant in turn based on the misorientations with adjacent variants and as a result can be described as a variant based approach to β reconstruction. A variant based approach is ideally suited to reconstructing deformed β grains. The reconstruction procedure could be applied to microstructures consisting of 100% α_s i.e. consisting entirely of β phase at high temperature as well as bi-modal microstructures, which contained both α_p and β at high temperature. For the reconstruction of these bimodal microstructures, the α_p was first separated from the α_s using the phase separation technique described previously so that this phase could be excluded from the reconstruction procedure.

The theoretical aspects of the reconstruction procedure are described in section 4.6.1. The way in which this was applied to the automated reconstruction of the β map from the α_s map follows in section 4.6.2 and is explained with the aid of a sequence of maps shown in Fig. 4.18. The maps in Fig. 4.18 used an EBSD dataset of an inherited α_s microstructure which was centred on a triple point between three prior β grains. The reconstruction technique is validated using a metastable β alloy in section 4.6.3. In the remaining sections, the suitability of the reconstruction technique to different map resolutions and α_s microstructures formed under a variety of cooling rates is explored.

4.6.1 Theoretical Aspects of the Method

The following section gives the important theoretical aspects of the β reconstruction technique, which is primarily based on the paper by Humbet *et al.* (1995).

4.6.1.1 Determination of the Inherited α_s Variants for a Given β Orientation

The crystallographic orientation of a cubic β crystal can be expressed by a rotation g^{β}, which transforms the sample coordinate system into the crystal coordinate system. Due to the symmetry of the cubic crystal, g^{β} can be expressed by a set of 24 rotations given by:

$$S_1^{\beta} g^{\beta},...S_i^{\beta} g^{\beta},...S_{24}^{\beta} g^{\beta} \tag{4.3}$$

Where $S_1^{\beta}...S_i^{\beta}...S_{24}^{\beta}$ are the 24 rotations of the cubic symmetry group (listed in section 2.5.1.3). The Burgers relation, which describes the orientation relation between the α and β lattices (equation 2.3) can also be expressed as a rotation D, which in matrix form is given by

$$D = \begin{bmatrix} -0.5\left(1+1/\sqrt{6}\right) & 0.5\left(1/\sqrt{3}-1/\sqrt{2}\right) & 1/\sqrt{2} \\ 0.5\left(1+1/\sqrt{6}\right) & -0.5\left(1/\sqrt{3}-1/\sqrt{2}\right) & 1/\sqrt{2} \\ -0.5\left(1-2/\sqrt{6}\right) & 0.5\left(1/\sqrt{3}+2/\sqrt{2}\right) & 0 \end{bmatrix} \tag{4.4}$$

The orientations of the inherited α variants, g^{α}, are therefore given by

$$DS_1^{\beta} g^{\beta},...DS_i^{\beta} g^{\beta},...DS_{24}^{\beta} g^{\beta} \tag{4.5}$$

Due to the symmetry of the hexagonal crystal, each inherited α variant can be expressed by a set of 12 rotations. Thus to fully characterise the possible α orientations, equation 4.5 becomes:

$$S_j^{\alpha} DS_1^{\beta} g^{\beta},...S_j^{\alpha} DS_i^{\beta} g^{\beta},...S_j^{\alpha} DS_{24}^{\beta} g^{\beta} \tag{4.6}$$

At first sight, equation 4.6 suggests that there should be 24 possible α orientations depending on the identity of S_i^{β}, with S_j^{α} forming the full set of symmetrically equivalent rotations. However, Humbert *et al.* (1995) showed that there is a commutation relation between the symmetry operators and the Burgers relation such that

$${}^{H}C_{2z} D = D^{C} C_{2a} \tag{4.7}$$

This relation means that the set of 24 S_i^β 's can be split into two subsets. The first set is formed by

$$S_1^\beta ... S_{12}^\beta = E, {}^{C}C_{4z}^{+}, {}^{C}C_{2z}, {}^{C}C_{4z}^{-}, {}^{C}C_{4x}^{+}, {}^{C}C_{34}^{-}, {}^{C}C_{2f}, {}^{C}C_{32}^{-}, {}^{C}C_{31}^{+}, {}^{C}C_{2c}, {}^{C}C_{34}^{+}, {}^{C}C_{4y}^{+} \tag{4.8}$$

and the second set by

$$S_{13}^\beta ... S_{24}^\beta = {}^{C}C_{2a}, {}^{C}C_{2x}, {}^{C}C_{2b}, {}^{C}C_{2y}, {}^{C}C_{32}^{+}, {}^{C}C_{2e}, {}^{C}C_{33}^{+}, {}^{C}C_{4y}^{-}, {}^{C}C_{4x}^{-}, {}^{C}C_{33}^{-}, {}^{C}C_{2d}, {}^{C}C_{31}^{-} \tag{4.9}$$

where

$$S_{13}^\beta ... S_{24}^\beta = {}^{C}C_{2a} S_1^\beta ... {}^{C}C_{2a} S_{12}^\beta \tag{4.10}$$

It can be seen that the second set is redundant, since they are already characterised by

$$DS_{12+i}^\beta g^\beta = {}^{H}C_{2z} DS_i^\beta g^\beta \tag{4.11}$$

Thus only 12 distinct α variants can be formed from a Burgers type transformation of a given β orientation and equation 4.6 becomes

$$S_j^\alpha DS_1^\beta g^\beta , ... S_j^\alpha DS_i^\beta g^\beta , ... S_j^\alpha DS_{12}^\beta g^\beta \tag{4.12}$$

With S_i^β restricted to the half set of 12 rotations given in (4.8).

4.6.1.2 Determination of the Potential Orientations for the Parent β Crystal for a Given α_s Orientation

The crystallographic orientation of a hexagonal α crystal can be expressed by a rotation g^α. Due to the symmetry of the hexagonal crystal, g^α can be expressed by a set of 12 rotations given by:

$$S_1^\alpha g^\alpha , ... S_j^\alpha g^\alpha , ... S_{12}^\alpha g^\alpha \tag{4.13}$$

where $S_1^\alpha ... S_j^\alpha ... S_{12}^\alpha$ are the 12 rotations of the hexagonal symmetry group (listed in section 2.5.1.3). The potential orientations of the β parent crystal, g^β, are therefore given by

$$D^{-1}S_1^\alpha g^\alpha, ... D^{-1}S_j^\alpha g^\alpha, ... D^{-1}S_{12}^\alpha g^\alpha \tag{4.14}$$

Due to the symmetry of the cubic crystal, each potential orientation for the parent β can be expressed by a set of 24 rotations. Thus to fully characterise the potential parent β orientations, equation 4.14 becomes:

$$S_i^\beta D^{-1}S_1^\alpha g^\alpha, ... S_i^\beta D^{-1}S_j^\alpha g^\alpha, ... S_i^\beta D^{-1}S_{12}^\alpha g^\alpha \tag{4.15}$$

At first sight, equation 4.15 suggests that there should be 12 potential orientations for the parent β depending on the identity of S_j^α, with S_i^β forming the full set of symmetrically equivalent rotations. However, due to the commutation relation in equation 4.7, the set of 12 S_j^α's can be split into two subsets. The first set formed by

$$S_1^\alpha ... S_6^\alpha = E, {}^H C_{3z}^+, {}^H C_{6z}^+, {}^H C_{21}', {}^H C_{22}', {}^H C_{23}' \tag{4.16}$$

and the second set by

$$S_7^\alpha ... S_{12}^\alpha = {}^H C_{2z}, {}^H C_{6z}^-, {}^H C_{3z}^-, {}^H C_{21}'', {}^H C_{22}'', {}^H C_{23}'' \tag{4.17}$$

where

$$S_7^\alpha ... S_{12}^\alpha = \left({}^H C_{2z}\right)^{-1} S_1^\alpha ... \left({}^H C_{2z}\right)^{-1} S_6^\alpha \tag{4.18}$$

It can be seen that the second set is redundant, since they are already characterised by

$$D^{-1}S_{6+j}^\alpha g^\alpha = {}^C C_{2a} D^{-1}S_j^\alpha g^\alpha \tag{4.19}$$

Thus there are only 6 potential orientations for the β parent for a given α orientation resulting from a Burgers type transformation and equation 4.15 becomes

$$S_i^\beta D^{-1}S_1^\alpha g^\alpha, ... S_i^\beta D^{-1}S_j^\alpha g^\alpha, ... S_i^\beta D^{-1}S_6^\alpha g^\alpha \tag{4.20}$$

With S_j^α restricted to the half set of 6 rotations in (4.16).

4.6.1.3 Determination of the Potential Orientations for the Parent β Crystal for a Misorientation Formed Between Two Inherited α_s Orientations

With a single α orientation it is not possible to find the correct parent β orientation from the six potential ones calculated using equation 4.20. However, by analysing the misorientation between two different α orientations inherited from the same parent, the number of potential solutions is reduced to four or less and in many cases leads to a single solution (Germain *et al.*, 2007). Humbert *et al.* (1995) showed how one can calculate the potential solutions from a misorientation between two inherited α variants.

If we know the orientation of two different α variants inherited from the same β grain, $g^{\alpha'}$ and $g^{\alpha''}$, then according to equation 4.12, these orientations are related to the orientation of the parent, g^{β}, by

$$g^{\alpha'} = S^{\alpha}_{j_1} DS^{\beta}_{i_1} g^{\beta} \tag{4.21}$$

and

$$g^{\alpha''} = S^{\alpha}_{j_2} DS^{\beta}_{i_2} g^{\beta} \tag{4.22}$$

In which the indices i_1 and i_2, determining the cubic symmetry elements, and j_1 and j_2, determining the hexagonal symmetry elements, are fixed but unknown. The misorientation between the two variants is formed by

$$\begin{aligned} g^{\alpha'}\left(g^{\alpha''}\right)^{-1} &= S^{\alpha}_{j_1} DS^{\beta}_{i_1} g^{\beta}\left(S^{\alpha}_{j_2} DS^{\beta}_{i_2} g^{\beta}\right)^{-1} \\ &= S^{\alpha}_{j_1} DS^{\beta}_{i_1}\left(S^{\beta}_{i_2}\right)^{-1} D^{-1}\left(S^{\alpha}_{j_2}\right)^{-1} \end{aligned} \tag{4.23}$$

In equation 4.23, the product of $S^{\beta}_{i_1}$ and $\left(S^{\beta}_{i_2}\right)^{-1}$ is another rotation also belonging to the set of 24 rotations of the cubic symmetry group, which we will define as S^{β}_{k}, thus equation 4.23 becomes

$$g^{\alpha'}\left(g^{\alpha''}\right)^{-1} = S^{\alpha}_{j_1} DS^{\beta}_{k} D^{-1}\left(S^{\alpha}_{j_2}\right)^{-1} \tag{4.24}$$

In equation 4.24, the rotation $DS^{\beta}_{k} D^{-1}$ completely determines the misorientation, whereas $S^{\alpha}_{j_1}$ and $S^{\alpha}_{j_2}$ merely describe the symmetrically equivalent misorientations. When $S^{\beta}_{k} = E$, i.e. the identity matrix, then $g^{\alpha'}$ and $g^{\alpha''}$ must be from the same variant.

Thus, at first sight, equation 4.24 suggests that there are 23 possible misorientations between different inherited variants depending on the identity of S_k^β. However, if the set of 24 S_k^β's is split into the two half sets given in (4.8) and (4.9), then the misorientations formed by the second half set can be can be expressed in terms of the first set by

$$DS_{13\ldots24}^{\beta}D^{-1} = D^{C}C_{2a}S_{1\ldots12}^{\beta}D^{-1} \tag{4.25}$$

Due to the commutation relationship in (4.7), it can be seen that the second set of misorientations is redundant, since they are already characterised by

$$^{H}EDS_{13\ldots24}^{\beta}D^{-1\,H}E = {}^{H}C_{2z}DS_{1\ldots12}^{\beta}D^{-1\,H}E \tag{4.26}$$

Thus, using the first half set, we can restrict the study to 11 possible misorientation types between different inherited variants

$$S_{j_1}^{\alpha}DS_k^{\beta}D^{-1}\left(S_{j_2}^{\alpha}\right)^{-1} \quad \text{for } 2 \le k \le 12 \tag{4.27}$$

Using the triplet of rotations $S_{j_1}^{\alpha}$, S_k^{β} and $S_{j_2}^{\alpha}$ that solve (4.27), one can find potential parent orientations for the misorientation. For all of the misorientation types i.e. S_k^{β} where $2 \le k \le 12$, there is a common solution, **A**, for the parent β crystal given by

$$\textbf{A.} \quad S_{i_1}^{\beta}g^{\beta} = \left(S_{j_1}^{\alpha}D\right)^{-1}g^{\alpha'} \text{ or } S_{i_2}^{\beta}g^{\beta} = \left(S_{j_2}^{\alpha}D\right)^{-1}g^{\alpha''} \tag{4.28}$$

For the misorientations S_k^{β} where $k = 2, 4, 5, 7, 8, 9, 10$ *and* 12, this is the only solution. Thus 8 out of the 11 misorientation types lead to a single solution for g^{β}. Humbert *et al.* (1995) showed that for the misorientations S_k^{β} where $k = 3, 6$ *and* 11 i.e. ${}^{C}C_{2z}$, ${}^{C}C_{34}^{-}$ and ${}^{C}C_{34}^{+}$ respectively, there are additional solutions for g^{β}. For $S_3^{\beta} = {}^{C}C_{2z}$, there are two additional solutions, **B** and **C**, given by

$$\textbf{B.} \quad S_{i_1}^{\beta}g^{\beta} = \left({}^{H}C_{3z}^{+}\right)^{-1}\left(S_{j_1}^{\alpha}D\right)^{-1}g^{\alpha'} \text{ or } S_{i_2}^{\beta}g_{\beta} = \left({}^{H}C_{3z}^{+}\right)^{-1}\left(S_{j_2}^{\alpha}D\right)^{-1}g^{\alpha''} \tag{4.29}$$

and

$$\textbf{C.} \quad S_{i_1}^{\beta}g^{\beta} = \left({}^{H}C_{6z}^{+}\right)^{-1}\left(S_{j_1}^{\alpha}D\right)^{-1}g^{\alpha'} \text{ or } S_{i_2}^{\beta}g^{\beta} = \left({}^{H}C_{6z}^{+}\right)^{-1}\left(S_{j_2}^{\alpha}D\right)^{-1}g^{\alpha''} \tag{4.30}$$

For $S_6^{\beta} = {}^{C}C_{34}^{-}$ and $S_{11}^{\beta} = {}^{C}C_{34}^{+}$ there is one additional solution, given by

$$\textbf{D.} \quad S_{i_1}^{\beta} g^{\beta} = \left({}^{H}C_{22}^{'}\right)^{-1} \left(S_{j_1}^{\alpha} D\right)^{-1} g^{\alpha'} \text{ or } S_{i_2}^{\beta} g^{\beta} = \left({}^{H}C_{22}^{'}\right)^{-1} \left(S_{j_2}^{\alpha} D\right)^{-1} g^{\alpha''} \qquad (4.31)$$

The potential solutions according to the identity of the rotation S_k^{β} are summarised in Table 4.1.

Table 4.1 Potential parents according to S_k^{β}.

k	S_k^{β}	Solutions for g^{β}
2	${}^{c}C_{4z}^{+}$	**A**
3	${}^{c}C_{2z}$	**A, B or C**
4	${}^{c}C_{4z}^{-}$	**A**
5	${}^{c}C_{4x}^{+}$	**A**
6	${}^{c}C_{34}^{-}$	**A or D**
7	${}^{c}C_{2f}$	**A**
8	${}^{c}C_{32}^{-}$	**A**
9	${}^{c}C_{31}^{+}$	**A**
10	${}^{c}C_{2c}$	**A**
11	${}^{c}C_{34}^{+}$	**A or D**
12	${}^{c}C_{4y}^{+}$	**A**

4.6.2. Automatic Reconstruction of the β Map From the α_s Map

As explained in section 4.6.1.2, for a given α_s orientation resulting from a Burgers type transformation, there are six potential solutions for the parent β orientation. Thus, in order to successfully reconstruct an α_s orientation, one must find which of these six solutions is the correct one. If the correct solution is found, it can be applied to all α_s orientations within a variant to calculate the equivalent set of β orientations. The automated reconstruction program uses such an approach to reconstruct the β orientations for each α_s variant in turn. In order to choose the correct solution for reconstructing each variant from the six potential ones, the misorientations between points at the edges of a variant and the adjacent points in adjacent variants are examined i.e. the points on either side of the variant boundaries. As explained in section 4.6.1.3, using the misorientation between two different inherited α_s orientations, the number of potential solutions for the parent is reduced from 6 to 3 or less but in most cases to a single unique solution. Thus, by compiling the results of these misorientation analyses between points in the variant and adjacent points in adjacent variants, the correct solution should be that which is

obtained most often. Such an approach leads to a single solution in the vast majority of cases, enabling the majority of α_s variants to be successfully reconstructed in a first pass of the reconstruction procedure. In certain cases, the misorientation analyses for a variant may give equal weighting to two or three potential solutions and in these cases it is not possible to select a single correct solution. This means that a small fraction of variants remain unreconstructed after the first pass of the reconstruction procedure. However, most of these unsolved variants can be reconstructed in a second pass of the procedure now that the β orientations for the majority of adjacent variants are known. Using this additional information, allows one to select the correct solution from the potential solutions which had equal weighting.

In the remainder of this section, the various aspects of the reconstruction procedure are explained in more detail using an α_s dataset as an example. The raw dataset for this example is shown in Fig 18(a) and is a map containing α_s variants, centred on the triple point between three parent β grains. The reconstruction procedure can be broken down into the following stages:

(1) Extrapolate non indexed points in the original α_s dataset.
(2) Primary reconstruction
    (i) Detecting variants
    (ii) Calculating the average α_s orientation of a variant
    (iii) Calculating a reference set of 6 potential β solutions for a variant using the average α_s orientation
    (iv) Misorientation analyses between adjacent α_s points from adjacent variants
    (v) Compiling the misorientation analyses for a variant to find its correct solution
    (vi) Using the correct solution to calculate β orientations for all α_s points in a variant
(3) Secondary reconstruction
(4) Converting β orientations to the reduced Euler space used by HKL software

(1) Extrapolate non indexed points in the original α_s dataset.

Before running the reconstruction program, it is first necessary to extrapolate the non indexed points in the map. This is necessary because the subsequent reconstruction stages require that there are adjacent α_s pixels in adjacent variants. In EBSD maps there are quite often non indexed points in the region of grain/variant boundaries due to either poor pattern quality resulting from imperfections in the crystal structure close to the boundaries, or because the Kikuchi pattern obtained is actually composed of two overlapping patterns (one from each grain/variant) and thus cannot be indexed. Additionally, on the boundaries between variants in Widmanstätten α_s microstructures,

there are thin films of retained β phase, which for many alloy compositions are too thin to be indexed using EBSD but will be a contributing factor to the number of non indexed points at the variant boundaries.

The raw EBSD data for the example shown in Fig. 4.18(a), was 64% indexed. The non indexed points are extrapolated from neighbouring indexed points using the standard routine in the HKL Tango program. The resulting extrapolated map is shown in Fig. 4.18(b). For stage 2, the data from this map is exported into the CTF file format, so that it can be opened in the post-processing program.

(2) Primary reconstruction

(i) Detecting variants

Since the reconstruction proceeds on a variant by variant basis, the program must have a means of identifying the points belonging to each variant. This detection routine is based on a user defined minimum misorientation (typically 3°). Variants are defined as regions of points completely enclosed by boundaries with misorientations greater than this value. For each point in the map, the misorientation with the point below and the point to the right is calculated and stored in a 2 dimensional array. This misorientation array is then used to find the extent of each variant, with each identified variant being assigned a unique variant identification number. The first point in the map is assigned to variant number 1 and neighbouring points are assigned to this variant in a spiral-like manner until the grain is completely bounded by boundaries greater than the minimum value. After reconstructing this variant, the program proceeds to the next unassigned point in the map, which is assigned to variant number 2 and neighbouring points are added to this variant in the same way. The identification and reconstruction of variants continues until all of the points in the map have been assigned a variant identification number. Fig. 4.18(c) shows a boundary map for misorientations greater than 3° to show the extent of each identified variant in the map.

(ii) Calculating the average α_s orientation of a variant

From the set of α_s orientations in a variant, the average α_s orientation is calculated using quaternions as explained in section 2.5.1.5. As discussed in this section, in order to avoid averaging errors due to crystal symmetry and the 'Umklapp' effect, the Euler space populated by the raw EBSD data must be reduced to the fundamental zone using the symmetry of the hexagonal crystal structure and turned towards the centre of this zone using the inverse of one of the orientations in the set. The first point to be assigned the variant's identification number is used as the reference orientation for this 'Umklapp'

rotation. After calculating the average orientation for the set, the inverse of the Umklapp rotation is applied to the average to return it to the correct reference frame.

(iii) Calculating a reference set of 6 potential β solutions for a variant using the average α_s orientation

Using the average α_s orientation for a variant, the set of six potential parent orientations, G_1^{β}, G_2^{β}, ... G_6^{β}, is calculated from it using equation 4.20, derived in section 4.6.1.2. These six orientations now act as the reference set against which the solutions derived from the misorientation analyses can be compared.

(iv) Misorientation analyses between adjacent α_s points from adjacent variants

For each variant, misorientation analyses based on section 4.6.1.3 are carried out between every point along the border of the variant and the adjacent points in adjacent variants. Each misorientation matrix between two adjacent points is compared with the ideal misorientation matrices that are formed by every possible combination of $S_{j_1}^{\alpha}$, S_k^{β} and $S_{j_2}^{\alpha}$, that form the triplet in equation 4.27. The triplet whose ideal misorientation matrix has the minimum misorientation angle with respect to the measured misorientation matrix is selected as the most probable solution and the value of this misorientation gives the deviation from the ideal Burgers orientation relation. If this deviation is below a user defined value (typically 4°), then the experimental misorientation is accepted as a Burgers type orientation relation, which means it is likely that both points were inherited from the same parent β grain. When this condition is met, then the identity of $S_{j_1}^{\alpha}$ and S_k^{β} in the triplet is used to calculate between 1 and 3 potential solutions for the parent orientation of the point in the variant. The calculation of the potential g^{β} orientations is made using one or more of equations 4.28 to 4.31. The number of potential solutions (between 1 and 3) and which of these equations is used for a particular point depends on the identity of S_k^{β} in the chosen triplet as shown in Table 4.1. In the case of the example, the points involved in these misorientation analyses are shown in Fig. 4.18(d) coloured blue.

(v) Compiling the misorientation analyses for a variant to find its correct solution

For each variant, the potential solutions calculated from the misorientation analyses are compared with the 6 reference orientations, $G_{i=1\rightarrow 6}^{\beta}$, that were calculated from the variant's average orientation. If the misorientation, ε, between a potential solution and one of the reference orientations is less than a user defined value, ε_0, then a coincidence number, r_i, for the reference orientation is incremented by 1. When the results of all the

misorientation analyses for a variant have been compiled in this way, one of the coincidence numbers is usually higher than any other. In this case, *i*, characterises which of the six potential parent solutions is the correct one for reconstructing the β orientations in the variant.

To demonstrate this method of obtaining the correct solution, we will focus on a particular variant in the example dataset. This variant is shaded grey in Fig. 4.18(e). Fig. 4.18(f) shows the same variant in detail with the results of the misorientation analyses indicated by different colours on the variant's boundary. Parts of the variant's boundary which remain black are misorientations which were not accepted as a Burgers orientation relation. These may indicate that a prior β boundary exists between these points. Boundaries which comprise of a single colour mean that the misorientation analysis produced a single solution for the parent whereas boundaries comprising two colours mean there were two potential solutions. In this particular case, there were no misorientations which led to three potential solutions. The coincidence number for each potential solution is shown graphically in Fig. 4.18(g). The highlighted variant will be reconstructed using the solution with the highest coincidence number, which in this case is G_2^{β}.

(vi) Using the correct solution to calculate β orientations for all α_s points in a variant

When a correct solution is found for a variant, this solution is then used to calculate a β orientation for all the α_s points in the variant. Fig. 4.18(h) is an IPF map showing the reconstructed β variants after the primary reconstruction. The vast majority of identified variants (127 out of 135), were reconstructed in this primary reconstruction. The map can be seen to contain three β grains and it is now clear that in the case of the highlighted variant, the parts of the boundary that did not meet the burgers orientation relation are the boundaries between the β grains. The coincidence number of 6 obtained for G_5^{β} (Fig. 4.18(g) also arose from misorientations on a prior β boundary. These are examples of cases where the misorientation between adjacent variants inherited from different parent β grains coincides with the Burgers orientation relation. However, these false solutions are clearly outnumbered by the much higher coincidence number which was obtained for G_2^{β}. The morphology of the variants is such that even if a large part of a β boundary coincided with the Burgers orientation relation, the variants affected are likely to have a larger portion of their boundaries in contact with other variants inherited from the same parent β grain. Thus in almost all cases, there will still be a higher coincidence number for the correct solution. This is supported by the reconstructed map for the example because there are no apparent reconstruction errors due to these 'coincidental misorientations'.

(3) Secondary reconstruction

After the primary reconstruction, 8 variants in the example dataset remained unsolved. Some of these unsolved variants can be due to there being an equal coincidence number for two or three potential solutions. This scenario is more likely for variants in the map which have only a small number of adjacent variants inherited from the same parent grain. Such variants tend to be small and are often sited next to a β boundary or the edge of the map. In the secondary reconstruction, the reconstruction procedure is repeated for these unsolved variants. In most cases, the β orientations for the points in the adjacent variants will have been calculated in the primary reconstruction enabling an additional comparison to be made. For the misorientation analyses which give two or three potential solutions, these solutions are compared with the β orientation of the point in the misorientation, which lies in the adjacent variant. The potential solution closest to the β orientation of this point is selected as the correct solution and only the coincidence number for this solution is incremented by 1. The misorientation analyses can now be compiled in the same way and where a single solution is now found, the variant can be reconstructed in the manner described previously. Fig. 4.18(i) shows the reconstructed IPF map after the secondary reconstruction. It can be seen that a further four variants are successfully reconstructed, leaving only 4 out of 135 variants (0.52% of the points) unsolved.

(4) Converting β orientations to the reduced Euler space used by HKL software

The final stage of the reconstruction procedure is to reduce the Euler space populated by the reconstructed β orientations so that symmetrically equivalent orientations are described by a single rotation. This requires that the range of the β phase Euler angles be reduced from

$$0 \leq \phi_1, \phi_2 \leq 360, \text{ and } 0 \leq \Phi \leq 180 \tag{4.31}$$

to

$$0 \leq \phi_1 \leq 360, 0 \leq \phi_2 \leq 90, \text{ and } 0 \leq \Phi \leq \Phi_{max} \tag{4.32}$$

where Φ_{max}, depends on the value of ϕ_2. For $0 \leq \phi_2 \leq 45$, Φ_{max} is given by

$$\cos\phi_{max} = \frac{\cos\phi_2}{\sqrt{1+\cos^2\phi_2}} \tag{4.33}$$

while for $45 \leq \phi_2 \leq 90$, Φ_{max} is given by

$$\cos\phi_{max} = \frac{\cos\left(\pi/2 - \phi_2\right)}{\sqrt{1+\cos^2\left(\pi/2 - \phi_2\right)}} \tag{4.34}$$

This complex shaped subspace arises from the 3-fold symmetry axes, i.e. 120° rotations about <111> (Randle and Engler, 2000). The orientation matrix for each β orientation is multiplied by each of the 24 cubic symmetry operators until the orientation with Euler angles within the reduced range is found.

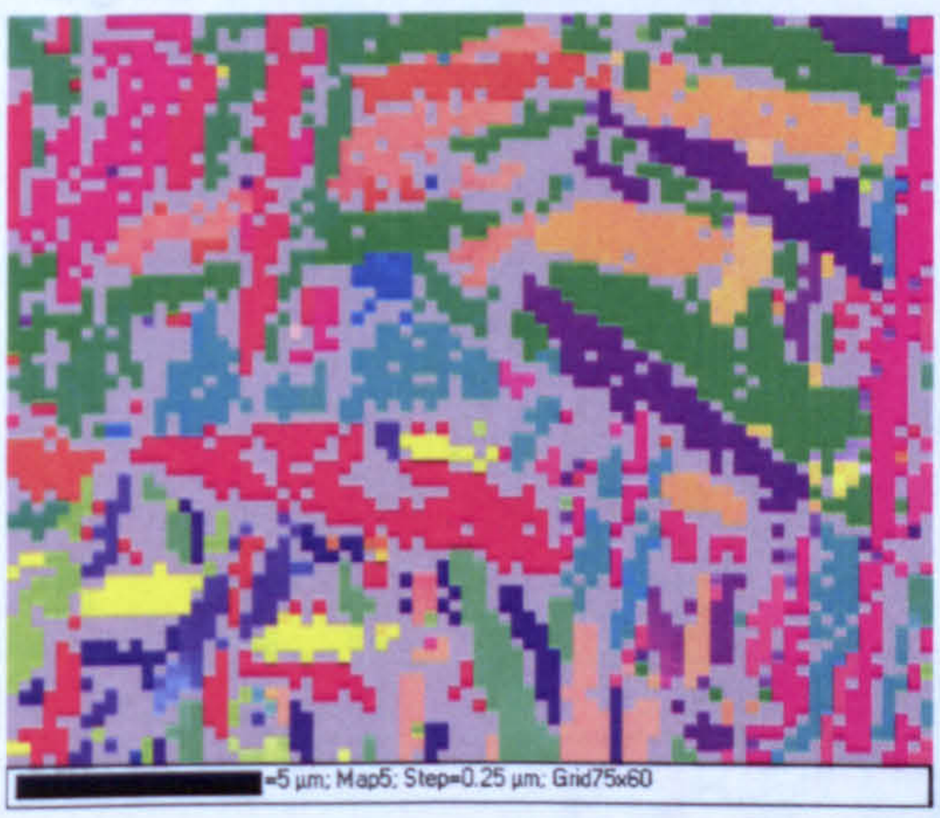

Fig. 4.18(a) Raw EBSD dataset of an α_s microstructure. 64% indexed.

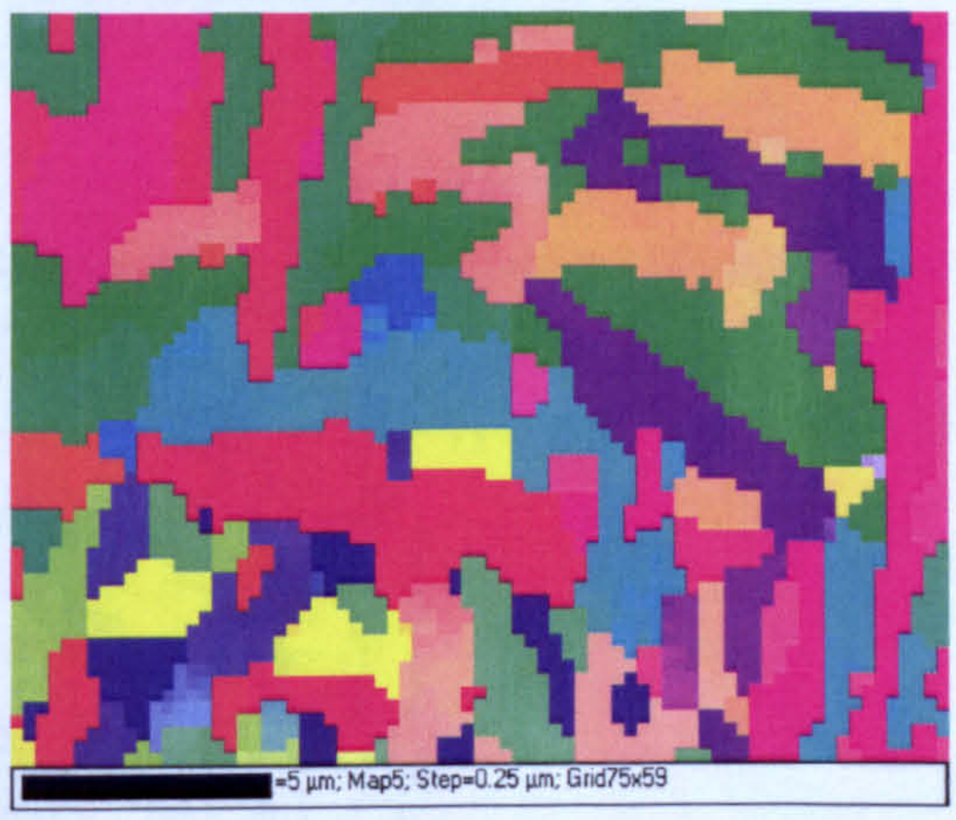

Fig. 4.18(b) Non indexed points extrapolated.

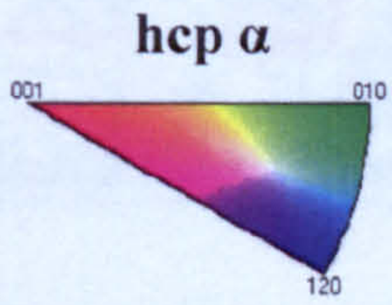

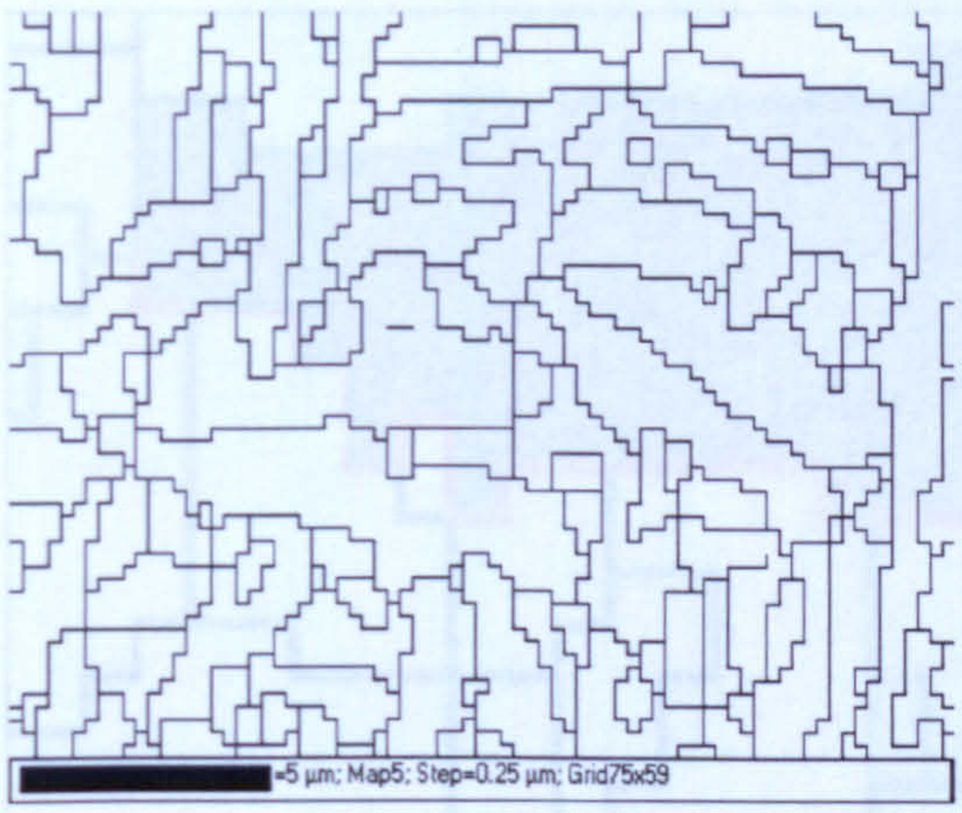

— Misorientations greater than a minimum angle (3°).

Fig. 4.18(c) A minimum misorientation angle is used to identify the extent of each α_s variant.

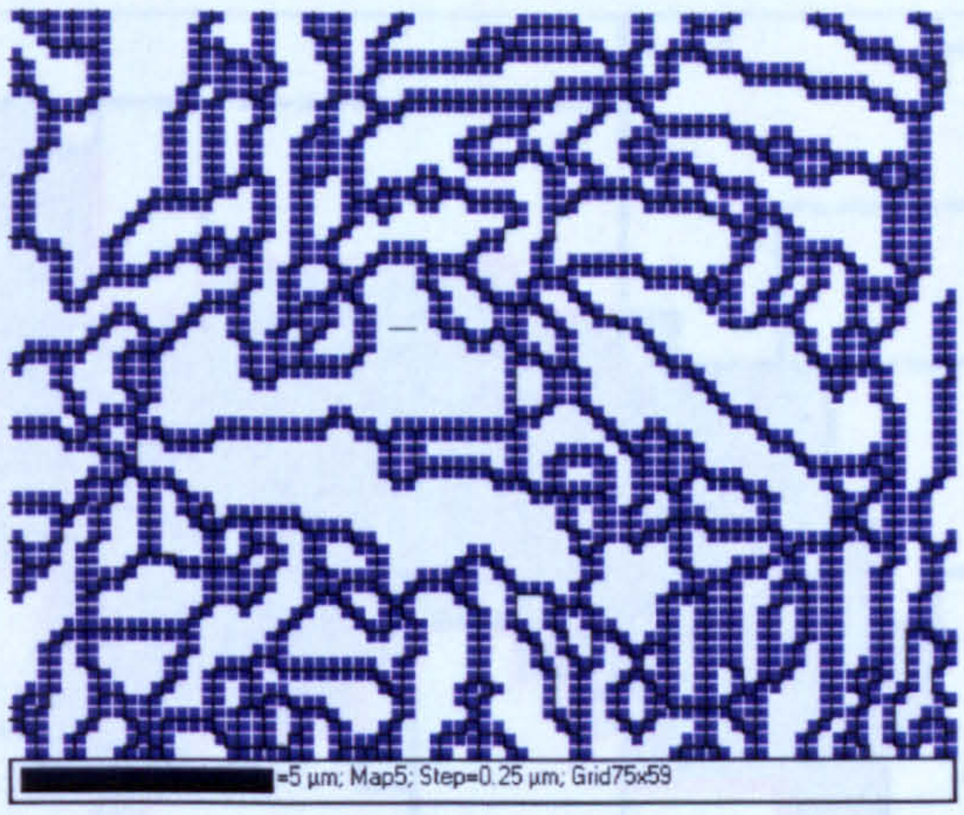

Fig. 4.18(d) Points used in the misorientation analyses for all variants.

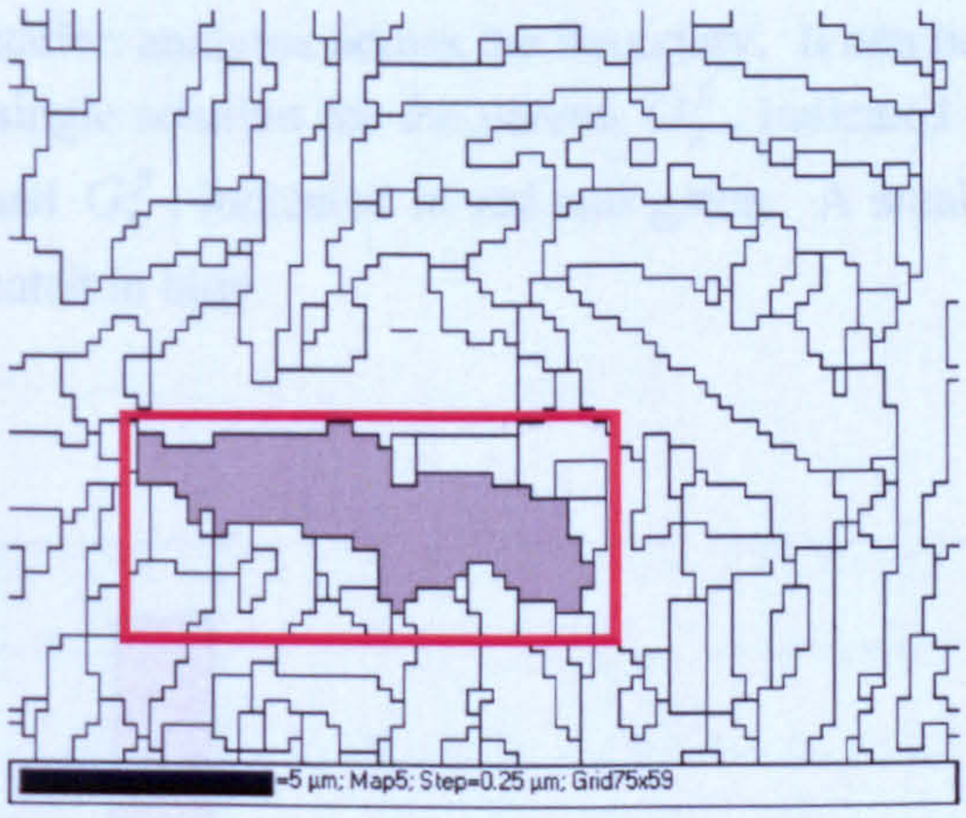

Fig. 4.18(e) The results of the misorientation analyses for variant highlighted in this map are shown in Fig. X(f) and (g) below.

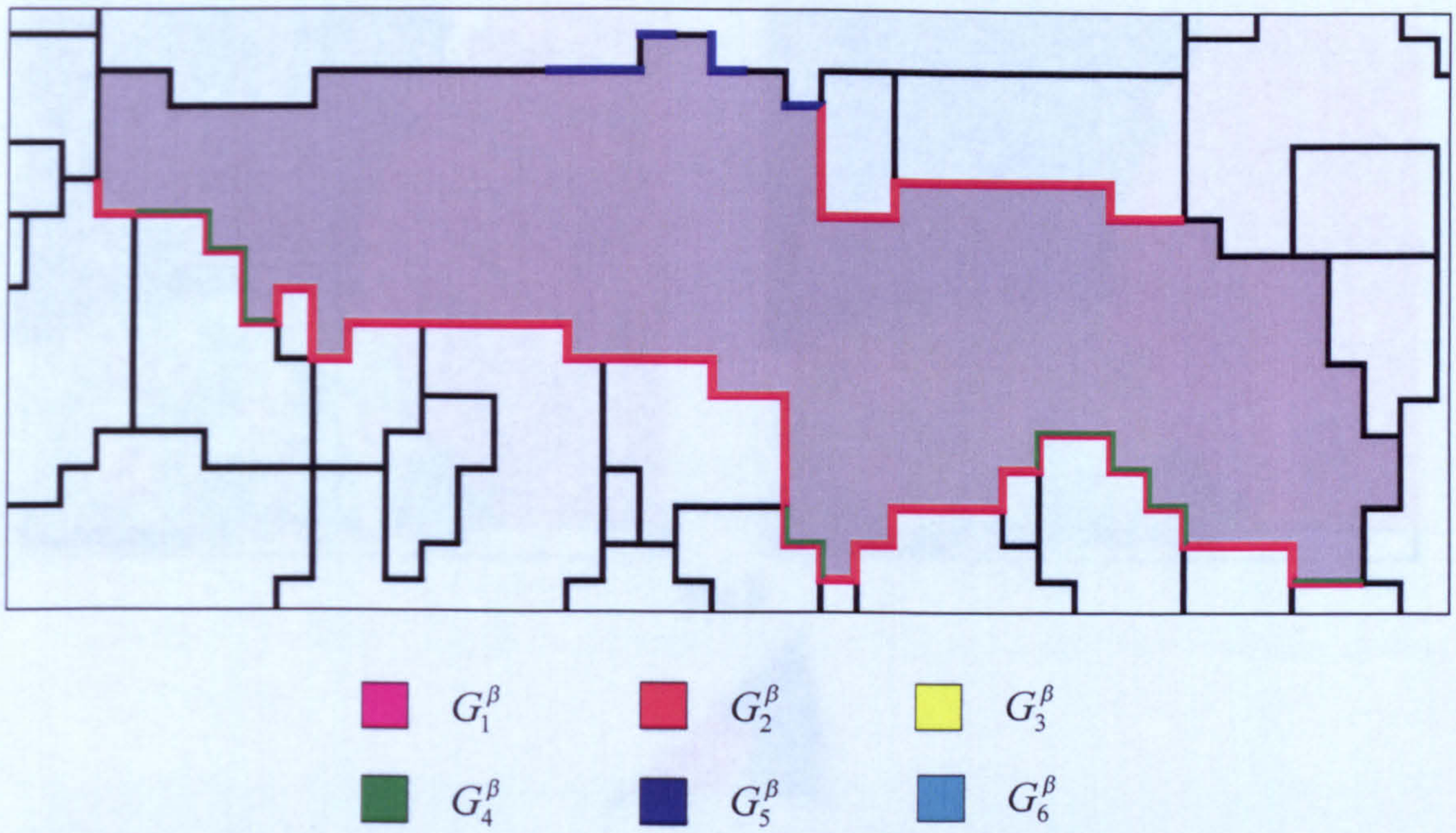

Fig. 4.18(f) The potential parent solutions for points in the variant adjacent to the boundary, derived from the misorientation analyses across the boundary. It can be seen that the majority of misorientations lead to a single solution for the parent, G_2^β, indicated in red. Some lead to two potential solutions, G_2^β and G_4^β, indicated in red and green. A small number also lead to the single solution, G_5^β, indicated in blue.

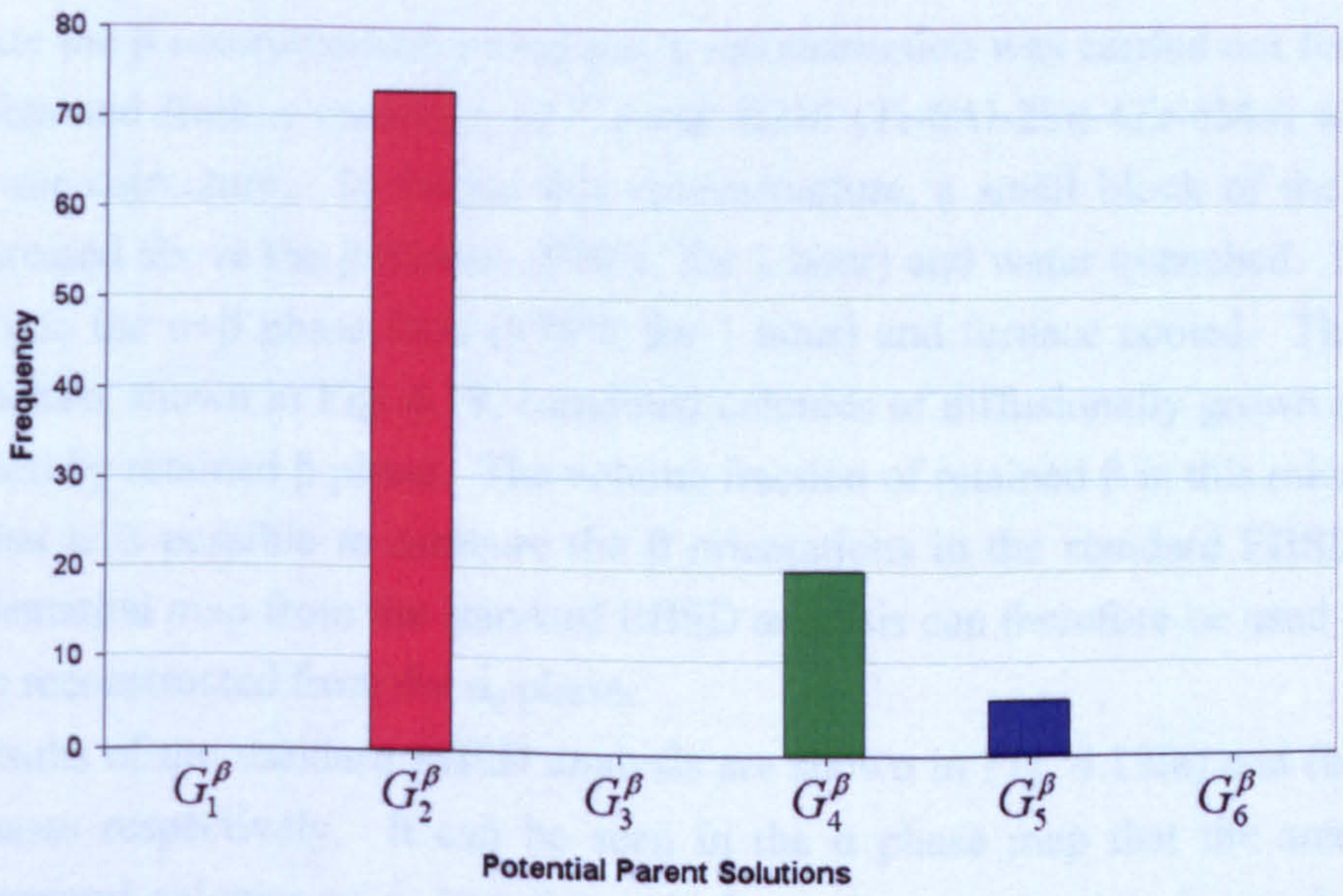

Fig. 4.18(g) Coincidence numbers for each potential solution for the highlighted variant. In this case, G_2^β would be selected as the correct solution for reconstructing the variant.

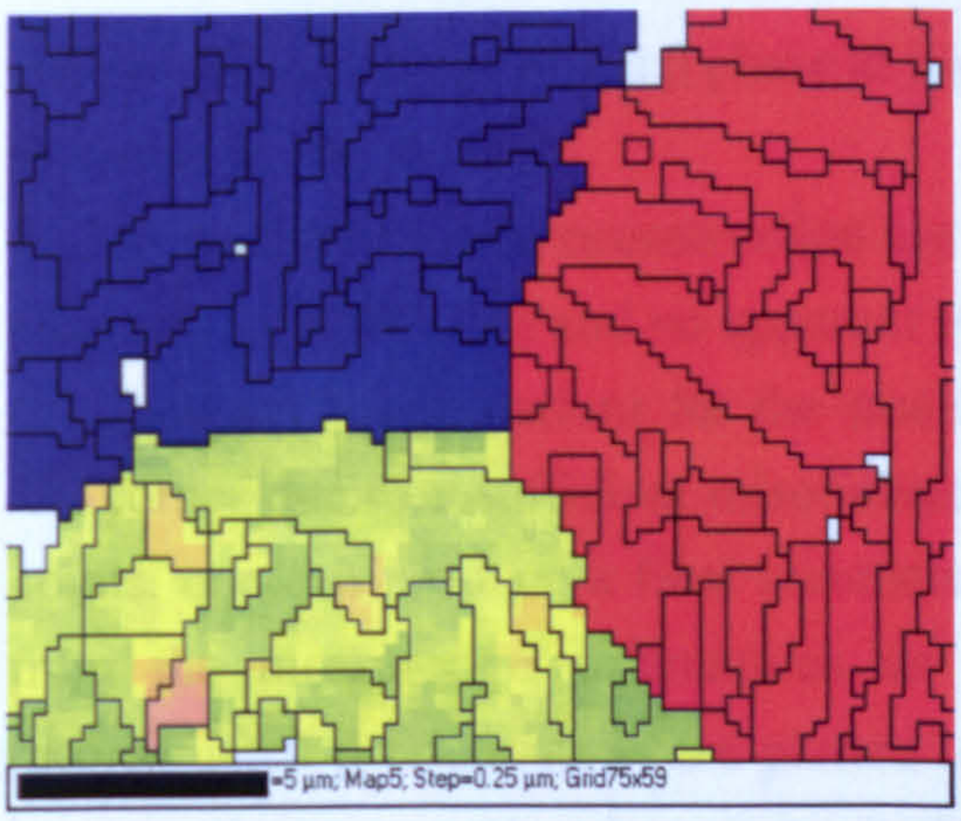

Fig. 4.18(h) IPF map of the β phase after primary reconstruction with the boundaries of the original α_s variants superimposed. Unreconstructed variants are shown in white.

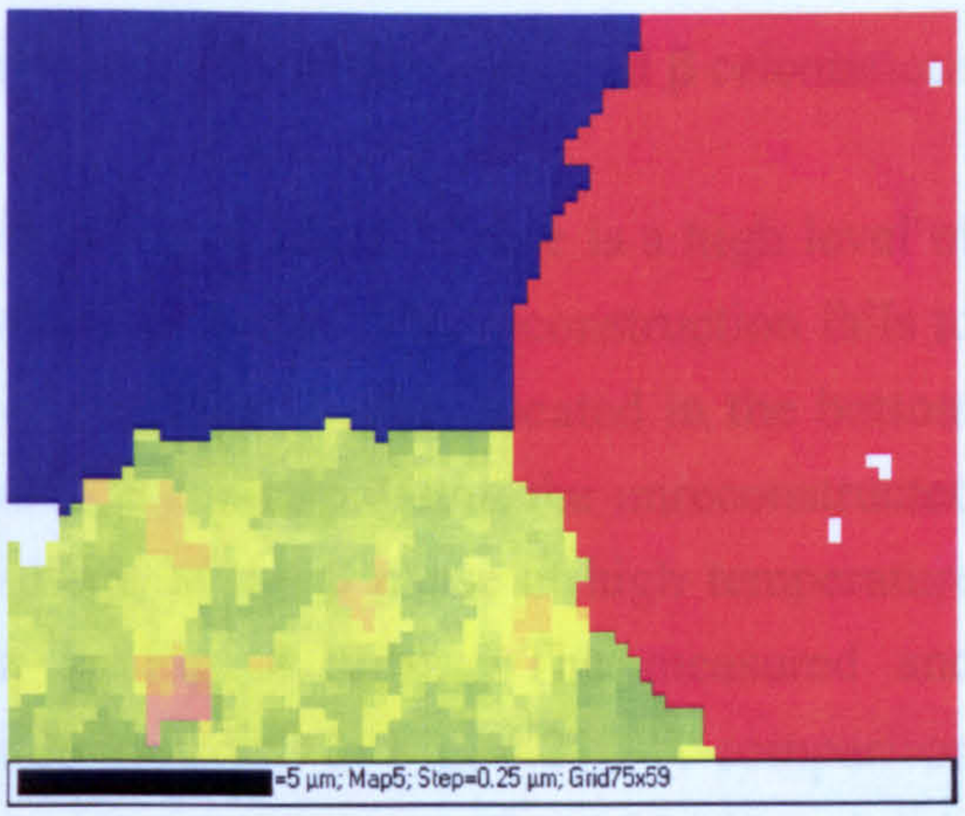

Fig. 4.18(i) IPF map of the β phase after secondary reconstruction.

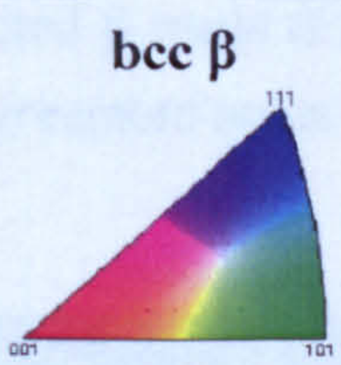

Fig. 4.18 A step by step demonstration of the variant based β reconstruction procedure.

4.6.3 Validation of the β Reconstruction Technique

To validate the β reconstruction technique, a reconstruction was carried out for an EBSD dataset obtained from a specimen of Timetal 6246 (Ti-6Al-2Sn-4Zr-6Mo) with a fully lamellar microstructure. To obtain this microstructure, a small block of the alloy was solution treated above the β transus (970°C for 1 hour) and water quenched. It was then reheated into the α+β phase field (875°C for 1 hour) and furnace cooled. The resulting microstructure, shown in Fig. 4.19, contained colonies of diffusionally grown α_s lamellae interspersed by retained β phase. The volume fraction of retained β in this microstructure is such that it is possible to measure the β orientations in the standard EBSD analysis. The β orientation map from the standard EBSD analysis can therefore be used to validate the β map reconstructed from the α_s phase.

The results of the standard EBSD analysis are shown in Fig. 4.19(a) and (b) for the α and β phases respectively. It can be seen in the α phase map that the area analysed contains several colonies of α_s lamellae, which overlap one another to varying degrees. The β phase map shows that the area analysed consists of 2 main prior β grains with a small part of a third β grain in the bottom left corner. Within these β grains, there is a small amount of false β orientations due to misindexing errors. By removing the points of misindexed β and the α phase, and then extrapolating the remaining β orientations, one

can produce an image of the β phase at high temperature from the measured β orientations as shown in Fig. 4.19(c).

The results of the β reconstruction are shown in Fig. 4.20(a). There is a high level of reconstruction (97.6%) and no apparent reconstruction errors. The reconstruction fails to calculate any β orientations for the small part of the third β grain located in the bottom left corner due to insufficient misorientation data. By extrapolating the unreconstructed points, one can produce a final reconstructed image of the β phase at high temperature from the measured α orientations as shown in Fig. 4.20(b). The measured and reconstructed β orientations are plotted in pole figure form in Fig. 4.21. A comparison between the measured and reconstructed β maps (Fig. 4.19(c) and Fig. 4.20(b)) and pole figures (Fig. 4.21) shows excellent agreement apart from the small area of the third grain already mentioned.

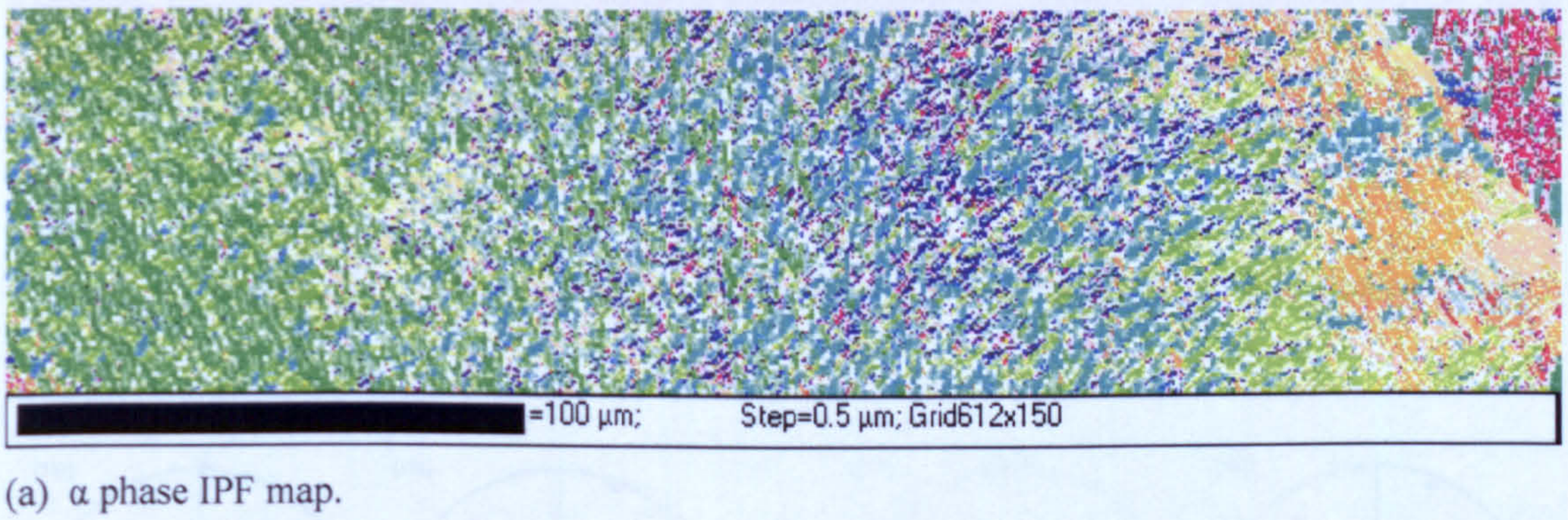

(a) α phase IPF map.

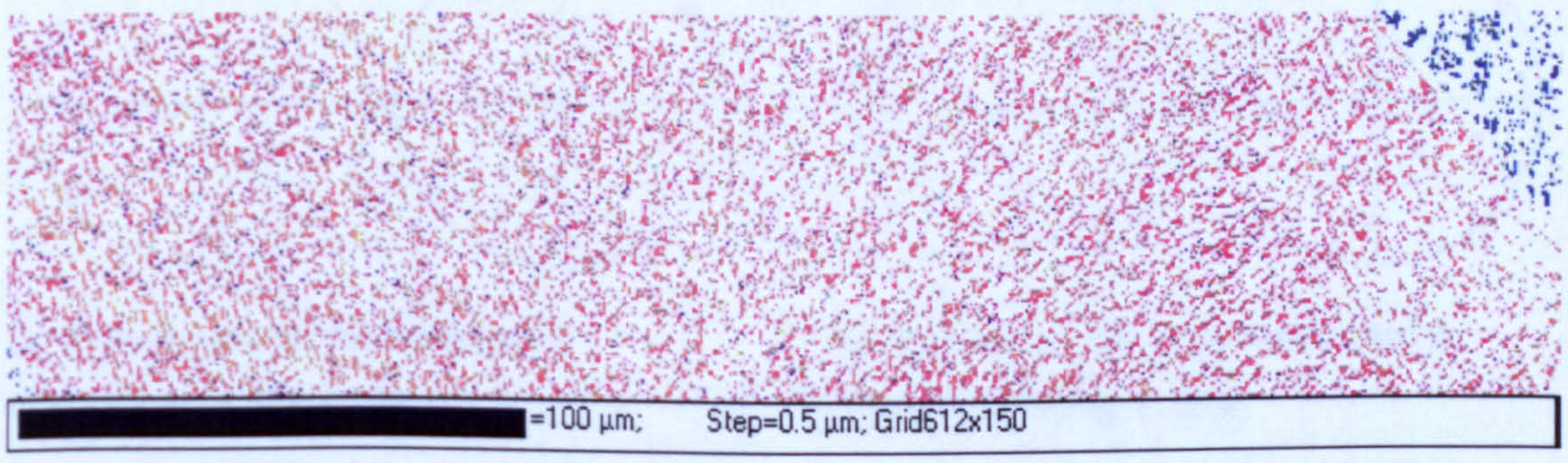

(b) β phase IPF map.

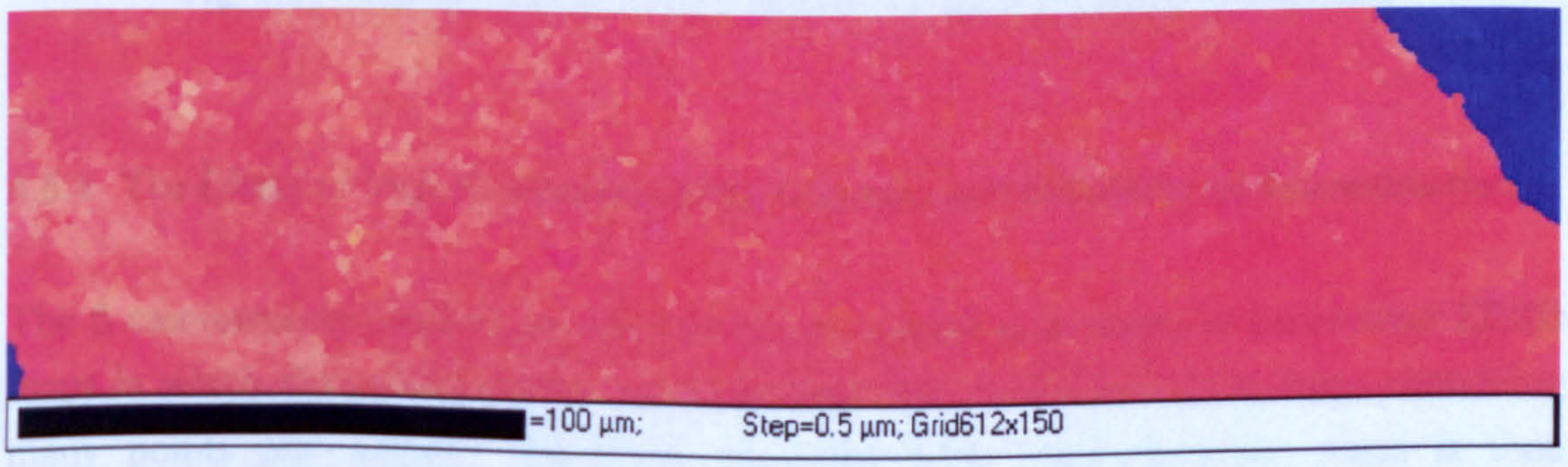

(c) Extrapolated β phase map.

Fig. 4.19 A standard EBSD analysis on a fully lamellar microstructure in Timetal 6246.

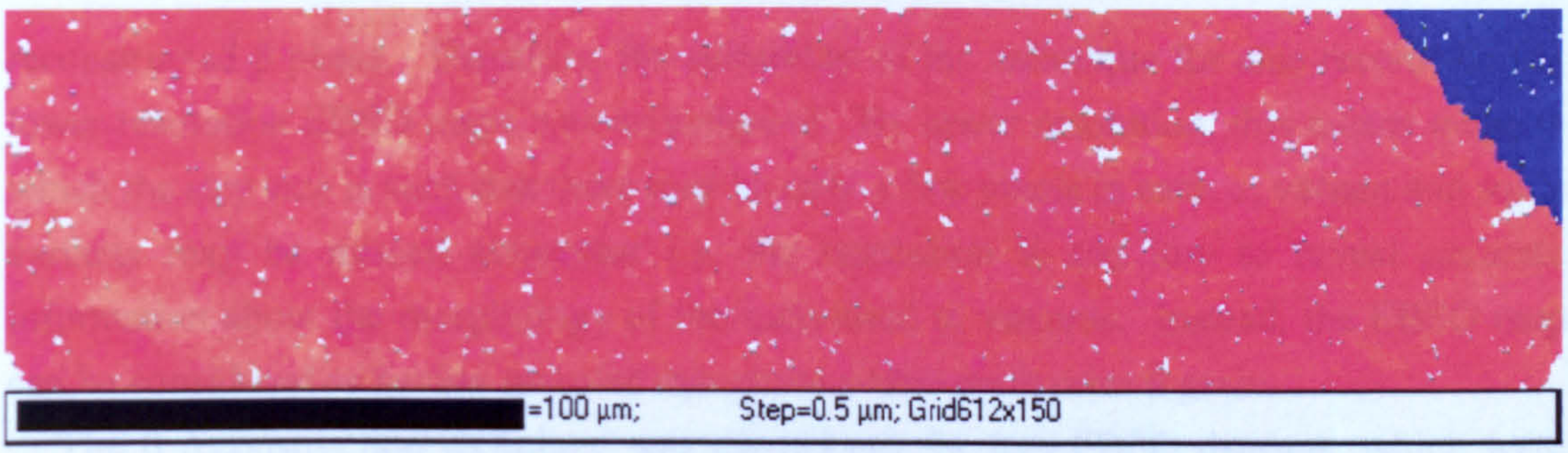

(a) The reconstructed β phase (97.6% of α_s reconstructed).

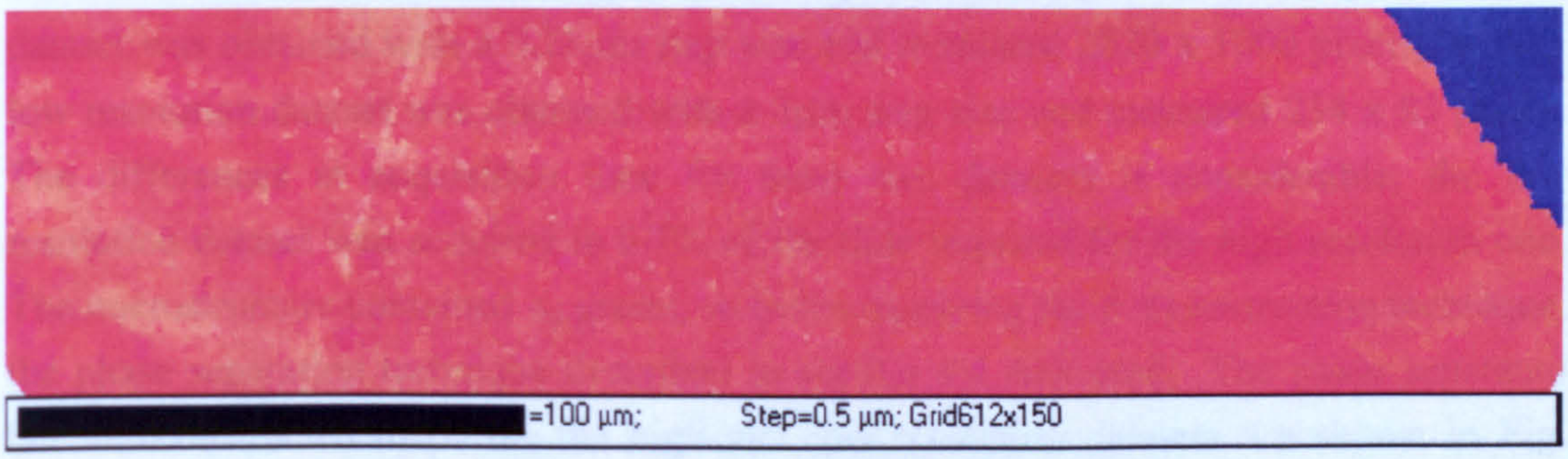

(b) The reconstructed β phase after extrapolating unreconstructed points.

Fig. 4.20 Results of the β reconstruction for the fully lamellar microstructure in Timetal 6246.

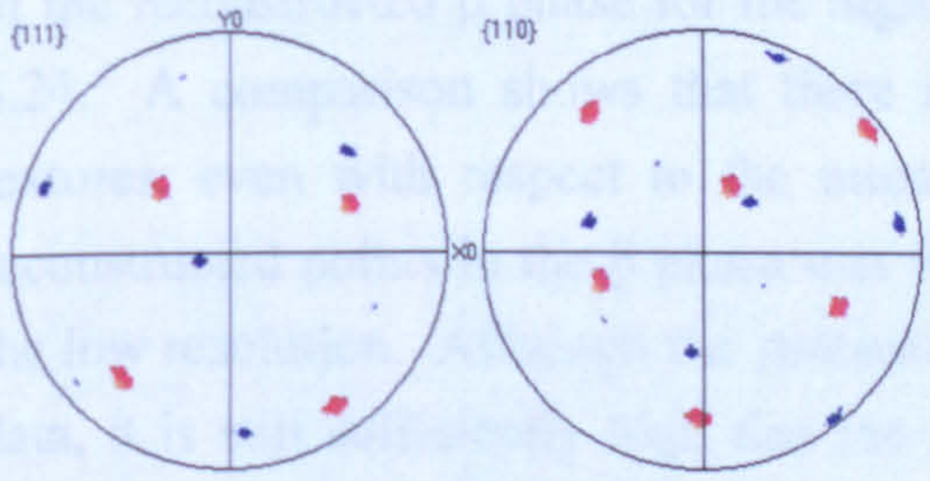

(a) Pole figures for the measured β orientations in Fig. 4.19(c).

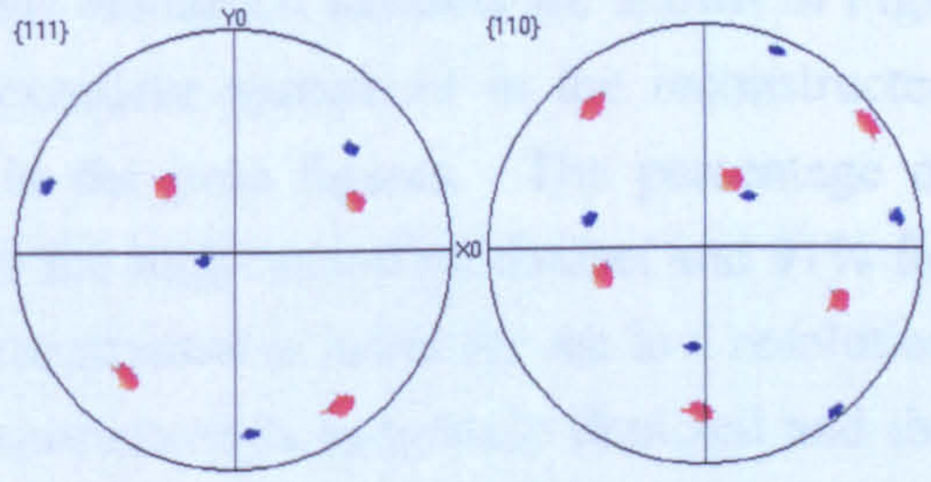

(b) Pole figures for the reconstructed β orientations in Fig. 4.20(b)

Fig. 4.21 Pole figure plots of the measured and reconstructed β orientations.

4.6.4 The Effect of Map Resolution on the Accuracy and Reliability of Reconstruction

The β reconstruction technique was initially envisaged as a means to reconstruct EBSD maps in which the transformed α_s microstructure was well resolved i.e. maps containing many points per variant. However, obtaining large high resolution maps is time consuming and as a result, it is usually unpractical to acquire maps containing a sufficient number of prior β grains to give statistically representative texture information for the

reconstructed β phase. Therefore, the suitability of the technique for also reconstructing lower resolution EBSD maps was investigated. By lower resolution, this means maps in which the step size is such that there may be only a few pixels in each α_s variant and some variants may be missed altogether i.e. the resolution is too low to reveal accurate information about the morphology of the individual α_s variants. Instead, the EBSD map can be considered as having sampled this phase within each prior β grain.

The β reconstruction technique was carried out for two EBSD datasets, which were obtained from the same area of a specimen using different step sizes. The high resolution dataset was obtained with a 0.25μm step size and measured 2820 x 1000 pixels, while a low resolution dataset was obtained with a 3μm step size and measured 234 x 83 pixels. The differences in acquisition time for these two datasets is considerable; the low resolution dataset was acquired in 0.7% of the time required for the high resolution one. The microstructure contained α_p grains, so before applying the β reconstruction technique, the phase separation technique described in section 4.4 was used. The phase separated but unreconstructed maps for the high and low resolution datasets are shown in Fig. 4.22(a) and Fig 4.23(a) respectively. The corresponding reconstructed maps are shown in Fig. 4.22(b) and Fig. 4.23(b) and after extrapolating the unreconstructed points, in Fig. 4.22(c) and Fig. 4.23(c). A comparison between the two figures shows there is good agreement between the reconstructed microstructures. Pole figures showing the textures of the reconstructed β phase for the high and low resolution datasets are shown in Figs. 4.24. A comparison shows that there is an excellent agreement in the reconstructed textures, even with respect to the intensities in the pole figures. The percentage of reconstructed points in the β phase was 98% for the high resolution dataset and 91% for the low resolution. Although the percentage reconstructed is lower for the low resolution data, it is still sufficiently high that the β microstructure is accurately depicted and the textures accurately reproduced. For the same acquisition time, an area 140 times greater can be acquired with a 3μm step size compared to a 0.25μm. This shows that the β reconstruction technique has the capability to acquire statistically representative textures using lower resolution, large area maps.

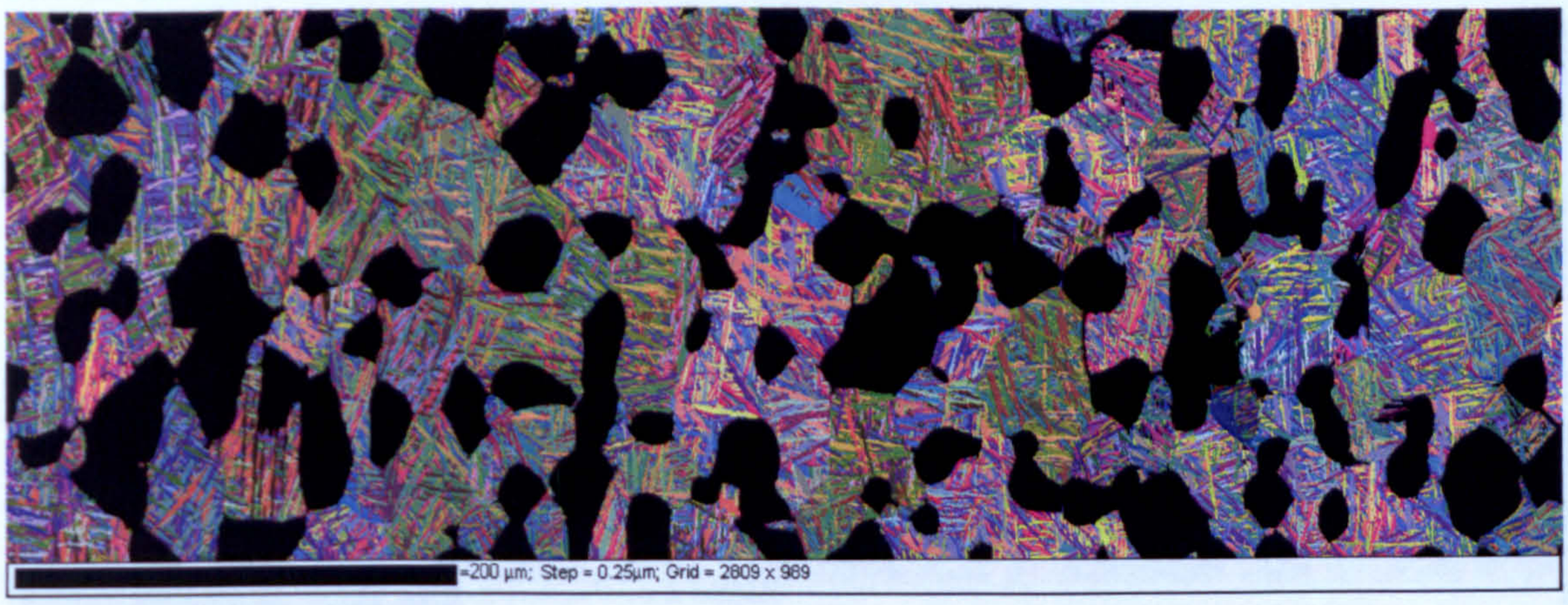

(a) The separated α_s phase (α_p grains coloured black).

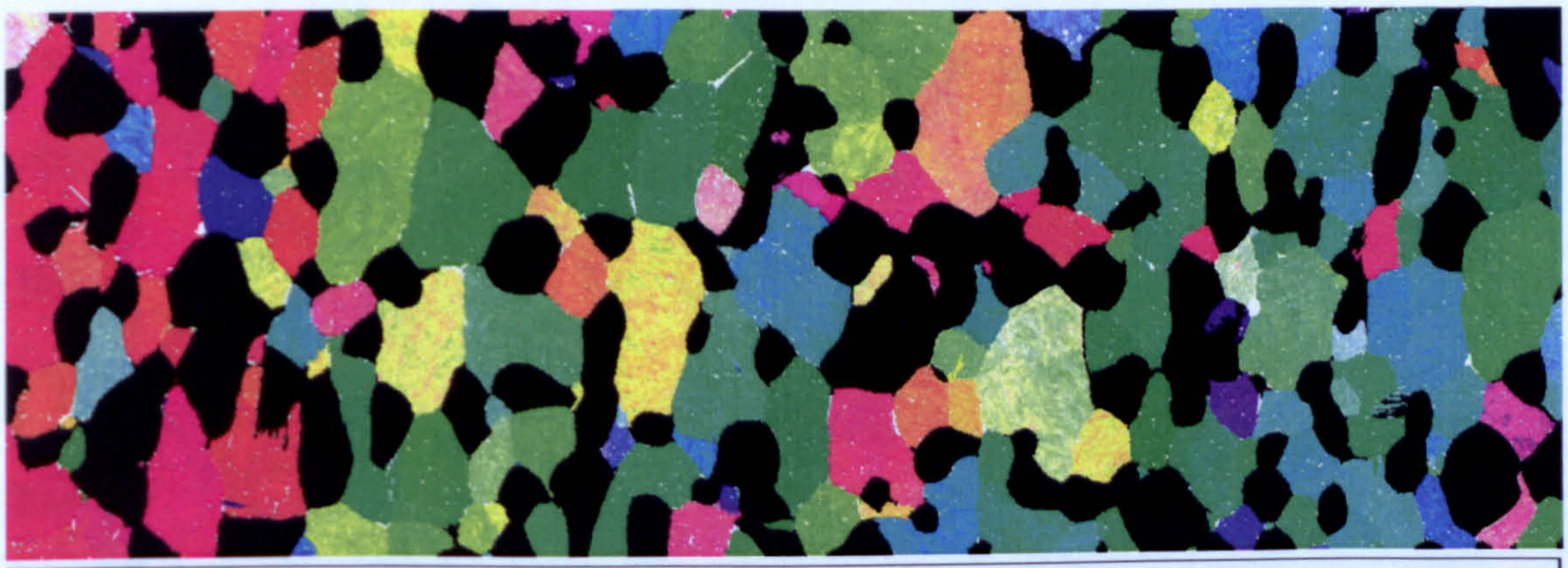

(b) The reconstructed β phase (97.7% of α_s reconstructed).

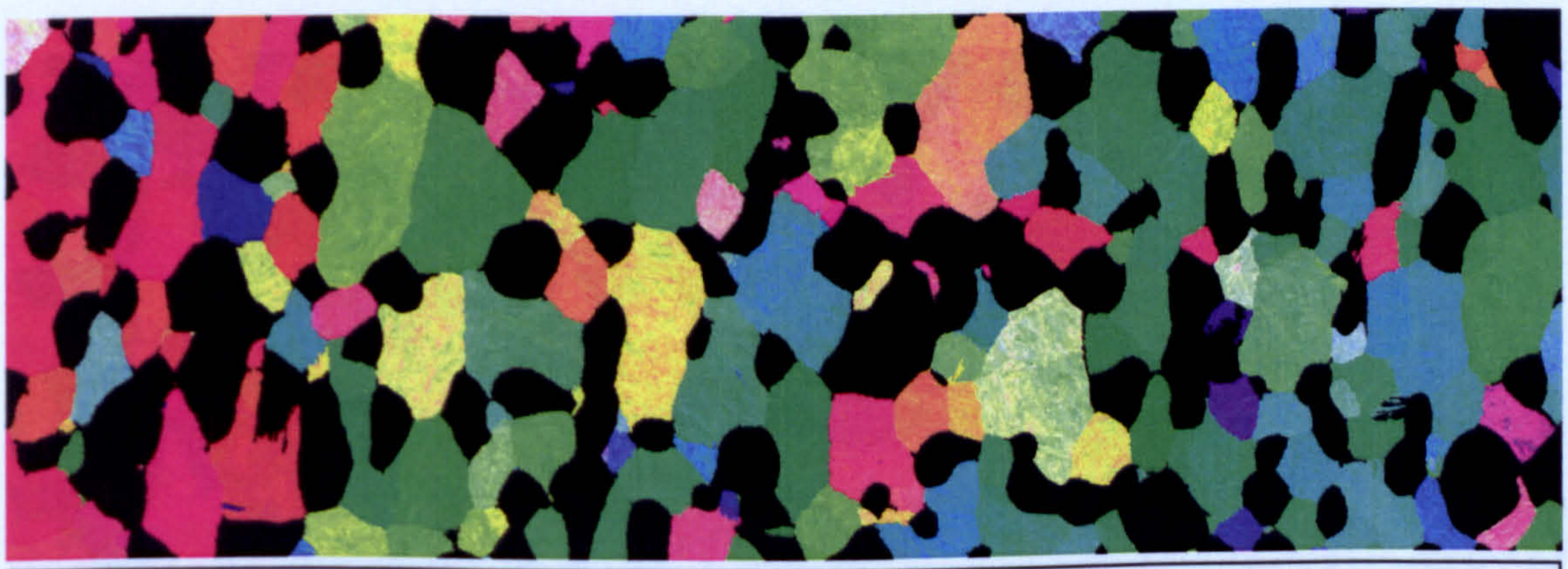

(c) The reconstructed β phase after extrapolating the unreconstructed points.

Fig. 4.22 The β reconstruction technique applied to a bimodal high resolution (0.25µm step size) EBSD dataset obtained from the same area shown in Fig. 4.23.

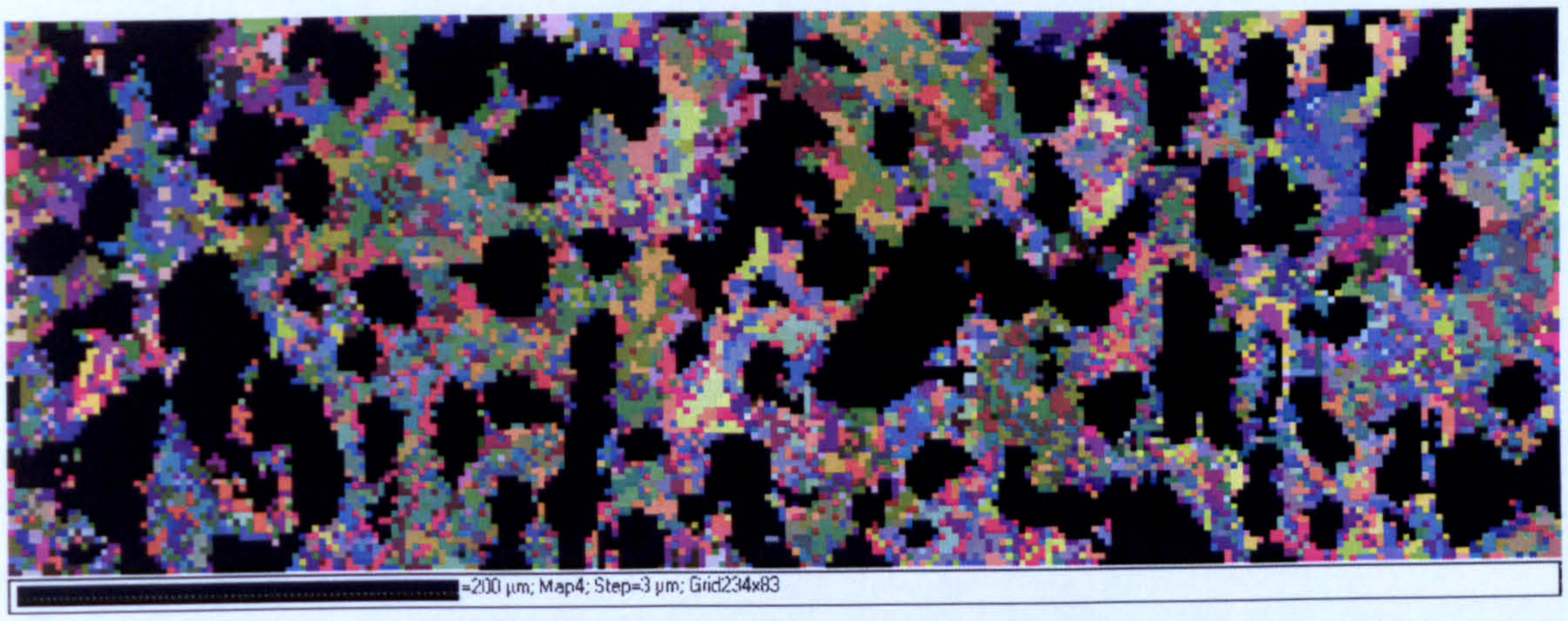

(a) The separated α_s phase (α_p grains coloured black).

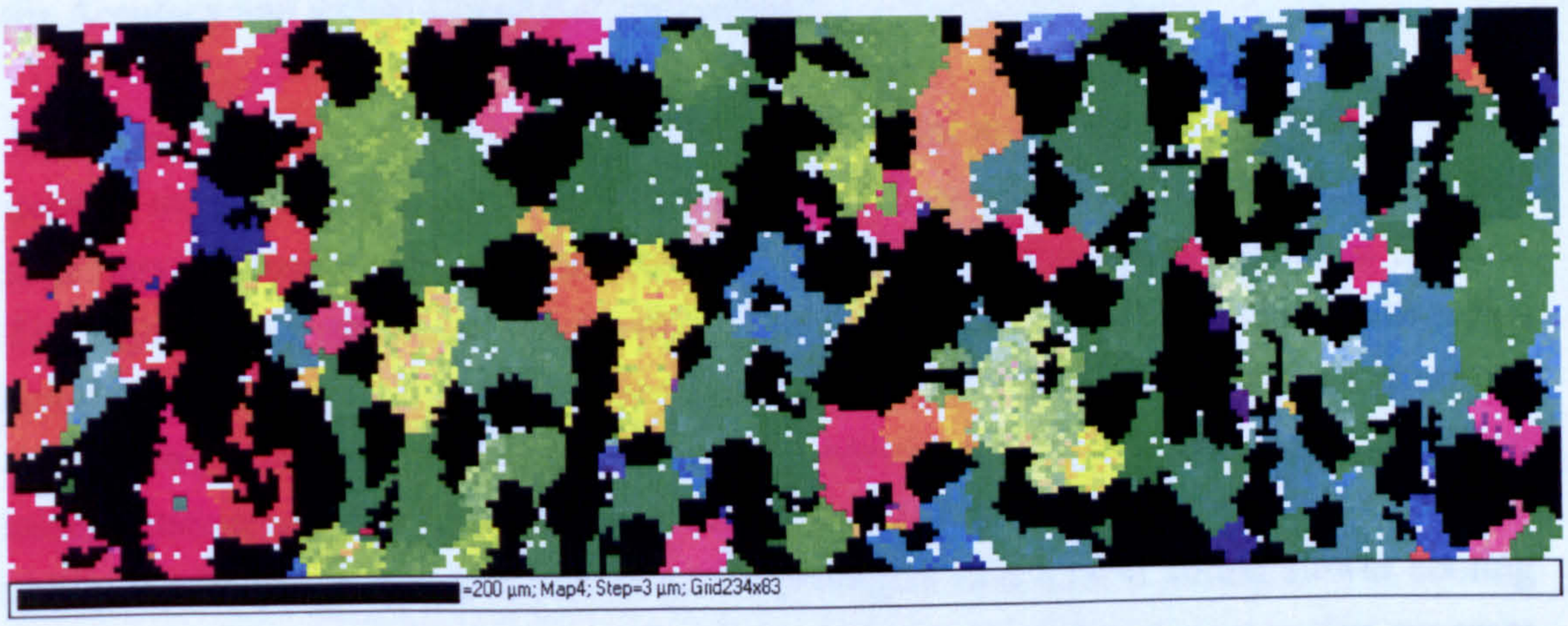

(b) The reconstructed β phase (91% of α_s reconstructed).

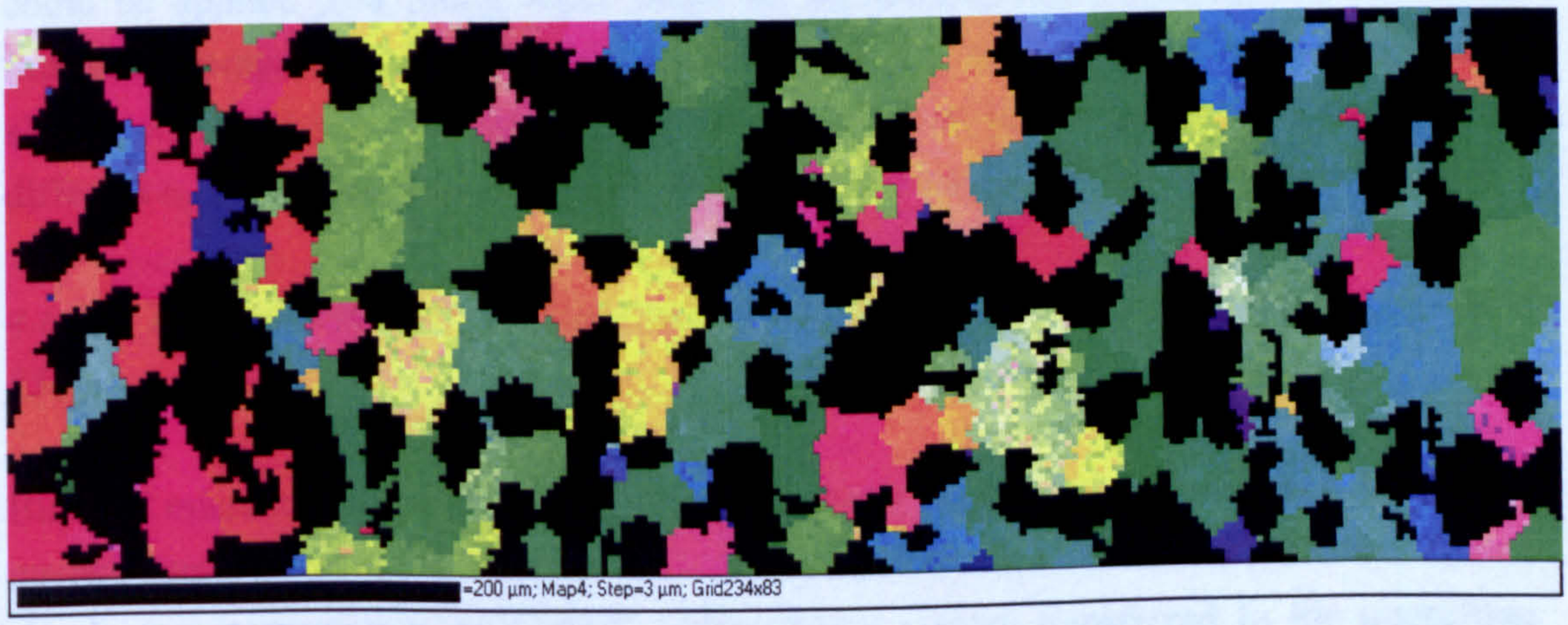

(c) The reconstructed β phase after extrapolating the unreconstructed points.

Fig. 4.23 The β reconstruction technique applied to a bimodal low resolution (3µm step size) EBSD dataset obtained from the same area shown in Fig. 4.22.

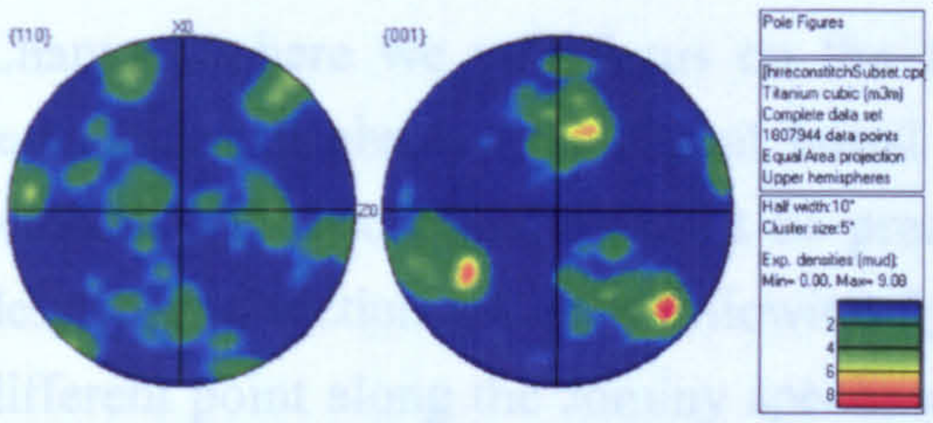

(a) High resolution

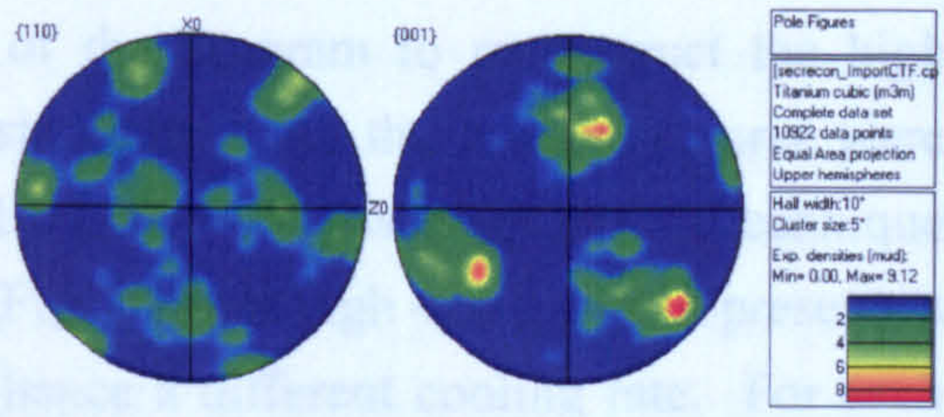

(b) Low resolution

Fig. 4.24 Texture of the reconstructed β phase for the high and low resolution EBSD datasets.

4.6.5 The Effect of α_s Microstructures Formed as a Result of Different Cooling Rates, on the Accuracy and Reliability of Reconstruction

The β reconstruction technique was initially envisaged as a means to reconstruct EBSD maps in material originating from laboratory specimens, which had been water quenched to preserve as much as possible the post deformed state of the high temperature β phase. The high cooling rates associated with this type of test tends to produce α_s with a fine acicular morphology. In this microstructure, each α_s variant tends to share its boundary with a large number of adjacent variants, which makes it highly likely that the misorientation analyses for a particular variant will lead to a single correct solution. The ability for the program to reconstruct α_s morphologies which form during slower cooling rates would also be desirable because this would mean that the reconstruction program could be applied to a much wider range of microstructures, including those found in industrial components, which due to their larger size tend to experience significantly slower cooling rates. To investigate the suitability of the program for reconstructing different α_s morphologies, tests were carried out for a range of different microstructures.

4.6.5.1 Tests on Bimodal Microstructures From a Range of Cooling Rates Using Timetal 834

Bimodal microstructures for a range of cooling rates were obtained using the adapted end quench Jominy procedure (see section 3.4). In this experiment, the test piece was heated slowly to a temperature of 1010°C before being rapidly transferred to the quenching stand. The resulting bimodal microstructures contained approximately 40% α_p and α_s morphologies resulting from a range of cooling rates. The slow heat treatment was expected to produce a high temperature microstructure in which the β grains were well restored prior to quenching. EBSD datasets were acquired for several points along the centre of the Jominy specimen, so that the reconstruction program could be tested for a range of α_s morphologies. For a more detailed discussion of the microstructures, see

Chapter 7; here we will focus on the ability of the program to reconstruct the high temperature β phase for different initial microstructures. As the microstructures were bimodal, the reconstruction must be preceded by the direct phase separation technique described in section 4.4. The following figures (Fig. 4.25 through 4.31), each represents a different point along the Jominy specimen and hence a different cooling rate. For each figure, four different EBSD maps are shown, these are: (a) band contrast map, (b) standard inverse pole figure (IPF) map, (c) a boundary map indicating proximity to the ideal Burgers orientation relation, and (d) IPF map of the separated and reconstructed β phase. The band contrast map gives information similar to an optical micrograph. The standard IPF map shows the orientation data obtained in the initial analysis prior to extrapolating the non indexed points and separating the phases. The boundary map shows all misorientations greater than 3° and by use of a colour key, their misorientation from the closest Burgers type orientation relation. This map is useful as it highlights the probable prior β and α_p boundaries as these tend to be white unless coincidentally close to a Burgers type relation. It also shows within the α_s phase, the density of misorientation information available for the reconstruction and how strictly these misorientations obey the Burgers orientation relation. In the IPF map of the reconstructed β phase, the separated α_p is coloured black and unreconstructed variants are shown in white.

Fig. 4.25 shows the reconstruction results for the microstructure resulting from the highest cooling rate. This dataset was obtained approximately 150μm from the quenched end to avoid the layer of α case which formed at the surface of the specimen. The cooling rate curve plotted from the thermocouple data (Fig. 3.9) cannot be extrapolated with confidence this close to the edge of the specimen but it is believed that the instantaneous cooling rate at 900°C (CR_{900}) would have been in excess of $1000°Cs^{-1}$. It can be seen in Fig. 4.25(a) that the α_s microstructure has an acicular morphology and is extremely fine. At this cooling rate, any diffusional transformations will have been suppressed and the α_s will therefore be martensitic α'. The corresponding orientation data is shown in Fig. 4.25(b). In order to achieve a percentage of indexed points higher than 50% in the α_s phase, a reduced step size (0.15μm as opposed to 0.3μm) and increased number of frames was used compared to the other EBSD datasets acquired along the Jominy specimen. These revised parameters resulted in 65% indexing in the α_s phase; however, the acquisition time for the equivalent sized map was over four times longer. The direct phase separation technique was accurate and easy to perform on this microstructure requiring no manual correction. This is due to the large difference in average band contrast and grain size between the α_p and α_s phase. It can be seen in 4.25(c) that there is a high density of misorientation data within the α_s phase with which to reconstruct the β phase and that the misorientations are in general within about 3° of the ideal Burgers orientation relation. This is within the range of error for misorientations between EBSD measurements and means that the adherence to the Burgers relation is strict. This strict

adherence to the ideal orientation relation means that the error in the reconstructed β orientations should be relatively small. The map for the reconstructed β phase is shown in (d). It can be seen that the level of reconstruction attained in the separated α_s phase is over 97%. The unreconstructed variants, which remain as small groups of white pixels, originate from the extrapolation of misindexed pixels in the raw data. These remain unreconstructed because the misorientations analysed for these erroneous variants do not fulfil the Burgers orientation relation. Occasionally, where some of the misorientations coincide with the orientation relation, the erroneous variants are reconstructed producing small reconstruction errors. These are the small regions of coloured pixels which lie within the larger correctly reconstructed β grains. The error or orientation noise in the reconstructed β phase can be assessed by plotting a misorientation profile across a reconstructed grain. Fig. 4.25(e) shows a misorientation plot for the red arrow on Fig. 4.25(d). The β grain appears well recovered and contains no substructure, thus the misorientations in the profile represent the orientation error or 'noise'. It can be seen that this tends to fall within the range 0-3°. For comparative purposes, a misorientation plot across part of an α_p grain (red arrow on Fig. 4.25(b)) is also plotted to show the equivalent orientation noise in the raw EBSD data. It can be seen that in the raw data, the orientation noise tends to fall within the range 0-1°. Thus, orientation noise in the reconstructed β phase is approximately 3 times greater than is typically obtained in the raw EBSD data.

Fig. 4.26 shows the reconstruction results for a dataset obtained 1mm from the quenched end. Extrapolation of the cooling rate curve (Fig. 3.10) suggests that the cooling rate at 900°C would have been approximately 400°C s^{-1} at this point. It can be seen in Fig. 4.26(a) that the α_s microstructure has a similar acicular morphology to the highest cooling rate. Here again, the α_s is believed to be martensitic α' although slightly coarser. For this reason, the step size was increased to 0.3μm and the number of frames reduced, which resulted in a fourfold improvement in acquisition speed whilst still attaining an indexing rate of nearly 50% in the α_s. Phase separation and reconstruction proved to be straightforward for this microstructure. The density of misorientation data within each β grain remains high and the misorientations are in general within about 3° of the ideal Burgers orientation relation.

Fig. 4.27 and 4.28, show reconstruction results for datasets obtained for cooling rates at 900°C s^{-1} of approximately 160 and 63°C s^{-1} respectively. It can be seen that at these lower cooling rates, the α_s variants continue to become coarser but have a similar morphology to that seen at higher cooling rates. The coarser α_s means that the level of indexing in the α_s phase increases while the density of misorientation data decreases. The adherence of the misorientations to the Burgers relation remains strict i.e. generally less than 3°. Phase separation was again straightforward for these microstructures requiring little or no manual correction. The reconstructions also appeared to be accurate, with few apparent errors and a high level of reconstructed variants.

Fig. 4.29 shows the reconstruction results for a dataset obtained for a cooling rate at 900°C s^{-1} of 22°C s^{-1}. The α_s morphology has a different appearance to that which is seen at the higher cooling rates. Here, the α_s variants are coarser and in places variants with the same orientation are aligned in colonies. It is believed that this microstructure consists predominantly of diffusional Widmanstätten α_s platelets. Phase separation of this microstructure was less straightforward because some of the larger α_s platelets and colonies cannot be distinguished from the α_p automatically using the difference in size and average band contrast. Thus, some manual correction is required to either add α_s or subtract α_p, to complete the separation. The coarser nature of the transformation product means the density of misorientation data within each β grain is significantly lower than for the higher cooling rates but the adherence to the Burgers relation remains good.

The reconstruction resulted in a high level of reconstruction. However, there are some noticeable errors and unreconstructed variants in the map, which although relatively small in number warrant some discussion. Some of these errors have been labelled *a*, *b* and *c* in Fig. 4.29(d). The errors that are labelled *a*, have arisen where two adjacent α_s variants (or colonies) originating from different parent β grains happen to be separated by a misorientation lower than that used to detect the variants during the reconstruction i.e. typically 3°. When this happens, the two variants are detected as a single variant and misorientations are then analysed for the two variants combined. This results in one of the variants being falsely reconstructed with orientations close to the orientation of the adjacent β grain. These errors have been commented upon in the reconstruction method described by Germain *et al.* (2007). The specific misorientations between adjacent β grains able to share a common variant were listed in Table 2.7.

Whenever one of the specific misorientations exists between two β grains, there is the possibility that closely orientated variants will form adjacent to one another, which will result in an erroneously reconstructed variant. Several authors have reported that closely orientated variants from different β grains actually form preferentially during diffusional transformations as the result of a local variant selection mechanism (Stanford and Bate, 2004. Bhattacharyya *et al.*, 2007). This type of error will therefore be more prevalent in slower cooled microstructures where the α_s forms by a diffusional transformation. Also, at slower cooling rates, the larger size of individual variants and colonies means that erroneous variants can occupy a significantly larger portion of a β grain.

The variants labelled *b* are unreconstructed variants that lie along the prior β grain boundaries. If the boundary map (Fig. 4.29(c)) is examined for these variants, it can be seen that the misorientations along their boundaries do not show strict adherence to the burgers orientation relation and thus it was not possible to reconstruct the parent β orientation for these variants. Often these variants are connected to an α_p grain at one end, giving the appearance that the α_p grain may simply have grown along the prior β boundary; however, in most cases they are not closely orientated to the neighbouring α_p

grain, so this is clearly not the case. These variants, which are not present at the higher cooling rates are believed to be nucleated grain boundary α (α_{GB}). At slower cooling rates, where β transforms to α_s by diffusion, the transformation is known to begin by the formation of α_{GB} (Stanford and Bate, 2004). Stanford and Bate (2004), showed that α_{GB} can precipitate prolifically along a prior β boundary with a number of orientations that quite often are not the same as the Widmanstätten α_s on either side of the boundary. This was found to be particularly the case when two β grains shared a common {110} pole. In this case, the grain boundary allows precipitation of any number of variants within about 15° of the Burgers relation from either side. This suggests that at cooling rates where α_{GB} forms, it may not always be possible to reconstruct this form of α as often it does not adhere strictly to the Burgers relation.

The variants labelled *c* are erroneously reconstructed variants that lie along prior β boundaries and have reconstructed orientations that are misorientated from both β grains. Most of these errors appear to result from the erroneous reconstruction of the α_{GB} mentioned above.

The errors noted in this reconstruction where the α_s forms by diffusion are generally confined to variants on the prior β boundaries and can be attributed in most cases to either α_{GB} or closely orientated variants that arise from a variant selection mechanism. Despite these errors, the majority of the α_s microstructure is still reconstructed correctly.

Fig. 4.30 shows the reconstruction results for a dataset obtained for a cooling rate at 900°C s^{-1} of 15°C s^{-1}. Parts of the α_s microstructure contain colonies approaching the size of the α_p grains and some prior β grains contain a limited number of different α_s orientations. The presence of large colonies means that the phase separation technique requires a significant amount of manual intervention and even this can be quite subjective in determining what is and isn't α_s. It can be seen in the boundary map that the density of misorientation data varies and is particularly low where β grains contain only a few large colonies. Furthermore, adherence to the Burger orientation relation is significantly lower compared to the higher cooling rates. The resulting reconstruction appears to reconstruct complete β grains in the majority of cases but these grains contain a significant number of erroneously reconstructed variants, both at the β boundaries and also in the grain interiors. Clearly, the reconstruction is far less accurate at this slower cooling rate. At these cooling rates, better reconstruction results may be achieved using the grain based techniques described by previous authors. The phase separation may also be easier using techniques which make use of either an optical micrograph or a back scattered electron image to provide contrast between the phases.

Fig. 4.31 shows an EBSD dataset obtained for the cooling rate at 900°C s^{-1} of approximately 1.7°C s^{-1}. Reconstruction of this microstructure was limited and is not shown. This was partly due to significant growth of the α_p grains, which reduces the amount of β phase that transforms to α_s. Furthermore, the α_s is coarse, meaning that the

density of misorientation data contained within it is low. In some cases, the 2-d section does not reveal sufficient misorientation data to find a single solution for a variant or colony. It is clearly not very practical to accurately reconstruct such microstructures by any means. Further reductions in cooling rate result in increased growth of the α_p grains on cooling at the expense of α_s formation.

The results show that optimum β reconstruction in the bimodal microstructures is achieved with α_s morphologies formed as a result of high cooling rates. However, at very high cooling rates, the α_s microstructure is very fine and it can be more difficult and time consuming to acquire an initial EBSD dataset. At cooling rates which coincide with the cooling rates for the quenched plane strain compression testpieces used elsewhere in this work, it was straightforward to achieve a good initial EBSD analysis and the phase separation and reconstruction procedures performed extremely well. This is encouraging as it means the program is ideally suited to investigating microstructural evolution in the β phase using these laboratory specimens. At slower cooling rates, the α_s morphology becomes coarser and the α_s forms by diffusional mechanisms. Here, the phase separation technique requires some manual intervention, which itself becomes subjective as the α_s becomes increasingly coarse. In these cases, alternative phase separation techniques may be more suitable. Initially, the program is able to reconstruct the diffusional α_s microstructures with the exception of some erroneous and unreconstructed variants. These are primarily found on the prior β boundaries and are in most cases due to either α_{GB}, which does not adhere as strictly to the Burgers relation, or variant selection, which results in closely aligned α_s colonies for specific misorientations between β grains. As the cooling rate decreases further, the reconstruction becomes more prone to errors and the value of performing the reconstruction becomes limited due to the coarseness of the α_s and its decreasing volume fraction due to α_p grain growth. Accurate reconstruction of the high temperature β phase in bimodal microstructures of Timetal 834 using the techniques developed in this work was limited to cooling rates in excess of approximately 15°C s^{-1}.

(a) Band contrast map.

(b) raw data, IPF map (α_s 65% indexed).

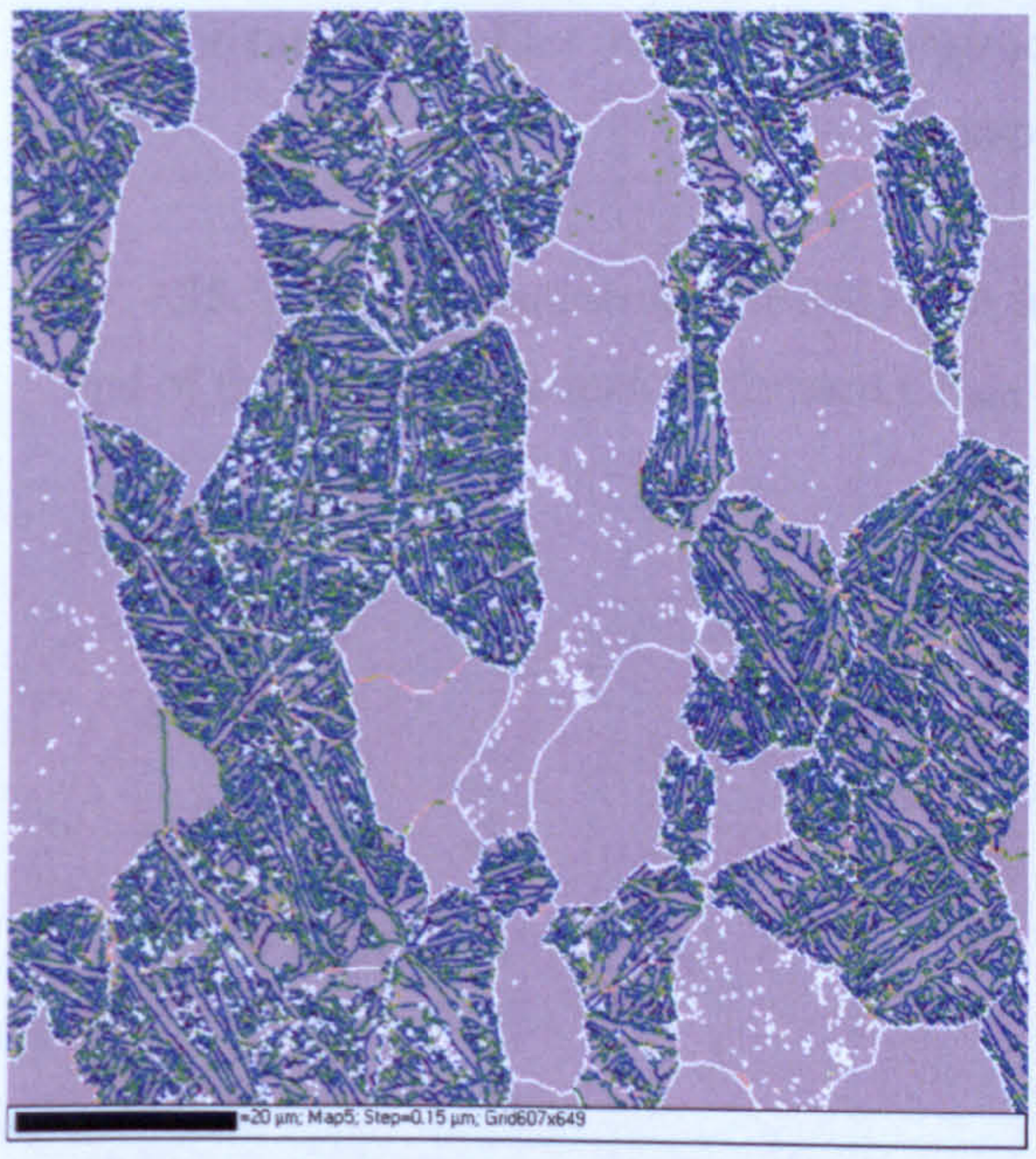

(c) Misorientations > 3° are coloured according to their deviation from the Burgers relation. Deviations > 6° are coloured white.

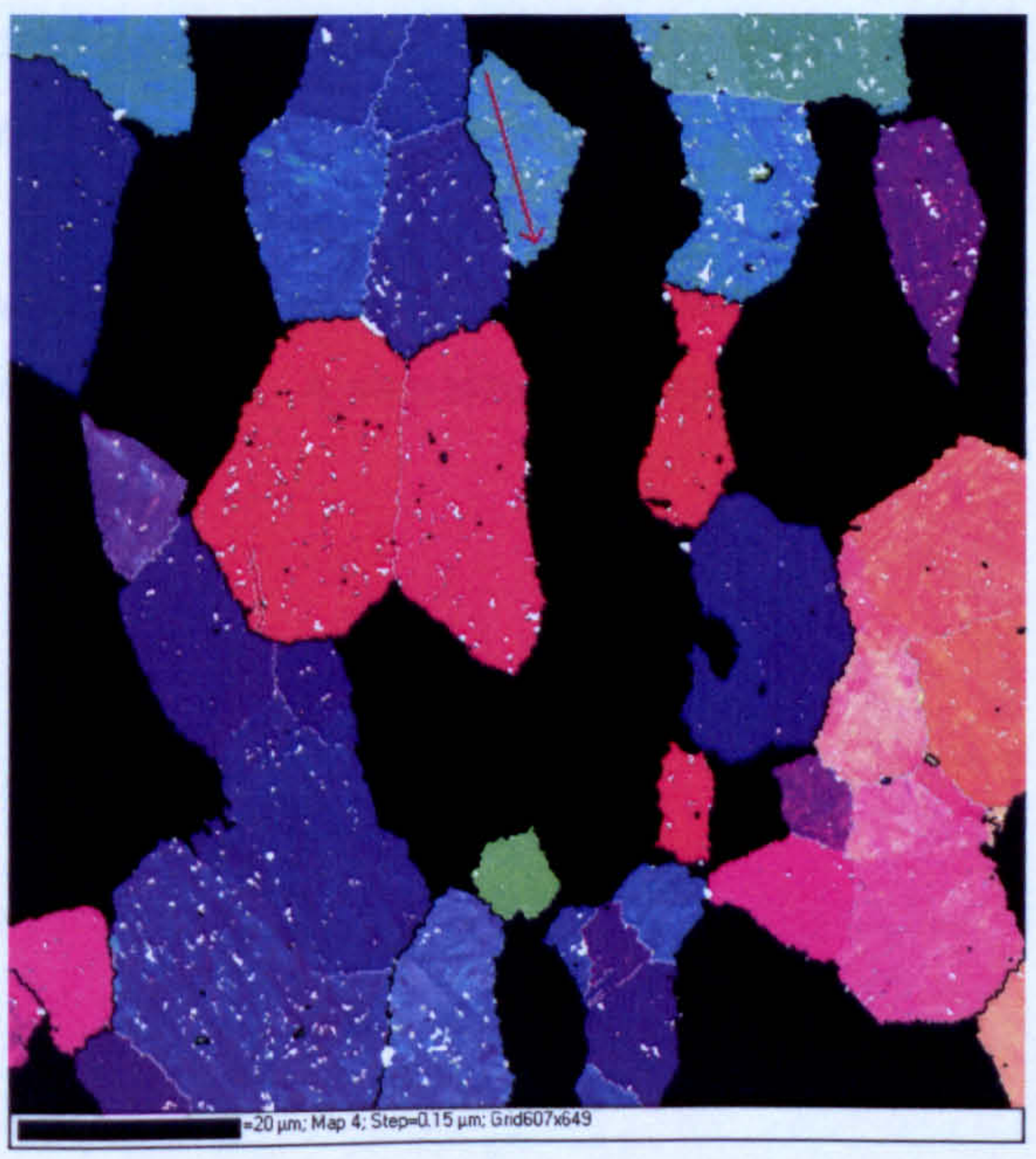

(d) reconstructed β, IPF map (α_s 97% reconstructed).

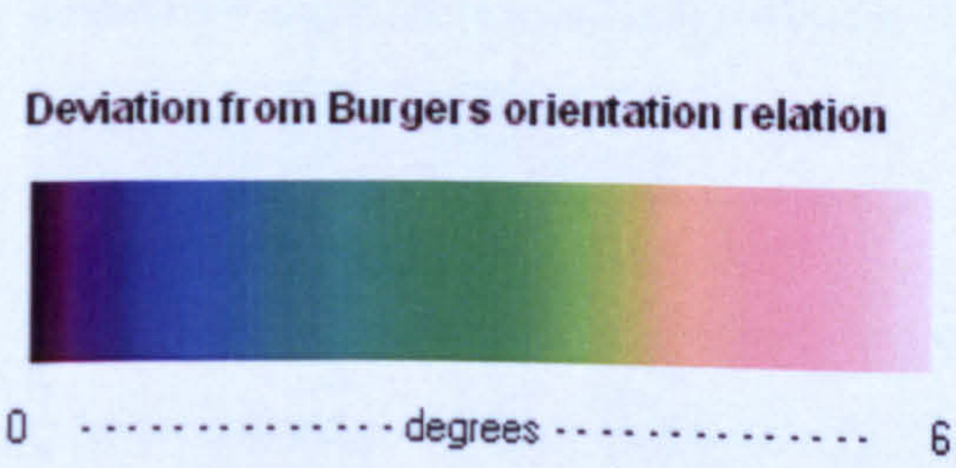

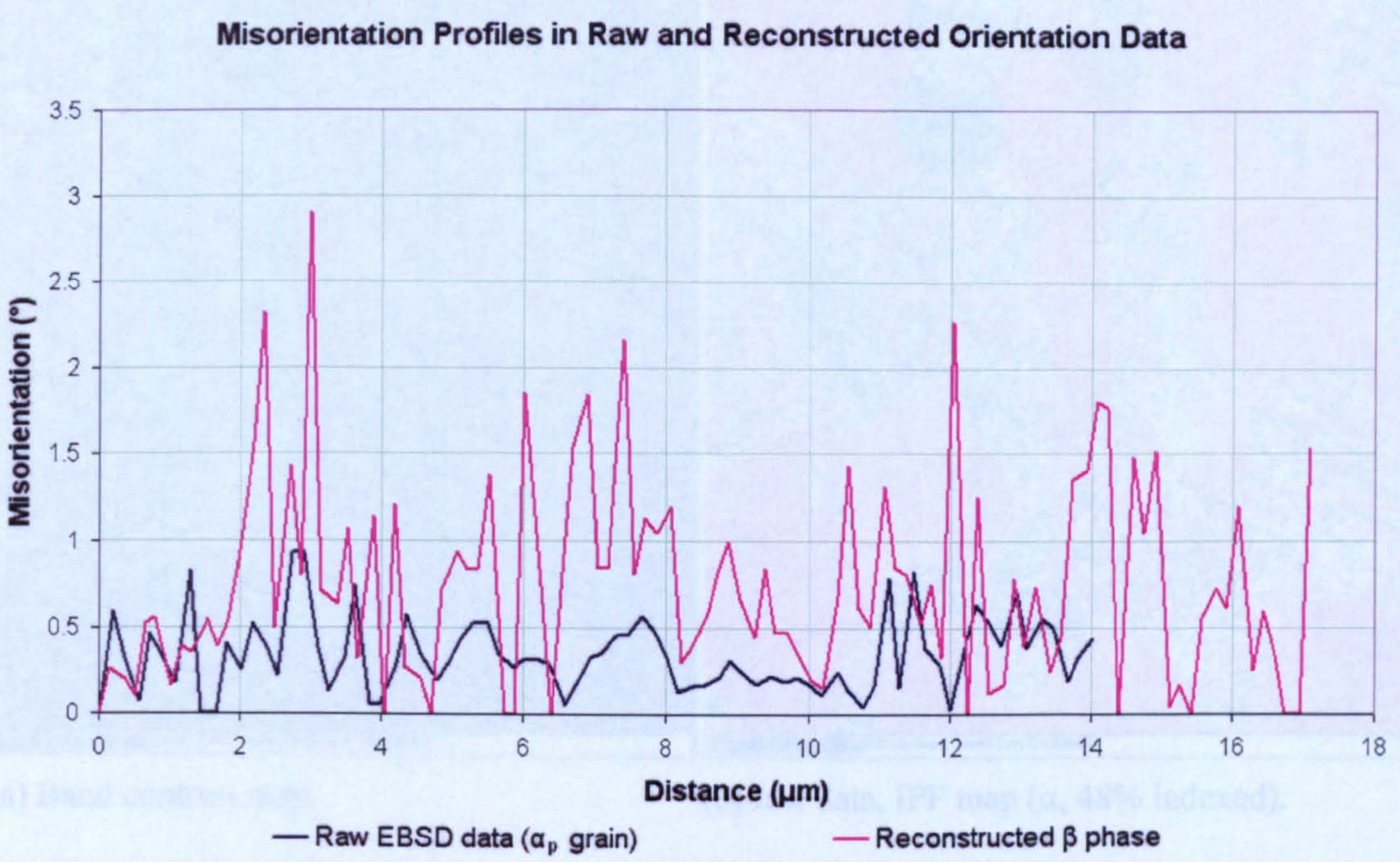

(e) misorientation profiles in raw and reconstructed orientation data for the red arrows in (b) and (d) respectively.

Fig. 4.25. Raw and reconstructed EBSD data for the microstructure 0.2 mm from the quenched end of the Jominy specimen (estimated CR_{900} >>500°C s^{-1}). A step size of 0.15µm was used.

(a) Band contrast map.

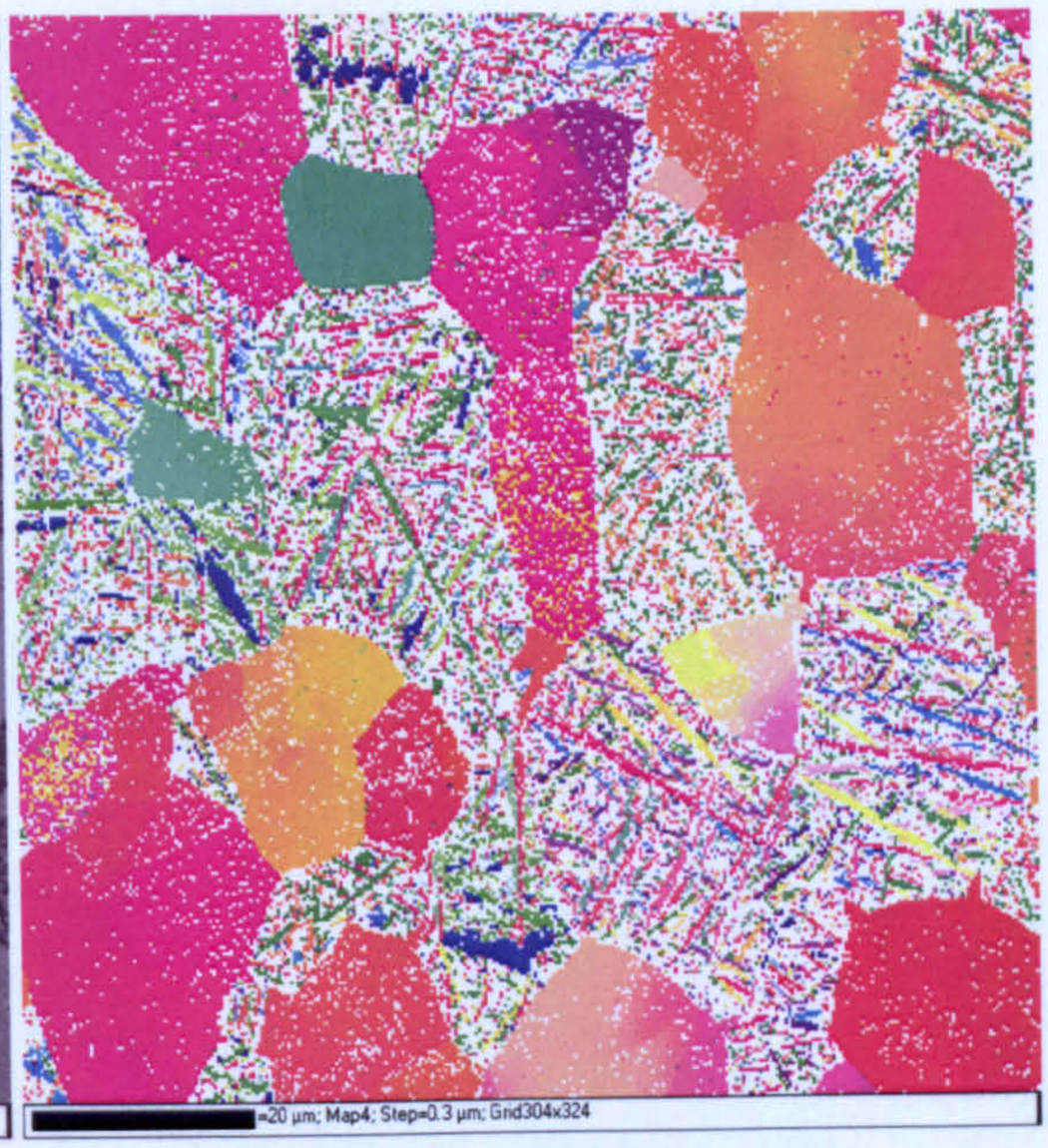

(b) raw data, IPF map (α_s 48% indexed).

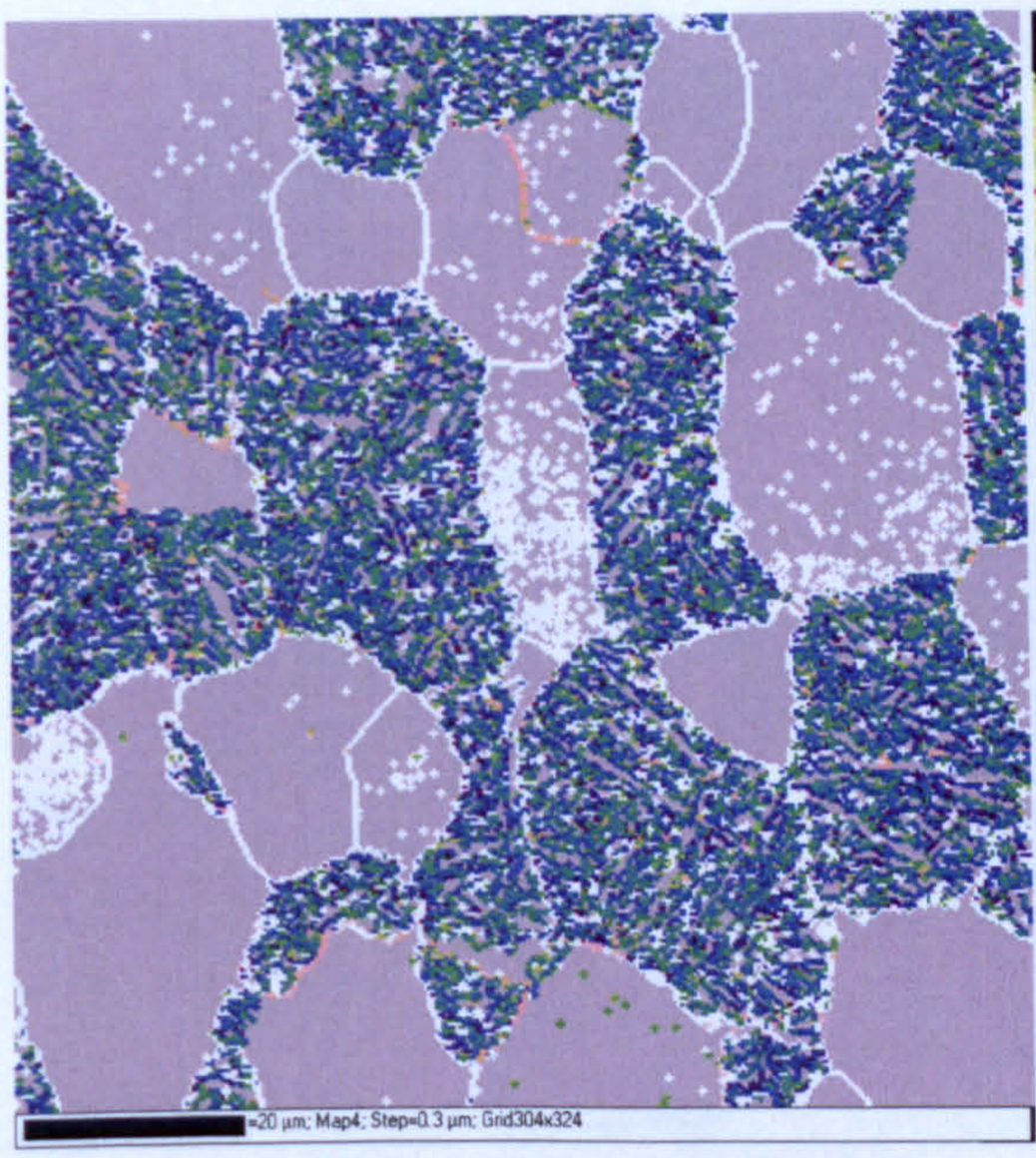

(c) Misorientations > 3° are coloured according to their deviation from the Burgers relation. Deviations > 6° are coloured white.

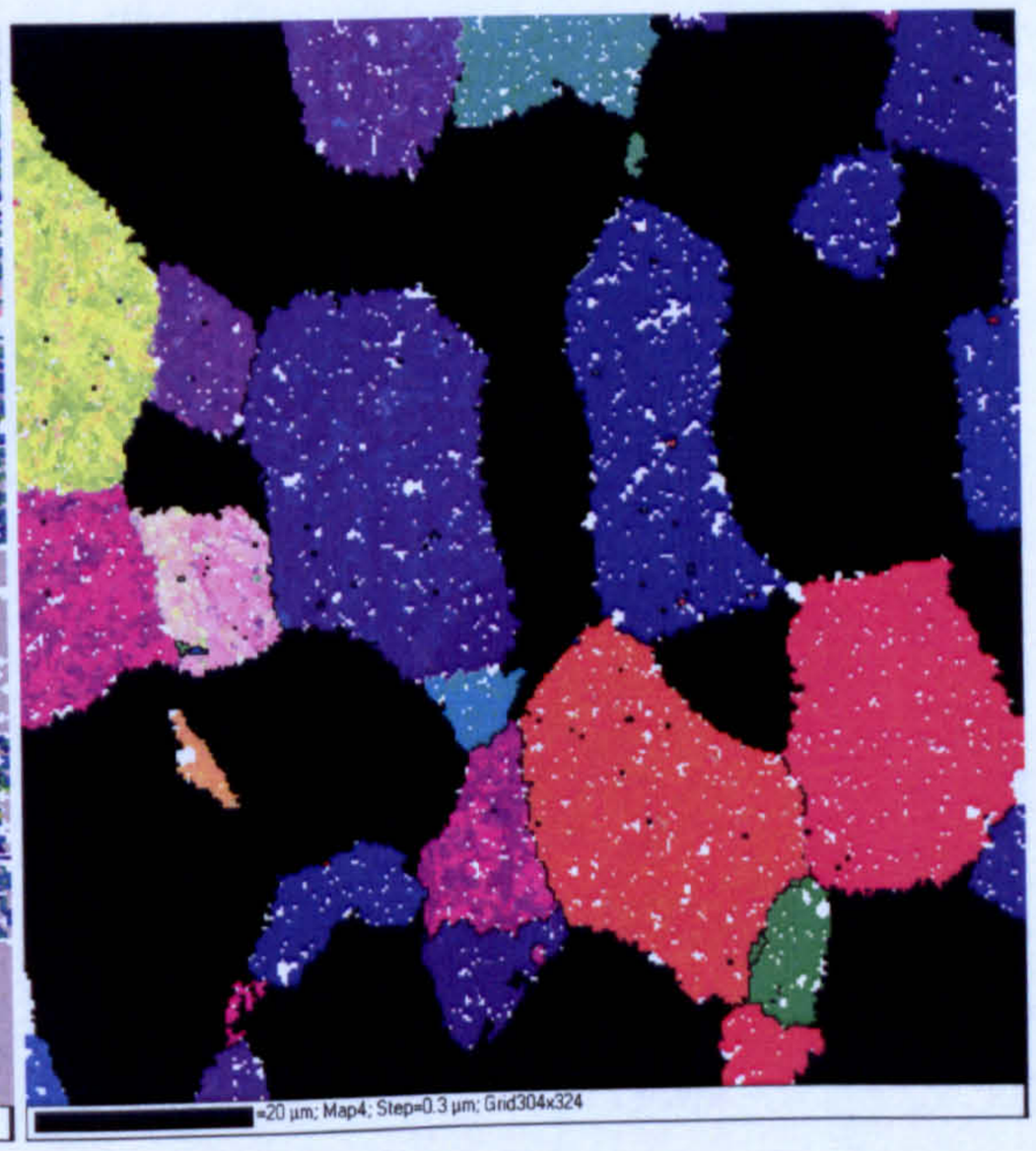

(d) reconstructed β, IPF map (α_s 94% reconstructed).

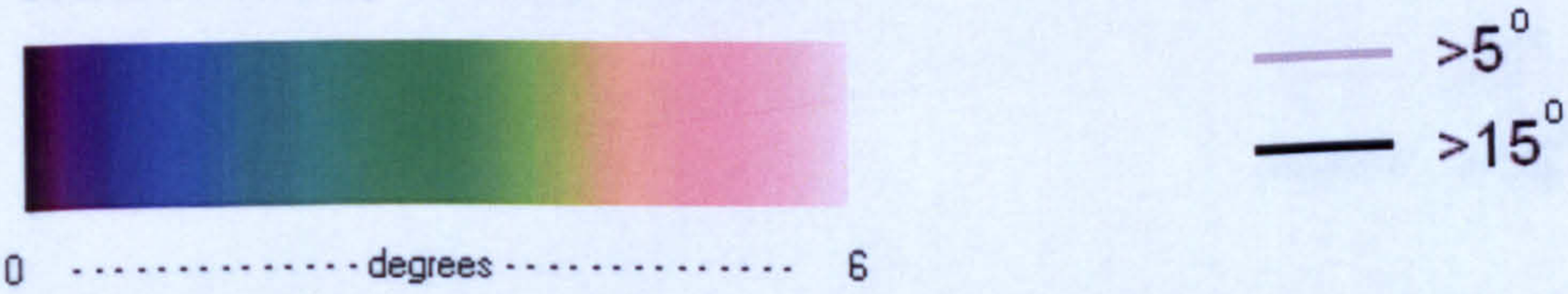

Fig. 4.26 Raw and reconstructed EBSD data for the microstructure 1mm from the quenched end of the Jominy specimen ($CR_{900} \sim 400°C\ s^{-1}$). A step size of 0.3µm was used.

(a) Band contrast map.

(b) raw data, IPF map (α_s 57% indexed).

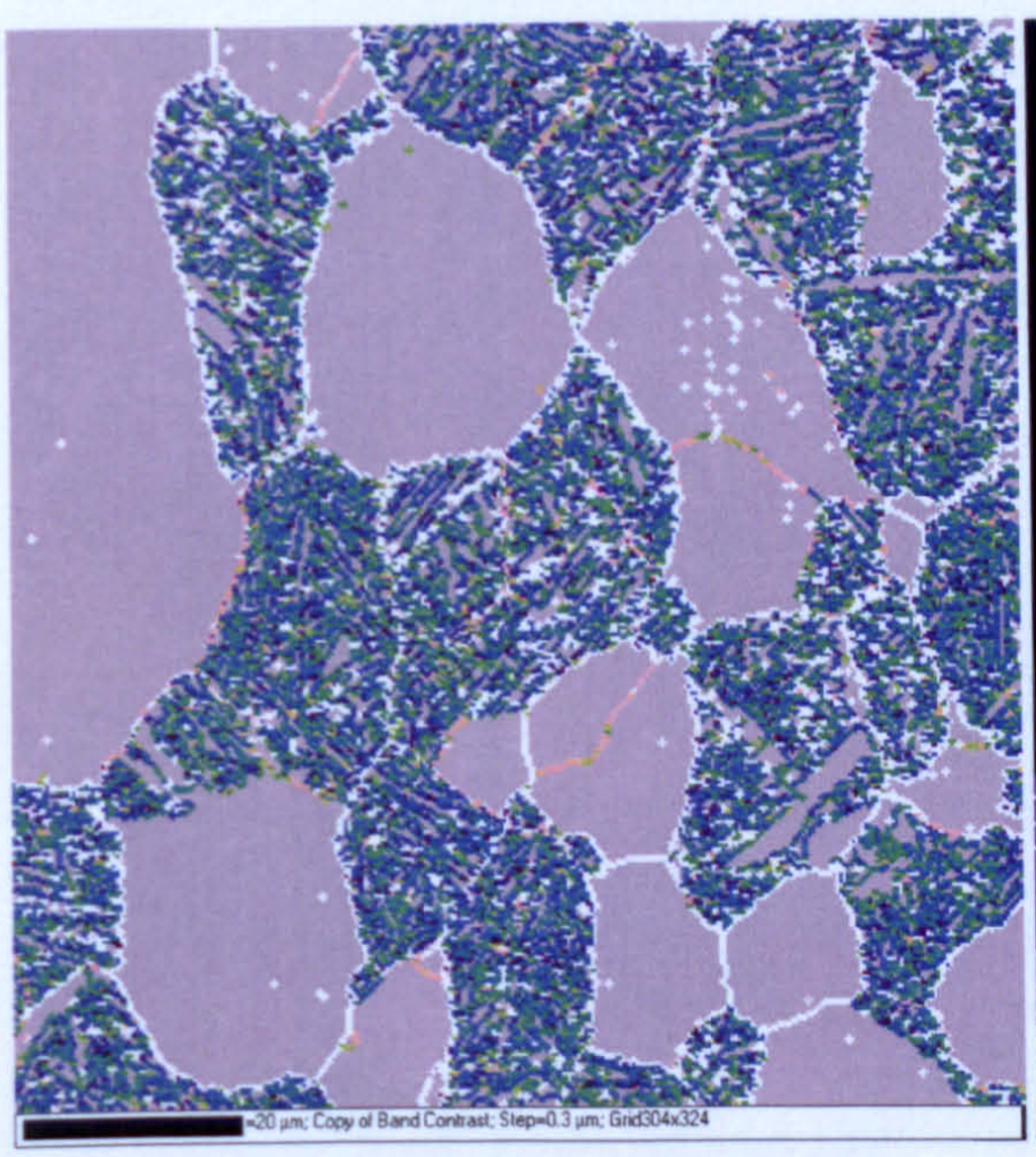

(c) Misorientations > 3° are coloured according to their deviation from the Burgers relation. Deviations > 6° are coloured white.

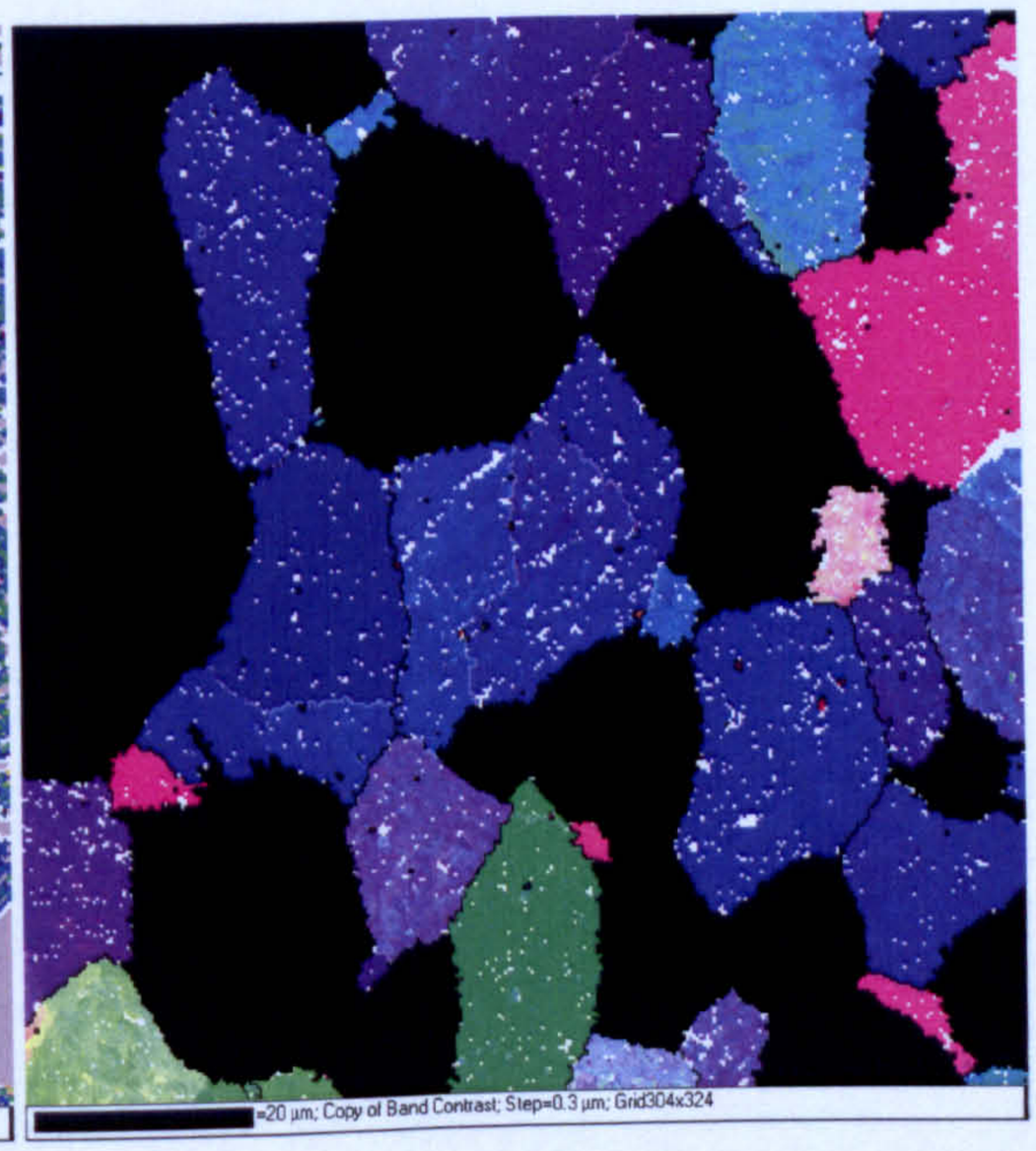

(d) reconstructed β, IPF map (α_s 98% reconstructed).

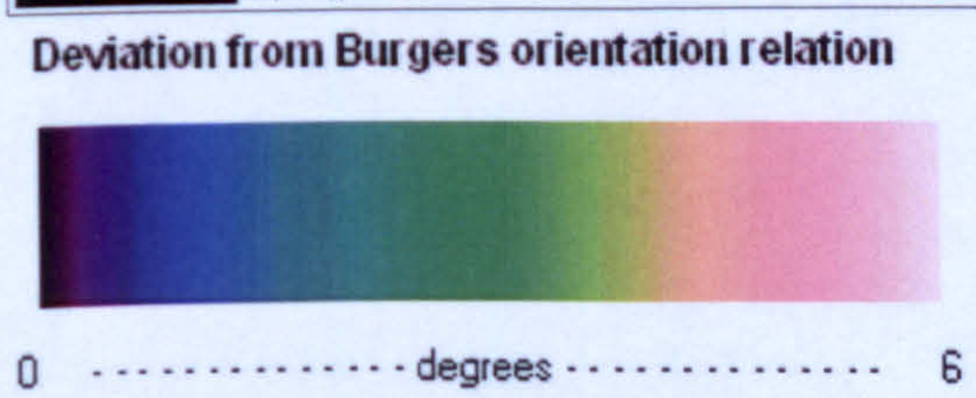

Fig. 4.27 Raw and reconstructed EBSD data for the microstructure 2.0mm from the quenched end of the Jominy specimen (CR_{900} ~160°C s^{-1}). A step size of 0.3µm was used.

(a) Band contrast map.

(b) raw data, IPF map (α_s 67% indexed).

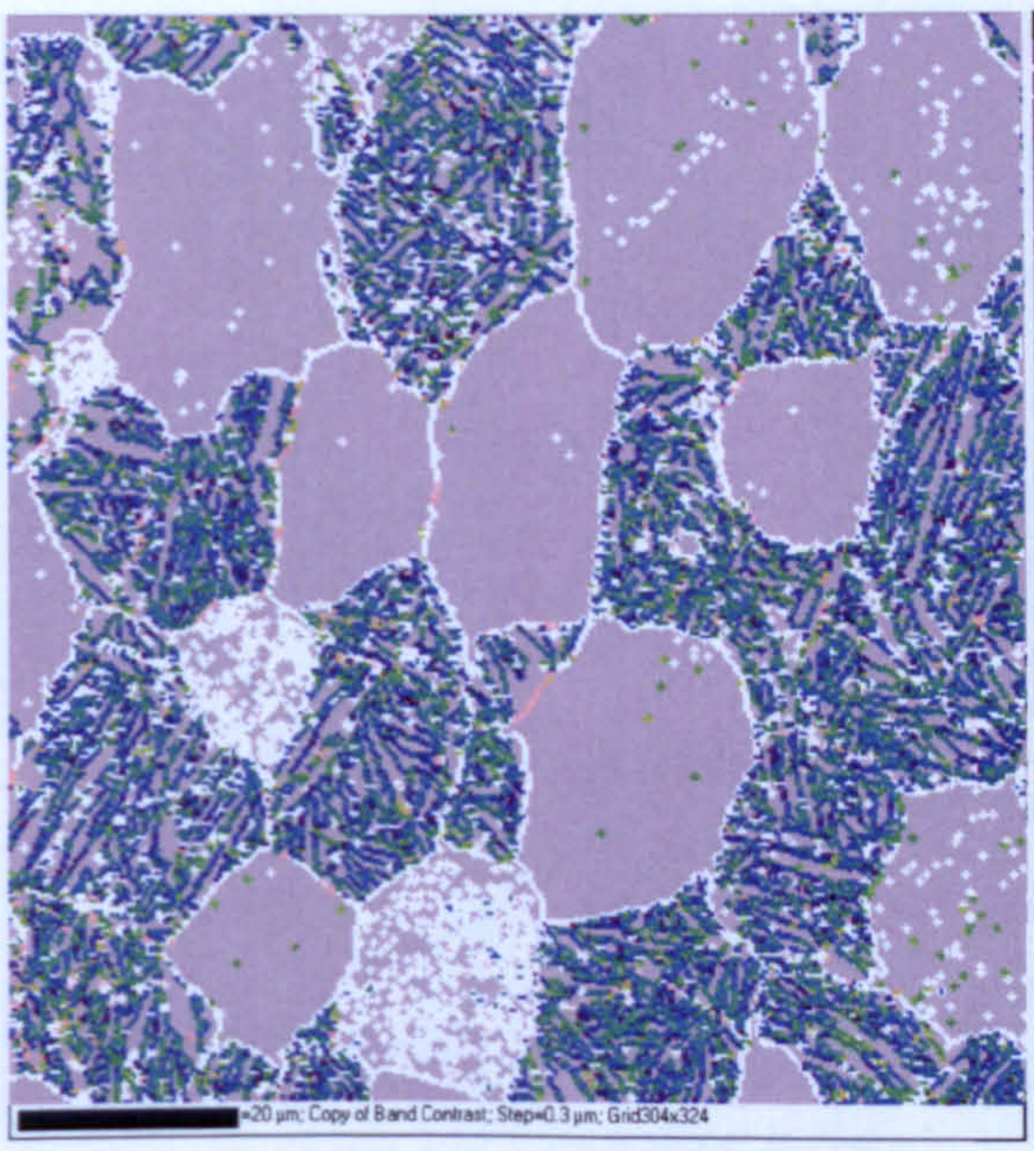

(c) Misorientations > 3° are coloured according to their deviation from the Burgers relation. Deviations > 6° are coloured white.

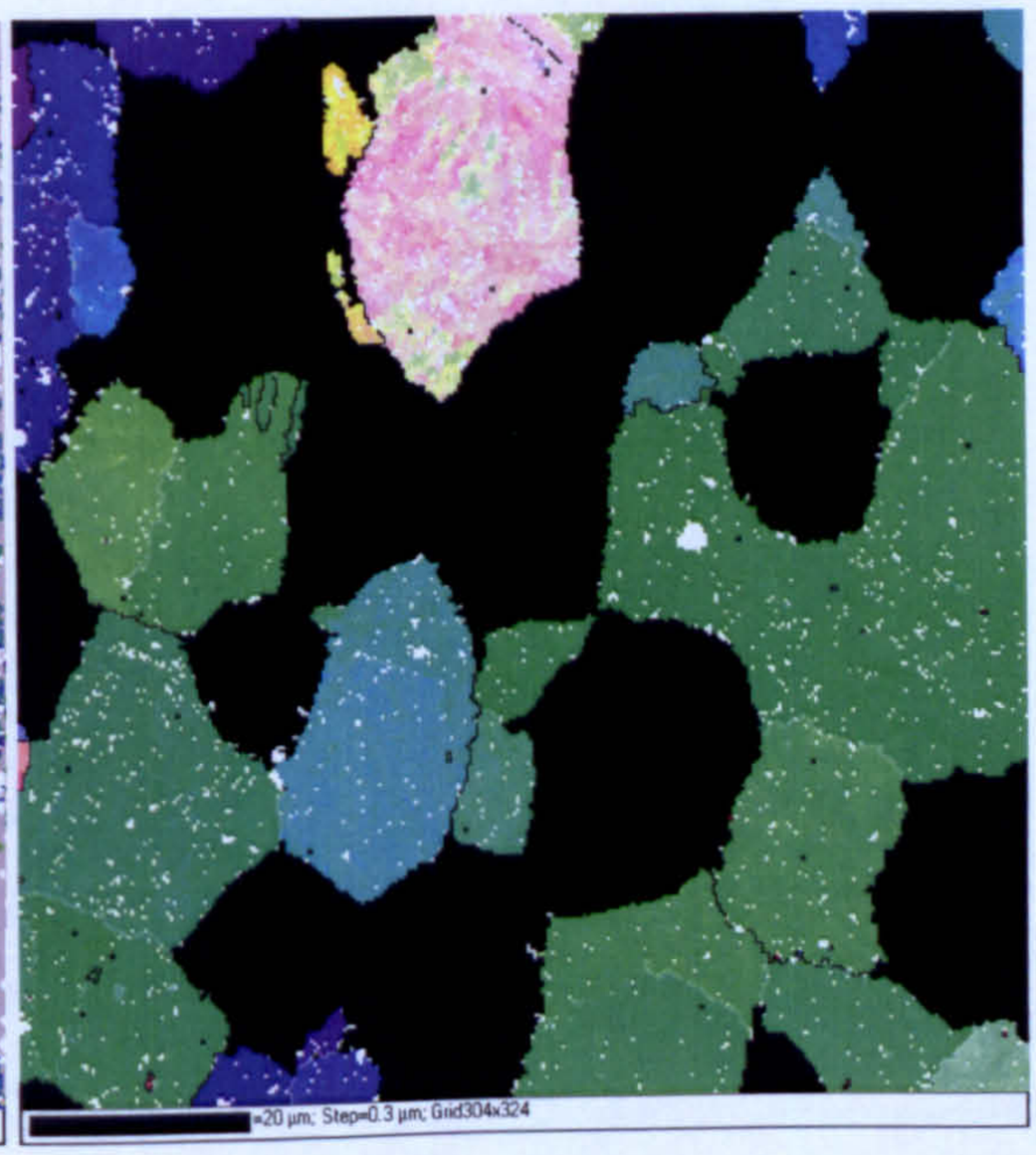

(d) reconstructed β, IPF map (α_s 98% reconstructed).

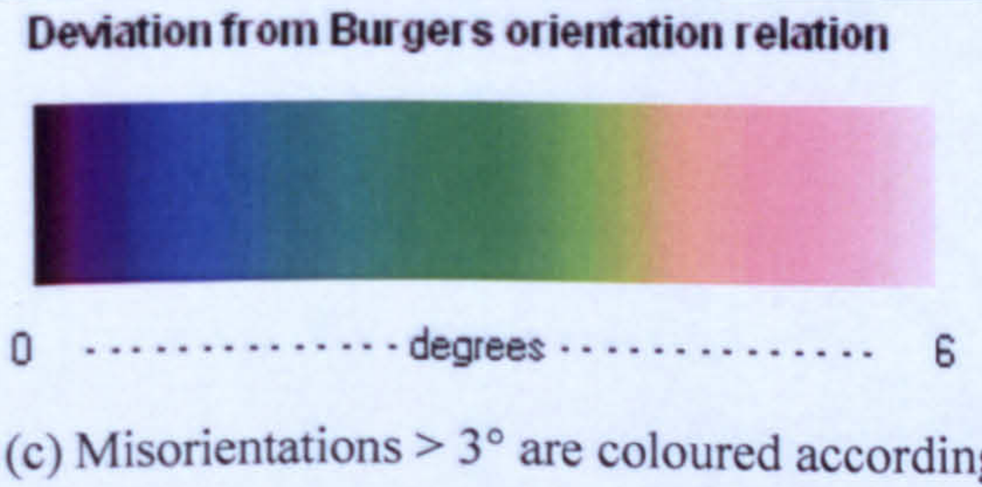

Fig. 4.28 Raw and reconstructed EBSD data for the microstructure 4.0mm from the quenched end of the Jominy specimen (CR_{900} = 63°C s^{-1}). A step size of 0.3µm was used.

(a) Band contrast map.

(b) raw data, IPF map (α_s 77% indexed).

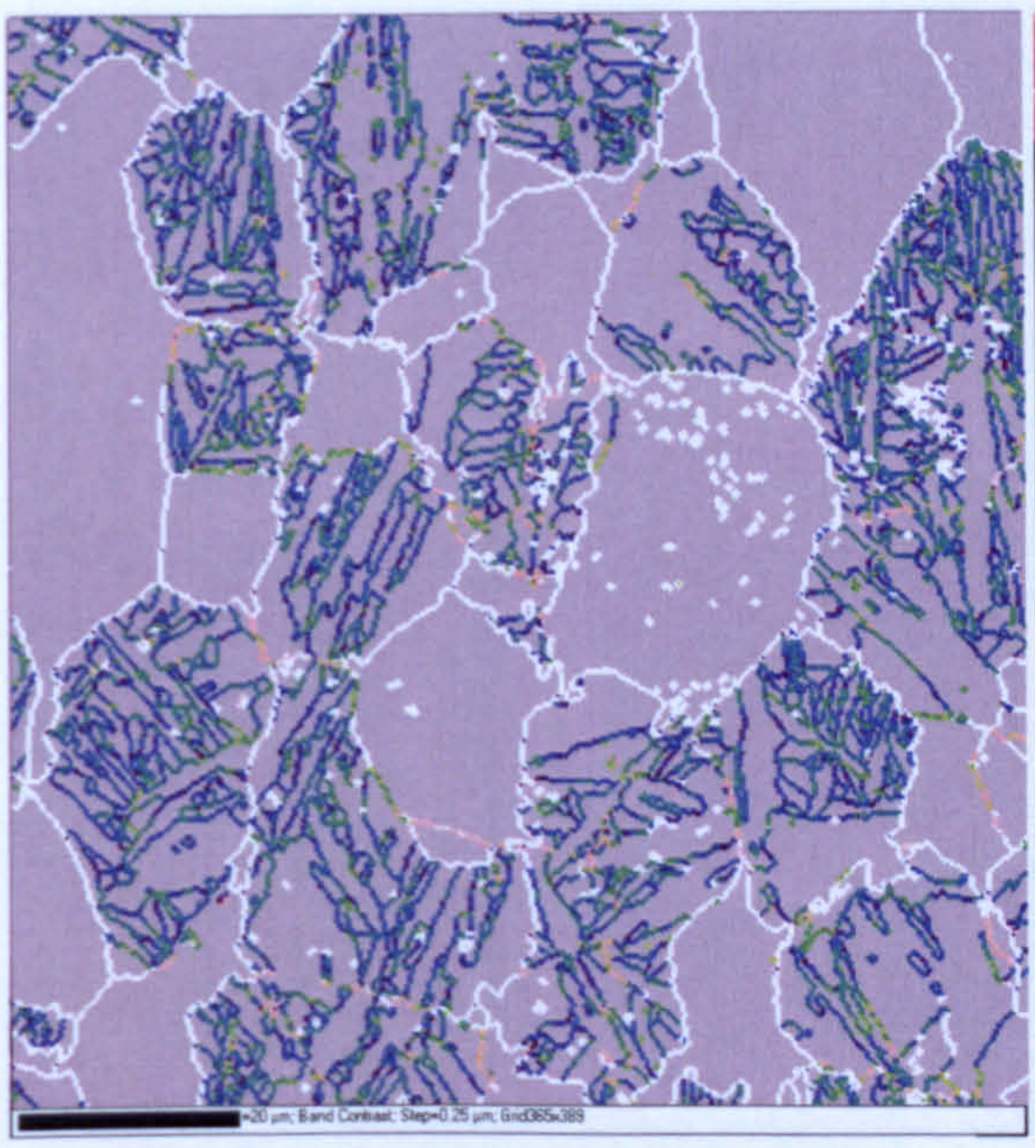

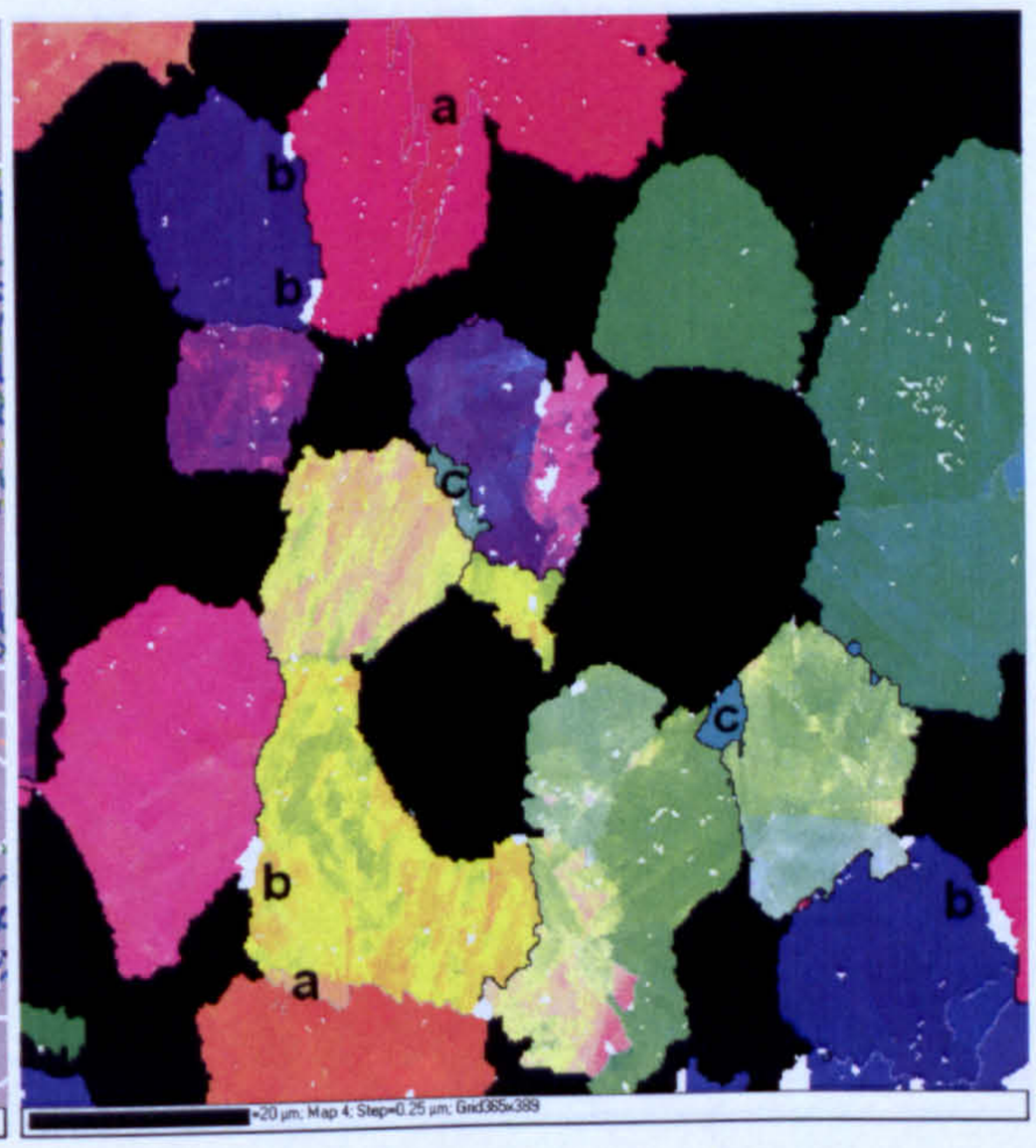

Deviation from Burgers orientation relation

(c) Misorientations > 3° are coloured according to their deviation from the Burgers relation. Deviations > 6° are coloured white.

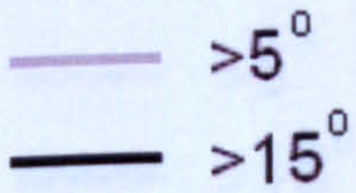

(d) reconstructed β, IPF map (α_s 99% reconstructed).

Fig. 4.29 Raw and reconstructed EBSD data for the microstructure 8.7mm from the quenched end of the Jominy specimen ($CR_{900} = 22°C\ s^{-1}$). A step size of 0.3μm was used.

(a) Band contrast map.

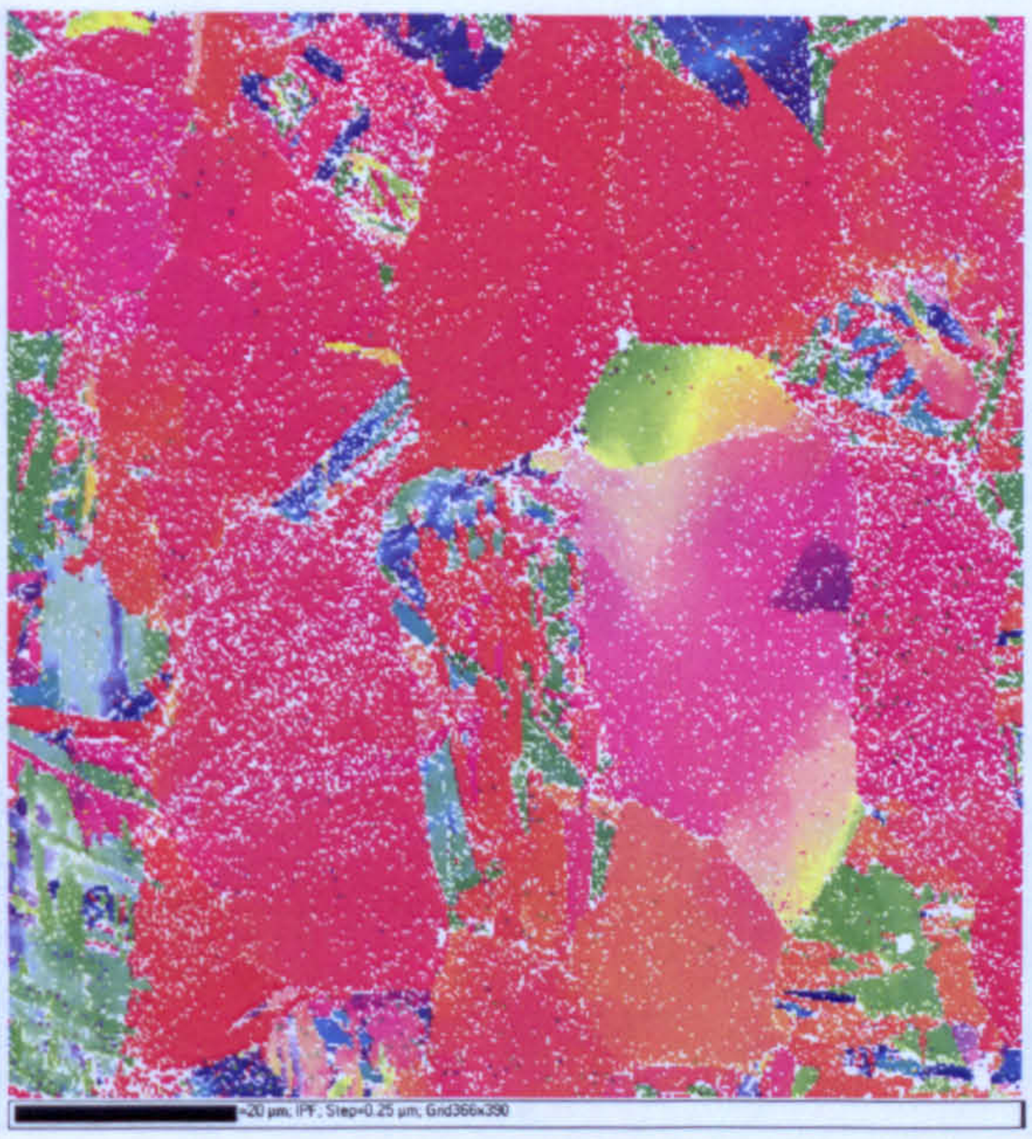

(b) raw data, IPF map (α_s 81% indexed).

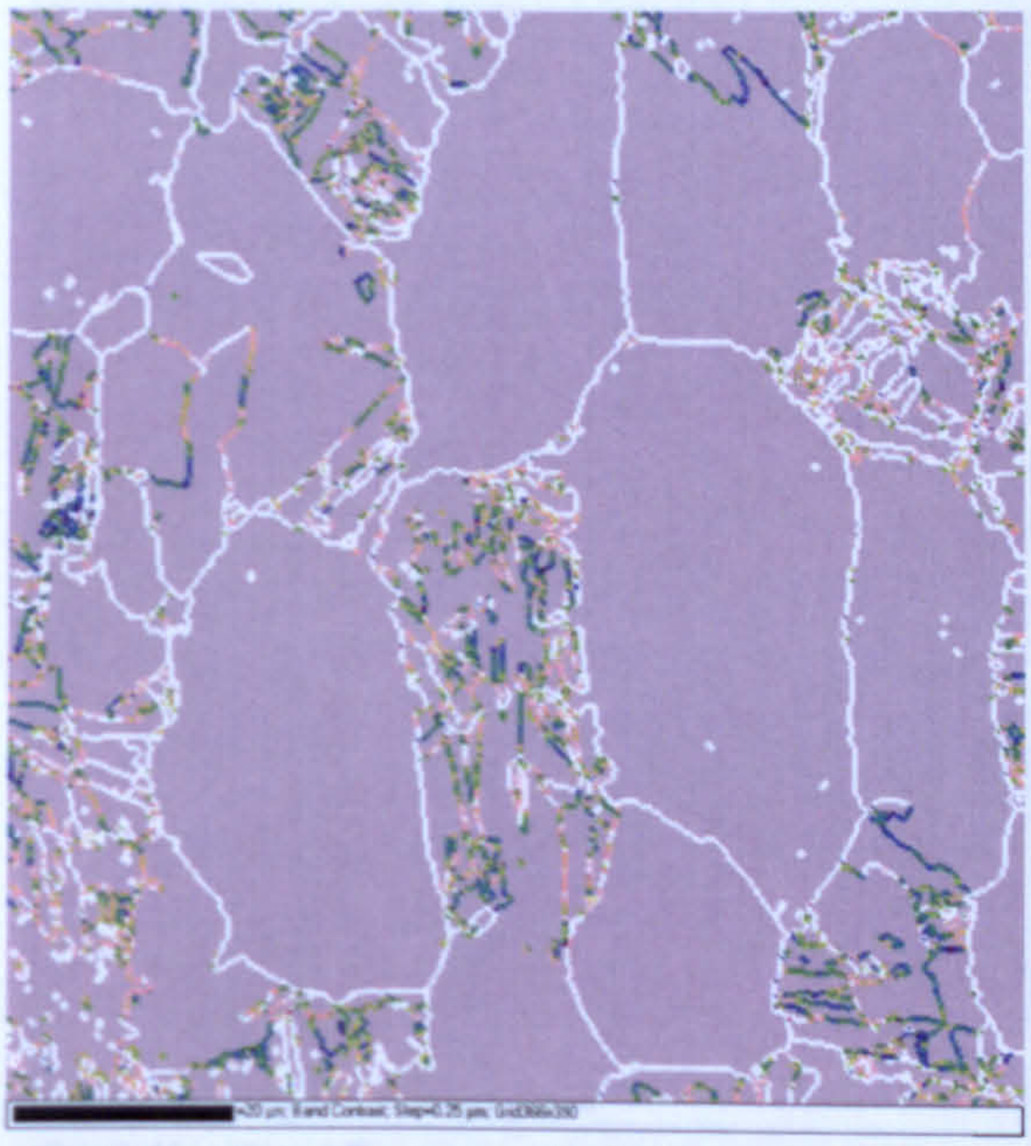

Deviation from Burgers orientation relation

(c) Misorientations > 3° are coloured according to their deviation from the Burgers relation. Deviations > 6° are coloured white.

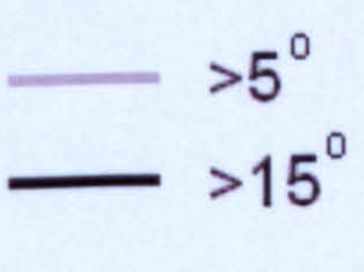

(d) reconstructed β, IPF map (α_s 97% reconstructed).

Fig. 4.30 Raw and reconstructed EBSD data for the microstructure 12mm from the quenched end of the Jominy specimen (CR_{900} = 15°C s^{-1}). A step size of 0.3μm was used.

(a) Band contrast map.

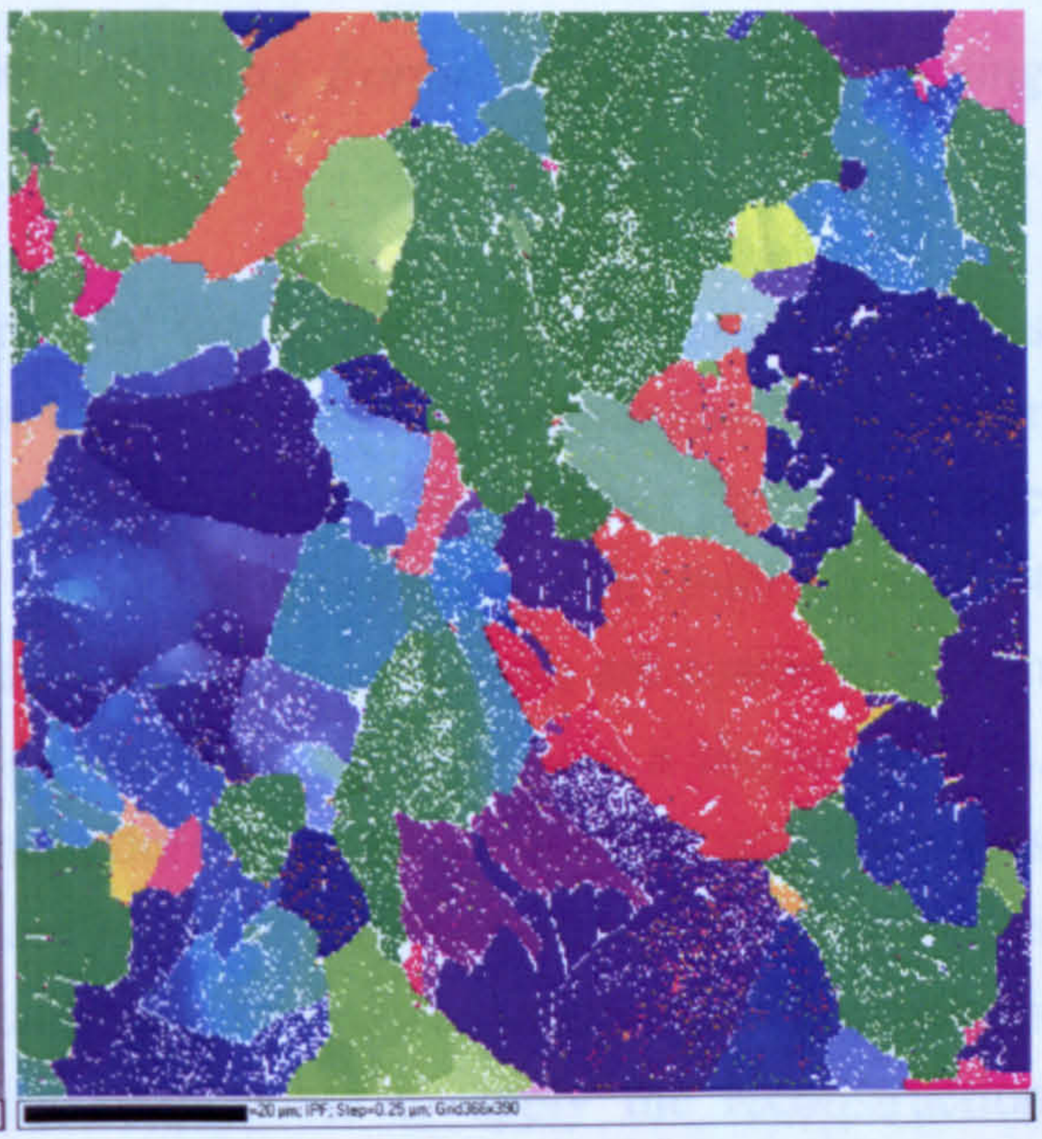

(b) raw data, IPF map (α_s 90% indexed).

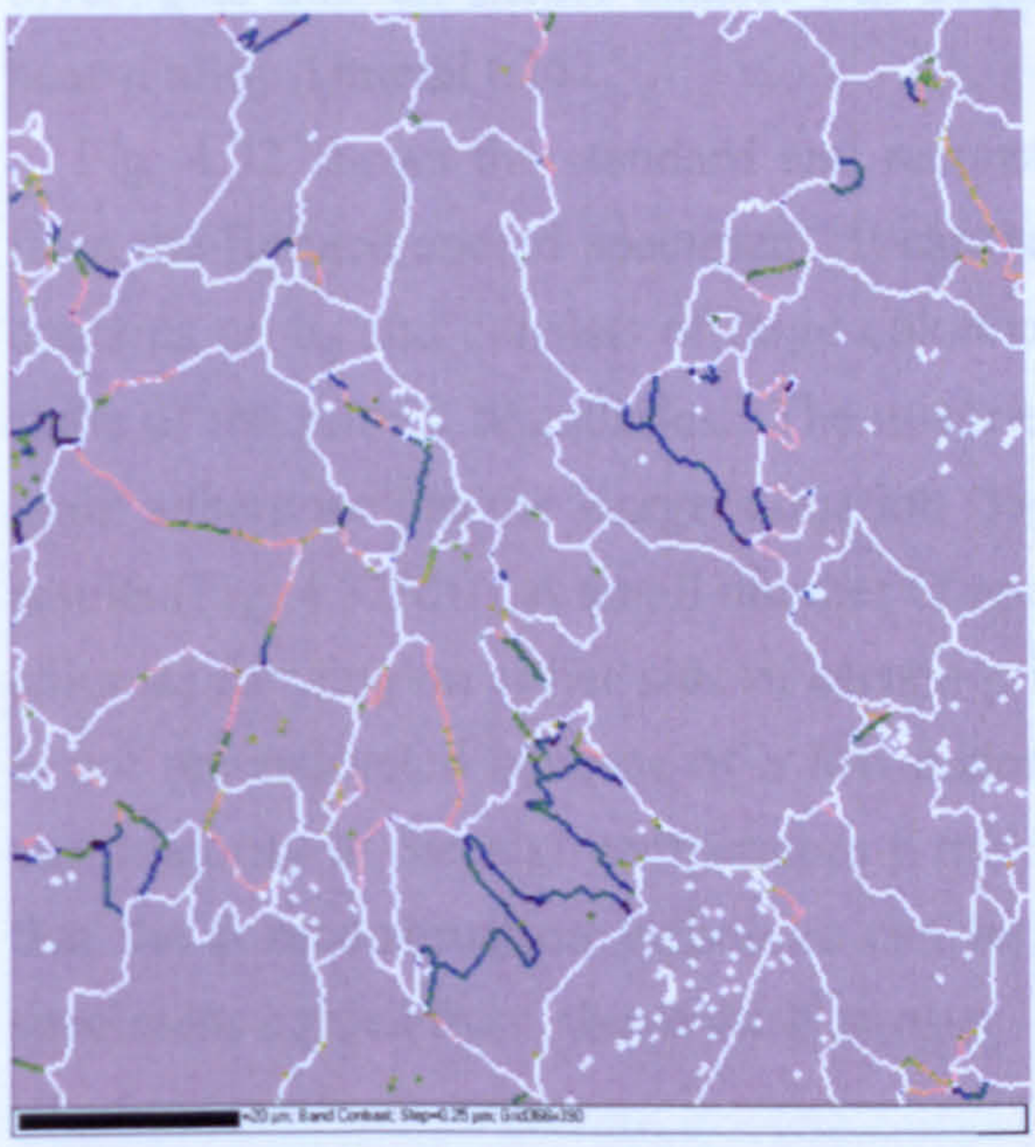

Deviation from Burgers orientation relation

(c) Misorientations > 3° are coloured according to their deviation from the Burgers relation. Deviations > 6° are coloured white.

Fig. 4.31 EBSD data 60mm from the quenched end of the Jominy specimen (CR_{900} = 1.7°C s^{-1}). Only a very limited reconstruction of the β phase was possible. Step size 0.3μm.

4.6.5.2 Tests on a Unimodal Microstructure (100% α_s) Formed From a Slow Cooling Rate Using Timetal 6242.

The tests on bimodal microstructures showed that the α_s produced by fast cooling rates can be easily reconstructed using the variant based reconstruction technique. At slower cooling rates the reconstruction is limited by the presence of α_p grains. This is because variants in contact with α_p grains have fewer neighbouring variants with which to conduct the misorientation analyses, which is significant when the α_s variants are coarse and form in colonies as there may be insufficient neighbouring variants to give a single solution. Furthermore the α_p grains grow into the β phase during very slow cooling, which reduces the amount of β which transforms to α_s. These limitations do not exist if the specimen is cooled from temperatures above the β transus because there are no pre-existing α_p grains in the microstructure. In this case, it may be possible to apply the reconstruction technique to much slower cooling rates compared to bimodal microstructures. To investigate this, an EBSD dataset was acquired from a furnace cooled specimen of the near-α alloy Timetal 6242.

Fig. 4.32 shows the standard and reconstructed EBSD results for a dataset obtained from the furnace cooled specimen. It can be seen in Fig. 4.32(a) that the microstructure contains no α_p and consists of large colonies of α_s. There is also a thin layer of α_{GB} on some of the prior β boundaries. The misorientations between colonies within the same β grain adhere well to the Burgers relation (Fig. 4.32(c)) and a high level of reconstruction results (Fig. 4.32(d)). A small number of reconstruction errors result from closely aligned colonies forming on either side of certain prior β boundaries. Also, some of the thin α_{GB} is not reconstructed because of a low adherence to the Burgers relation. However, the vast majority of the high temperature β microstructure is well reconstructed. This shows that the β reconstruction technique can be extended to much slower cooling rates for specimens cooled from above the β transus.

(a) Band contrast map.

(b) Standard EBSD data, IPF map.

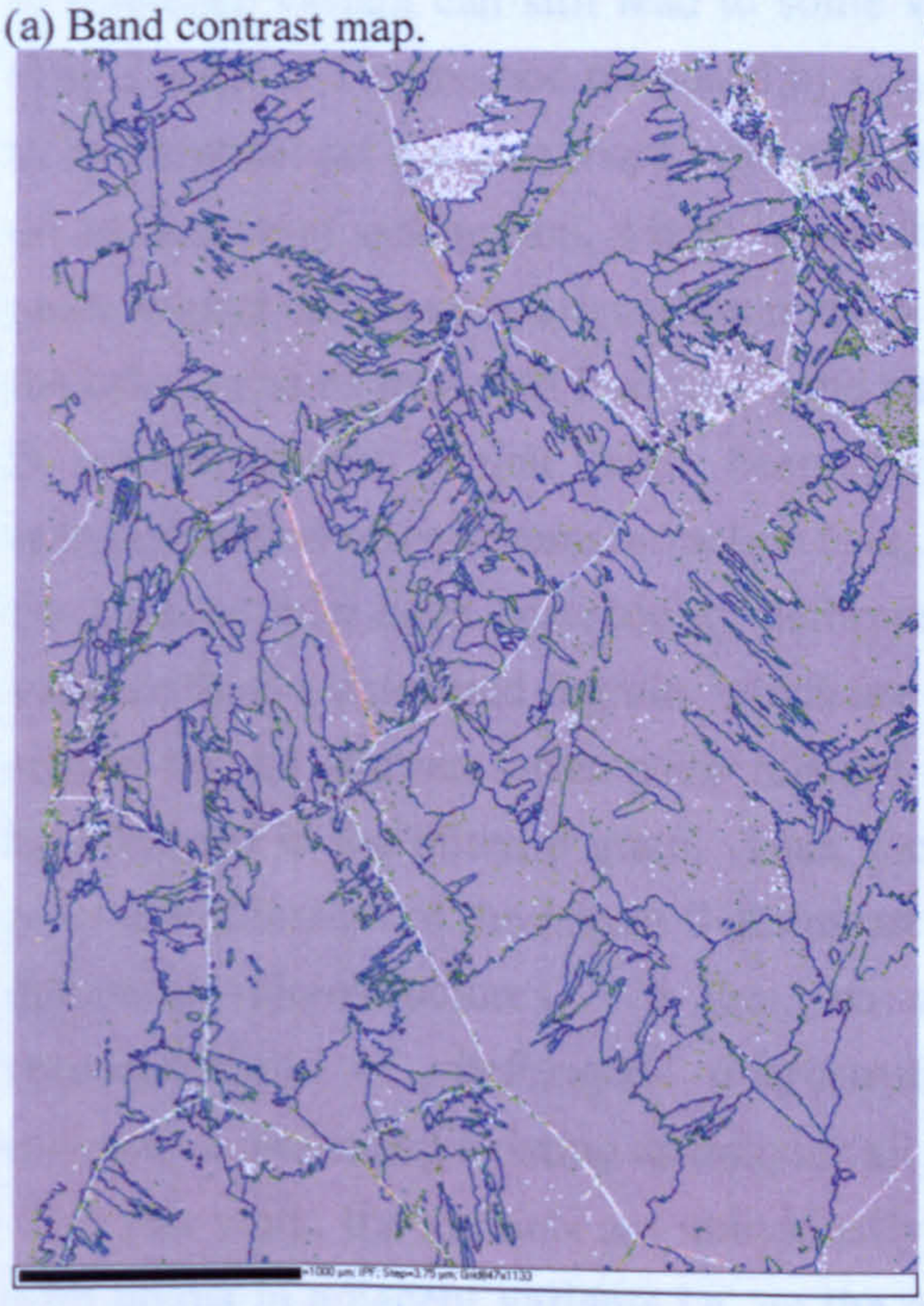

(c) Misorientations > 3° are coloured according to their deviation from the Burgers relation.
Deviations > 6° are coloured white.

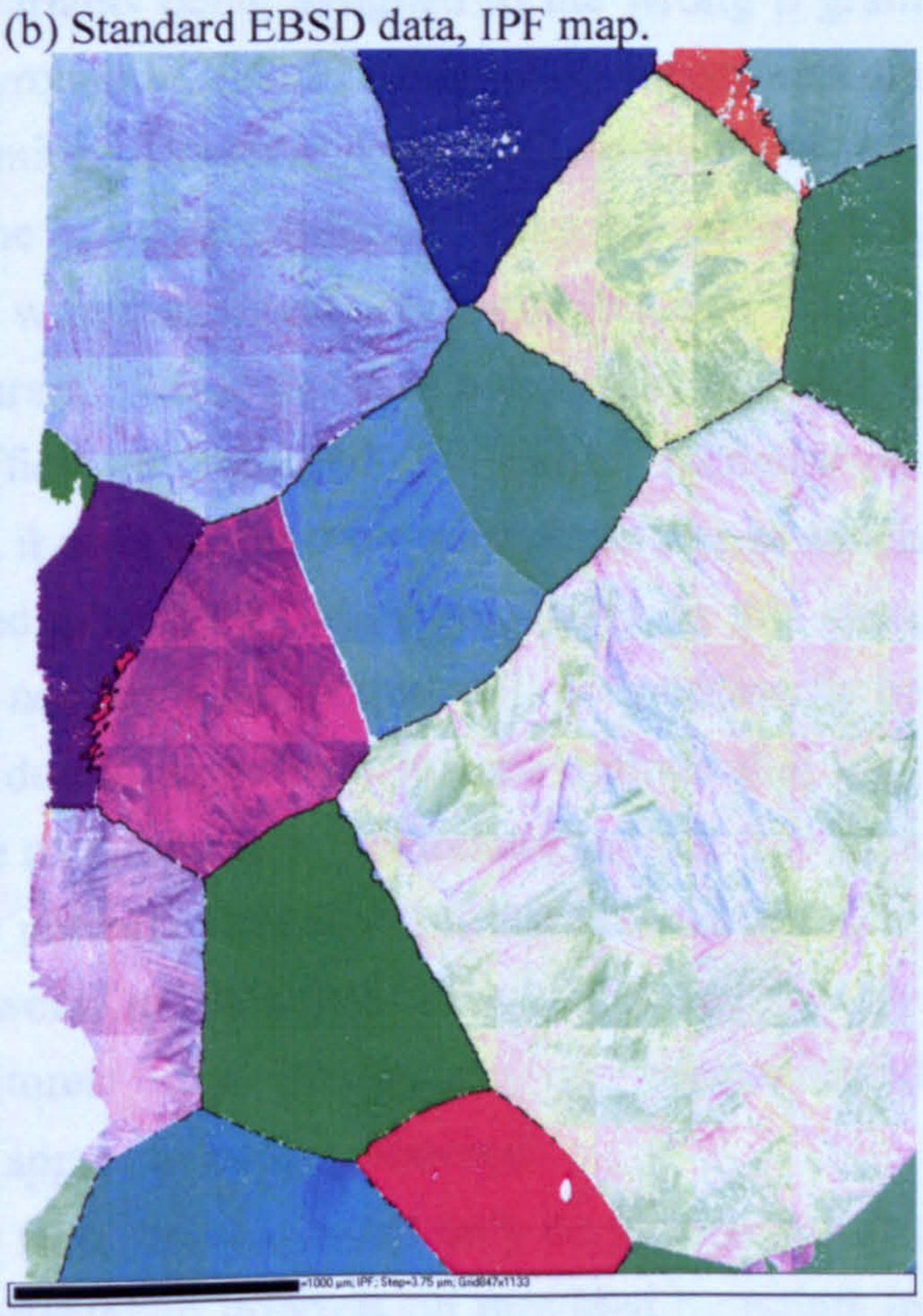

(d) reconstructed β, IPF map.

Fig. 4.32 Standard and reconstructed EBSD data for a 100% α_s furnace cooled microstructure in a specimen of Timetal 6242. A step size of 3.75μm was used.

4.6.6 An Appraisal of the Variant Based β Reconstruction Technique

The main difference between the approach developed in this work and those of previous authors is that it is a variant based reconstruction as opposed to a grain based reconstruction, and as a result is much better suited to the reconstruction of microstructures in which the β phase may be highly deformed. This is because the grain based reconstruction methods rely on a prior identification of the parent β grains i.e. which α_s variants belong to which parent. As was discussed in the literature review and illustrated in Fig. 2.39(a), gathering together the variants belonging to each β grain cannot be accomplished simply by using the misorientations between neighbouring variants because some prior β boundaries will coincide with the specific misorientations between variants inherited from the same grain. As a result, this neighbour to neighbour approach inevitably leads to incorrectly unified β grains and subsequent errors in the reconstructed orientations. To overcome the ambiguities introduced by the neighbour to neighbour approach, Germain *et al*, (2007) introduced a third reference variant (Fig. 2.39(c)). This is a relatively computationally fast approach to the problem but depending on the choice of reference variant can still lead to some variants being assigned to the wrong β grain (Fig. 2.39(d)). The method proposed by Cayron *et al*. (2006) using group theory appears to be more robust but also more time consuming. However, both of these solutions rely on an important assumption, which is that the α_s variants inherited from the same parent grain respect the Burgers orientation relation with their direct neighbours but also with all the other variants inherited from the same parent. While this assumption may be valid in β microstructures which have been sufficiently restored by either recovery or recrystallisation prior to transformation to α_s, it does not hold for microstructures in which the β phase may have been highly deformed prior to the transformation. In this case, variants from a deformed β grain, which are not direct neighbours will not necessarily be related by the Burgers orientation relation due to significant misorientations that may have existed in the initial β grain. Thus, the reconstruction methodologies that rely on a prior identification of the parent β grains are not very well suited to the reconstruction of deformed microstructures. In fact, no work to date has been published on the reconstruction of deformed microstructures; the examples of reconstructed microstructures using existing techniques all appear to be well restored.

In this work, the variants are individually reconstructed based only on misorientations with points in adjacent variants i.e. on the orientation information provided by points in direct contact with the variant itself. As a result, this approach is better suited to the reconstruction of deformed β microstructures. A potential problem with a variant based approach is that there may be fewer available variants with which to find a unique solution compared to a grain based approach. To overcome this, instead of simply calculating all six potential parents for the points adjacent to the variant, the

misorientations across a variant's boundary are used instead. By incorporating the misorientation analysis developed in the early work of Humbert *et al.* (1995), fewer potential parents are predicted for each point. In fact, in over 72% of cases a single parent solution results. Using these misorientation analyses greatly increases the likelihood that a single correct solution will be found for the parent orientation of each variant.

An additional advantage resulting from a variant based approach is that any reconstruction errors are always restricted to single variants and will readily stand out as inconsistencies in otherwise correctly reconstructed β grains. In a grain based approach, any errors in the reconstruction may present themselves in larger areas of the reconstructed map and be less apparent.

A potential disadvantage of the variant based approach may be for transformations, notably where diffusion is involved, where the Burgers orientation relations are not so strictly observed. In the misorientation analyses, one typically accepts a misorientation as a valid Burgers type if it is within a defined tolerance (say 5°) of the ideal orientation relation. If a significant number of misorientations did not meet the tolerance value or the tolerance has to be set too high in order to include sufficient misorientations, then either a poor level of reconstruction or errors in the reconstructed orientations may result. In such cases, a grain based reconstruction may prove more efficient. However, tests on a range of microstructures and different alloys have shown that the variant based approach works well for a range of α_s morphologies. Lower adherence to the Burgers relation is seen for slower cooled bimodal microstructures in some cases but where this reaches a level that may cause problems in the reconstruction program; there are in general too few variants per β grain for a successful β reconstruction by any means i.e. in some cases, the EBSD analysis may reveal only one variant per β grain in that particular 2-d section, which does not allow one to find a single solution for the parent grain.

Tests with different α_s datasets have shown that the variant based reconstruction technique is robust and capable of accurately reconstructing β microstructures in a variety of titanium alloys, for both high and low resolution maps and for a range of α_s morphologies. The variant based approach means that the technique can reconstruct deformed as well as restored β microstructures. When combined with the direct phase separation technique, the technique can be used to efficiently reconstruct the α_s phase in bimodal microstructures.